Transactions of the ASME®

Journal of Fluids Engineering

Published Quarterly by The American Society of Mechanical Engineers

VOLUME 110 • NUMBER 4 • DECEMBER 1988

(Contents continued on page 372)

Transactions of the ASME, The Journal of Fluids Engineering (ISSN 0098-2202) is published quarterly (Mar., June, Sept., Dec.) for $100 per year by The American Society of Mechanical Engineers, 345 East 47th Street, New York, NY 10017. Second class postage paid at New York, NY and additional mailing offices. POSTMASTER: Send address changes to The Journal of Fluids Engineering, c/o THE AMERICAN SOCIETY OF MECHANICAL ENGINEERS, 22 Law Drive, Box 2300, Fairfield, NJ 07007-2300.
CHANGES OF ADDRESS must be received at Society headquarters seven weeks before they are to be effective. Please send old label and new address.
PRICES: To members, $29.00, annually: to nonmembers, $100. Add $15.00 for postage to countries outside the United States and Canada.
STATEMENT from By-Laws. The Society shall not be responsible for statements or opinions advanced in papers or . . . printed in its publications (B7.1, Par. 3),

INDEXED by Applied Mechanics Reviews and Engineering Information, Inc.

Contents (Continued)

Laser Velocimeter Measurements in a Model Propeller Flowfield

J. Lepicovsky
Lockheed Aeronautical Systems Company
Georgia Division
Marietta, Ga.;
Present address:
TEXTRON Lycoming,
Stratford, Conn.

The objective of this work was to demonstrate the usability of a laser velocimeter data acquisition and reduction techniques for ensemble-averaged velocity measurements near and between rotating propeller or fan blades. A relatively simple experiment was set up to measure the flowfield of a two-bladed model propeller operating at static (non-flight) conditions to verify the data reduction procedures. The mean velocity and ensemble-averaged blade-to-blade velocity distributions were acquired. The experimental results, plotted in a novel consise form, showed separated and reversed flow regions on a rotating static propeller. The flowfield distortion along the blade height in the vicinity of the propeller disc was also observed.

Introduction

Current interest in propfan, unducted fan, and counter-rotating propeller technology will drive an upsurge in experimental studies of the flow phenomena involved in these propulsion-system components. A full understanding of the details of complex, three-dimensional propeller or propfan flowfields, including their interaction with wing or fuselage segments, is important before successful applications of propfan technology to production aircraft can be achieved. Improved measurements of propeller flowfield which are needed dictate the use of advanced, noninvasive experimental techniques in propeller research.

The laser velocimeter is probably the most suitable choice for nonstationary propeller-flowfield measurements. Early experiments using laser velocimetery for measurements in fluid machinery are summarized in reference [1]. Recent results are reported in references [2 through 10].

The study described in this paper had two objectives. The first objective was to verify the feasibility of mean and nonstationary phase-locked (ensemble-averaged) flowfield measurements about a rotating static propeller using a laser velocimeter. The second objective was to develop data reduction and presentation routines to "visualize" in a concise, short, and understandable form the preponderance of acquired experimental data. The paper presents additional results from the experimental effort previously reported in reference [7].

Technical Approach

The laser velocimeter used in this study was a Doppler type, two-color, four-channel system design and manufactured by the Georgia Division of the Lockheed Aeronautical Systems Company. The system can measure two velocity components simultaneously. It was arranged in the forward-scatter mode with the collecting optics placed 30 deg off axis. The effective length of the measurement volume was 1 mm, and its diameter was 0.15 mm. Before each test run, the measurement volume was aligned with a fine notch mark on the blade to "home" the traverser with respect to the propeller coordinate system; positioning accuracy was better than ±0.25 mm. The seeding particles were generated by heating oil to create a fog, and the average particle diameter was 0.9 μm. During the experiments, the average validated data rate was between 500 to 2000 samples per second (peak values up to 3000 validated samples per second). Additional details may be found in references [1 and 7].

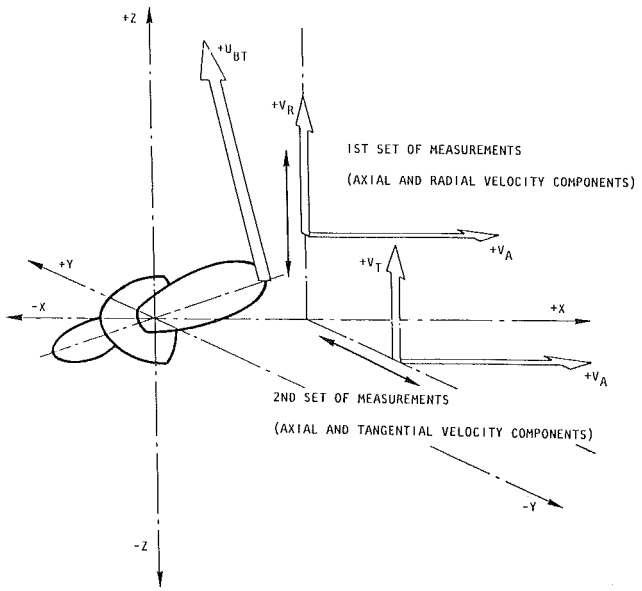

Fig. 1 Propeller coordinate system

Contributed by the Fluids Engineering Division for publication in the JOURNAL OF FLUIDS ENGINEERING. Manuscript received by the Fluids Engineering Division August 27, 1986.

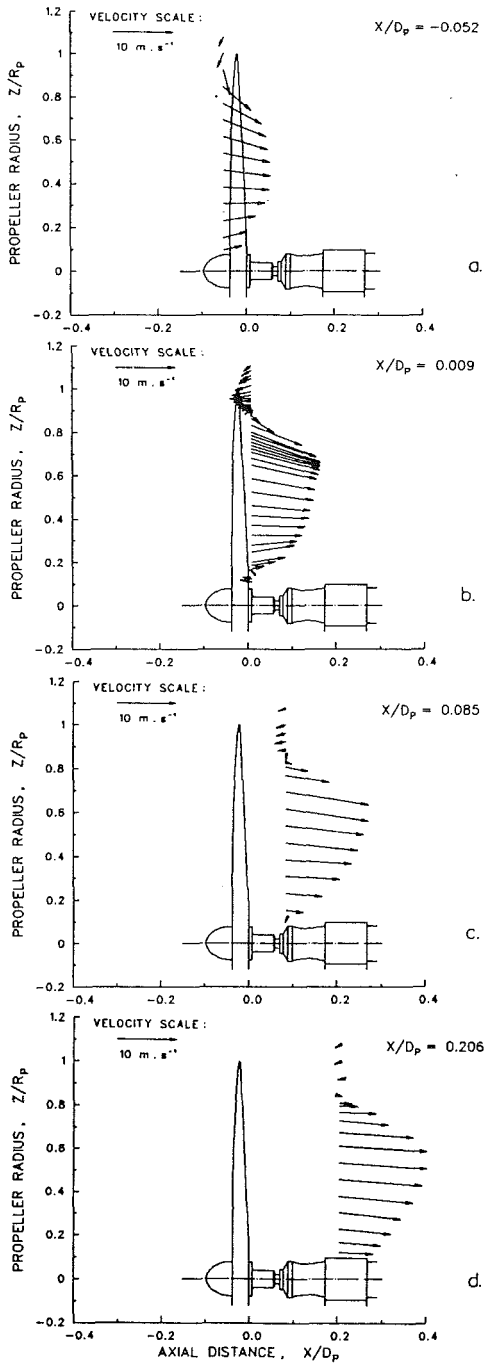

Fig. 2 Flow patterns in axial-radial plane. Velocity uncertainity ±0.3 m/s.

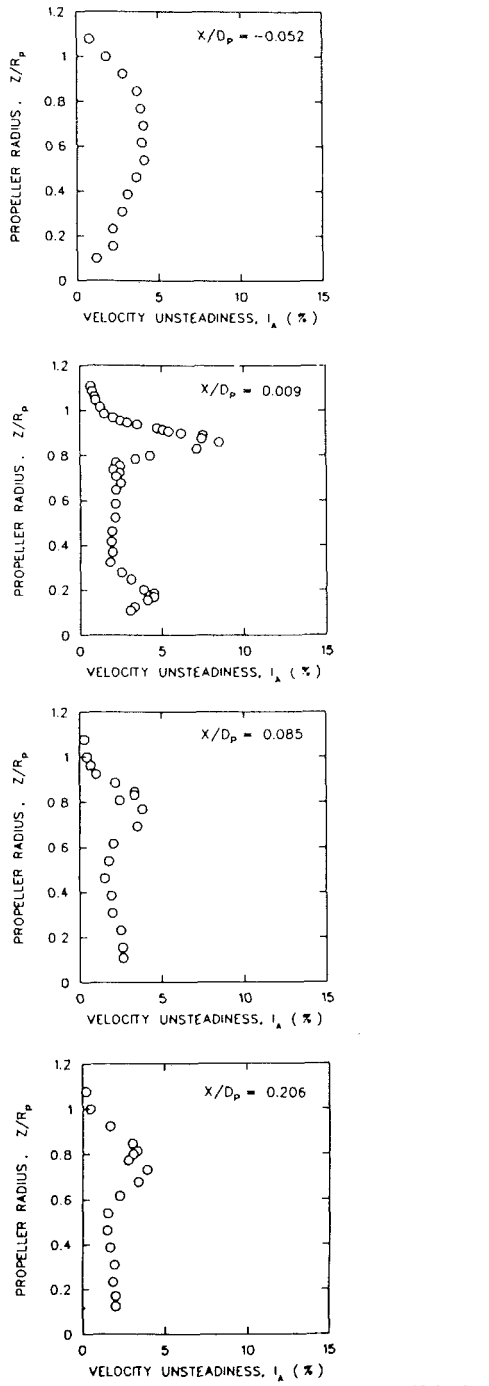

Fig. 3 Radial profiles of axial velocity unsteadiness. Velocity unsteadiness uncertainity ±0.2 percent.

A unique data-reduction subroutine enabling phase-locked conditional sampling and ensemble averaging, as needed for nonstationary measurements in periodic flowfields, has been included in this laser velocimeter system in 1982 [1, 7]. To verify this ensemble averaging subroutine, a relatively simple experiment was set up to measure the flowfield of a propeller

Nomenclature

c = blade cord
D = propeller tip diameter
I = total velocity unsteadiness (turbulence + periodic unsteadiness)
M = Mach number
n = number of revolutions
R = propeller tip radius
U = circumferential velocity
V = absolute mean velocity
X, Y, Z = coordinates
ν = local absolute velocity
θ = circumferential position
ω = blade angular position

Subscripts

A = axial
BT = blade tip
P = propeller
R = radial
T = tangential

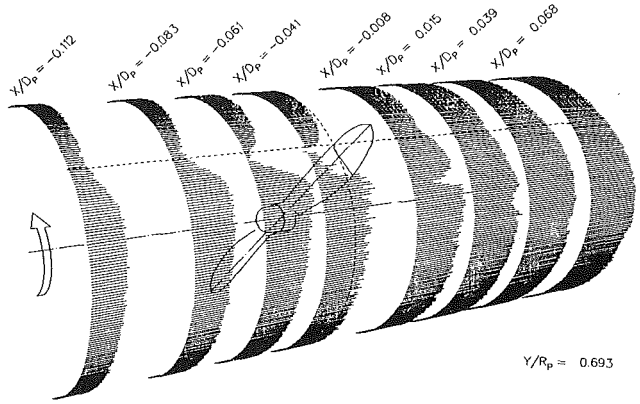

Fig. 4 Static-propeller phase-locked axial velocity field

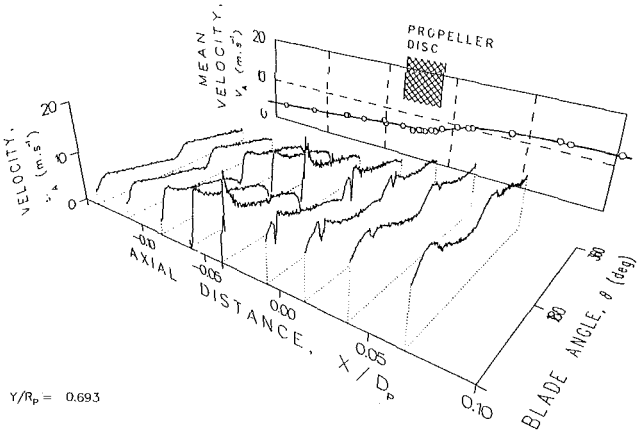

Fig. 5(a)

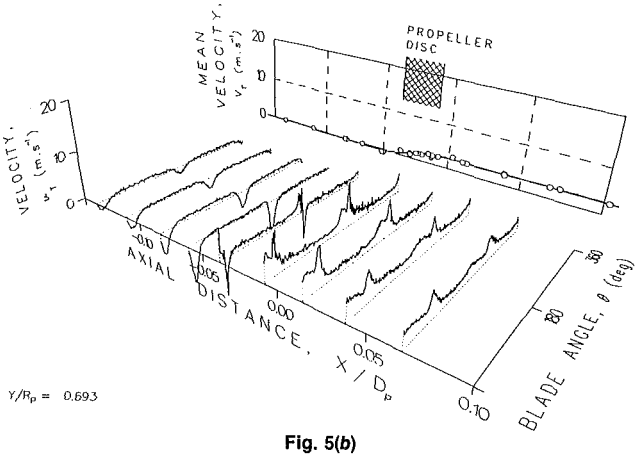

Fig. 5(b)

Fig. 5 Static-propeller phase-locked velocity field. Axial distributions: (a) Axial component; (b) Tangential component.

operating at static (non-flight) conditions. A two-bladed, wooden, model airplane propeller with a diameter of 330.2 mm was used. This was driven by a pneumatic motor through a flexible shaft. The propeller was run at only one speed of $n_p = 4250$ rpm. The corresponding blade tip velocity and average blade-tip Mach number were $U_{BT} = 73.5$ m/s and $M_{BT} = 0.215$. The propeller geometrical characteristics are given in reference [1].

The experimental program consisted of acquiring time-averaged (mean) and ensemble-averaged (blade-to-blade) distributions of velocity and velocity unsteadiness data for all three velocity components. Because Lockheed's laser velocimeter, at the time of this study, enabled simultaneous measurement of only two velocity components, two sets of

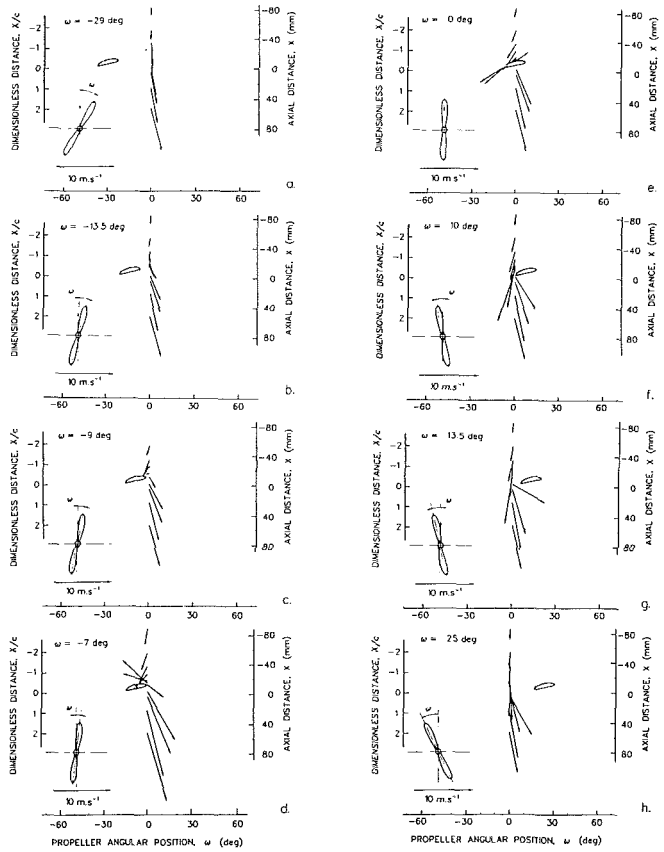

Fig. 6 Flow pattern in axial-tangential plane at $Y/R_p = 0.693$, $Z/R_p = 0$. Velocity uncertainity ± 0.3 m/s.

measurements were needed to acquire all three components, as indicated in Fig. 1. Along the X-axis, the distributions of velocity and unsteadiness components were measured at a given radial station, and radial profiles of these components were also acquired at four axial stations. Finally blade-to-blade distributions were measured at selected locations in front of and behind the propeller disc. Blade-to-blade distributions are plotted with a circumferential resoltuion of 1 deg. Each point in these distributions represents an average of 100 ± 40 validated LV samples.

Experimental Results

Mean Flow Patterns. Mean-velocity and velocity-unsteadiness intensity profiles measured very close to the propeller disc reveal that part of the propeller disc experiences a reverse flow at the given test conditions. To further examine the mean flow pattern, the vector plots of the mean velocity component in the axial-radial plane were generated. These vector plots, for four axial stations, are shown in Fig. 2. The regions of flow separation and reversed flows at the blade tip and hub sections are clearly visible at measurement stations behind the propeller disc. The axial velocity-unsteadiness profiles acquired at the same axial locations, shown in Fig. 3, indicate corresponding regions of increased intensity of the velocity unsteadiness; and as expected, the velocity-unsteadiness level reaches its local maxima in the regions of flow separation. The velocity unsteadiness was computed as a root mean square standard deviation of local velocity fluctuations normalized by blade tip velocity U_{BT}.

Axial Distributions. A general view of the ensemble-averaged, axial-velocity flowfield measured at different axial stations in the vicinity of the propeller disc is shown in Fig. 4. The experimental data are arranged in a form in which the ax-

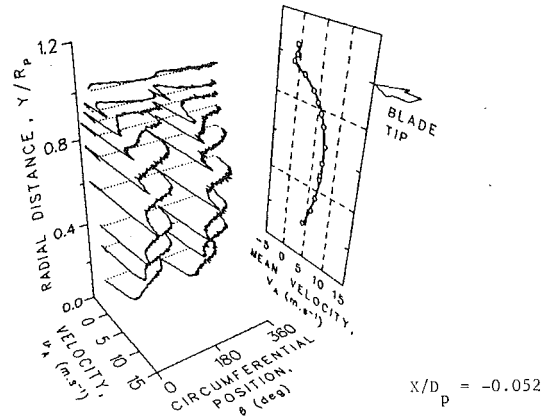

Fig. 7(*a*)

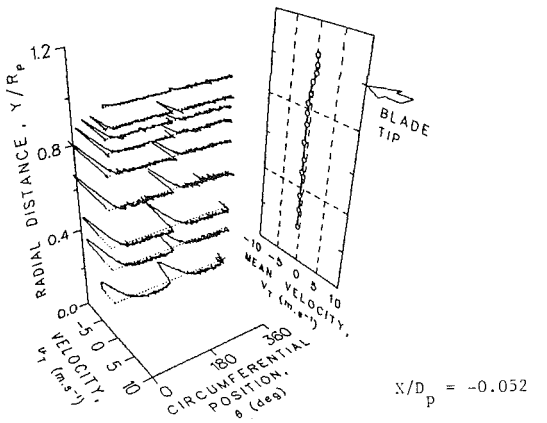

Fig. 7(*b*)

Fig. 7 Static-propeller phase-locked velocity field. Radial distributions: (*a*) Axial component; (*b*) Tangential component.

ial velocity at a dimensionless radius of 0.69 would be seen if the flowfield were visualized by strobing the flow synchronously with the propeller revolutions. The figure shows the flowfield distortion in front of the propeller disc due to the propeller presence and the decay of the viscous blade wake behind the propeller.

The blade-to-blade distributions of the ensemble-averaged axial and tangential velocity components, for locations just ahead of and just behind the propeller disc, are shown in Fig. 5 together with the corresponding mean velocity distributions. In this figure, the mean velocity distribution is plotted on the background grid in each plot, whereas the blade-to-blade distributions are shown in front of the plot. Points on the mean velocity curves represent the time-averaged values of the ensemble-averaged blade-to-blade velocity distributions. The ensemble-averaged distributions confirm the results of the mean velocity measurements, but in addition, they also show a significant nonuniformity of the measured parameters in the circumferential direction. This innovative way of result plotting clearly illustrates the inadequacy of mean velocity measurements alone to describe all the aspects of flow behavior about a rotating propeller.

Local Induced Flow. To visualize the changes in the flowfield due to the blade-induced local flow, a sequence of vector plots was generated from measurements at different axial stations. These plots, depicted in Fig. 6, are restricted to two-dimensional velocity changes only, in the axial and tangential directions. The plots are generated at a propeller dimensionless radius of 0.69. A small insert has been included in each of the plots to help visualize the relative position of the

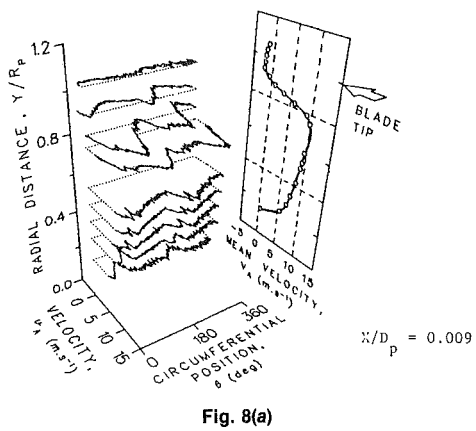

Fig. 8(*a*)

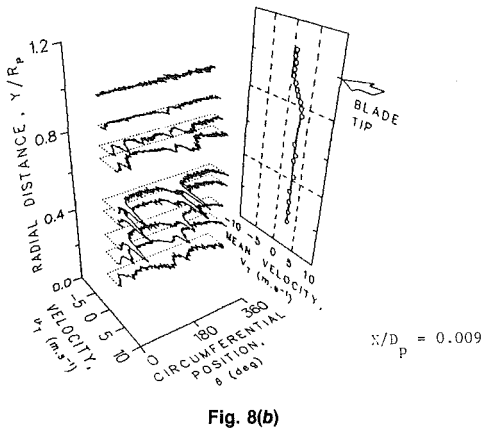

Fig. 8(*b*)

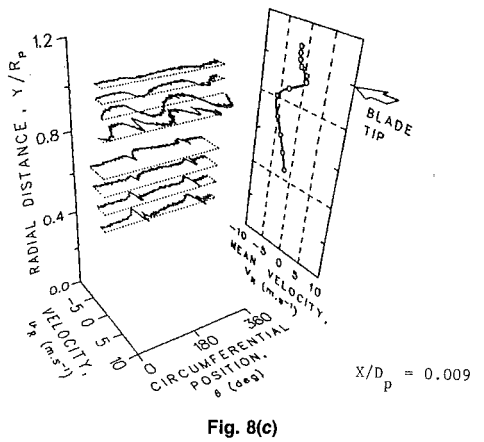

Fig. 8(*c*)

Fig. 8 Static-propeller phase-locked velocity field. Radial distributions: (*a*) Axial component; (*b*) Tangential component; (*c*) Radial component.

propeller blade and the axial line of measurement stations. Axial distances from the blade profile trailing edge along the line of measurements are expressed in fractions of the local blade chord ($c = 28$ mm).

As the blade approaches the line of measurements, the effect of the blade presence becomes more and more visible (Fig. 6(*a*, *b*)). The flow in front of the propeller starts to turn against the blade motion (Fig. 6(*c*)) and even reverses in the axial direction in the region close to the stagnation point on the blade surface (Fig. 6(*d*, *e*)). Also, a velocity increase is seen downstream of the propeller blade (Fig. 6(*d*)). As the blade leaves the line of measurements, a large velocity increase is observed at the trailing edge (Fig. 6(*e*, *f*)). With increasing distance of the blade from the line of measurements, wake development and its subsequent decay is observed. Due to the small relative velocity of the fluid in the blade wake, the absolute velocity of the fluid in the wake has a different flow direction from the rest of the fluid outside the wake and, thus,

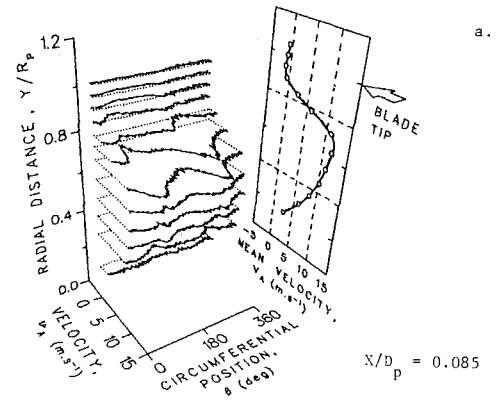

Fig. 9(a)

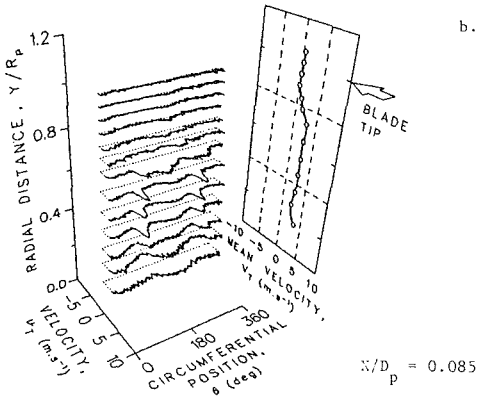

Fig. 9(b)

Fig. 9 Static-propeller phase-locked velocity field. Radial distributions: (*a*) Axial component; (*b*) Tangential component.

generates the propeller flow swirl (Fig. 6(*g*, *h*)).

Radial Distributions. The variation of the blade-to-blade velocity distributions along the blade height is shown in Figs. 7 through 9. These radial distributions were measured at the axial stations identical to those of the first three mean velocity patterns shown in Fig. 2. In Figs. 7 and 9, only the axial and tangential velocity components are shown; Fig. 8 includes also the blade-to-blade radial velocity distributions. The plots in these figures are arranged similarly to those of Fig. 5, showing simultaneously the results of the mean and ensemble-averaged measurements.

The figures show interesting features of the propeller velocity flowfield in the separated and reversed flow region at the blade tip. Viscous wakes can be seen in front of the propeller disc due to the reverse flow direction (second profile from the top in Fig. 7(*a*)), whereas in the unseparated flow region, the figure shows potential flow distributions in front of the propeller disc. Behind the propeller, axial velocity component shows violent velocity fluctuations in the separated flow region (Figs. 8(*a*) and 9(*a*)). The radial velocity component also experiences severe velocity fluctuations in the same region (Fig. 8(*c*)). Tangential velocity component, however, does not seem too affected to the same extent as the axial and radial velocity components (Figs. 7(*b*), 8(*b*), and 9(*b*)). In brevity, the ensemble-averaged, blade-to-blade distributions reveal significant details which could not be seen if only mean velocity measurements were available.

Summary of Results

A summary of key observations and conclusions is given below:

The presented results confirm the ability of Lockheed's laser-velocimeter system to conduct detailed and efficient measurements in three-dimensional, complex flowfield of a rotating propeller.

Data reduction and presentation procedures can "visualize" extensive sets of experimental data in a short, concise form for a quick qualitative evaluation of the nonstationary flowfield behavior.

Separated and reversed flow regions were locally observed on a rotating propeller under static (non-flight) conditions.

Blade-to-blade velocity distributions revealed important details of the propeller flowfield development.

The blade-induced, local flow pattern has been reconstructed from ensemble-averaged velocity measurements.

Acknowledgment

This work was conducted under Lockheed-Georgia IRAD funding. The author is grateful to Dr. H. K. Tanna for initiating this work and to Dr. K. K. Ahuja for his support throughout the course of this work. Technical help from Dr. W. A. Bell is particularly acknowledged.

References

1 Lepicovsky, J., and Bell, W. A., "Aerodynamic Measurements about a Rotating Propeller with a Laser Velocimeter with Conditional Sampling," Lockheed-Georgia Co., Report LG83ER0008, 1983.

2 Powell, J. A., Strazisar, A. J., and Seasholtz, R. G., "Efficient Laser Anemometer for Intra-Rotor Flow Mapping in Turbomachinery," ASME *Journal of Engineering for Power*, Vol. 103, 1981, pp. 424–429.

3 Strazisar, A. J., and Powell, J. A., "Laser Anemometer Measurements in a Transonic Axial Flow Compressor Rotor," ASME *Journal of Engineering for Power*, Vol. 103, 1981, pp. 430–437.

4 Gill, M. E., Forster, C., and Elder, R. L., "Analysis of Laser Doppler Anemometer Data Arising from High Speed Turbomachinery Studies," Measurement Techniques in Turbomachines, VKI Lecture Series 1981–1987, 1981.

5 Neumann, H. E., and Serafini, J. S., "LV Measurements with an Advanced Turboprop," Flow Visualization and Laser Velocimetry for Wind Tunnels, NASA CP2243, 1982, pp. 253–256.

6 Neumann, H. E., Bober, L. J., Serafini, J. S., and Chang, L. K., "An Analytical and Experimental Comparison of the Flow Field of an Advanced Swept Turboprop," AIAA Paper, AIAA-83-0184, 1983.

7 Lepicovsky, J., and Bell, W. A., "Aerodynamic Measurements about a Rotating Propeller with a Laser Velocimeter," *Journal of Aircraft*, Vol. 21, 1984, pp. 264–271.

8 Murthy, K. N. S., and Lakshminarayana, B., "Laser Doppler Velocimeter Measurements in the Tip Region of a Compressor Rotor," AIAA Paper, AIAA-84-1602, 1984.

9 Kobayashi, S., "Propeller Wake Survey by Laser-Doppler Velocimeter," Laser Anemometry in Fluid Mechanics," IST Lisbon, 1984, pp. 195–209.

10 Jessup, S. D., Schott, C., Jeffers, M., and Kobayashi, S., "Local Propeller Blade Flows in Uniform and Sheared Onset Flows Using LDV Techniques," 15th ONR Symposium on Naval Hydrodynamics, Hamburg, 1984.

Experimental and Numerical Study of the Response of an Axial Compressor to Distorted Inlet Flow

G. Billet

J. Huard

P. Chevalier

P. Laval

Office National d'Etudes et de Recherches Aérospatiales
BP 72 - 92322 Châtillon Cedex, France

A model representing the response of fixed or rotating axial compressor blade-rows is coupled to a 3-D numerical simulation of the flow outside the blade rows. The code can be used to study nonuniform compressible 3-D flows through turbomachines. The fluid is assumed to be inviscid in the space outside the rows, while the viscous effects are taken into account inside. Numerical results are compared with experimental data obtained on a test stand with steady distorted inflow. This comparison shows that this numerical approach is capable of predicting the response of the compressor. This work is part of a larger project aimed at predicting the response of a compressor to a nonuniform inlet flow that is periodic in time, or fully unsteady.

1 Introduction

Many aircraft flight configurations can create difficult operating conditions for the engines; these problems are related to air inlet disturbances which often result in a substantial decrease in the compressor surge margin. It is now known that the performance and operational stability of axial compressors are sensitive to nonuniformities in the inlet section. Such nonuniformities mainly consist of low frequency bursts. In extreme cases, this distortion in the engine inlet section can result in the stalling of the compressor with such detrimental effects on the operation of the engine as blowout of the combustion chamber. Since linearized methods [1] would have, in this case, insufficient accuracy, a numerical approach is the only way to analyze this complex problem of a compressor subjected to strong aximuthal distortions in the inlet section or operating near the stall limit at a high back pressure and low flow rate where small disturbances can be considerably amplified. In the nonlinear domain, the problem has mainly been approached by using 2D models [2–5]. However, Greitzer and Strand [6] have shown that superimposing substantial swirling and nonuniformities of the total pressure produced 3D effects which cannot be accounted for by 2D approaches. Under these conditions, it appeared necessary to develop a more complete numerical model capable of taking into account the radial effects as well as the azimuthal phenomena. With this aim, this paper is devoted, in particular, to the numerical analysis of compressible, unsteady, nonuniform, 3D flows in a single stage axial compressor with steady distorted inflow.

The numerical approach based on a fully unsteady finite difference splitting-up method has been developed to analyze an inviscid nonuniform flow in an annular channel, simulating the engine duct located upstream of the compressor [7]. In the work discussed, we used this approach to solve the Euler equations in the blade-free domain. In the fixed or rotating blade rows, the equations are solved by coupling the global equations modeling the behavior of the blade rows with the Euler equations used in the blade-free domain. This unsteady model with an essentially phenomenological basis associates three integral equations (conservation of mass, momentum and energy) and two time-lag equations for the pressure loss coefficient and the outlet flow angle. A final equation relative to the radial variation of the streamline through the blade rows is used to close the system of equations which relates the various aerothermodynamic values defined, respectively upstream and downstream of each blade row.

The comparisons of numerical and experimental results have been realized at several stations, in particular at the stations upstream and downstream of the rotor, where a detailed experimental study has been made.

2 Principle of the Method

The computation domain consists of an annular channel with a variable section limited by the inner and outer casings of the machine and by an inlet plane and an outlet plane located upstream of the first blade row and downstream of the last blade row respectively.

To simplify the numerical process, the annular physical field is transformed into a parallelpiped computation domain by a linear transformation:

$$r \to R = \frac{r - r_i(z)}{r_e(z) - r_i(z)}. \tag{1}$$

The surfaces of the hub and the outer casing, generated by meridians $r_i(z)$ and $r_e(z)$ respectively, are represented by planes $R=0$ and $R=1$ in the transformed domain.

Contributed by the Fluids Engineering Division for publication in the JOURNAL OF FLUIDS ENGINEERING. Manuscript received by the Fluids Engineering Division February 5, 1987.

(a) Equations Solved in the Blade-Free Domain. As the flow is assumed inviscid in this domain, we consider the system of Euler equations:

$$\frac{\partial \bar{U}}{\partial t}+\frac{\partial \bar{F}(\bar{U})}{\partial z}+\frac{\partial \bar{G}}{\partial \theta}(\bar{U},\theta,r)+\frac{\partial \bar{H}}{\partial r}(\bar{U},\theta)=0, \tag{2}$$

expressed in the (r, θ, z) reference frame related to the compressor channel.

$$\bar{U}=r\begin{bmatrix}\rho\\ \rho V_z\\ \rho(V_r\sin\theta+V_\theta\cos\theta)\\ \rho(V_r\cos\theta-V_\theta\sin\theta)\\ E\end{bmatrix},$$

where E represents the total energy-per-unit volume which, in the case considered of a perfect gas ($\gamma=$ const.), is expressed:

$$E=\frac{p}{\gamma-1}+\frac{1}{2}\rho V^2.$$

Transformation (1) preserves the conservative character of system (2) of equations which is then expressed in the new coordinate system $Z=z$, $\Theta=\theta$, R, t:

$$\frac{\partial U}{\partial t}+\frac{\partial F}{\partial Z}(U)+\frac{\partial G}{\partial \Theta}(U,Z,\Theta,R)+\frac{\partial H}{\partial R}(U,Z,R)=0 \tag{2'}$$

where $U=\bar{U}\bar{r}$. The expressions for the components of vectors F, G, and H are given in [7].

(b) Modeling of the Blade Rows. Computation of the "true" 3D flow in all of the blade-to-blade channels of a compressor stage cannot be contemplated with computers currently available as the processing times are prohibitive. We will have to wait for the next generation of computers to perform these computations.

This is why we have chosen the modeling of the flow in the blade rows, which obviates the need to use a mesh inside the blade rows. This makes it possible to analyze the physical phenomena in a complete compressor with a reasonable number of grid points. However, the models used give only a general approximation of the physical phenomena and often require experimental values (in particular concerning the pressure-loss coefficient χ and the outlet angle in a relative reference frame β_2) to make up for the lack of information inside the blade rows.

The model, similar to a semi-actuator disk, is obtained by a simplification of the full Navier-Stokes equations written in conservative form. These equations are first integrated in a stream tube (Ω). Each domain (Ω) is limited by the profiles of two adjacent blades in the aximuth direction, by the inlet and outlet sections of the blade-to-blade channel in the axial direction and by two stream surfaces in the radial direction (Fig. 1). Letting $\partial\Omega$ represent the boundary surrounding (Ω), the three equations can be expressed in the relative reference frame after a few calculations [8]:

$$\left.\begin{aligned}
&(a)\quad \int_\Omega \frac{\partial \rho}{\partial t}\,d\Omega+\int_{\partial\Omega}\rho v\cdot n\,d\Omega=0,\\
&(b)\quad \int_\Omega \frac{\partial}{\partial t}\left(\rho\frac{v^2}{2}-\rho\frac{\omega^2 r^2}{2}\right)d\Omega\\
&\qquad+\int_{\partial\Omega}\left(p+\rho\frac{v^2}{2}-\rho\frac{\omega^2 r^2}{2}\right)vn\,d\Omega-\int_\Omega p\ \mathrm{div}\ v\,d\Omega\\
&\qquad+\int_\Omega \rho r(v_\theta+\omega r)\frac{d\omega}{dt}\,d\Omega=\mathcal{P},\\
&(c)\quad \frac{1}{\gamma-1}\int_\Omega\frac{\partial p}{\partial t}\,d\Omega+\int_\Omega p\ \mathrm{div}\ v\,d\Omega\\
&\qquad+\frac{1}{\gamma-1}\int_{\partial\Omega} p\,v\cdot n\,d\Omega=-\mathcal{P},
\end{aligned}\right\} \tag{3}$$

where:

$$\mathcal{P}=-\int_{\partial\Omega}\mathcal{P}^r_{\mathrm{ext}}(\sigma)d\Omega+\int_\Omega \dot{q}\,d\Omega+\omega\int_\Omega\sigma_{r\theta}\,d\Omega-\int_\Omega\rho\,T\frac{ds}{dt}\,d\Omega.$$

It is obvious that equations (3) cannot be used in this form

Nomenclature

r, θ, z = cylindrical coordinates in the physical domain
R, Θ, Z = coordinates in the transformed reference frame
t = time
V = absolute velocity
v = relative velocity
V_r, V_θ, V_z = components of the absolute velocity
v_r, v_θ, v_z = components of the relative velocity
ω = angular velocity of the rotor (may depend on time)
γ = ratio of the specific heats
c = local speed of sound
M = local Mach number
φ = radial flow angle
β = relative azimuthal flow angle
ρ = density
p = static pressure
P = total pressure
T = absolute temperature
s = specific entropy
$\dot{q}$ = heat rate per unit volume
$\mathcal{P}^r_{\mathrm{ext}}(\sigma)$ = power of the external forces in the relative reference frame
$\sigma_{r\theta}$ = component of the tensor of the viscous stresses
χ = pressure loss coefficient
δ = cascade stagger angle
r = radius
$\tilde{r}$ = channel height
l_z = axial chord length
l = pitch
h = height of the stream tube
n = outward unit normal
N = number of blades in the cascade

Subscripts

1 = blade row inlet plane
2 = blade row outlet plane
i = hub
e = outer casing
ss = steady state

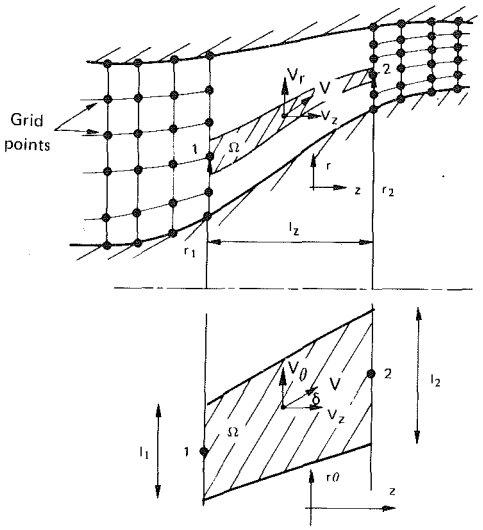

Fig. 1 Modeling of the blade rows in the physical plane

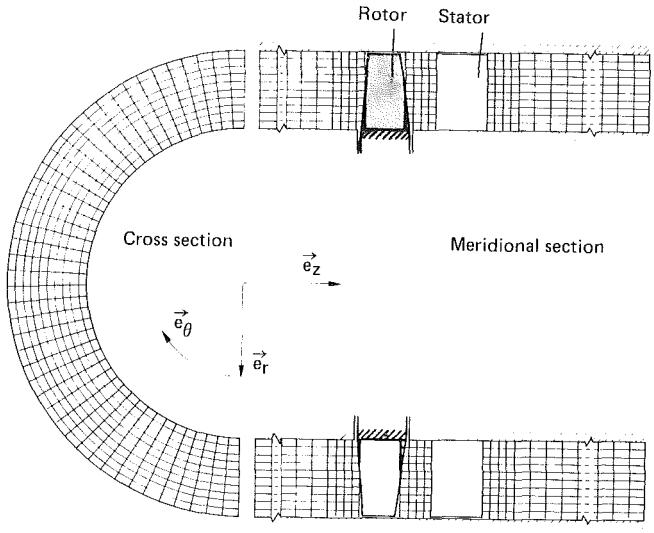

Fig. 2 Computational grid in the blade free domain

and that a few simplifying assumptions are necessary. We therefore assume that the aerothermodynamic variables:
– vary linearly along each stream tube (Ω);
– are constant in the inlet and outlet sections of the domain (Ω), i.e., that the wavelength of the circumferential disturbance is large with respect to the pitch.

We admit that in each stream tube (Ω):
– the flow is tangent to the blade profile:

$$v_\theta = v_z \tan\delta;$$

The radial evolution of the streamlines through the blade rows is known and is time-independent. It is given by a 2D meridional computation code at the initial time:

$$v_r = v_z\, r^{**} \text{ at } t = t_0, \text{ with } r^{**} = r^{**}(r) \tag{4}$$

Additionally assuming that the variation is adiabatic, that the viscous effects in the inlet and outlet sections are negligible and that the displacement thickness of the boundary layers on the profiles always remains low with respect to the pitch, the term $\mathcal{P}$ can be simplified as follows:

$$\mathcal{P} = -\int_\Omega \rho\, T \frac{ds}{dt}\, d\Omega.$$

Expressed in this way, this unsteady loss term is difficult to compute. Analogy with the steady loss term of an incompressible flow through fixed blade rows [3] suggests expressing $\mathcal{P}$ in discrete form by the equation:

$$\mathcal{P} = -\frac{1}{2}\,\rho_1\, v_1^2 \left(\frac{v_{z1}S_1 + v_{z2}S_2}{2}\right)\chi,$$

where $S_1 = h_1 l_1$ and $S_2 = h_2 l_2$ define the areas of the inlet and outlet sections, respectively, of the stream tube (Ω). χ is determined as in [2 to 5] by the following transfer model:

$$\tau\frac{\partial\chi}{\partial t} + \chi = \chi_{ss}. \tag{5}$$

Here, τ represents a time constant related to convection of the disturbances in the boundary layer. It is generally obtained by experimental measurements. The steady state loss term χ_{ss} is a concave parabolic function of β_1, different according to the value of the Mach number M_1 at the inlet of the blade row.

The unsteady equations (3) can then be expressed in a discrete form which relates the inlet values (density, specific axial kinetic energy and static pressure) at grid point 1 to the outer values at grid point 2 of the semi-actuator model (Fig. 1):

$$\frac{V_\Omega}{2}\frac{\partial}{\partial t}(\rho_1+\rho_2) + \rho_2 v_{z2}\, S_2 - \rho_1 v_{z1} S_1 = 0 \tag{6a}$$

$$\begin{aligned}
&\frac{V_\Omega}{4}\left(\tan^2\delta + 1 + \frac{(r_1^{**}+r_2^{**})^2}{4}\right)\frac{\partial}{\partial t}(\rho_1 v_{z1}^2 + \rho_2 v_{z2}^2) \\
&\quad - \frac{V_\Omega}{4}\frac{\partial}{\partial t}(\rho_1\omega^2 r_1^2 + \rho_2\,\omega^2 r_2^2) \\
&\quad + \left[(p_2 - p_1) + \left(\rho_2\frac{v_2^2}{2} - \rho_1\frac{v_1^2}{2}\right)\right. \\
&\left. - \left(\rho_2\frac{\omega^2 r_2^2}{2} - \rho_1\frac{\omega^2 r_1^2}{2}\right)\right]\left(\frac{v_{z1}S_1 + v_{z2}S_2}{2}\right) \\
&\quad + \frac{1}{4}(v_{z2}S_2 - v_{z1}S_1)(\rho_1 v_1^2 - \rho_1\omega^2 r_1^2 \\
&\qquad + \rho_2 v_2^2 - \rho_2\omega^2 r_2^2) \\
&\quad + \frac{V_\Omega}{2}\left[(\rho_1 r_1 v_{z1} + \rho_2 r_2 v_{z2})\tan\delta\right. \\
&\left. + \omega(\rho_1 r_1^2 + \rho_2 r_2^2)\right]\frac{d\omega}{dt} = \mathcal{P}'
\end{aligned} \tag{6b}$$

$$\begin{aligned}
&\frac{V_\Omega}{2(\gamma-1)}\frac{\partial}{\partial t}(p_1+p_2) + \left(\frac{p_1+p_2}{2}\right)(v_{z2}S_2 - v_{z1}S_1) \\
&\quad + \frac{1}{\gamma-1}(p_2 v_{z2}S_2 - p_1 v_{z1}S_1) = -\mathcal{P}'
\end{aligned} \tag{6c}$$

where:

$$\mathcal{P}' = \frac{N}{2\pi}\,\mathcal{P} \text{ and } V_\Omega = \frac{l_z}{3}\left[l_2\left(h_2 + \frac{h_1}{2}\right) + l_1\left(h_1 + \frac{h_2}{2}\right)\right]$$

represents the approximated volume of (Ω).

The variation of the rotor speed ω (equation 6*b*) can be taken into account and permits a study of the response of the compressor to acceleration and deceleration phases.

Grid points 1 and 2 also belong to the blade-free domain and the equations defined in this domain can be applied to them.

The axial velocity of the flow is assumed subsonic in the inlet and outlet planes of the blade rows. In this case, based on

the theory of the characteristics, we can integrate four equation for the inlet and a single one for the outlet. For inlet grid point 1, considering equation (4), one of the equations degenerates and the system is expressed as follows in the relative reference frame:

– inlet grid point 1:

$$v_{r_1} = v_{z_1} r_1^{**} \tag{7a}$$

$$\frac{\partial p_1}{\partial t} + \rho_1 c_1 \frac{\partial v_{z1}}{\partial t} + A_1 = 0 \tag{7b}$$

(along the characteristic line $C+$)

$$\frac{\partial \rho_1}{\partial t} + B_1 = 0 \tag{7c}$$

$$\frac{\partial v_{\theta_1}}{\partial t} + C_1 = 0 \tag{7d}$$

where

$$A_1 = (v_{z_1} + c_1) \frac{\partial p_1}{\partial Z} + \rho_1 c_1 (v_{z_1} + c_1) \frac{\partial v_1}{\partial Z} + \frac{\rho_1 {c_1}^2}{r_1} \frac{\partial v_{\theta_1}}{\partial \Theta}$$

$$+ \left(\frac{v_{\theta_1}}{r_1} - t \frac{d\omega}{dt} \right) \frac{\partial p_1}{\partial \Theta} + \rho_1 c_1 \left(\frac{v_{\theta_1}}{r_1} - t \frac{d\omega}{dt} \right) \frac{\partial v_{z_1}}{\partial \Theta}$$

$$+ \rho_1 c_1 (v_{z_1} + c_1) (r_1^{**} - r_1^{*}) \frac{\partial v_{z_1}}{\partial R} + \frac{1}{\tilde{r}_1} [v_{z_1} (r_1^{**} - r_1^{*})$$

$$- c_1 r_1^{*}] \frac{\partial p_1}{\partial R} + \frac{{c_1}^2 \rho_1 v_{z_1}}{r_1} \frac{\partial r_1^{**}}{\partial R} + \frac{c_1^2 \rho_1 v_{z_1} r_1^{**}}{r_1}$$

$$B_1 = \frac{\partial}{\partial Z} (\rho_1 v_{z_1}) + \left(\frac{v_{\theta_1}}{r_1} - t \frac{d\omega}{dt} \right) \frac{\partial \rho_1}{\partial \Theta} + \frac{\rho_1}{r_1} \frac{\partial v_{\theta_1}}{\partial \Theta}$$

$$+ \frac{r_1^{**} - r_1^{*}}{\tilde{r}_1} \frac{\partial}{\partial R} (\rho_1 v_{z_1}) + \frac{\rho_1 v_{z_1}}{\tilde{r}_1} \frac{\partial r_1^{**}}{\partial R} + \frac{\rho_1 v_{z_1} r_1^{**}}{r_1}$$

$$C_1 = v_{z_1} \frac{\partial v_{\theta_1}}{\partial Z} + \left(\frac{v_{\theta_1}}{r_1} - t \frac{d\omega}{dt} \right) \frac{\partial v_{\theta_1}}{\partial \Theta} + \frac{1}{\rho_1 r_1} \frac{\partial p_1}{\partial \Theta}$$

$$+ \frac{v_{z_1} (r_1^{**} - r_1^{*})}{\tilde{r}_1} \frac{\partial v_{\theta_1}}{\partial R} + 2\omega v_{z_1} r_1^{**} + \frac{v_{\theta_1} v_{z_1} r_1^{**}}{r_1} + r_1 \frac{d\omega}{dt}$$

– outlet grid point 2:

$$v_{r_2} = v_{z_2} r_2^{**} \tag{8a}$$

$$\frac{\partial p_2}{\partial t} - \rho_2 c_2 \frac{\partial v_{z_2}}{\partial t} + A_2 = 0 \tag{8b}$$

(along the characteristic line $C-$)

where:

$$A_2 = (v_{z_2} - c_2) \frac{\partial p_2}{\partial Z} - \rho_2 c_2 (v_{z_2} - c_2) \frac{\partial v_{z_2}}{\partial Z} + \frac{\rho_2 c_2^2}{r_2^2} \frac{\partial v_{\theta_2}}{\partial \Theta}$$

$$+ \left(\frac{v_{\theta_2}}{r_2} - t \frac{d\omega}{dt} \right) \frac{\partial p_2}{\partial \Theta} - \rho_2 c_2 \left(\frac{v_{\theta_2}}{r_2} - t \frac{d\omega}{dt} \right) \frac{\partial v_{z_2}}{\partial \Theta}$$

$$- \rho_2 c_2 (v_{z_2} - c_2) (r_2^{**} - r_2^{*}) \frac{\partial v_{z2}}{\partial R}$$

$$+ \frac{1}{\tilde{r}_2} [v_{z_2} (r_2^{**} - r_2^{*}) + c_2 r_2^{*}] \frac{\partial p_2}{\partial R} + \frac{c_2^2 \rho_2 v_{z_2}}{\tilde{r}_2} \frac{\partial r_2^{**}}{\partial R}$$

$$+ \frac{c_2^2 \rho_2 v_{z_2} r_2^{**}}{r_2}$$

In these expressions:

$$r_j^{*} = \tan \varphi_i + R (\tan \varphi_e - \tan \varphi_i), \; (j = 1,2).$$

A final equation is necessary to close the system. It makes use of transfer model on the unsteady outlet flow angle β_2.

This equation can be expressed as follows (see [2] for instance):

$$\tau' \frac{\partial \beta_2}{\partial t} + \beta_2 = \beta_{2_{ss}}, \tag{9}$$

where β_{2ss}, like χ_{ss}, is a function of β_1 given by experimental results. τ' is a constant which can vary according to β_1. The equation which relates β_2 to the velocity components is:

$$\beta_2 = \text{Arctan} \frac{v_{\theta_2}}{v_{z_2}}.$$

Coupling of equations (6*a*), (6*b*), (6*c*), (7*b*), (7*c*), (7*d*), (8*b*), and (9) leads to the following system of eight equations:

$$\frac{\partial \mathfrak{U}}{\partial t} + \mathfrak{A} \frac{\partial \mathfrak{U}}{\partial Z} + \mathfrak{B} \frac{\partial \mathfrak{U}}{\partial \Theta} + \mathfrak{C} \frac{\partial \mathfrak{U}}{\partial R} + \mathfrak{D} = 0, \tag{10}$$

where: $^t\mathfrak{U} = [\rho_1, v_{z_1}, v_{\theta_1}, p_1, \rho_2, v_{z_2}, v_{\theta_2}, p_2]$.

The elements of matrices $\mathfrak{A}$, $\mathfrak{B}$, and $\mathfrak{C}$ and the components of $\mathfrak{D}$ depend on the components of $\mathfrak{U}$ and the geometry of the compressor channel [8]. After solving this system of equations, the radial velocity components are obtained for grid points 1 and 2 by equations (7*a*) and (8*a*). The unsteady pressure loss coefficient χ given by (5) appears in nonhomogeneous term $\mathfrak{D}$.

The problem is numerically solved by a second order explicit splitting-up (or distintegration) method. This method is an extension to 3D of the method developed in [9] and applied to 2D transonic computations. The numerical approach is described in detail in [10–11].

3 Results

The computations were performed on a CRAY-1S computer in vector mode. The computation grid of the channel includes approximately 78000 grid points (78 in axial direction, 91 in azimuthal direction and 11 in radial direction) (Fig. 2). Convergence to the steady state solution requires approximately 1000 time steps, which corresponds to a computation time of one hour and a physical time of 20 ms. All the results given were obtained at convergence (steady state).

In the computer code, the inlet boundary conditions are written so that different kinds of inlet distortion can be studied. An inlet total temperature distortion T_0 and/or an inlet total pressure distortion P_0 can be applied, both coupled with an inlet radial and/or aximuthal flow angle distortion φ_0 and/or β_0. Herein, the case of an inlet total pressure distortion as given by the experimental data (the other variables being constant in the inlet section) is considered. The inlet station is at one radius upstream of the rotor. Downstream of the stage, the experimental static pressure distribution defines the outlet boundary condition.

The computed results were compared to those obtained on a test stand which is a low-pressure single-stage axial compressor with a constant section annular duct [12]. Although the compressor speed is low, a loading similar to those found on actual core compressors is used. The study has been realized for the maximum mass flow on the characteristic.

The principal characteristics of the nominal point are the following:

– mean increase of total pressure $\frac{2\Delta P}{\rho V^2} = 0.62$

– mass flow 6.96 kg/s
– power absorbed 18.73 kW
– rotational speed 3500 r.p.m.
– hub-tip ratio 0.668

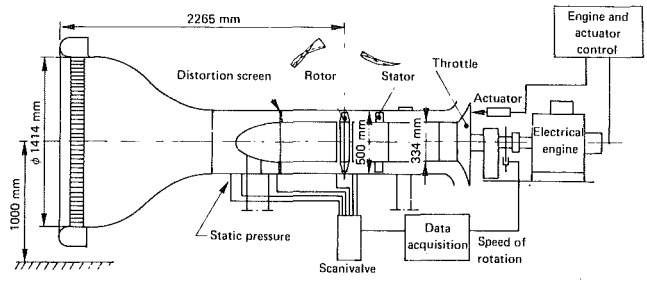

Fig. 3 Test facility

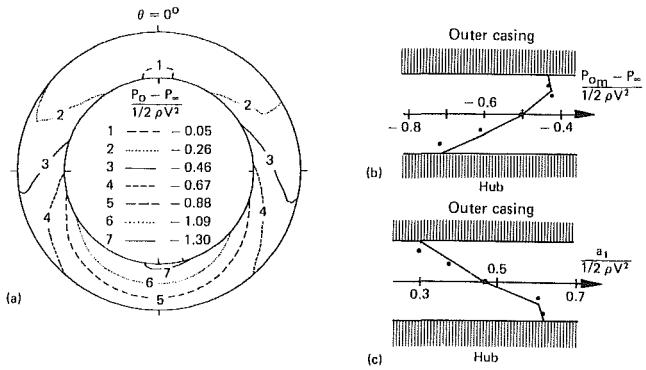

Fig. 4 Inlet total pressure distribution. (*a*) Cross section — $P_0(r,\theta) = P_{0m}(r) + \sum_{n=1}^{5} a_n(r)\cos n\theta + b_n(r)\sin n\theta$ (*b*) Radial evolution of $P_{0_m}(r)$ • Experimental data (c) Radial evolution of $a_1(r)$ — Evolution used in the computations

Figure 3 shows the general arrangement of the test facility and the shape of the blades.

At one diameter upstream of the rotor, a distortion of total pressure is obtained by means of a variable permeability screen (Fig. 4(*a*)). This perturbation induces a quasi sinusoidal distribution of the total pressure at each radius r = constant in the inlet section and the following incidences on the blades of the rotor:

r/r_e	incidence with distortion screen
0.96	−3° to +2°
0.92	−3.8° to +2.7°
0.84	−4.4° to +2.6°
0.76	−5.2° to +4.2°
0.70	−5.4° to +2.6°

A special procedure is used to introduce the boundary conditions in the inlet plane: the initial values obtained by a meridian flow computation are gradually modified with time according to a linear law until they correspond to the imposed distorted values. The computations presented correspond to the following boundary conditions:

– at the Channel inlet:

$$P_0(r,\theta) = P_{0_m}(r) + \sum_{\eta=1}^{5} (a_n(r)\cos n\theta + b_n(r)\sin n\theta)$$

$T_o = 288°\text{K}$

$\varphi_0 = \beta_0 = 0°$

The radial evolutions of $P_{0_m}(r)$, $a_n(r)$ and $b_n(r)$ ($n = 1, \ldots, 5$) are obtained from the experimental data. Figures (4*b*) and (4*c*) show the evolutions of P_{0_m} and a_1. The inlet total pressure distribution is presented in Fig. 4(*a*). $P_\infty = 101325$ pa and $\frac{1}{2}\rho V^2 = 2130$ pa define respectively the inlet total pressure and the inlet dynamic pressure measured when the flow is homogeneous (without distortion screen).

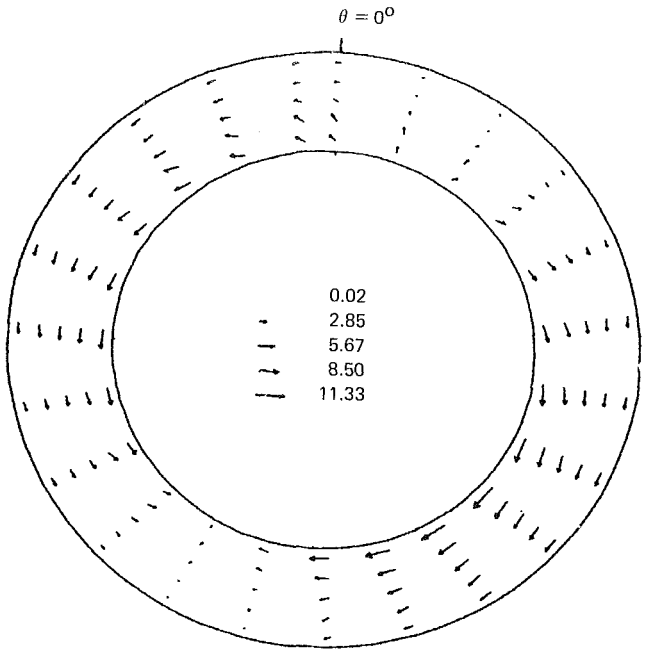

Fig. 5 Projection of the absolute velocity in the inlet section of the rotor (M/S)

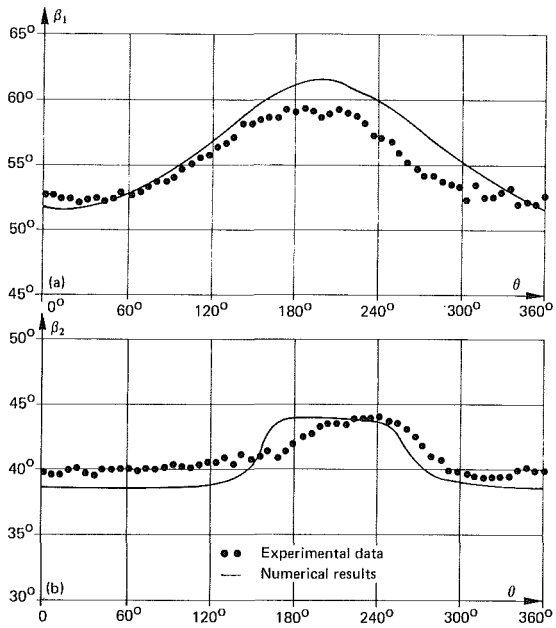

Fig. 6 Azimuthal flow angle distribution. (*a*) In front of the rotor: (*b*) Downstream of the rotor.

The average level of distortion is approximately 50 percent of the average inlet dynamic pressure and represents a severe distortion level (see Fig. 4(*c*)).

– at the channel outlet:

The experimental static pressure imposed in the outlet section is quasi-constant $p \simeq 101480$ pa [11].

Figure 5 represents the projection of the absolute velocity in the inlet section of the rotor (numerical results). Two distinct regions with some redistributed flow can be observed. Some flow is deflected from the high total pressure zone towards the low total pressure zone. Moreover, the inlet radial total pressure gradient creates some radial flow towards the outer casing in the high total pressure region, while in the low total pressure zone the radial flow is towards the hub. These

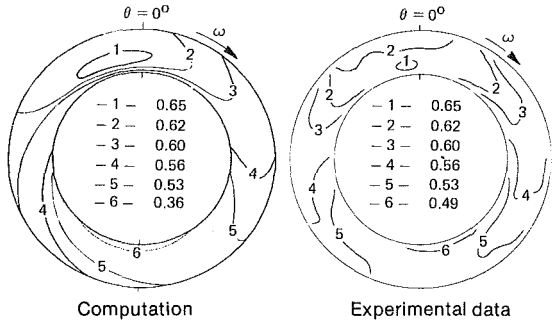

Fig. 7 Mass flow coefficient—Downstream of the rotor. $V_z/\omega r_e$

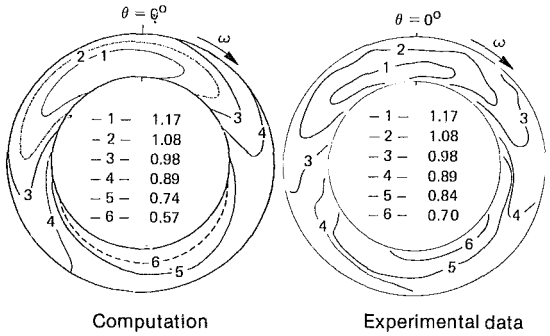

Fig. 8 Total pressure distributions – Downstream of the rotor. $(P-P_\infty)/(\frac{1}{2}\rho V^2)$.

phenomena show that the flow is really 3D when a distortion is imposed in the inlet section even if, in this case, the compressor has a constant section annular duct.

The azimuthal relative flow angle distribution in the inlet and outlet section of the rotor at the mean radius is given on Figs. 6(*a*) and 6(*b*). The value of the computed mass flow is weaker than the experimental mass flow (3 percent). Consequently, the numerical values of β_1 are a little higher than the experimental ones in some regions (2° max), but both evolutions are comparable. For the angle β_2, the experimental steady values β_{2ss} are imposed and the β_2-distribution is obtained by the time-lag equation (6) where $\tau' = 0.5$. In some regions, we have good agreement between the experimental data and the numerical results. We can see that this model is not able to accurately describe the phenomena of the progressive boundary layer separation approximately between 100° and 240°, but the fast boundary layer reattachment (between 240 and 300 deg) is suitably represented.

Figure 7 shows the experimental and numerical mass flow level lines downstream of the rotor. The levels are well represented except in the lower total pressure region where a decreasing of the numerical mass flow coefficient appears. The shape of the lines obtained by the computation and the experimentation are similar. In particular, in the left-hand part of the annulus, the same stretching of the level lines 4 and 5 is visible and in the right-hand part, the climb of the level lines (4 and 5) near the outer casing is well represented. In the high total pressure zone, the lines have a tendency to close around a core (line 1) shifted 10 deg with regard to $\theta = 0°$ in the opposite direction of the rotational speed. This phenomenon is also perceptible on Fig. 8 where the total pressure level lines have been drawn.

This displacement of the maximum of P is due to a strong negative gradient of the incidence, in the direction of the rotational speed, which causes a reduction of the work in the rotor and consequently displaces the maximum in the opposite direction. As above, the numerical values are fairly close to the experimental data, except in the lower part of the section. Downstream of the stator, the flow direction is practically axial. The static pressure no longer varies in the azimuthal direction, but the stator does not change the shape of the total pressure distribution [12]. All these results show that this code is capable of foreseeing the overall response of a compressor to a distortion, but improvements have to be realized in particular on the losses or flow angle models so as to apprehend the details of the flow in the compressor.

4 Conclusion

This computer code is validated by the detailed comparative results presented. It has also been applied to industrial compressors [13] (in particular to the first stage of a booster) but without comparisons with experimental values. This code should help the design of compressors, in particular in the estimation of the surge margin for different flight configurations. Besides, some modifications of this code should allow us to study unsteady phenomena, such as rotating stall or surge.

However, some weaknesses of the row model exist, in particular in the loss and flow angle models that are not well adapted in the regions where strong boundary layer separations appear.

References

1 Fabri, J., "Growth of a Perturbation in an Axial Flow Compressor," ASME Paper No. 78-GT-30.

2 Nagano, S., Takata, H., "Non-linear Analysis of Rotating Stall," Institute of Space and Aeronautical Science, University of Tokyo. Report No. 449, 1970.

3 Adamczyk, J. J., and Carta, F. O., "Unsteady Fluid Dynamic Response of an Axial Flow Compressor Stage with Distorted Inflow," Project SQUID. Technical Report UARL-2-PU, 1973.

4 Pandolfi, M., and Colasurdo, G., *A Contribution to the Prediction of Distorted Flow in Axial Compressors. Recent Developments in Theoretical and Experimental Fluid Mechanics*. Springer-Verlag, 1979, pp. 284–292.

5 Colpin, J., "Propagation of Inlet Flow Distortions Through an Axial Compressor Stage," ASME Paper No. 78-GT-34.

6 Greitzer, E. M., and Strand, T., "Asymmetric Swirling Flows in Turbomachine Annuli," ASME Paper No. 78-GT-109.

7 Bry, P., Laval, P., and Billet, G., "Distorted Flow Field in Compressor Inlet Channels," 27th Annual International Turbine Conference ASME. London (1982) ASME Paper 82-GT-125. Published in ASME *Journal of Engineering for Gas Turbine and Power*, July 1985, pp. 782–791.

8 Billet G., Laval, P., "Méthode de calcul de l'écoulement tridimensionnel instationnaire dans une turbomachine axiale alimentée sous conditions hétérogenes," Rapport Technique ONERA unpublished, 1981.

9 Laval, P., "Schémas explicites de désintégration du second ordre pour la résolution des problèmes hyperboliques non linéaires: théorie et applications aux écoulements transsoniques," NT ONERA 1981-10. English Trans. ESA TT-768.

10 Billet, G., Laval, P., and Chevalier, P., "Response of an Axial Compressor to Distorted Inlet Flow," Conference on Computational Methods in Turbomachinery. University of Birmingham, 1984, TP ONERA 1984-13.

11 Billet, G., Chevalier, P., and Laval, P., "Etude numérique de la Transmission d'une Distorsion Dans un Compresseur Axial," AGARD/PEP Réponse d'un Moteur à Des Distorsions de l'écoulement d'Entrée. Munich, 8, 9, Septembre 1986.

12 Huard, J., "Experimental Determination of the Transfer Function of An Axial Compressor to Distorted Inlet Flow," 68th AGARD/PEP Conference, Munich (FRG), September 8, 9, 1986.

13 Billet, G., Laval, P., and Chevalier, P., "Numerical Simulation of the Response of An Axial Compressor to a Nonhomogeneous Flow," La Recherche Aérospatiale 1985-4. English Trans. ESA TT-960.

Measurement of Intake Valve/Cylinder Boundary Flows Using a Multiple Orientation Hot-Wire Technique

T. C. Wagner

J. C. Kent

Ford Motor Co.,
Dearborn, Mich. 48121-2053

A new measurement method is utilized to determine velocity distributions on the intake-valve/cylinder boundary for different induction system designs. The velocity information is being used to calculate the angular momentum flux and to define local discharge coefficients around the valve periphery. The contribution of local flow direction (effective area) and local flow speed (velocity losses) to the global discharge coefficients is examined. The dependence of the discharge coefficient on the flow direction and mean velocity magnitude provides useful diagnostic data to relate intake port geometry and flow performance. The measurement technique is also described in detail. The directional response of a single hot-wire anemometer is utilized along with sequential sampling of the signal as the probe shaft is rotated through 360 deg. Within the range of velocity and flow direction required, the velocity magnitude and direction can be determined to within 2 percent and 2 deg, respectively.

Introduction

The 3-D velocity distribution over the boundary between the intake valve and the cylinder is of importance for combustion in piston engines. This is because it carries the influence of the induction system design on the development of the turbulent fluid motion within the cylinder, which in turn, affects both the ignition process and the flame propagation rate.

Preliminary experiments on the flow velocity distributions produced by different induction systems utilized single hot-wire probes which were sequentially set in three orthogonal orientations (Haghgooie et al., 1984). Velocity vector data were extracted assuming that the hot-wire responded only to the normal component of the velocity. That study indicated the desirability of further research based on correlation between engine burn rate and valve flow quantities such as the fluxes of kinetic energy and angular momentum.

The work reported in the following was initiated with two main objectives. First, it was desired to enhance the above methodology by increasing the measurement accuracy. This is accomplished by utilizing both the pitch and yaw response of a single hot-wire sampled at many orientations. Second it was desired to apply the new technique to various induction system hardware to identify key local and global features of the valve flow. Features contributing to swirl production and flow resistance (namely the discharge coefficient) were initially of interest.

Contributed by the Fluids Engineering Division of THE AMERICAN SOCIETY OF MECHANICAL ENGINEERS and presented at the Fluids Engineering Conference, June 1987, Cincinnati, Ohio. Manuscript received by the Fluids Engineering Division, Aug. 14, 1987.

2 The Measurement Technique

The principle of a Constant Temperature Anemometer (C.T.A.) is that the bridge voltage required to maintain the wire at a constant resistance (i.e., temperature) is solely an indication of how much heat is being removed from the wire. Accurately modelling this process is required for successful application of the hot-wire anemometer.

Several heat transfer laws have been proposed in the past few decades. The first is the analytical expression derived by King (1914). Others worthy of note are the exponent law (Collis and Williams (1959)), the extended power law (Siddal and Davies (1972)), and two polynomial laws proposed by George et al. (1981) and Swaminathan (1986), respectively.

$$\mathrm{Nu} = A + B^*\mathrm{Re}^{0.5} \tag{1}$$

$$\mathrm{Nu} = A + B^*\mathrm{Re}^{c} \tag{2}$$

$$\mathrm{Nu} = A + B^*\mathrm{Re}^{0.5} + C^*\mathrm{Re} \tag{3}$$

$$\mathrm{Re} = \Sigma C_i^*\mathrm{Nu}^{i/2} \quad (i=0,4) \tag{4}$$

$$\mathrm{Re} = \Sigma C_i^*\mathrm{Nu}^{i} \quad (i=0,2) \tag{5}$$

Re is the Reynolds number, Nu is the Nusselt number and A and B are constants. For the exponent law (equation (2)) $c \simeq .45$. Swaminathan et al. (1986) examined the relative merits of these heat transfer laws for two flow ranges (0-35m/s; 0-100m/s) and concluded that there were no statistically significant differences between the standard deviations for each of the models. They also calculated the uncer-

tainties in the fitted coefficients and found that the extended power law (equation (3)) gave the minimum uncertainty in fitted coefficients.

The present authors compared the relative merit of equation (2) and equation (4). Little difference was observed in the two heat transfer laws in the flow range initially of interest (10-40 m/s). (This is the flow range used in the directional sensitivity studies.) However, when attempting to calibrate over a wider range of velocities equation (2) gave a much better fit. For the experiments on directional sensitivity the polynomial law was used. For valve flow studies the power law became necessary because a wider range of velocities was observed (10-100m/s for a given flow condition). The dimensionless numbers, Nu and Re were used to minimize any effects due to variations in ambient temperature in the laboratory.

2.1 Hot-Wire Directional Sensitivity. The coordinate system used is shown in Fig. 1. All coordinates are relative to the wire since it is the sensing element. The x'-axis is parallel to the shaft; and y'-axis is parallel to the wire; and the z'-axis is normal to the wire and the x'-y' plane. It is a right handed system and it is treated as such in any discussions concerning rotation.

Consider a case where the wire is calibrated with the flow direction parallel only to the x'-axis. When the flow direction deviates from the x'-axis an effective velocity, U_e, is measured that deviates from the true velocity. Jorgensen (1971) postulated that the effective velocity could be expressed in terms of its Cartesian components:

$$U_e^2 = U_{x'}^2 + k1^2 U_{y'}^2 + k2^2 U_{z'}^2 \tag{6}$$

The vector is expressed as a function of its normal component, $U_{x'}$. The tangential and pitch components are weighted by the yaw coefficient, $k1$, and the pitch coefficient, $k2$, respectively. Then for the geometry shown in Fig. 1, equation (6) becomes

$$U_e^2 = U_0^2(\cos^2\phi + (k1\sin\phi\sin\gamma_0)^2 + (k2\sin\phi\cos\gamma_0))^2 \tag{7}$$

The effective velocity can then be expressed in terms of its magnitude, U_0, and its directional angles, ϕ, and τ_0.

The reviewed literature indicates that there are two effects that cause the hot-wire response to deviate from responding only to the true normal component of velocity; pitch and yaw. Using the coordinate system of Fig. 1 the tangential component ($U_{y'}$) must be accommodated by a factor, $k1$, on the order of 0.20 (Champagne (1968), Jorgensen (1971), Adrian (1984), and Moborak (1986)) and the "pitch" component ($U_{z'}$) must be accommodated by a factor, $k2$, on the order of 1.10 (Jorgensen (1971), Adrian (1984), and Moborak (1986)). If the pitch and yaw effects are not incorportaed into data reduction an error results. To exemplify this error we considered the case where the vector lies on the cone 45 deg. off the x'-axis. Neglecting these effects will yield a measured velocity 6 percent too high in magnitude. In analyzing induction flows, several of the parameters calculated include the square and cube of the velocity, and thus it was desired to minimize the error in the velocity measurement to the extent possible.

2.2 Accuracy of the Measurement Technique. A series of experiments were conducted to identify any limitations of using equation (7) to model the effects of combined pitch and yaw. All experiments were carried out in a uniform 15.2 mm diameter jet with a turbulence intensity in the free stream not greater than 2 percent. A Dantec (formerly Disa) 55M01 Constant Temperature Anemometer employing type 55P11 hot wires was used. Data acquisition was performed with a Data Translation 1711 A/D converter and a PDP-11/34 minicomputer. The temperature of the jet was controllable to within 1°C for the duration of any given run.

The hot wires were calibrated in zero pitch and zero yaw.

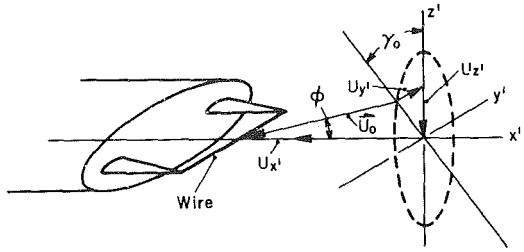

Fig. 1 Coordinate system for directional response of a single hot-wire

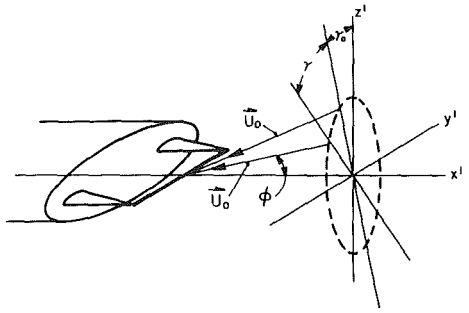

$$U_e^2(\gamma) = U_0^2((\cos\phi)^2 + (k_1\cdot\sin\phi\cdot\sin(\gamma+\gamma_0))^2 + (k_2\cdot\sin\phi\cdot\cos(\gamma+\gamma_0)^2)$$

Fig. 2(*a*) Rotation of velocity vector about the probe axis

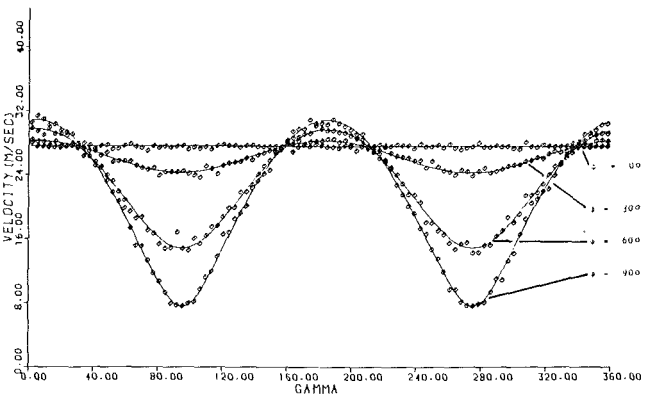

Fig. 2(*b*) Effective measured velocity as a function of rotation angle

The Reynolds number of the hot wire ($U_0 d_w/\nu$) was fitted as a fourth order polynomial of the square root of Nusselt number as in equation (4). Initially, independent pitch and yaw coefficients were measured and found to agree well with those in the literature for non-plated wires ($l/d = 200$). The pitch coefficients are on the order of 1.1 and the yaw coefficients are on the order of 0.15. However it will be shown that the current technique is not appreciably sensitive to the yaw coefficient.

The technique combining pitch and yaw in a multiple orientation fashion was evaluated. For the geometry shown in Fig. 1 the effective measured velocity is given by equation (7). Now if the wire is rotated some angle γ in the negative direction as shown in Fig. 2 (*a*) then at the new position the effective measured velocity can be expressed as:

$$U_e^2(\gamma) = U_0^2(\cos^2\phi + (k1\sin\phi\sin(\gamma+\gamma_0))^2 + (k2\sin\phi\sin(\gamma+\gamma_0))^2) \tag{8}$$

So if the wire is set at some initial position and then rotated in incremental steps a full 360 deg a function $U_e(\gamma)$ is obtained. Using a least squares regression the velocity

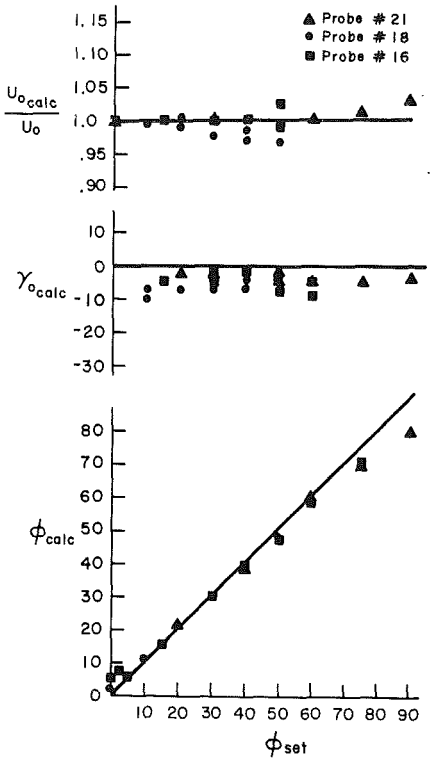

Fig. 3 Accuracy of technique in calculating U_0, Γ_0, and ϕ. $k2 = k2(U_0)$; $k1 = 0.0$.
Probe 21: $k2 = 1.10$ $U_0 = 27.5$ m/s.
Probe 18: $k2 = 1.11$ $U_0 = 27.8$ m/s.
Probe 16: $k2 = 1.11$ $U_0 = 21.8$ m/s.

magnitude, the cone angle ϕ and the phase angle γ_0 can be obtained from equation (8). These are measured relative to the initial position of the wire at γ_0. Figure 2 (*b*) shows typical data sets of $U_e(\gamma)$ for four different cone angles (including $\phi = 0$ deg).

Experiments were conducted to identify any limitations of using this model. The flow speed was varied between 18 m/s and 45 m/s and the cone angle between 0 and 90 deg. The turbulence intensity was varied between 2 and 6 percent. It follows from equation (8) that the accuracy of the calculation depends upon appropriate selection of $k1$ and $k2$. In measuring independent pitch and yaw coefficients a slight velocity dependence was observed in $k2$ and considerable scatter in $k1$. Acceptable accuracy of the calculation was obtained if $k2$ is selected at a velocity within 50 percent of the velocity to be measured and if $k1$ is set to zero (Wagner and Kent (1988)). The calculations presented in Fig. 3 were obtained using this approach. As Fig. 3 (*a*) illustrates, the magnitude is predicted within 3 percent in the worst case ($\phi = 90$ deg) and within 2 percent for the range of application ($\phi < 60$ deg). The cone angle is calculated within a degree for 15 deg $< \phi <$ 30 deg, within 2 deg for 30 deg $< \phi <$ 60 deg, within 5 deg at $\phi = 75$ deg and within 15 deg at $\phi = 90$ deg. Below 15 deg the cone angle is in error because the signal variation due to directional sensitivity is of the same order of magnitude as the turbulence ($\simeq 2$ percent). The fact that the cone angle deviates substantially above $\phi = 75$ deg is attributable to the fact that the tangential component has been neglected and in this region it is no longer negligible. The phase angle γ_0 is consistently measured as -3.6 ± 2 deg, and the non-zero indication is due to the initial alignment to the flow direction. The technique appears to work equally well at a turbulence intensity of 6 or 2 percent; this is reassuring for valve flow studies. Finally it was observed that the technique works as well for increments of $\Delta\gamma = 36.0$ deg or $\Delta\gamma = 3.6$ deg. Thus the methodology adopted

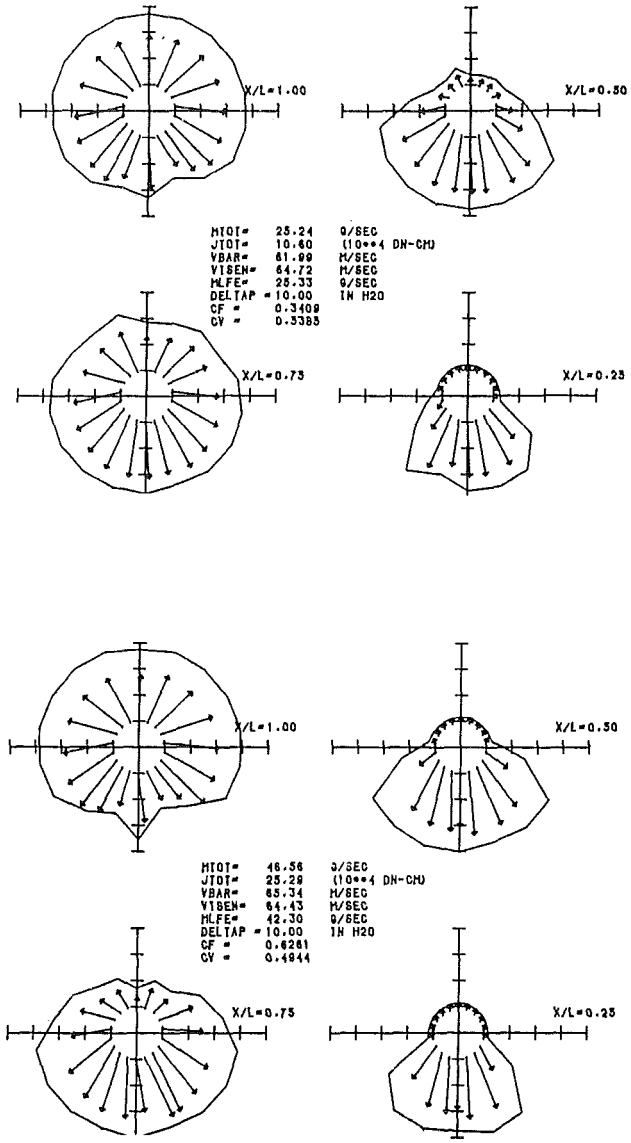

Fig. 4 Typical velocity data for a given port.
***(a) L/D* = 0.15; *dP* = 11.0″ H20;**
***(b) L/D* = 0.31; *dP* = 13.0″ H20.**

for induction hardware application was accomplished with only ten measurements for a given velocity vector.

3 Valve Flow Measurements

The measurement of velocity distributions around the periphery of the intake valve have been of interest for several years (Brandstatter et al. (1985), Arcoumanis and Gosman (1982)). Previous authors have been primarily interested in determining boundary conditions for CFD calculations of in-cylinder flows. This work, however, is the first to use data of this kind to clarify contributions of local flow characteristics to global discharge coefficients.

The initial application of the technique to induction system hardware involved the investigation of a directed port at two valve lifts. The obtained velocity profiles are shown in Fig. 4(*a*) and 4(*b*). The four plots in each group correspond to four axial locations for a set valve lift. For each axial position the velocity at eighteen azimuthal positions (Θ) around the valve were obtained. The ratio X/L is the axial distance from the head normalized against the valve lift; hence $X/L = 0.0$ corresponds to the case where the probe would be at the head face. The ratio L/D is the valve lift, L, normalized against the

valve seat diameter, D. The arrows in Fig. 4 correspond to the component of velocity parallel to the plane of the head surface. The solid lines correspond to the magnitude of velocity at the given azimuthal position. Four runs were taken for each valve lift setting. Figure 4 represents a single run for each respective lift but is indicative of the specific features of the flow.

Figure 4(*a*) shows the case of $L/D = .15$. At $X/L = 1.0$ and $X/L = .75$ the flow is evenly distributed around the valve with a nominal velocity of 63 m/s. The flow is not radial. Except at $\Theta = 180$ and $\Theta = 0$ deg the vector lies nearly 10 deg off the radius always in the direction of the port. At $X/L = .50$ the velocity is substantially reduced on the upstream side of the valve (120 deg $< \Theta <$ 240 deg) and at $X/L = .25$ this occurs on the entire rear side of the valve. It is assumed that this is attributable to separation on the rear side of the valve. This reduction in velocity produces a bias in the flow direction which contributes to the port's ability to create swirl. Figure 4(*b*) shows the case of $L/D = .31$. The features of the flow are similar to 4(*a*) with the exceptions that in some instances the vectors are as much as 20 deg off the radius in the direction of the port and that at $X/L = .75$ the velocity has already begun to decrease on the rear side of the valve. In this same region at $X/L = .50$ the velocity is less than 5 percent of the maximum. This implies larger flow losses for the larger lift.

3.1 Global Quantities. Two integrated quantities were calculated from these valve curtain velocity profiles; namely mass flux and angular momentum flux. The results from the four runs of each lift setting were averaged and compared to the bulk flow measurements. The mass flux from integrating the hot-wire data over the valve curtain area was compared to the mass flux measured from a laminar flow element and was 2 percent higher at an L/D of .15 and 10 percent higher at an L/D of 0.31. For an integration using four values of X/L this agreement was considered acceptable.

Angular momentum flux measurements at the valve have been shown to correlate with combustion duration (Haghgooie and Kent (1984)) and are therefore of interest. The angular momentum flux past the valve was calculated using the velocity data. This was compared to the angular momentum flux measured one bore diameter downstream from the valve under the same flow conditions using the Ford Swirl Meter (Davis and Kent, 1979). The measurement of angular momentum flux using the FSM is based on the measurement of torque exerted on a flow straightener matrix due to its removal of swirl rotation from the flow (Rodig and Zalud, 1969, Tippleman, 1977). This is the traditional method for evaluating the swirl producting characteristics of different intake port designs. At $L/D = .15$ the angular momentum flux at the valve is 50 percent higher than the bulk FSM measurement and at $L/D = .31$ it is 75 percent higher than the bulk FSM measurement. The lower values observed with the FSM are attributed to losses in angular momentum flux due to the interaction of the flow with surfaces in between the valve and the FSM sensor. Combustion data for this particular head was not yet available.

3.2 The Localized Discharge Coefficient. The discharge coefficient is one of the principal parameters used in quantifying the mass flow efficiency of various port designs. We define it as the observed mass flow rate divided by the isentropic mass flow rate for a circular orifice having a diameter equal to the valve seat diameter and a pressure drop corresponding to that across the port/valve.

$$C_f = \dot{m}_{\text{obs}}/(\rho A_{\text{ref}} V_{\text{isen}}) \tag{9}$$

ρ = downstream density
$A_{\text{ref}} = \pi R_s^2$
R_s = valve seat radius
V_{isen} = isentropic velocity based on ΔP across the valve

Typically $\dot{m}_{\text{obs}}$ is a bulk measurement from a calibrated flow meter.

Using the local velocity data provided by our measurement technique it is possible to evaluate local discharge coefficients and their variation around the periphery of the valve. To do this the valve curtain area is broken down into 72 regions (four axial regions for each of the eighteen azimuthal positions $\Delta\Theta = 20$ deg) as shown in Fig. 5. For each region the local mass flux is defined as

$$\dot{m}_{ij} = \rho A_{ij} V_{ij} \cos\beta_{ij} \tag{10}$$

where

i = azimuthal index (1, 18)
j = axial index (1, 4)
ρ = downstream density
$A_{ij} = 2\pi R_v L/72$
V_{ij} = local velocity magnitude by hot wire
β_{ij} = angle between local velocity vector and the normal to A_{ij}
R_v = valve radius
$\cos\beta_{ij} = \sin\phi_{ij} \cdot |\cos(\gamma_{0ij} - \Theta_i)|$ (11)

It was desired to express the discharge coefficient as a function of azimuthal position around the valve. The mass flow rate summed over the axial position is

$$\dot{m}_i = \rho \sum_{j=1}^{4} A_{ij} V_{ij} \cos\beta_{ij} = \rho \bar{V}_i \sum_{j=1}^{4} A_{ij} \cos\beta_{ij} \tag{12}$$

where we have defined

$$\bar{V}_i = \frac{\sum_{j=1}^{4} A_{ij} V_{ij} \cos\beta_{ij}}{\sum_{j=1}^{4} A_{ij} \cos\beta_{ij}} \tag{13}$$

V_i is a local mean velocity magnitude. If A_{ij} is constant (as it is here) V_i can be interpreted as the mean radial component divided by the local mean directional cosine. We also define a local reference area. It is the total reference area divided by the number of azimuthal positions.

$$A_{refi} = \pi R_s^2/18 \tag{14}$$

Using the local mass flow rate in (12) and the local reference area in (14) we define a local discharge coefficient and multiply by unity:

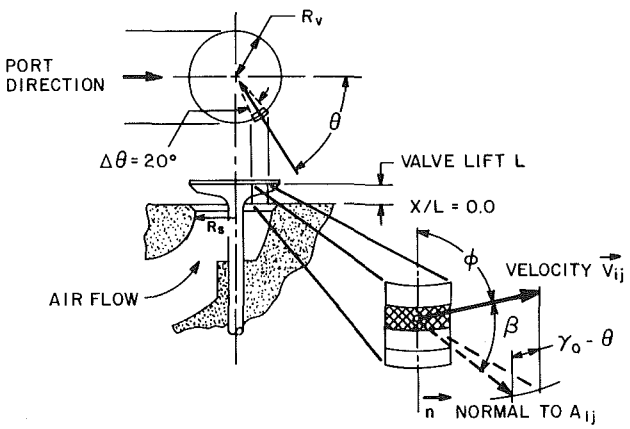

Fig. 5 Definition of port/valve geometry for analyzing valve flows

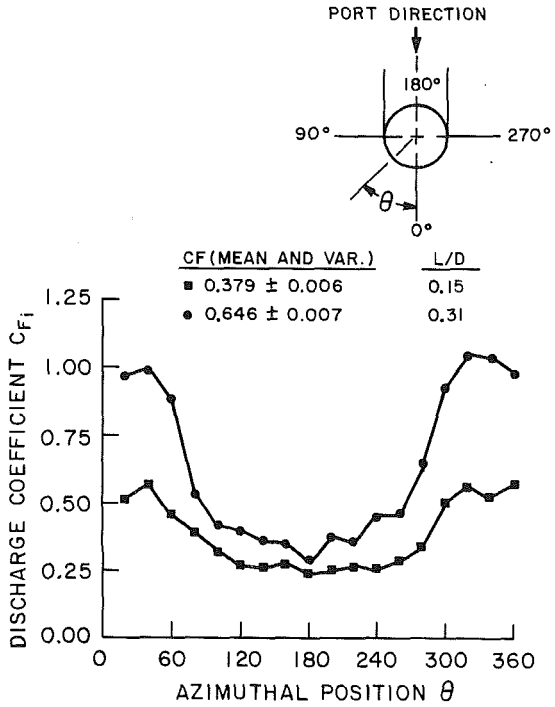

Fig. 6 Local discharge coefficient as a function of azimuthal position, Θ, around the valve

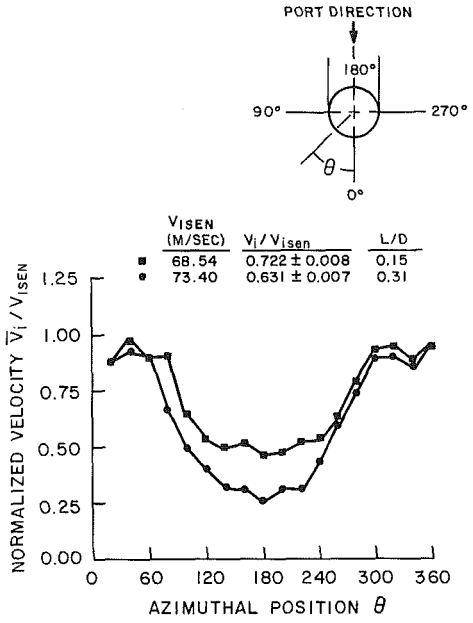

Fig. 7 Normalized local mean velocity as a function of azimuthal position, Θ, around the valve

$$C_{fi} = \frac{\sum_{j=1}^{4} A_{ij} V_{ij} \cos\beta_{ij}}{A_{refi} V_{isen}} \cdot \frac{\sum_{j=1}^{4} A_{ij} \cos\beta_{ij}}{\sum_{j=1}^{4} A_{ij} \cos\beta_{ij}} \tag{15}$$

We define the local effective area as the local mean flow direction normalized against the local reference area as

$$A_{effi} = \frac{\sum_{j=1}^{4} A_{ij} \cos\beta_{ij}}{A_{refi}} \tag{16}$$

The localized discharge coefficient (equation (15)) becomes

$$C_{fi} = A_{effi} \bar{V}_i / V_{isen} \tag{17}$$

The global coefficient is then the mean of the local discharge coefficients:

$$C_f = \sum_{i=1}^{18} C_{fi}/18 \tag{18}$$

The coefficient is the product of an effective area and a velocity ratio. The effective area depends on mean flow direction for a given azimuthal position; a smaller effective area indicates a higher β implying a larger angle between velocity and area and thus a lower efficiency. The weighted velocity defined in equation (13) can be interpreted as a mean velocity magnitude. It is the mean radial component normalized against the mean flow direction at the given azimuthal position.

Figure 6 shows the local discharge coefficient profile as a function of azimuthal position, Θ, around the valve for $L/D = .15$ ($L = 0.20$) and $L/D = .31$ ($L = 0.40$). Bear in mind that the magnitude of the coefficient for the two cases is due to the incorporation of the valve lift in the definition. Assuming no differences in the flow losses a C_f at $L/D = .30$ would be twice that of C_f and $L/D = .15$. Note the large variation of C_f versus Θ_i for both valve lifts. For $L/D = .15$ the plot is symmetric about $\Theta = 180$ deg. Here C_f attains a maximum of 0.56 at $\Theta = 0$, 40, and 320 deg. C_f drops 45 percent between $\Theta = 40$ and $\Theta = 120$ deg. This indicates that flow losses exist even on the forward side of the valve. For 120 deg $< \Theta <$ 240 deg C_f is nearly constant at .25. The flow losses are largest on the rear side of the valve. This follows from the velocity profiles in Fig. 4(*a*). The minimum flow coefficient is 45 percent of the maximum. For $L/D = .31$ there is slight asymmetry in the profile. C_f attains a maximum of 1.05 at $\Theta = 320$ and 340 deg. A slight dip 1.0 is observed at $\Theta = 0$, 20, and 40 deg. C_f drops 47 percent for 40 deg $< \Theta <$ 80 deg and 40 percent for 320 deg $> \Theta >$ 280 deg. Contrast this to only a 30 percent drop in C_f in the same region for the lower lift case. In addition the coefficient does not level off but continues to decrease for $\Theta > 80$ deg reaching a minimum at $\Theta = 180$ deg. The ratio of minimum to maximum coefficient is .30. Contrast this value to 0.45 for the lower lift.

Figure 7 shows the local mean velocity magnitude normalized against the isentropic velocity for both lifts. Note the similarity in profiles. Both profiles are symmetric about $\Theta = 180$ deg. There is large variation as a function of Θ_i. Maximums occur at $\Theta = 0$, 40, and 320 deg. Again there are slight dips at $\Theta = 20$ and 340 deg. The velocity magitude is nearly the isentropic velocity at the maximums (i.e., the flow losses are minimal here). Moving around the valve the velocity drops reaching its minimum at $\Theta = 180$ deg as we would expect. The larger valve lift shows substantially larger losses here than the smaller lift. Contrast the ratios of .25 for $L/D = .15$ to .45 for $L/D = .31$. An L/D of .31 corresponds to the case where valve lift is larger than the valve seat diameter. Under these conditions separation of the flow over a large portion of the lift on the rear side of the valve is anticipated. For 0 deg $< \Theta <$ 60 deg and 300 deg $< \Theta <$ 360 deg the velocity ratios are nearly identical. Examine the decline in velocity ratio in the region 40 deg $< \Theta <$ 80 deg and 320 deg $> \Theta >$ 280 deg. The drops in these regions are not as severe as in the case of the discharge coefficients. The reason for this is explained in the context of the effective area.

Figure 8 shows the effective area for both valve lifts. For $L/D = .15$ the effective area varies between .58 and .42 displaying minimums at $\Theta = 100$ and 260 deg. At $\Theta = 180$ deg it attains a local maximum of .50. For $L/D = .31$ the effective

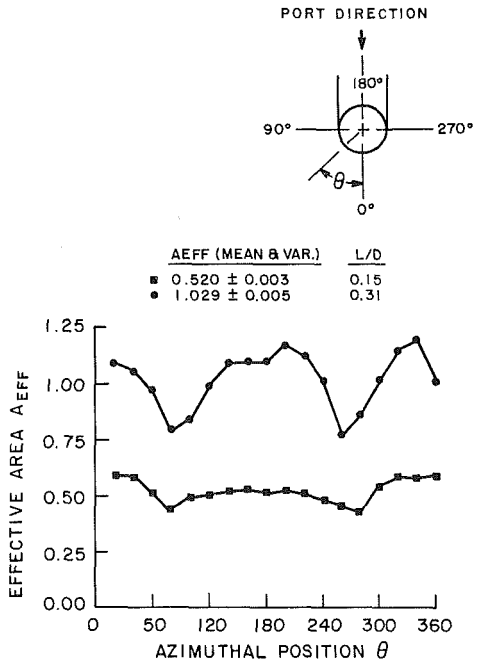

Fig. 8 Normalized local effective area as a function of azimuthal position, θ, around the valve

area displays local minimums at $\Theta = 80$ deg and at $\Theta = 240$ deg and resumes its maximum near $\Theta = 180$ deg. The maximum area ratios correspond to mean flow directions of 35.5 and 41.7 deg for $L/D = .15$ and $L/D = .31$, respectively. Similarly the minimum effective areas correspond to mean flow directions of 52.3 and 57 deg, respectively. The valve seat angle for this geometry was 45 deg. The smaller the flow direction angle, β the higher the efficiency. The discharge coefficient showed noticeable drops for 40 deg $< \Theta <$ 80 deg and 320 deg $> \Theta >$ 280 deg but the velocity ratio did not entirely account for this behavior. The local minimum in effective area is also responsible. The data indicate that in the forward region of the valve flow losses are occurring due to large flow angles. The increase in effective area coupled with the velocity decrease on the rear side of the valve indicate that the discharge coefficient is primarily dependent on velocity ratio in this region.

Figures 6, 7, and 8 combined indicate the following. The larger valve lift showed larger flow losses particularly in the rear of the valve. This is assumed to be attributable to separation from the valve seat of a larger portion of the flow field as demonstrated in Fig. 4(*b*). Both lifts exhibited nearly identical velocity ratios in the forward region of the valve. Local minimums were observed in the effective area profiles on the forward side of the valve. These minimums coupled with the velocity ratio result in a large drop in discharge coefficient on the forward side of the valve (beginning at $\Theta = 40$ and $\Theta = 320$ deg). The effective areas of both lifts increased in the rear of the valve. In both cases the mean direction in this region was less than or equal to the valve seat angle. It is important to note that the very mechanisms contributing to mass flow losses; namely low velocities at the rear of valve are going to contribute to swirl production due to the velocity bias in the direction of the port.

In summary it has been shown that the mass flow losses at the valve can be analyzed in terms of the flow direction and the velocity magnitude. Examination of these quantities as a function of position around the valve provide valuable diagnostic information for understanding flow losses and development of ports with high flow efficiency.

4 Conclusions

1. A measurement technique has been employed to provide accurate three-dimensional information around the curtain area of an intake valve under steady flow conditions.
2. Integration of the velocity measurements yields mass flux measurements that correlate well with bulk flow measurements.
3. Integration of the angular momentum flux provides the swirl condition at the boundary. The detailed velocity information provide insight as to what elements of the valve flow boundary condition produce in-cylinder swirl. Significant losses in angular momentum flux between the valve and a plane located one bore diameter downstream from the cylinder head were observed.
4. A local discharge coefficient has been evaluated in terms of local effective area and the local velocity magnitude. It has been observed that both contribute to flow losses and the effects of the two can be separated and identified. Identification of large local flow losses provides information which is valuable for improving port designs.

References

Adrian, R. J., Johnson, R. E., Jones, B. G., Merati, P., and Tung, A. T-C., 1984, "Aerodynamic Disturbances of Hot-wire Probes and Directional Sensitivity," *J. Phys. E:Sci. Instrum.*, Vol. 17, pp. 62–71.

Arcounmanis, C., Bicen, A. F., and Whitelaw, J. H., 1982, "Effects of Inlet Parameters on the Flow Characteristics in a Four-Stroke Model Engine," SAE Paper 82070.

Brandstatter, W., Johns., R. J. R., and Wigley, G., 1985, "The Effect of Inlet Port Geometry on In-Cylinder Flow Structure," SAE Paper 850499, Feb.

Champagne, F. H., Schleicher, C. A., and Wehrmann, O. H., 1967, "Turbulence Measurements with Inclined Hot-wires Part," *J. Fluid Mech.*, Vol. 28, pp. 153–175.

Collis, D. C., and Williams, M. J., 1959, "Two-Dimensional Convection From Heating Wires at Low Reynolds Numbers," *J. Fluid Mech.*, Vol. 6, pp. 357–384.

Davis, G. C. and Kent, J. C., 1979, "Comparison of Model Calculations and Experimental Measurements of The Bulk Cylinder Flow Process in A Motored PROCO Engine," SAE Paper 790290.

Dvorek, K., and Syred, N., 1972, "The Statistical Analysis of Hot Wire Anemometer Signals in Complex Flow Fields," DISA Conference, University of Leicester.

George, W. K., Beuther, P. D., and Ahmad, M., 1981, "Polynomial Calibration and Quasi-Linearization of Hot-Wires," Turbulence Research Laboratory Report, SUNY, Buffalo.

Haghgooie, M., Kent, J. C., and Tabaczynski, R. J., 1984, "Intake Valve Cylinder Boundary Flow Characteristics in an Internal Combustion Engine," *Comb. Sci. Tech.*, Vol. 38, pp. 49–57.

Hinze, J. O., 1959, *Turbulence*, 1st ed., New York, McGraw-Hill Chapter 2. Jorgensen, F. E., 1971, "Directional Sensitivity of Wire and Fiber-Film Probes," *DISA Information*, No. 11, pp. 31–7.

King, L. V., 1914, "On the Convection of Heat From Small Cylinders in a Stream of Fluid," *Phil. Trans. Roy. Soc.*, Vol. 214a, pp. 373–432.

Moborak, A., Sedrak, M. F., and El Telbany, M. M. M., 1986, "On the Direction Sensitivity of Hot-Wire Probes," Dantec Information, No. 2 pp. 7–9.

Rodig, J., and Zalud, F., 1969-1970, "Some Contributions to Experimental Combustion Research," Paper No. 19, Diesel Engine Combustion, Proc. Instn. Mech. Engrs., 184, Part 3J, pp. 203–211.

Swaminathan, M. K., Rankin, G. W., and Sridhar, K., 1986, "A Note on the Response Equations for Hot-Wire Anemometry," ASME JOURNAL OF FLUIDS ENGINEERING, Vol. 108, pp. 115–118.

Siddal, R. G., and Davies, T. W., 1972, "An Improved Response Equation for Hot-Wire Anemometry," *Int. J. Heat Mass Transfer*, Vol. 15, pp. 367–368.

Tippleman, G., 1977, "A New Method of Investigation of Swirl Ports," SAE Paper No. 770404, Feb.

Wagner, T. C., and Kent, J. C., 1988, "On the Directional Sensitivity of Hot-Wires: A New Look at an Old Phenomenon," Accepted for publication in *Experiments in Fluids.*

Radial and Axial Turbulent Flow Measurements With an LDV in an Axisymmetric Sudden Expansion Air Flow

R. P. Durrett

W. H. Stevenson

H. D. Thompson

School of Mechanical Engineering,
Purdue University,
West Lafayette, Ind. 47907

Radial velocity component measurements in cylindrical tubes have been difficult to make because of optical aberrations introduced by the curved tube wall. This is particularly troublesome in gas flows where refractive index matching techniques cannot be employed. The present investigation utilized a specially designed correction lens system to overcome this problem. As a result it was possible to map the axial and radial velocity behavior in detail for the air flow downstream of a sudden expansion in a cylindrical duct. Quantities measured and derived included mean velocities, turbulence intensities, turbulent kinetic energy and Reynolds stress. The weak secondary recirculation zone existing just below the sudden expansion was clearly identified and mapped. Where possible the measurements were compared with numerical predictions based on a k-ϵ *model.*

Introduction

The turbulent flow field downstream of an axisymmetric sudden expansion is of significant importance from both a fundamental and a practical standpoint. As a result such flows have been the focus of numerous analytical and experimental investigations. A variety of experimental techniques have been employed including flow visualization, hot wire and hot film anemometry, and laser Doppler velocimetry. The LDV investigations include those by Freeman (1975), Moon and Rudinger (1977), and Stevenson, Thompson, and Craig (1984). All of the LDV studies reported to date utilized a single component system and measurements were confined to the tube diameter coinciding with the optical axis of the LDV system. This permits axial velocity measurements to be made across the tube diameter. Measurement of the tangential velocity component is also possible in principle, but is of little interest unless swirl exists. Radial velocity measurements along the perpendicular tube diameter are of interest, but aberrations caused by the curved tube walls have prevented such measurements in the region where the radial component is significant.

The present investigation was undertaken in an attempt to map the radial as well as the axial velocity field near a sudden axisymmetric expansion using an LDV. A major factor in the attainment of this objective was the use of a correction lens system which overcame the aberration problem and permitted radial velocities to be measured. Using this lens system it was possible to make radial velocity measurements over more than 80 percent of the tube diameter. The lens system insured both proper intersection of the input beams and proper imaging of the scattered light from the probe volume on the detector pinhole.

Most of the measurements were made in a sudden expansion test section with a diameter ratio of 1.9 at a Reynolds number of 8.4×10^4 based on inlet diameter. Axial and radial mean velocities and turbulence intensities as well as Reynolds stress and turbulence kinetic energy were determined at six planes corresponding to downstream distances from 2 to 20 step heights. A preliminary study was also undertaken to determine if the flow field in the weak secondary recirculation zone formed close to the step could be measured. An expansion ratio of 2.7 was used in this case to enhance the magnitude of the small radial velocity component. Although a limited set of data was taken, the secondary flow was clearly identified.

The Sudden Expansion Flowfield

The separated flow following a sudden expansion is complex, consisting of a potential core, a free shear layer with high turbulence levels, a primary recirculation zone, and a postulated secondary recirculation zone or corner eddy very close to the step. Following reattachment of the shear layer at the wall, the flow proceeds to develop and, in the case of an axisymmetric sudden expansion, a fully developed turbulent pipe flow is eventually achieved. Figure 1 illustrates the general nature of the flowfield. The present study was primarily concerned with the flow prior to reattachment. In this region a wide variation of turbulence levels is found and the radial velocity can be significant.

Numerous studies of 2-D and axisymmetric sudden expansions have been conducted. Comprehensive reviews of 2-D step flow studies have been presented by Eaton and Johnston (1980) and Bremmer et al. (1980). Stevenson, Thompson, and Luchik (1982) reviewed a number of axisymmetric sudden ex-

Contributed by the Fluids Engineering Division for publication in the JOURNAL OF FLUIDS ENGINEERING. Manuscript received by the Fluids Engineering Division August 13, 1987.

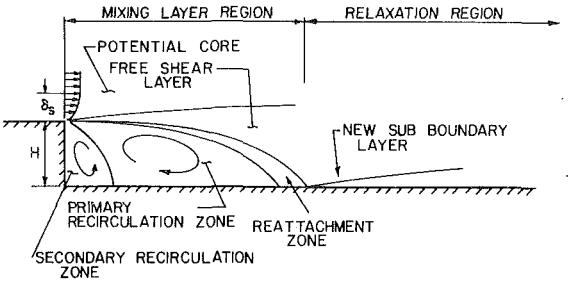

Fig. 1 Flow regions in a sudden expansion

pansion flow investigations, including those of Freeman (1975) and Moon and Rudinger (1977) which were the first in which LDV measurements were reported. Freeman's work was conducted with water, while Moon and Rudinger used air as the working medium. Gould et al. (1983) investigated both isothermal air flow and flow with combustion in a sudden expansion.

Cross-stream (radial) velocity information is not reported in any of the axisymmetric sudden expansion studies noted above, primarily because of the difficulty involved in measuring radial velocity in a cylindrical geometry with an LDV. Velocity measurements in the secondary recirculation zone have also not been reported, although its presence has been indicated indirectly by a water injection technique used by Kangovi and Page (1979) to find zero skin friction locations on the tube wall. Driver and Seegmiller (1982) and de Brederode and Bradshaw (1972) performed similar studies with an oil film in 2-D sudden expansions. All three studies indicated the presence of a weak corner eddy within one step height of the sudden expansion.

Experimental Apparatus

LDV System. Figure 2 shows the single-component LDV system used in the present study. Optical elements for beam splitting, frequency shifting, and probe volume formation are mounted on a platform which can be rotated about the optical axis to measure the desired velocity component. Differential frequency shifting is employed, with a net shift of 10 MHz. The combination of two adjustable mirrors and sliding prism following the acousto-optic frequency modulators allows beam separation to be varied and also permits the focused beams to be precisely intersected at their waists for optimum signal quality. A focusing lens with 250 mm focal length is employed. Probe volume dimensions are controlled by this lens, the beam spacing, and the input beam diameter as determined by the beam expander telescope.

Signal processing was done with a TSI Model 1980 burst counter. The digital output was fed to a microcomputer which stored the data and controlled the sampling rate. A sample of 4500 individual velocity realizations was accumulated at each measurement point. These data were then transferred to floppy disk and later to a CDC 6600 mainframe computer for analysis. The technique of heavily seeding the flow and sampling at a lower rate to attain equal time interval velocity samples was used to eliminate velocity bias. This method has previously been described by Stevenson, Thompson, and Roesler (1982) and its effectiveness confirmed in subsequent studies, including the work of Gould et al. (1983) and Craig et al. (1986).

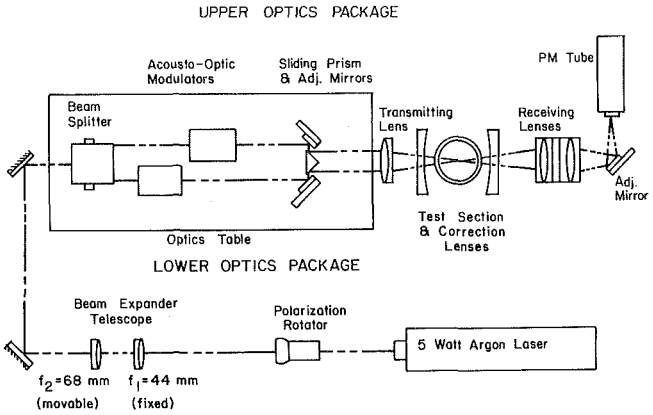

Fig. 2 LDV optical configuration

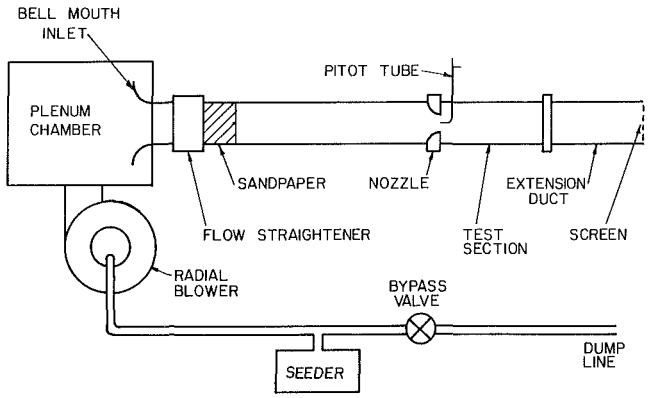

Fig. 3 Flow system

Flow System. The flow system used for the experiments is illustrated in Fig. 3. A radial blower provided the air flow, which entered a large plenum chamber. A bell mouth nozzle with a 4:1 area ratio formed the inlet to the upstream cylindrical pipe section. A flow straightener containing 18 mesh screen followed the bell mouth nozzle. The Plexiglas pipe which formed the connecting duct between the flow straightener and test section had an inside diameter of 95.2 mm (3.75 in.) and was approximately 3 meters long.

Seeding was supplied by a TSI Model 3076 liquid atomizer followed by a TSI Model 3072 evaporation-condensation monodisperse aerosol generator. This produced seeding particles one micron or less in diameter using a 100 percent solution of Dioctyl Phthalate (DOP). Seeding density was controlled with a bypass dump. A particle arrival rate in the probe volume of approximately 20,000 Hz was maintained for the experiments. Seed particles were introduced at the blower inlet, resulting in a reasonably uniform seed density throughout the flow.

Two test sections, shown in Fig. 4, were used. Both consisted of a converging nozzle section followed by a straight pipe section the same diameter as the inlet duct. The first nozzle, used for most of the measurements, had an area ratio of 1.9. The second nozzle had an area ratio of 2.7, which enhanced the size and strength of the secondary recirculation zone. This second nozzle was also designed to permit optical access closer to the step. Both nozzles had provision for inserting a pitot tube near the exit plane centerline (as shown in Fig.

Nomenclature

H = step height $= R_2 - R_1$
r = radius
R_1 = inlet radius at step
R_2 = downstream duct radius
$\bar{u}_r$ = mean radial velocity
$\bar{u}_x$ = mean axial velocity
u_r' = radial velocity fluctuation
u_x' = axial velocity fluctuation
U_0 = centerline velocity at inlet

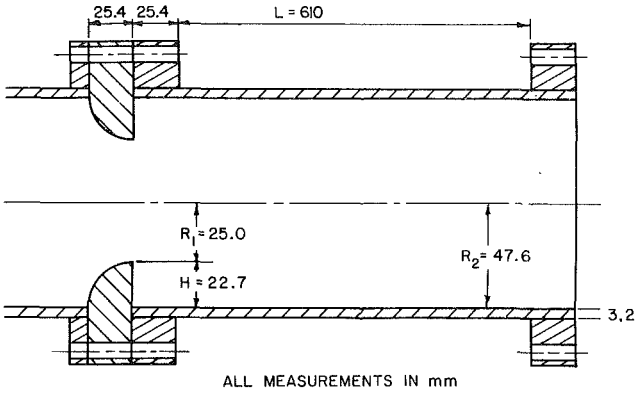

Fig. 4(*a*) 1.9 Area ratio

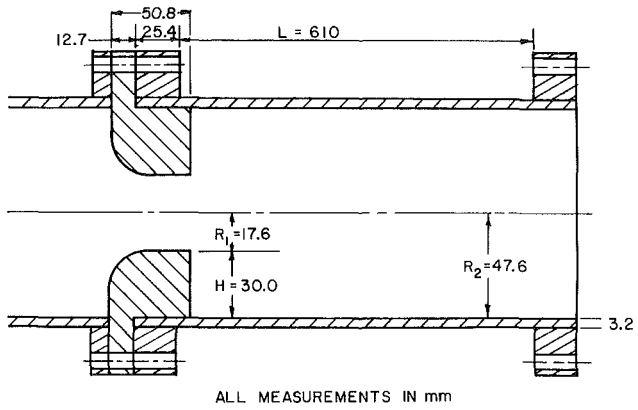

Fig. 4(*b*) 2.7 Area ratio

Fig. 4 Test section geometries

3) to monitor the flow at regular intervals, thus insuring that steady conditions were maintained. Care was also taken to achieve flow symmetry, which was checked by measuring the mean velocity profile along perpendicular diameters with the LDV.

Correction Lens System. A key element in this investigation was the correction lens system developed to minimize the effect of optical aberrations on the probe volume when the measurement point was moved off of the horizontal plane of the cylindrical tube. Details of the correction lens design and fabrication have been previously reported by Durrett et al. [13]. Therefore only a brief description will be presented here. A ray tracing program was developed to describe the optics involved. It was found that aberration effects could be reduced to a minimal level over most of the tube diameter with a simple system consisting of two cylindrical plano-convex lenses placed symmetrically on opposite sides of the tube as shown in Fig. 5. With this arrangement good signals were obtained over better than 80 percent of the tube diameter. In fact, the input beam plane could be rotated about the LDV optical axis without loss of signal. Thus two-component measurements are possible, although only a single component was used in the present study.

Experimental Results

Measurements in the 1.9 Area Ratio Expansion Flow. A majority of the measurements made in this investigation were carried out using the 1.9 area ratio sudden expansion test section. Measured and derived quantities included axial and radial mean velocity and turbulence intensity as well as Reynolds stress and turbulent kinetic energy. Figure 6 shows the mean axial velocity profiles at 2, 4, 6, 8, 12, and 20 step heights downstream of the sudden expansion. The velocity

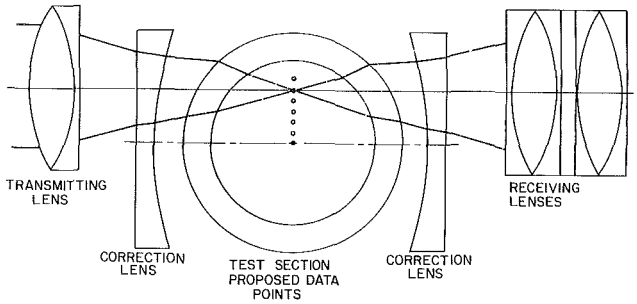

Fig. 5 Correction lens system

profile at the inlet plane (obtained from pitot tube measurements) was very flat with a centerline value U_0 of 27.9 m/s corresponding to a Reynolds number of 8.4×10^4 based on inlet diameter. Boundary layer thickness at the step edge was approximately 1.2 mm.

The solid lines in Fig. 6 represent numerical predictions from the CHAMPION 2/E/FIX code of Pun and Spalding (1976) assuming a uniform velocity at the inlet plane. The computational mesh contained 40 points across the tube diameter. Fairly good agreement exists, although the centerline velocity is first underpredicted and then overpredicted as observed in the earlier study by Stevenson, Thompson, and Luchik (1982). A 1/7 power law profile scaled to match the inlet mass flux is shown in Fig. 6 for comparison with the measured profile at $x/H = 20$. This indicates that the flow is close to redevelopment at 20 step heights, although complete redevelopment is not attained until further downstream. Eaton and Johnston (1980) estimate that 50 step heights is required for full development in 2-D flows.

The measured mean velocity profiles were curve fitted and integrated to compute the mass flux at each downstream position. All results agreed to within ± 3 percent, indicating that the velocity bias elimination technique described previously was effective.

The primary objective of the study was to examine the radial velocity behavior. Radial mean velocity measurements obtained using the correction lens are shown in Fig. 7 for the same downstream locations as in Fig. 6. General trends are as predicted by the numerical code, but data scatter is larger than for the axial mean velocities. This would be expected, since for many of the locations the mean velocity is much less than the fluctuations, with local radial turbulence intensities of several hundred percent. Perhaps more significant, however, is the problem posed by probe volume alignment. Care was taken to align the optics so that the measured component would be normal to the tube axis. However, the radial velocity is more than an order of magnitude less than the axial velocity, except near the wall, and a small angular misalignment of the probe volume (or a slight asymmetry in the flow) can introduce a large measurement error. This is especially significant near the tube axis close to the step, which probably accounts for the obvious discrepancy in the radial mean velocity data at $x/H = 2$. An angular error of 2 degrees would produce the deviation from zero observed in the value of $\bar{U}_r$ on the axis at this point. At locations further downstream the predicted results are closely approximated. Unfortunately it was not possible to recheck the measurements at $x/H = 2$ due to other demands on the test facility.

An important parameter in sudden expansion flows is the reattachment length for the shear layer. A stream function contour map derived from the mean velocity data indicated that reattachment occurred at $x/H \approx 8.3$. This agrees well with results from earlier studies. In general, therefore, results of the mean velocity measurements were as expected and the 2/E/FIX code was found to provide a reasonably good prediction of both the axial and radial mean velocity field.

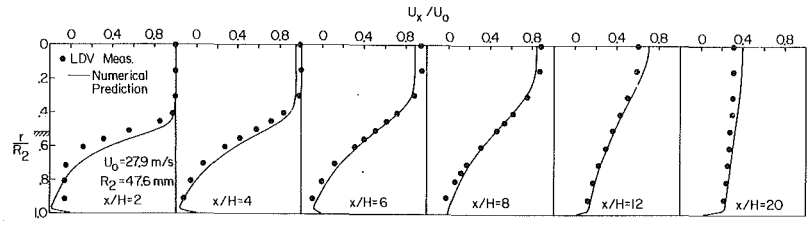

Fig. 6 Axial mean velocity profiles

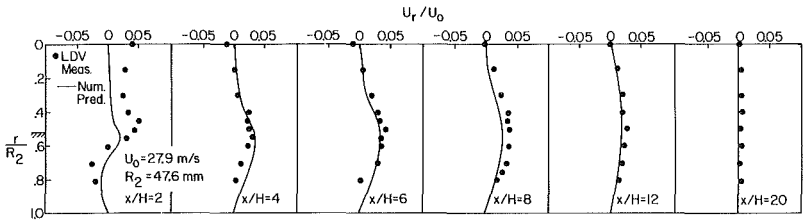

Fig. 7 Radial mean velocity profiles

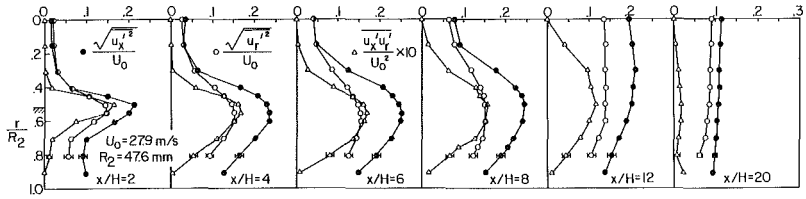

Fig. 8 Axial and radial normalized turbulence intensity and Reynolds stress

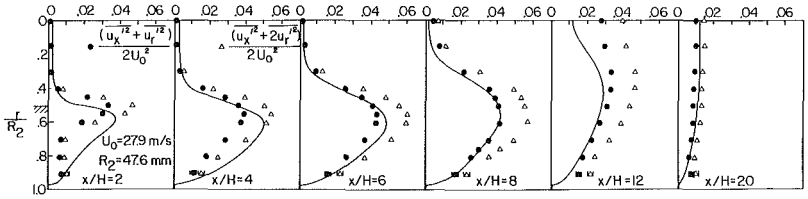

Fig. 9 Turbulence kinetic energy

Normalized axial and radial turbulence intensity profiles, together with Reynolds stress profiles computed from turbulence intensities measured at ±45 degrees from the tube axis using the method of Logan (1972), are shown in Fig. 8. The normalized axial intensities are greater than the corresponding radial intensities at all points, even at 20 step heights downstream where the two profiles become nearly flat. This is another indication that complete redevelopment has not yet been attained at this point.

The use of Logan's method to compute Reynolds stress from independent single component measurements is subject to errors, since differences of two nearly equal large numbers are involved. Nevertheless, the results in Fig. 8 are consistent with expected trends and the values at $x/H=20$ are close to those predicted for fully developed pipe flow based on a 1/7 power law for the mean velocity profile. The decrease in Reynolds stress observed at this location for $0.5<r/R_2<0.8$ may be due to measurement errors, although measurements in a more fully developed pipe flow 40 diameters downstream of the inlet exhibited the same behavior.

Peak values of axial turbulence intensity in the shear layer were 21 percent at $x/H=2$ and 24 percent at $x/H=8$. These values are similar to those found in earlier studies at our facility. Freeman observed peak values of 17 and 20 percent at approximately the same locations. However, his inlet velocity profile approached that for fully developed pipe flow and the velocity gradient was therefore lower at the edge of the step.

Turbulence intensity is not predicted by the 2/E/FIX program, so normalized turbulence kinetic energy (TKE) values were computed to allow comparison with numerical predictions. Both partial and full TKE values were determined from equations (1) and (2), respectively.

$$\text{PTKE}=(\overline{u'^2_x}+\overline{u'^2_r})/2U_0^2 \tag{1}$$

$$\text{FTKE}=(\overline{u'^2_x}+\overline{2u'^2_r})/2U^2{}_0) \tag{2}$$

In computing FTKE the assumption was made that radial and tangential intensities were approximately equal as indicated by Hinze (1975) for a free jet. The measured FTKE can be compared with 2/E/FIX predictions which assume isotropic turbulence. As Fig. 9 shows, the predicted trends were observed, but measured values were larger. This is consistent with results found in an earlier axisymmetric sudden expansion study (Stevenson, Thompson and Luchik, 1982).

The difference between FTKE and PTKE values represents the contribution of the radial (or tangential) fluctuations to the total kinetic energy. Thus it should be directly related to the local turbulence intensity level. A comparison of Figs. 8 and 9 shows that this is indeed the case. While not surprising in view of the mathematical relationship between intensity and TKE, the internal consistency evident in the data is encouraging.

Measurements in the 2.7 Area Ratio Expansion Flow. Measurements in the 2.7 area ratio sudden expansion

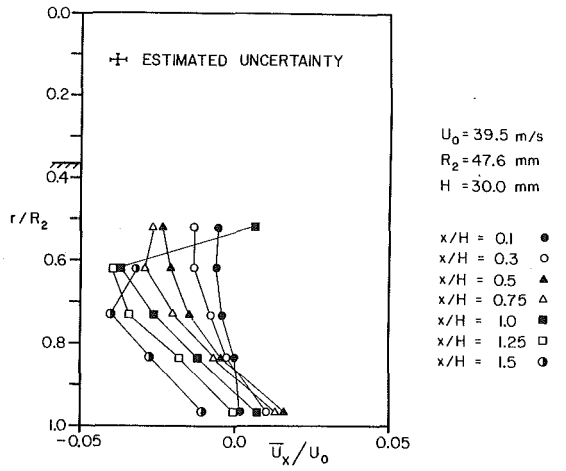

Fig. 10(a) Axial

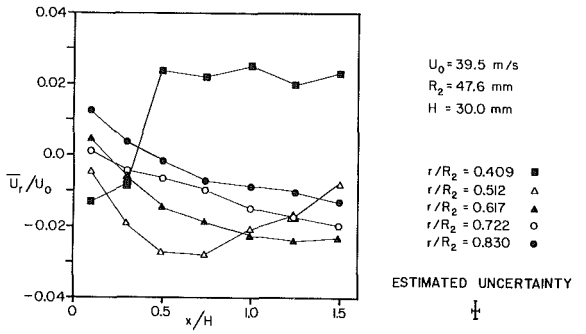

Fig. 10(b) Radial

Fig. 10 Mean velocity profiles in the 2.7 area ratio expansion

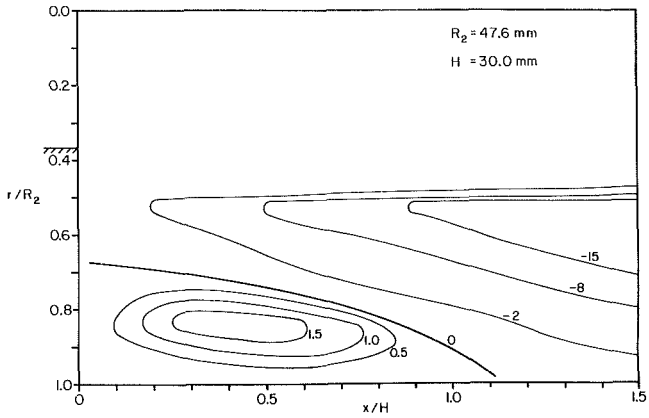

Fig. 11 Stream function contours near the step in the 2.7 area ratio expansion

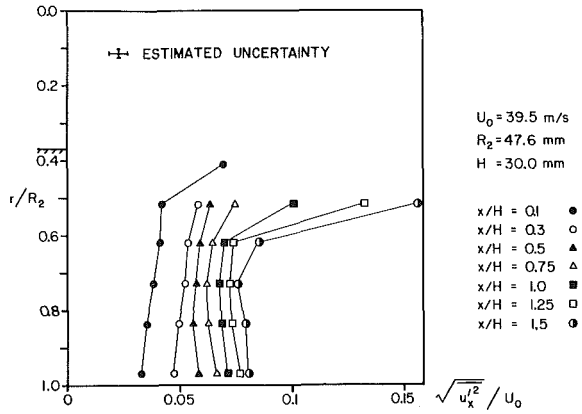

Fig. 12(a) Axial

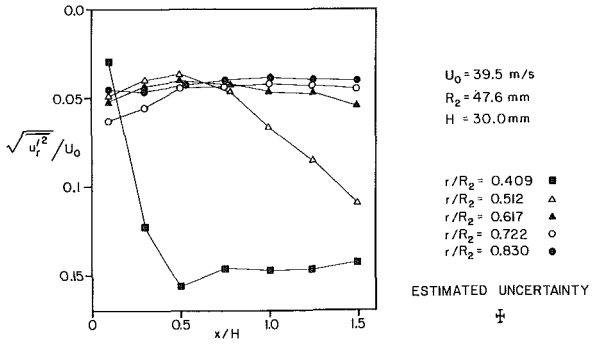

Fig. 12(b) Radial

Fig. 12 Turbulence intensities in the secondary recirculation zone

test section were designed to identify and quantify the secondary recirculation zone flowfield. The inlet velocity was increased to 39.5 m/s to match the Reynolds number condition of the 1.9 area ratio flow. Figure 10 shows the axial and radial mean velocities at several downstream locations, all of which are within 1.5 step heights of the inlet plane. The axial velocities are plotted in the usual fashion, while the radial velocities are plotted with normalized radial position as the parameter to clarify the behavior at a given radius as one moves downstream.

Figure 11 shows stream function contours determined from the data in Fig. 10. The secondary recirculation zone is seen to extend from $r/R_2 \approx 0.7$ out to the wall and from $X/H = 0$ to 1.2 where the secondary reattachment point occurs. This secondary reattachment location agrees well with results from wall shear stress measurements (deBrederode and Bradshaw, 1972; Kangoui and Page, 1979; Driver and Seegmiller, 1982). Primary reattachment in the 1.9 area ratio sudden expansion flow occurred at $x/H \approx 8.3$ and one would expect a similar result for this case. A small portion of the primary recirculation zone can be seen in Fig. 11.

Normalized axial and radial turbulence intensities were nearly uniform at approximately five percent throughout the recirculation zone, compared with the wide range from near zero to approximately 25 percent observed in the primary zone. Profiles are shown in Fig. 12.

Experimental Uncertainty. Uncertainty in single component LDV measurements arises from the normal statistical uncertainty associated with a finite set of data samples in a turbulent flow, drift in mean flowrate during a test run, and possible inaccuracies in individual velocity realizations due to systematic instrument errors. The latter would include errors in the assumed fringe spacing and frequency shift as well as the orientation of the fringes relative to the flow direction. There is also a possible uncertainty due to data grouping in a given histogram sample as a result of the discrete nature of the digital output from a counter type signal processor.

The method of Yanta (1980) was used to estimate the statistical uncertainty. This proved to be less than 0.5 percent for the mean velocity even at turbulence intensities of 25 percent. Uncertainty in the standard derivation was 2.5 percent. Flow system drift was estimated to introduce a mean velocity error of no more than 2 percent based on pitot tube monitoring of the flow at regular intervals.

The dominant source of systematic error in the LDV system was determined to be uncertainty in the fringe spacing which was estimated as 2 percent of the mean velocity. Possible angular misalignment of the fringes was not accounted for directly. It would have negligible effect on the mean axial velocity, but could introduce significant errors in the radial

velocity as was noted in the paper. A comparable effect could result from flow asymmetry.

Total uncertainty in the results based on the root mean square of the individual uncertainties noted above is:

Mean axial velocity ± 3 percent
Mean radial velocity ± 25 percent (Based on observed data scatter.)
Turbulence intensity ± 4 percent
Reynolds stress ± 0.015 or 6 percent of maximum Reynolds stress
Turbulence kinetic energy ± 0.002 or 3 percent of maximum TKE

Conclusions

The availability of a special correction lens system has permitted the measurement of both axial and radial velocities in an axisymmetric sudden expansion air flow using an LDV. As a result it was possible to experimentally map this flow field in considerable detail. Important results and observations from this study are:

1. The 2/E/FIX code based on the k-ϵ turbulence model was reasonably effective in predicting the mean radial velocity as well as the mean axial velocity.
2. The code underpredicted turbulence kinetic energy in regions of significant turbulence.
3. Turbulence intensity and Reynolds stress are not predicted by the code, but the measured values appear to be reasonable and are internally consistent.
4. As expected, a weak secondary recirculation zone was found to exist near the step. Mean velocities are much lower than in the primary zone and the turbulence intensity is low and relatively uniform compared to that in the primary zone. Further details of the investigation are available in Thompson et al. (1984).

Acknowledgment

This work was sponsored by the United States Air Force Wright Aeronautical Laboratories under Contract F33615-81-K-2003. Dr. Roger Craig was the project monitor.

References

Bremmer, R., Thompson, H. D., and Stevenson, W. H., 1980, "An Experimental and Numerical Comparison of Turbulent Flow Over a Step," AFWAL-TR-80-22105, Air Force Wright Aeronautical Laboratories.

Craig, R. R., Nejad, A. S., Hahn, E. Y., and Schwartzkopf, K. G., 1986, "Approach for Obtaining Unbiased Laser Doppler Velocimeter Data in Highly Turbulent Flows," *Journal of Propulsion and Power*, Vol. 2, pp. 541–545.

de Brederode, V., and Bradshaw, P., 1972, "Three Dimensional Flow in Nominally Two-Dimensional Separation Bubbles; I. Flow Behind a Rearward Facing Step," Aero Report 72-19, Imperial College, London.

Driver, D. M., and Seegmiller, H. L., 1982, "Features of a Reattaching Turbulent Shear Layer Subject to an Adverse Pressure Gradient," AIAA-82-1029, AIAA/ASME Third Joint Thermophysics, Fluids, Plasma, and Heat Transfer Conference, St. Louis, Mo.

Durrett, R. P., Gould, R. D., Stevenson, W. H., and Thompson, H. D., 1985, "A Correction Lens for Laser Doppler Velocimeter Measurements in a Cylindrical Tube," *AIAA Journal*, Vol. 23, pp. 1387–1391.

Eaton, J. K., and Johnston, J. P., "An Evaluation of Data for Backward Facing Step Flow," 1980, Conferences on Complex Turbulent Flows, Stanford University, Department of Mechanical Engineering.

Freeman, A. R., 1975, "Laser Anemometer Measurements in the Recirculating Region Downstream of a Sudden Pipe Expansion" *Proceedings of the LDA-Symposium*, Copenhagen, pp. 704–709.

Gould, R. D., Stevenson, W. H., and Thompson, H. D., 1983, "Laser Velocimeter Measurements in a Dump Combustor," ASME Paper 83-HT-47, AICHE/ASME National Heat Transfer Conference, Seattle, Wash.

Kangovi, S., and Page, R. H., 1979, "Subsonic Turbulent Flow Past a Downstream Facing Annular Step," ASME JOURNAL OF FLUIDS ENGINEERING, Vol. 101, pp. 230–236.

Logan, S. E., 1972, "A Laser Velocimeter for Reynolds Stress and Other Turbulence Parameters," *AIAA Journal*, Vol. 19, pp. 933–935.

Moon, L. F., and Rudinger, G., 1977, "Velocity Distribution in an Abruptly Expanding Circular Duct," ASME JOURNAL OF FLUIDS ENGINEERING, Vol. 99, pp. 226–230.

Pun, W. M., and Spalding, D. B., 1976, "A General Computer Program for Two-Dimensional Elliptic Flows," HTS/76/2, Mechanical Engineering Department, Imperial College, London.

Stevenson, W. H., Thompson, H. D., and Craig, R. R., 1984, "Laser Velocimeter Measurements in High Turbulent Reciprocating Flows," ASME JOURNAL OF FLUIDS ENGINEERING, Vol. 106, pp. 173–180.

Stevenson, W. H., Thompson, H. D., and Luchik, T. S., 1982 "Laser Velocimeter Measurements and Analysis in Turbulent Flows With Combustion," AFWAL-TR-82-2076, Part I, Air Force Wright Aeronautical Laboratories.

Stevenson, W. H., Thompson, H. D., and Roesler, T. C., 1982, "Direct Measurement of Laser Velocimeter Bias Errors in a Turbulent Flow," *AIAA Journal*, Vol. 20, pp. 1720–1723.

Thompson, H. D., Stevenson, W. H., and Durrett, R. P., 1984, "Laser Velocimeter Measurements and Analysis in Turbulent Flows with Combustion," AFWAL-TR-82-2076, Part III, Air Force Wright Aeronautical Laboratories.

Yanta, W. D., 1980, "The Use of the Laser Doppler Velocimeter in Aerodynamic Facilities," AIAA-80-0435.

Symmetric and Asymmetric Turbulent Flows in a Rectangular Duct With a Pair of Ribs

T.-M. Liou
Professor.

C.-F. Kao
Graduate Student.

Department of Power Mechanical Engineering,
National Tsing Hua University,
Hsinchu, Taiwan 30043

Laser-Doppler velocimetry (LDV) measurements are presented of mean velocity and turbulence intensity for turbulent flows past a pair of ribs in a rectangular duct of aspect ratio 2. The Reynolds number based on the duct hydraulic diameter was varied in the range of 2.0×10^3 to 7.6×10^4. The experiments cover ribs with rib height to duct height ratios from 0.13 to 0.33 and with rib width to height ratios from 1 to 10. The critical rib height above which and the critical Reynolds number below which the flow patterns become asymmetric were determined from the results. In addition, the effects of the rib width and boundary layer thickness on the formation and the size of the separation bubbles on the top surface of the ribs as well as on the reattachment length behind the ribs were documented. Furthermore, the degree of turbulence enhancement was compared between the asymmetric and the symmetric flows.

Introduction

Flows through ducts with symmetric sudden contraction (Boger, 1982; Durst and Loy, 1985) or expansion (Abbott and Kline, 1962; Durst et al., 1974; Cherdron et al., 1978) in the cross-sectional area are some examples of separated and reattached flows that have been intensively studied in the past. This is partly because they are frequently encountered in engineering practice and partly because their numerical predictions are still not well developed. Furthermore, separated internal duct flows caused by obstructions on two sides of a duct or orifice flows in circular pipes are obviously very complicated since they have the combined features of both contraction and expansion. This type of flow appears in many practical applications such as the internal cooling of turbine blades, the cooling of electronic equipment, the measurement of flow rate, and the study of blood-vessel stenosis, etc. Therefore, a better understanding of such a flow field is highly desirable. However, the literature available is very limited. In addition, it is found that most of the previous work are relevant to orifice flows in circular pipes (Kim and Corcoran, 1974; Mattingly and Davis, 1977; Rastogi et al., 1981; Chen and Yu, 1983) and fewer to separated flows in a rectangular duct past a pair of ribs (Liou and Kao, 1987).

Previous studies pertinent to this work are briefly summarized below. Kim and Corcoran (1974) measured the turbulence spectra downstream from stenoses for Reynolds numbers of 800 to 2000; however, they did not report the velocity profile. Mattingly and Davis (1977) computed the orifice flow at different ratios of orifice hole to pipe diameter for Reynolds numbers of 10 and 50. Of particular interest was the finding of the velocity overshoot which refers to the velocity profile near the orifice surface is larger than that on the pipe centerline. Rastogi et al. (1981) measured and computed the mass transfer coefficients in a circular pipe containing a ring obstruction. Recently Chen and Yu (1983) solved the turbulent flow through an orifice flow in a pipe using the k–ϵ–E turbulence model and the Finite Analytic Method for a Reynolds number of 2×10^5. The results showed the reattachment length behind the orifice is about 0.7 times of that for a sudden expansion flow. The obtained velocity profile within the orifice also displayed the velocity overshoot. However, there is no experimental data for comparison with numerical prediction. In contrast to the above circular pipe configuration containing a ring obstruction, Liou and Kao (1987) made LDV measurements of the flow in a rectangular duct with a pair of obstacles; however, their measurements were carried out only at a single Reynolds number and at a fixed obstacle height.

The brief literature survey made above clearly indicates the lack of reliable experimental study on turbulent flows past a pair of ribs on two sides of a duct. Even the most basic experimental data such as profiles of mean velocity and turbulence intensity needed for comparison with theoretical prediction are lacking. Mathematical modeling of this type of duct flow is also lacking since calculations are usually performed with presumed symmetrical boundary conditions which are often not necessarily true. Therefore, the present paper attempts to experimentally characterize the turbulent flow upstream, through and downstream of a pair of ribs arranged on opposite sides of a rectangular duct at the same downstream location using LDV under a variety of flow and geometry conditions. LDV was chosen in this study since the flow reversals and large turbulence fluctuations in the separation zones make the use of hot wire technique unpractical. The gathered data and insight will be useful to those pursuing the task of numerical prediction in this area of research and development.

The following sections describe the details of the current

Contributed by the Fluids Engineering Division for publication in the JOURNAL OF FLUIDS ENGINEERING. Manuscript received by the Fluids Engineering Division, October 1987.

measurements. The experimental apparatus and conditions are described first. A discussion of data accuracy is given subsequently. The flow fields studied are then typified by a symmetric and an asymmetric flow pattern, based on the measured mean velocity and turbulence intensity as well as characteristic lengths and height of various separation bubbles in front of, on the top of, and behind the ribs. Finally, the effects of varying Reynolds number, rib height, rib width, and boundary layer thickness on the flow characteristics are investigated and discussed.

Experimental Apparatus And Conditions

Experimental System. The flow system and LDV experimental setup is shown in schematic form in Fig. 1. The velocity measurements were made in the LDV-Combustion Laboratory at National Tsing Hua University. Air was drawn into the test section through a flow straightener and six screens in the settling chamber and a 10 to 1 contraction by a turbo blower (3500 rpm/3 phase/10Hp) at the downstream end. The inlet flow established in this way was an essentially, uniform velocity profile. The air then flowed through the two opposite ribs, a flow straightener, a rotameter, a bellows, and was exhausted by the blower.

The LDV optics was set up in a dual beam forward scattering configuration. A linearly polarized 15-mw helium-neon laser (wavelength 632.8 nm) provided the coherent light source. This beam was split into two parallel beams of equal intensity by a beamsplitter. A Bragg cell was used to cause a 40 MHz frequency shift on one of the beams. The frequency shift is used to eliminate the directional ambiguity which is essential if there is flow reversal. The resulting pair of beams was then passed through a 120 mm or 250 mm focal-length lens. The focused beams entered the test section through the transparent plexiglass wall, intersected inside the duct giving a probe volume with dimensions of 0.52 mm by 0.097 mm (120 mm focal-length lens, forward scattering), or 1.96 mm by 0.189 mm (250 mm focal-length lens, forward scattering), and then passed through another side wall into the beam traps. The entire LDV system was mounted on a milling machine with four vibration isolation mounts. This arrangement allowed one to move the probe volume along X, Y, Z directions to any desired location without realigning the optical system. The position accuracy of the optical system was limited by the milling machine and was ± 0.01 mm in the X, Y, and Z movements. The light scattered from the seeding particles was

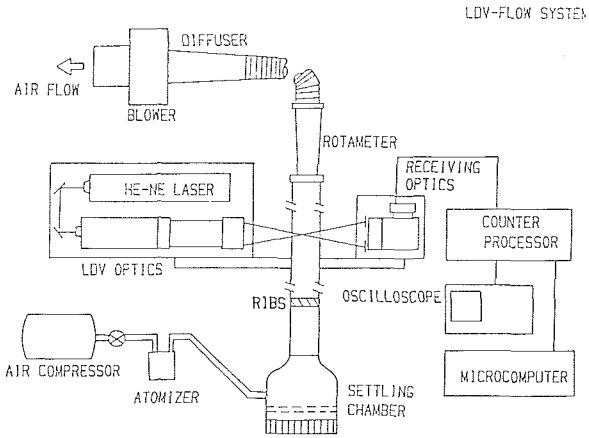

Fig. 1 Schematic drawing of overall experimental system

collected by a receiving optical package and a photomultiplier. The detected signal was electrically downmixed to the appropriate frequency shift (0.1 to 10 MHz in this experiment). Then, a counter processor with 2 ns resolution was used to process the Doppler signal. The Doppler signal was monitored on an oscilloscope and the digital output of the counter processor was fed directly to a micro-computer for storage and analysis. The seeding particles were introduced into the air stream by four atomizers symmetrically located on the walls of the settling chamber. The atomizers were operated by filtered compressed air and salt water and produced particles in the size range 0.5 μm to 5 μm. The salt solution was mixed to give a nominal 0.8 μm particle after the droplet dried.

Test Section and Experimental Conditions. The configuration of the duct, coordinate system, and dimensions are sketched in Fig. 2. The duct was made of a 5 mm plexiglass and had a cross-section of 60 mm $\times$ 30 mm. The ribs were arranged on opposite sides of the duct at the same downstream location which was 250 mm downstream of the bell-mouth 10 to 1 contraction.

The velocity measurements were carried out along the duct central plane ($Z/A = 0$) and were made at 23 stations. In each station the measurements were made at 13 to 15 locations for $X/W < -1$ and $X/W > 0$, and at 6 to 11 locations for $-1 \leq X/W \leq 0$. Within a given data plane, the probe volume was brought as near as 1 mm from the walls ($Y/B = \pm 1$) for

Nomenclature

A = half width of channel (mm)
B = half height of channel (mm)
D = channel hydraulic diameter (= 40 mm)
d = gap hydraulic diameter (= 32 mm for the base configuration)
H = rib height (mm)
L1 Thru L6 = characteristic length (mm)
P_c = static pressure along the center line (mm Aq)
P_w = static pressure on the rib top (mm Aq)
Re_D = Reynolds number based on duct hydraulic diameter ($= D\bar{U}_D/\nu$)
Re_d = Reynolds number based on gap hydraulic diameter
U = streamwise mean velocity (m/s)
U_{ref} = reference mean velocity ($= \bar{U}_D$ m/s)
$\bar{U}_D$ = channel bulk mean velocity (m/s)
$\bar{U}_d$ = gap bulk mean velocity (m/s)
u' = streamwise turbulence intensity (m/s)
v' = transverse turbulence intensity (m/s)
W = rib width (mm)
$\frac{X}{W}$ = normalized streamwise coordinate
$\frac{Y}{B}$ = normalized transverse coordinate
$\frac{Z}{A}$ = normalized spanwise coordinate
ν = kinematic viscosity (m^2/s)
δ_s = boundary layer thickness at the location where the ribs are going to be installed (defined at 0.95 of $U_{\max}$ locally) (mm)
ρ = air density (kg/m^3)
max = maximum value

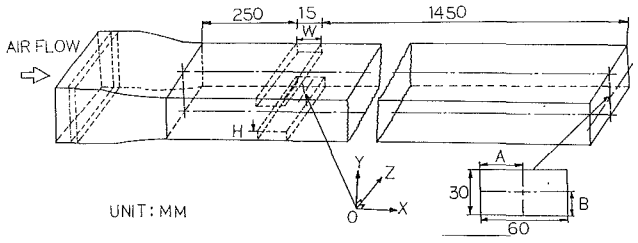

Fig. 2 Sketch of coordinate system and dimensions of rectangular duct with a pair of ribs. (Uncertainty in dimensions: see Table 1.)

streamwise velocity measurements and 4 mm from the walls for transverse velocity measurements, respectively. The bulk mean velocity $\bar{U}_D$ measured at upstream plane $X/W = -10.67$ where the velocity distribution is rather uniform was used as a reference to normalize the experimental results. The Reynolds number range of the investigation was from $\mathrm{Re}_D = 2.0\times10^3$ to 7.6×10^4 or $\mathrm{Re}_d = 2.2\times10^3$ to 8.3×10^4. Various rib heights and widths were also employed to study their effects on the reattachment length. The rib heights and widths were, respectively, as follows: $H = 4$, 5, 8, 10 (mm) and $W = 4$, 8, 15, 20, 32, 40 (mm) or corresponding to $H/2B = 0.13$, 0.17, 0.27, 0.33 and $W/H = 1$, 2, 3.75, 5, 8, 10. The baseline case selected had $H/2B = 0.13$, $W/H = 3.75$, $\bar{U}_D = 15.6$ m/s, and $\mathrm{Re}_D = 3.9\times10^4$.

Results and Discussion

Data Accuracy. The mean velocity and the turbulence intensity were calculated from the probability distribution function of the measurements. There were typically 2000 to 4000 measurements at each measuring location. The corresponding statistical error was between 0.5 to 2 percent in the mean velocity and between 2 to 3 percent in the turbulence intensity for 95 percent confidence level. The velocity measurements were repeated at least once and usually several times to ensure that the measured results were repeatable. The day to day variations were found to be within 1.1 percent in the mean velocity and within 2.3 percent in the turbulence intensity.

Various weighting methods have been proposed to correct the velocity bias effect, but none of these is entirely satisfactory. They all involve assumptions regarding the statistical distribution of particles in the flow. The weighting method proposed by McLaughlin and Tiederman (1973), in which the weighting factor is simply the inverse of the velocity or the particle residence time, has been widely used due to its simplicity. However, it is only appropriate when the turbulence level is below about 30 percent (Drain, 1980). This scheme was then used in this study for regions where local turbulence intensities were below 30 percent. The difference between weighted and unweighted data sets was found to be relatively small (below 2 percent). On the other hand, around the reattachment and within the separation zones the turbulence level was typically very high (Fig. 6 as will be shown later) and near-zero velocities frequenly appear due to flow reversal resulting in very large weighting factors and, in turn, in an overcorrection; therefore, the aforementioned weighting scheme is not really suitable for these regions. However, a few measurements at representative points ($X/W = 1,2,3,4,5,6,7$ for $Y/B = \pm0.87$) have been repeated using equal time interval averaging and the error due to velocity bias was found to be within 2.6 percent.

Velocity gradient broadening in this study was monitored by comparing the results obtained using focusing lenses with a focal length of 120 mm and 250 mm, respectively. The difference was found to be less than 1 percent. Other errors are summarized in Table 1.

In the following, the results for $\mathrm{Re}_D = 3.9\times10^4$, $H/2B = 0.13$, $U_{\mathrm{ref}} = 15.6$ m/s (referred to as case A) and $\mathrm{Re}_D = 3.0\times10^4$, $H/2B = 0.33$, $U_{\mathrm{ref}} = 11.5$ m/s (referred to as Case B), respectively, will be first used as examples to show the typical development of the separated flows measured in this study. As for quantitative data listings of all measurement obtained can be found in (Kao, 1987).

Table 1 The most probable measurement errors

Variable	Errors
Inlet test section	±0.5 mm to 1 mm
Rib height	±0.5 mm
Rib position at $X/W = 0.0$	±0.5 mm
Rib position at $Y/B = 0.0$	±0.5 mm
Rib position at $Z/A = 0.0$	±0.5 mm
Top and bottom ribs	±0.5 mm
Bulk velocity	±1 %
Reattachment length	±3 %

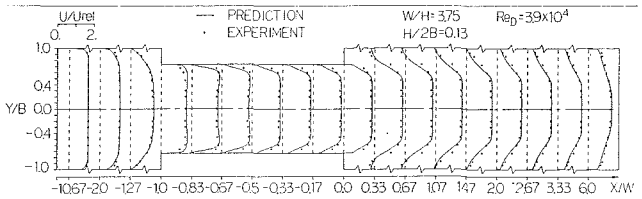

Fig. 3 Streamwise mean-velocity profiles at various stations along plane $Z/A = 0$ for case A. (Uncertainty in U/U_{ref}: less than ±3.2 percent, in Y/B: less than ±1.4 percent, in X/W: less than ±1.4 percent.)

Streamwise Mean Velocity. The streamwise mean velocity profile along $Z/A = 0$ plane is plotted versus dimensionless X coordinate for the aforementioned two typical cases in Figs. 3 and 4 where the X coordinate has been magnified three times in comparison to the Y coordinate for the gap regions, $-1 \le X/W \le 0$, since there are seven measured mean-velocity profiles within such a short distance. Also the solid lines in Fig. 3 represent the computational results (Kao, 1987) based on a modified version of the TEACH-2EF Computer code (Evans, 1981). As one can see the measured and calculated profiles are in good agreement. It is also seen that the streamwise mean-velocity profiles at inlet reference plane, $X/W = -10.67$, are rather uniform, except near the walls, due to the acceleration of the bell-mouth-like contraction. The corresponding turbulence levels and boundary layer thicknesses (defined at 0.95 of $U_{\max}$ locally) in cases A and B are 1 percent, 0.038D and 1.3 percent, 0.052D, respectively. The corresponding momentum thicknesses are 1.48×10^{-4} m and 2.02×10^{-4} m, respectively. At $X/W = -1.27$, however, the flow has adjusted itself with streamwise mean velocity increasing at the central part and decreasing near the walls. For case B (Fig. 4, $X/W = -1.33$), the negative velocity near the walls indicates the existence of two small separation regions in the concave corners of the abrupt contraction formed by ribs. Additional measurements further show the two separation regions are almost symmetric and equal in size with length L3 = 11 mm and height L4 = 3.25. Although for case A (Fig. 3) the aforementioned two separation zones are too small and too close to the walls to be measured by the LDV system in this work, the smoke and oil-film flow visualizations (Kao, 1987) indicate they have approximately 3.7 mm in length (L3) and 1.3 mm in height (L4).

From $X/W = -1$ to 0 the flow is flowing through the contraction passage between the two opposite ribs. To maintain the mass conservation, the flow is accelerated as shown in Figs. 3 and 4. It is worth noting that the velocity maxima at most stations between $X/W = -1$ and 0 are no longer occurring along the centerline except at $X/W = 0$. This phenomenon is often referred to as velocity overshoot and has also been computationally displayed by Mattingly and Davis (1977) for Reynolds number of 10 and 50 and by Chen and Yu (1983) for Reynolds number of 2×10^5, respectively, in a pipe with an orifice. Its formation is due to the curvature of the flow around and downstream of the salient separation point. Durst and Loy (1985) in their study of laminar flows in a pipe with

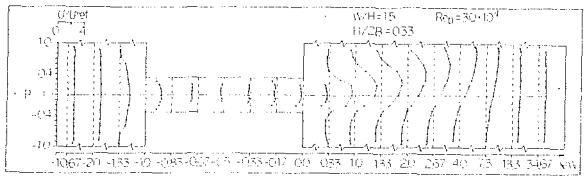

Fig. 4 Streamwise mean-velocity profiles at various stations along plane $Z/A = 0$ for case B. (Uncertainty in U/U_{ref}: less than ±3.2 percent, in Y/B: less than ±1.4 percent, in X/W: less than ±1.4 percent.)

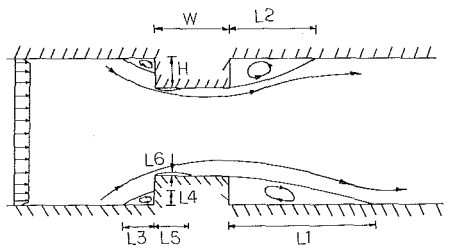

CASE A						CASE B					
$L1/H$	4	$L4/H$	0.33	$H/2B$	0.13	$L1/H$	11	$L4/H$	0.33	$H/2B$	0.33
$L2/H$	4	$L5/H$	0	W/H	3.75	$L2/H$	3	$L5/H$	0	W/H	1.5
$L3/H$	0.92	$L6/H$	0	Re_D	3.9×10^4	$L3/H$	1.1	$L6/H$	0	Re_D	3×10^4

Fig. 5 Sketch and summary of various characteristic lengths for cases A and B. (Uncertainty in L_1/H to L_6/H: less than ±6 percent.)

sudden contraction further indicated the velocity overshoot was associated with the pressure gradient overshoot.

One significant difference between cases A and B worth mentioning here is that for case A (Fig. 3) the flow is symmetric everywhere; however, for case B (Fig. 4) the flow becomes asymmetric downstream of sudden contraction plane ($X/W = -1$). The reason for the occurrence of asymmetric velocity profile in spite of symmetric test section and symmetric inlet velocity profile has been documented by Cherdron et al. (1978) for flows in symmetric ducts with sudden expansions. For certain Reynolds numbers and rib heights, the self-induced small disturbances generated at the rib leading corners are amplified (i.e., flow instabilities) in the shear layers formed between the main flow and the recirculating flows in the concave corners of rib trailing edges. The result is a shedding of eddy-like patterns (Cherdron et al., 1978, pp. 36, Fig. 9) which alternate from one side to the other. The vortex-like patterns influence the flow in the opposite half of the duct through velocity fluctuations, normal to main flow, which extend from each shear layer to the duct center. In general, if the fluctuating normal velocities originating from one shear layer are out of phase with those from the other, the shedding in vortex-like flow patterns is antisymmetric. The antisymmetric shedding causes asymmetric mean flow patterns, and hence recirculating flow regions of unequal length. For case B (Fig. 4) the long side is 110 mm (i.e., $X/W = 7.3$ or $X/H = 11$) and the short side 30 mm (i.e. $X/W = -2$ or $X/H = 3$), respectively. On the other hand, for case A (Fig. 3) the two recirculating regions are identical in size with a reattachment length of 16 mm (i.e., $X/M = 1.07$ or $X/H = 4$). Note that the reattachment point is defined as the x-location close to the wall where the mean velocity changes its sign. In this experiment, the reattachment point was first located visually by flow visualization using light thread attached to the wall, although at the reattachment point the thread was not very stationary owing to the turbulence. The reattachment point was then determined more precisely by near-wall LDV scanning (the probe volume of LDV is placed 1 mm from the wall) around the visually located point. By graphing the velocity at each point, the position at which the mean velocity changes sign could be found.

As the flow proceeds further downstream, case A (Fig. 3) shows the mean velocity decreases at the central part and increases near the walls. At $X/W = 3.33$ the flow appears to attain a profile similar to that upstream of the ribs at $X/W = -1.27$. In contrast, the asymmetric velocity profile in case B (Fig. 4) persists at least ten rib widths downstream of the ribs. The central core flow first moves progressively towards the top wall ($Y/B = 1$) and then gradually moves back again to central axis with more symmetric profile after about thirty rib widths, indicating the flow is gradually approaching fully developed.

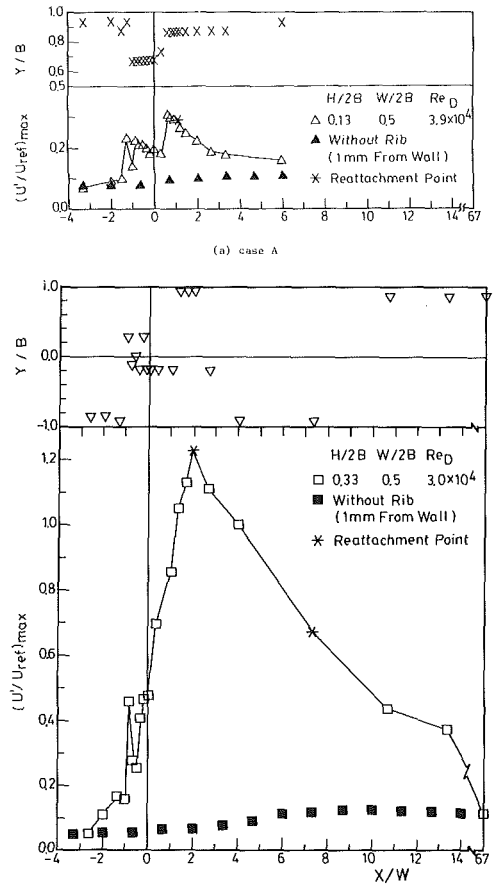

Fig. 6 Normalized streamwise maximum turbulence intensity and its corresponding position (Y/B) at a given station versus streamwise distance for (a) case A and (b) case B. (Uncertainty in $(u'/U_{ref})_{max}$: less than ±4.4 percent.)

To give a whole picture of the separation regions discussed above, Fig. 5 shows a summary of the corresponding characteristic lengths.

Streamwise Turbulence Intensity. It is of interest to observe the relative magnitude of the maximum streamwise turbulence intensities, $(u'/U_{ref})_{max}$, at various streamwise stations. This is shown in Fig. 6 where the results for the ribless duct flows are also included for the purpose of comparison. Note that the Y/B range for the present axial-velocity measurements is from -0.93 to $+0.93$ (i.e., 1 mm from the walls) due to the finite size probe spatial resolution and due to the noise associated with the walls. Hence $(u'/U_{ref})_{max}$ in this study is relative to the above Y/B range. In addition, $(u'/U_{ref})_{max}$ for the ribless duct flows was measured along $Y/B = 0.93$. As one can see the turbulence intensity is enhanced in the region between $X/W = -2$ and $X/W = 10$ for case A and between about $X/W = -2$ and $X/W = 70$ for case B, respectively. Furthermore, both cases show that the degree of turbulence enhancement is highest in the regions around the reattachment points. This is partly because the reattaching streamline occurs in the new shear layer which separates the old shear layer (i.e., free shear layer convected downstream from the rib top) from the

separated-flow region. The back flow in the separated-flow region increases the effective velocity difference across the new shear layer and hence tends to increase the turbulence intensity. Moreover, near reattachment the flow approaches the wall from a direction nearly normal to the wall and splits at reattachment in directions along solid boundaries. The reattachment point thus exhibits the characteristics of classical saddle point. As a result, the velocity histograms near reattachment often have the bimodal shape which results in the highest turbulence levels. In general, the local streamwise turbulence intensities around the reattachment points are 2 to 3 times as large as those for the ribless duct flow for case A and are 6 to 12 times for case B. More specifically, for case A the peak of maximum streamwise turbulence intensities is 31 percent of the corresponding bulk mean velocity and occurs at $X/W=0.67$ which is approximately 1.5 rib heights upstream of reattachment ($X/W=1.07$ or $X/H=4.0$) and, therefore, is in the recirculation zone. It is worth to point out that similar results have also been measured by others in sudden expansion pipe or channel flows where the peak of streamwise turbulence intensities was found to occur mostly at approximately one to two step heights upstream of reattachment (Eaton and Johnston, 1981). For case B, the peak has a value as large as 123 percent of corresponding bulk velocity and occurs at $X/W=2$ (or $X/H=3$) where the flow reattaches the top wall as shown in Fig. 5. It is also interesting to compare the degree of turbulence enhancement between the two cases. As shown in Fig. 6 the asymmetric flow can provide a turbulence enhancement up to 4 times greater than that of the symmetric flow.

The characteristics of the turbulence structure producing the very high turbulence levels in case B are related to the aforementioned coherent eddy-like structures which exist in two shear layers and can interact with each other because of confinement of the small dimensions of the present duct, as suggested by the smoke-visualization results of Cherdron et al. [1978] for sudden-expansion duct flows.

Transverse Turbulence Intensity. In this work the transverse component of the velocity can be measured to about 4 mm from top or bottom wall. Below 4 mm one of the laser beams will be blocked. Figure 7 is thus a plot of transverse turbulence intensity as a function of streamwise distance along $Y/B = 0.73$ or 4 mm from the top wall. Note that the rib height is also 4 mm for case A. In this case measurements downstream of the sudden expansion and along $Y/B=0.73$ are in the interacting region where the new shear layer spreads into the original shear layer (Bradshaw and Wong, 1972). Therefore, Fig. 7 shows the corresponding transverse turbulence intensities are relatively larger than that upstream of the sudden contraction.

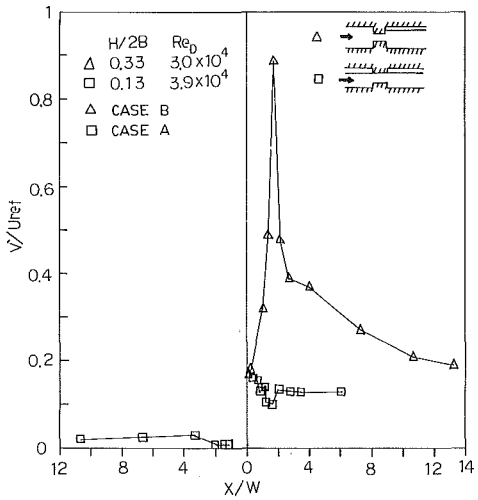

Fig. 7 Variation of normalized transverse turbulence intensity along $Y/B=0.73$ for Cases A and B. (Uncertainty in v'/U_{ref}: less than ±4.4 percent.)

For case B, measurements of the transverse turbulence intensity were only made downstream of ribs. As it can be seen v'/U_{ref} has a peak value of 90 percent of inlet bulk velocity near the reattachment point $X/W=2$ (or $X/H=3$). This is consistent with the observation previously made from the streamwise turbulence intensity in Fig. 6. These results illustrate the reason why the increase in heat and mass transfer generated by turbulence due to the ribs can be put to good use.

Spanwise Flow Distribution. The present experimental investigations were undertaken in a duct with an aspect ratio of 2. The same aspect ratio was also previously used by both Abbott and Kline (1962) and Cherdron et al. (1978) to study the asymmetric flow downstream of a plane symmetric sudden expansion. It is well worth here looking at the spanwise flow distribution in such a duct. The results show that at inlet reference plane $X/W=-10.67$ both mean velocity and turbulence intensity are symmetric and two-dimensional over the center 52 mm of its width (Z-direction) to within 1 percent (Kao, 1987). The two-dimensionality of the flow is also demonstrated by the spanwise location of the reattachment lines shown in Fig. 8 where the deviation from the constant value is within 6 percent for the short side and 3 percent for the long side, respectively. However, measurements made inside the separation zones indicate the three-dimensionality of the flow. One of the examples is thus shown in Fig. 8. It is seen that the flow structures in the separation zones ($X/W=-1.33, Y/B=-0.87$) upstream of the ribs are characterized by multi-vortices rotating about an axis parallel to the Y-axis. Similar vortex structures were also visualized by Abbott and Kline (1962) for flow downstream of a plane sudden expansion.

Effect of Reynolds Number. The normalized reattachment lengths measured from this study for $H/2B=0.13$ are plotted versus Reynolds number (Re_d) based on gap hydraulic diameter in Fig. 9 where some typical results obtained from flows in abruptly expanding circular ducts (Runchal, 1971; back and Roschke, 1972; Iribarne et al., 1972; Moon and Rudinger, 1977) are also included for comparison purpose. As it can be seen the results from this study show a clear transition in the flow field at about $Re_d = 5\times10^3$. Above this Reynolds number, the flow is quite symmetrical and the reattachment length remains nearly constant. In contrast, below this Reynolds number the large difference in the reattachment lengths between the top and bottom walls reveals the asymmetrical nature of the flow. The asymmetry is due to the instabilities of the detached shear layers (Iribarne et al., 1972; Cherdron et al., 1978) shedding from the rib leading edges as

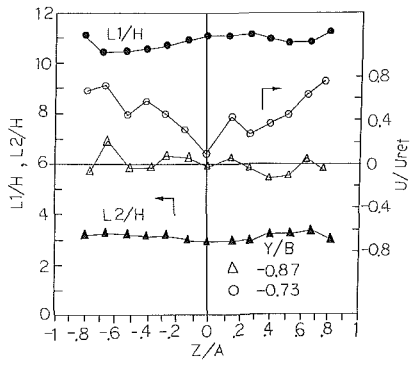

Fig. 8 Spanwise variations of the reattachment lengths and the streamwise mean velocities at $X/W=-1.33$ for case B. (Uncertainty in L_1/H and L_2/H: less than ±6 percent, in U/U_{ref}: less than ±3.2 percent, in Z/A: less than ±1.4 percent.)

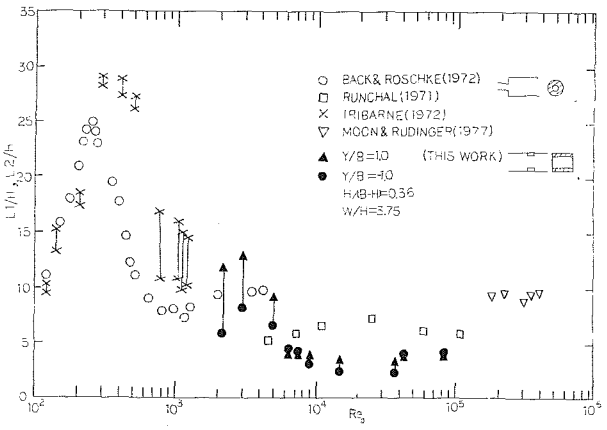

Fig. 9 A comparison of reattachment lengths versus Reynolds number measured by various researchers. (Uncertainty in L_1/H and L_2/H: less than ±6 percent, in Re_d: less than ±3.5 percent.)

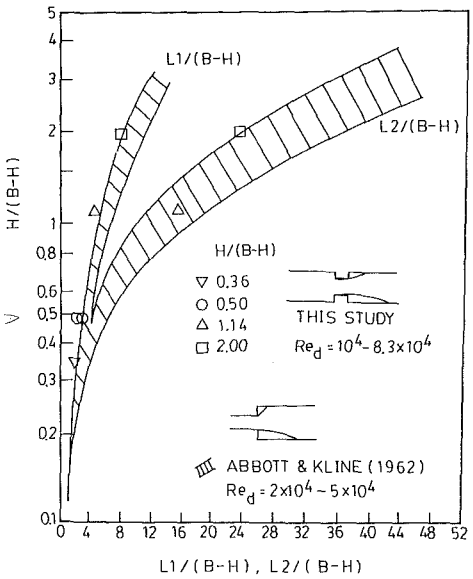

Fig. 10 Normalized rib height or step height versus reattachment lengths. (Uncertainty in $L_1/(B-H)$ and $L_2/(B-H)$: less ±6 percent.)

described earlier. It is believed that the behavior revealed from Fig. 9 would be a useful test of computational models.

Effect of Rib Height. Figure 10 shows the dimensionless reattachment lengths as a function of dimensionless rib height for $W/H = 3.75$. It is interesting to compare the present results with that of relevant prior investigation included in Fig. 10. Although there is geometrical difference between the two investigations, both results reveal the same trend. As it can be seen there exists a critical height of $H/(B-H) = 0.5$. The flow after the sudden expansion is symmetric for $H/(B-H) \leq 0.5$ and asymmetric for $H/(B-H) > 0.5$. Physically this behavior is because that the degree of the interaction between the two detached shear layers shedding from the rib leading corners increases with decreasing gap height $2(B-H)$. The above observation suggests that there exists a limitation on the rib height when one performs computational study of this type of duct flow using symmetrical boundary conditions.

Effect of Rib Width. The normalized reattachment lengths measured from this study are plotted versus normalized rib width in Fig. 11. Generally, the results show a decrease in reattachment length with increasing rib width for $W/H < 5$ and an almost constant reattachment length for $W/H > 5$. This behavior can be explained by looking at the dimen-

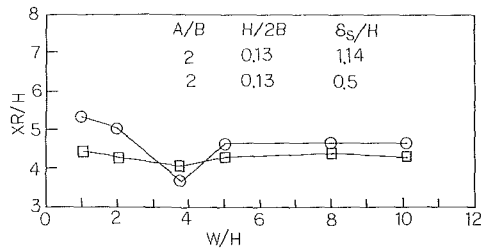

Fig. 11 Normalized reattachment length versus rib width. (Uncertainty in XR/H: less than ± 3 percent.)

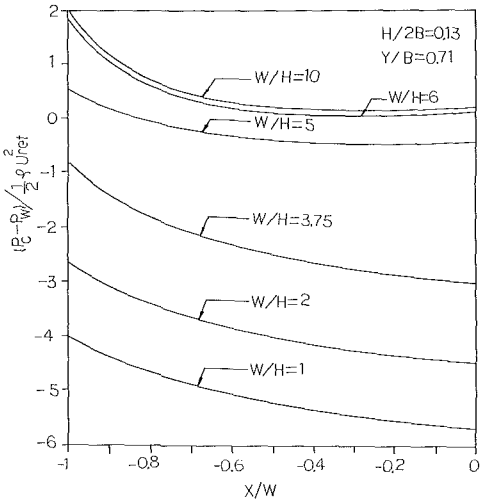

Fig. 12 Normalized pressure difference between the center line and the rib top versus X/W.

sionless pressure difference between the center line and the rib top as shown in Fig. 12 which was obtained by the authors' 2-D computation (Kao, 1987) (It is included here for the purpose of interpretation) using a modified version of the TEACH-2EF Computer code (Evans, 1981). As one can see the static pressure P_w on the top surface of the rib first decreases with increasing W/H and then it remains approximately constant for $W/H > 5$. Physically the reduction of the P_w with increasing W/H implies the suction of the leading corner detached shear layer towards the top surface of the rib (i.e., the angle of the separation line is decreased) resulting therefore in a quicker reattachment downstream of the rib, and thus a decrease in the reattachment length. Eventually ($W/H > 5$ at the present study) the detached shear layer from the leading corner will reattach on the top surface of the rib forming a small bubble. Once the aforementioned small bubble is formed the flow downstream will always separate at the rib trailing corner, and thus a nearly constant reattachment length.

The occurrence of the small bubble mentioned above was observed by the present study with the aid of flow visualization using the oil-film technique. The results are plotted versus W/H in Fig. 13. It is seen that both the maximum height (L6) and length (L5) of the aforementioned small bubble remains approximately constant for $W/H > 5$. This is consistent with the computational results shown in Fig. 12 where the curves for $6 \leq W/H \leq 10$ almost overlap.

Effect of Boundary Layer Thickness. It is of further interest to study the effect of boundary layer thickness on some characteristic lengths of the flow field. This is shown in Figs. 11 and 13. Note that δ_s is the boundary layer thickness at the location where the ribs are going to be installed. As it can be seen, both $\delta_s/H = 1.14$ and $\delta_s/H = 0.5$ curves obtained at the same rib height (Fig. 11) show that reattachment lengths behind the ribs remain constant for $W/H > 5$ due to the reason given in the previous section; however, the curve

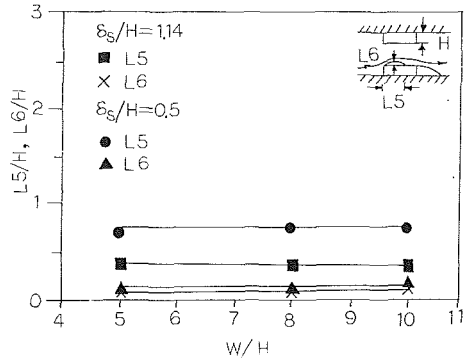

Fig. 13 Maximum length and height of the recirculating bubble on the rib top versus rib width. (Uncertainty in L_5/H and L_6/H: less than ±6 percent.)

$\delta_s/H = 1.14$ drops at a much slower rate than the curve $\delta_s/H = 0.5$ for $W/H < 5$ because the boundary layer thickness of the former is higher than the rib height. The comparison made above suggests that δ_s/H has significant influence on the dependence of the reattachment length upon the rib width provided there is no separating bubble formed on the top surface of the obstacle (i.e., $W/H < 5$). Furthermore, comparing Figs. 11 and 13, it is observed that the thinner the boundary layer thickness δ_s/H is, the longer the separating bubble length ($L5/H$) on the rib top and the reattachment length behind the rib ($L1/H$, $L2/H$) will be.

Conclusions

The paper presents the results of an experimental investigation of the turbulent flow in a rectangular channel, in which there are top and bottom wall symmetric protuberances in the form of forward and backward facing steps. Both symmetric and asymmetric flow patterns are studied. The new and significant information presented here is that the flow field studied behaves qualitatively like similar flow fields provided the Reynolds number is in the proper range; however, below a critical Reynolds number the flow assumes an asymmetric form. This behavior is a useful test of computational models.

Similarly, there exists a critical rib height above which the flow patterns become asymmetric downstream of the rib leading corners. This also poses a problem for numerical solutions of differential conservation equations. In addition, it is found that the reattachment length behind the rib first decreases and then remains constant as the rib width increases. This behavior is related to the formation of the small bubble on the top surface of the rib and can be interpreted using the computed pressure difference between the center line and the rib top.

The present study further shows that the flow structures in the separation zones in front of the ribs are three-dimensional and characterized by multi-vortices rotating about an axis parallel to the Y-axis. As for the turbulence level, the peak $(u'/U_{ref})_{max}$ is found to occur at the short reattachment point for the case of asymmetric flows and at approximately one to two rib heights upstream of the reattachment point for the case of symmetric flows. The former has a peak value of 123 percent which is about four times as large as that of the latter. Also the turbulence enhancement region for asymmetric flows is found to extend downstream a distance about seven times as far as that for symmetric flows.

As a final remark, to simulate the internal cooling passages of turbine blades, understanding the relative influence between successive ribs as well as the d- and k-type roughness effects in the boundary layers (Perry et al., 1969) is necessary. Thus additional work is planned for separated internal duct flows caused by repeated ribs arranged on opposite sides of a duct.

Acknowledgments

Support for this work was provided by the National Science Council of the Republic of China under contract NSC76-0401-E007-05.

References

Abbot, D. E., and Kline, S. J., 1962, "Experimental Investigations of Subsonic Turbulent Flow over Single and Double Backward-Facing Steps," ASME *Journal Basic Engineering*, Vol. 84, pp. 317-352.

Back, L. H., and Roschke, E. J., 1972, "Shear-Layer Flow Regimes and Wave Instabilities and Reattachment Lengths Downstream of an Abrupt Circular Channel Expansion," ASME *Journal of Applied Mechanics*, Vol. 16, pp. 677-681.

Boger, D. V., 1982, "Circular Entry Flows of Inelastic and Viscoelastic Fluids," *Advances in Transport Processes*, Vol. II, Wiley, Eastern Ltd., pp. 125-132.

Bradshaw, P., and Wong, F. Y. F., 1972, "The Reattachment and Relaxation of a Turbulent Shear Layer," *Journal of Fluid Mechanics*, Vol. 52, pp. 113-135.

Chen, C. J., and Yu, C. H., 1983, "The Finite Analytical Method," Vol. 6, *IIHR Report*, 232-VI, The University of Iowa, pp. 115-116.

Cherdron, W., Durst, F., and Whitelaw, J. H., 1978, "Asymmetric Flows and Instabilities in Symmetric Ducts with Sudden Expansions," *J. Fluid Mechanics.*, Vol. 84, Part 1, pp. 13-31.

Drain, L. E., 1980, *The Laser Doppler Technique*, Wiley, pp. 136-141.

Durst, F., Melling, A., and Whitelaw, J. H., 1974, "Low Reynolds Number Flow over a Plane Symmetric Sudden Expansion," *J. Fluid Mech.*, Vol. 64, Part 1, pp. 111-128.

Durst, F., and Loy, T., 1985, "Investigation of Laminar Flow in a Pipe with Sudden Contraction of Cross Section Area," *J. Computer and Fluids*, Vol. 13, No. 1, pp. 15-36.

Eaton, J. K., and Johnston, J. P., 1981, "A Review of Research on Subsonic Turbulent Flow Reattachment," *AIAA Journal*, Vol. 19, No. 9, pp. 1093-1100.

Evans, J. W., 1981, TEACH-2EF, Department of Material Science and Mineral Engineering, University of California, Berkeley, CA.

Iribarne, A., Frantisak, F., Hummel, R. L., and Smith, J. W., 1972, "An Experimental Study of Instabilities and Other Flow Properties of a Laminar Pipe Jet," *AIChE Journal*, Vol. 18, No. 4, pp. 688-698.

Kao, C. F., 1987, "Heat Transfer Enhancement of Turbulent Flows in a Rectangular Duct with a Pair of Ribs," Master Thesis, Dept. of Power Mech. Engrg., National Tsing Hua University, Hsinchu, Taiwan.

Kim, B. M., and Corcoran, W. H., 1974, "Experimental Measurements of Turbulence Spectra Distal to Stenoese," ASME *Journal of Biomechanics*, Vol. 7, pp. 335-342.

Liou, T. M., and Kao, C. F., 1987, "Experimental Measurements of Flow Past Double-Sided Wall Obstacles in a Rectangular Duct," *Proceedings of the Fourth National Conference on Mechanical Engineering*, Accepted for Publication.

Mattingly, G. E., and Davis, R. W., 1977, "Numerical Solutions for Laminar Orifice Flow," ASME Paper, 770WA-77/FE-13.

D. K., and Tiederman, W. G., 1973, "Biasing Correlation for Individual Realization of Laser Anemometer Measurements in Turbulent Flows," *Phys. of Fluids*, Vol. 16, No. 12, pp. 371-385.

Moon, L. F., and Rudinger, G., 1977, "Velocity Distribution in an Abruptly Expanding Circular Duct," ASME JOURNAL OF FLUIDS ENGINEERING, Vol. 15, pp. 226-230.

Perry, A. E., Schofield, W. H., and Joubert, P. H., 1969, "Rough Wall Turbulent Boundary Layers," *Journal of Fluid Mechanics*, Vol. 37, pp. 383-413.

Rastogi, A. K., Kvernold, O., and Sontvedt, T., 1981, "Flow and Mass Transfer in a Perturbed Turbulent Pipe Flow," Numerical Methods in Laminar and Turbulent Flow, edited by Taylor, C., and Schrefler, B. A., *Proceedings of the Second International Conference held at Venice*, (3th-16th) July, pp. 91-96.

Runchal, A. K., 1971, "Mass Transfer Investigation in Turbulent Flow Downstream of Sudden Enlargement of a Circular Pipe for Very High Schmidt Numbers," *Int. J. Heat and Mass Transfer*, Vol. 14, pp. 781-791.

Measurement and Prediction of the Effects of Nonuniform Surface Roughness on Turbulent Flow Friction Coefficients

R. P. Taylor

W. F. Scaggs[1]

H. W. Coleman

Thermal & Fluid Dynamics Laboratory,
Mechanical and Nuclear Engineering
Department,
Mississippi State University,
Mississippi State, MS 39762

The status of prediction methods for friction coefficients in turbulent flows over nonuniform or random rough surfaces is reviewed. Experimental data for friction factors in fully developed pipe flows with Reynolds numbers between 10,000 and 600,000 are presented for two nonuniform rough surfaces. One surface was roughened with a mixture of cones and hemispheres which had the same height and base diameter and were arranged in a uniform array. The other surface was roughened with a mixture of two sizes of cones and two sizes of hemispheres. These data are compared with predictions made using the previously published discrete element prediction approach of Taylor, Coleman, and Hodge. The agreement between the data and the predictions is excellent.

Introduction and Background

Friction coefficients can be significantly larger for turbulent flow over a rough surface as compared with an equivalent turbulent flow over a smooth surface. Surfaces in systems of engineering interest, such as turbine engines, aircraft, re-entry vehicles, missiles, ships, heat exchangers, piping systems, and atmospheric flows, are often rough in the aerodynamic sense. Therefore, there is significant interest in accurate predictive models for turbulent flows over rough surfaces.

There are two general approaches which are used in formulating roughness models—the classic equivalent sandgrain approach and the discrete element approach. The sandgrain approach attempts to reduce the roughness problem to some correlation of a single length scale. This scale is usually some equivalent height. The discrete element method considers the effects of a collection of individual roughness elements on the flow. This is generally done by including a form drag term in the momentum equation and accounting for the blockage effect of the elements on the flow. These two methods are discussed below with the main emphasis being placed on random and nonuniform roughness.

The Equivalent Sandgrain Approach was first proposed by Schlichting (1936) and is always ultimately anchored in the extensive data base for sand roughened pipes which was compiled by Nikuradse (1933). The basic idea is to obtain flow data for a particular surface—velocity profiles and friction factors—and to compare this data with Nikuradse's in order to determine which of Nikuradse's sands give similar flow parameters. Once the relative position in Nikuradse's data base is determined the correlations which are based on sand data can be used to extrapolate the limited data for the surface of interest. Therefore, the equivalent sandgrain roughness, k_s, is a scale of the flow over a rough surface and not a scale of the surface.

Typical computational models which use the equivalent sandgrain roughness are those of Cebeci and Chang (1978) and Ligrani (1979). Both use a modification of the common mixing length model. The mixing length is offset by an amount Δy

$$l_m = \kappa(y + \Delta y) \tag{1a}$$

Ligrani suggests the simple expression

$$\Delta y = 0.0307 k_s \tag{1b}$$

and Cebeci and Chang recommend

$$\Delta y = 0.9(\nu/u^*)[(k_s^+)^{1/2} - k_s^+ \exp(-k_s^+/6)] \tag{1c}$$

If these expressions or other correlations are to be used for a surface where no flow data is available, some means must be given to relate measures of the surface topography to sandgrain roughness.

Several correlations have been published which allow k_s to be determined based on various geometric characteristics of the roughness elements in a uniform array. Typical of these are Dvorak (1969), Simpson (1973) and Dirling (1973). These correlations do not correlate the data well. Berg (1977) found that Dirling's correlation gave k_s values which were 3 times his experimentally determined values. Also, they rely primarily on Schlichting's data which Coleman, Hodge and Taylor (1984) have shown to be in error.

For random roughness several authors have presented cor-

[1]Now with the Computational Fluid Dynamics Group, General Dynamics, Fort Worth, TX.

Contributed by the Fluids Engineering Division for publication in the JOURNAL OF FLUIDS ENGINEERING. Manuscript received by the Fluids Engineering Division January 11, 1988.

relations which relate k_s to some single statistical measure of the roughness height. Many have been based on the centerline average height, Ra, and some on the root mean square height, Rms. Bammert and Sandstede (1976) recommend

$$k_s = 2.19\,\mathrm{Ra}^{0.877} \tag{2}$$

and Koch and Smith (1976) give

$$k_s = 6.2\,\mathrm{Ra} \tag{3}$$

The values from equations (2) and (3) differ by a factor of 2 at Ra = 0.1. Also, equation (2) is dimensionally inconsistent, only holding true for μm units. Acharya et al. (1986) suggest a direct correlation of friction coefficient and Ra. King et al. (1981) recommend a correlation between k_s and the root mean square height

$$\mathrm{Rms} = 0.063 k_s \tag{4}$$

All of these approaches suffer from the omission of texture information. Two surfaces with the same average roughness height can have significantly different friction coefficients.

Taking a slightly different point of view, Townsin et al. (1985) present an equivalent height

$$h' = 53\frac{Ra^2}{Cl_{0.5}} \tag{5}$$

where $Cl_{0.5}$ is the correlation length required for the autocorrelation function of the surface profile to fall to 1/2 of its original value.

The Discrete Element Approach was introduced by Schlichting in the same paper in which he introduced equivalent sandgrain roughness. He proposed that the flow resistance be divided into two parts—form drag on the roughness elements and viscous shear on the smooth area between the elements. He used these ideas in a brief, simple analysis of some of his experimental data but evidently carried the idea no further. Liepmann and Goddard (1957) and Lewis (1975) also took this viewpoint.

The discrete element approach as a computational model for boundary layer flows has its recent origins in the work of M. L. Finson and his coworkers [Finson (1975), Finson and Wu (1979), Finson and Clark (1980) and Finson (1982)]. The model has evolved in the last decade with major contributions being given by Lin and Bywater (1980) and Taylor, Coleman, and Hodge (1984, 1985). Other work has been reported by Adams and Hodge (1977), Christoph and Pletcher (1983), and Christoph (1984).

The basic idea of the discrete element model is to consider the blockage, drag and heat transfer on each individual element. The roughness elements occupy a finite fraction of the space available to flow and thus block the flow. As the fluid flows over and around an element, form or pressure drag results; thus, momentum is extracted from the flow. Also, the elements can act as local heat sinks or sources if heat transfer is taking place.

Discrete element models have proven to be accurate and robust. The model of Taylor et al. (1984) has successfully computed the friction coefficients for fully developed channel flow, fully developed pipe flow and boundary layer flow for 27 different surfaces. The flow regimes ranged from aerodynamically smooth to fully rough, and the pipe Reynolds numbers encountered ranged from 10,000 to 600,000 . See Taylor et al. (1984, 1985) and Scaggs, Taylor, and Coleman (1988a) for these comparisons.

All previous work with discrete element approaches has been limited to using uniform arrays of identical elements in the models. Attempts have been made to postulate equivalent elements for surfaces with nonuniform or random roughness. Lin and Bywater computed sandgrain type roughness using an equivalent hemisphere model where the element spacing was set by numerical experiment—varying the hemisphere model until agreement with the flow data was achieved. Finson (1982) presents a procedure for developing an equivalent element based on surface profiles and profile height probability distribution. To quote Finson, "some judgement is required . . . " to use this procedure. A less judgmental model is presented by Tarada (1987). Tarada uses the height probability density function and the slope probability density function to develop a so-called average element and average element spacing.

The equivalent hemisphere or cone models offer nothing in addition to equivalent sandgrain models. One so-called standard roughness is replaced by another one with a much more restricted data base. The equivalent element models are an improvement over equivalent hemisphere or cone models if the judgement required can be minimized. However, there is still a dimension missing from these models. They average only over

Nomenclature

C_{Di} = local element drag coefficient, equation (9)
$Cl_{0.5}$ = 50 percent correlation length, equation (5)
D = test section diameter
$d_i(y)$ = local element diameter
d_0 = element base diameter
f = friction factor, equation (8) and equation (11)
h' = equivalent roughness height, equation (5)
k = roughness element height, Fig. 1
k' = projected height of a cone, Fig. 1
k_s = equivalent sandgrain roughness length scale
L_a^2 = plan area used for averaging in discrete element model
L = element spacing
l_m = mixing length
$N(y)$ = number of roughness elements, equation (7)
P = pressure
Q = volume flow rate
R = pipe radius
Ra = centerline average roughness height
Re = pipe Reynolds number, Du_{avg}/ν
Re_{di} = local element Reynolds number, $d_i(y)u/\nu$
Rms = root mean square roughness height
R_τ = roughness parameter, τ_R/τ_T
u = local time-averaged velocity
u_{avg} = average velocity in a pipe
u^* = friction velocity, $u_{\mathrm{avg}}\sqrt{f/2}$
y = coordinate normal to the wall
Y_k = height of the tallest element
β_x = blockage factor for a surface normal to x-direction
β_y = blockage factor for a surface normal to y-direction
ΔP = pressure drop
ΔX = distance over which ΔP is measured
Δy = mixing length offset, equation (1)
κ = Von Karman constant; taken as $\kappa = 0.4$
μ = viscosity
μ_T = turbulent eddy viscosity
ν = kinematic viscosity
ρ = density
τ_R = apparent wall shear stress caused by drag on the roughness elements
τ_T = total apparent wall shear stress on a rough surface

Superscripts

$+$ = indicates nondimensional length $(\bullet)u^*/\nu$

the surface geometry and ignore the fact that the desired result is the interaction of the surface and the flow, which is a *nonlinear* process. This would be appropriate if the drag coefficient, C_D, for the roughness elements was a constant value. However, the weight of the evidence indicates that the drag coefficient is a fairly strong nonlinear function of the local element Reynolds number.

A more appropriate approach would be to model the nonuniform roughness as a statistically equivalent distribution of elements of various sizes and shapes.

Discrete Element Model for Nonuniform Roughness

An adaptation of the discrete element model has been proposed by Taylor, Coleman, and Hodge (1985) for three-dimensional roughness elements of random shape, height and spacing. The idea is the same as that for uniform roughness. The physical effects of the roughness elements on the flow are modeled by considering the flow blockage and by postulating that the total force of the elements on the flow can be incorporated as a drag force.

For fully developed turbulent pipe flow the Reynolds-averaged momentum equation as presented by Taylor et al. reduces to

$$0=\frac{\mu}{R-y}\frac{d}{dy}\left[(R-y)\beta_y\left(1+\frac{\mu_T}{\mu}\right)\frac{du}{dy}\right]-\beta_x\frac{dP}{dx}-\frac{1}{2}\frac{\rho u^2}{(R-y)L_a^2/R}\sum_{i=1}^{N(y)}C_{Di}d_i(y), \tag{6}$$

where

$$\beta_x=\beta_y=1-\frac{\pi}{4(R-y)L_a{}^2/R}\sum_{i=1}^{N(y)}d_i^2(y) \tag{7}$$

The parameter $N(y)$ is the number of elements which penetrate a level y in a given wall area L_a^2; $d_i(y)$ is the diameter associated with each of these elements. The averaging area, L_a^2 must be large enough to contain a statistically representative sample of the surface. L_a is *not* the average element spacing as used in formulations for uniform arrays of roughness elements. The friction factor is defined as

$$f=\frac{\left(\beta_y\mu\frac{du}{dy}\right)_w+\frac{1}{2}\int_0^{Y_k}\frac{\rho}{L_a^2}u^2\left(\sum_{i=1}^{N(y)}C_{Di}d_i\right)dy}{\frac{1}{2}\rho u_{avg}^2}, \tag{8}$$

where Y_k is the height of the tallest element.

The drag coefficient, C_{Di}, is computed based on the local element Reynolds number using the calibration of Taylor et al.

$$\log_{10}C_{di}=-0.125\log_{10}(\mathrm{Re}_{di})+0.375 \quad ;\ \mathrm{Re}_{di}<6\times10^4$$
$$C_{di}=0.6 \quad ;\ \mathrm{Re}_{di}>6\times10^4 \tag{9}$$

Turbulence closure is achieved using the Prandtl mixing length formulation with van Driest damping as suggested by Kays and Crawford (1980). That is, near the wall

$$\mu_T=\rho l_m^2\left|\frac{du}{dy}\right| \tag{10a}$$

where

$$l_m=0.40y[1-\exp(-y^+/26)]$$

and

$$\mu_T=0.40\,\mu R^+/6 \tag{10b}$$

in the core region. The boundary between expressions (10*a*) and (10*b*) is taken to be where they give the same value of μ_T. This model was not modified to include roughness effects since the physical effects of the roughness on the flow are included explicitly in the differential equations.

The major difference between this model and the equivalent element models is that the averaging process in equations (6) and (8) is carried out over the product $C_{Di}d_i(y)$ and not just $d_i(y)$.

Experimental Apparatus and Procedures

The experimental apparatus and procedures used to collect the data are discussed in detail by Scaggs, Taylor and Coleman (1988a) and in the preceding companion article (Scaggs, Taylor and Coleman, 1988b). Only a brief outline of the apparatus and procedures are given here.

The apparatus is a closed loop water tunnel which is designed for fully developed flow experiments. The test section is 2.44 m (8 ft) long and 50 mm (2 in.) in diameter. This test section is specially constructed in two halves. In each half, molded silicone test surfaces containing the desired roughness pattern are glued into the test section. The test section is preceded by a 2.44 m (8 ft) long by 50 mm (2 in.) diameter entry section to insure fully developed flow. Using a pump-motor-eddy current clutch assembly to set pump speed, the test section Reynolds number can be set in the range 10,000 to 600,000.

The water tunnel is instrumented to measure the flow rate, water temperature and test section pressure drop. The flow rate is measured using a precision turbine meter. The water temperature is measured with a thermistor in a thermowell. The test section pressure drop is measured with a precision pressure transducer. The friction factor is computed from these measurements using

$$f=\frac{\pi^2\Delta PD^5}{32\rho\Delta XQ^2}. \tag{11}$$

The uncertainty in friction factor is estimated at 95 percent coverage as 4.7 percent. This uncertainty is essentially all bias. Precision errors were determined to be negligible relative to bias. The data points plotted in the figures correspond approximately in size to the measurement uncertainty in the friction factor. Details of the uncertainty analysis, calibrations and tabular data listings are presented in Scaggs et al. (1988a).

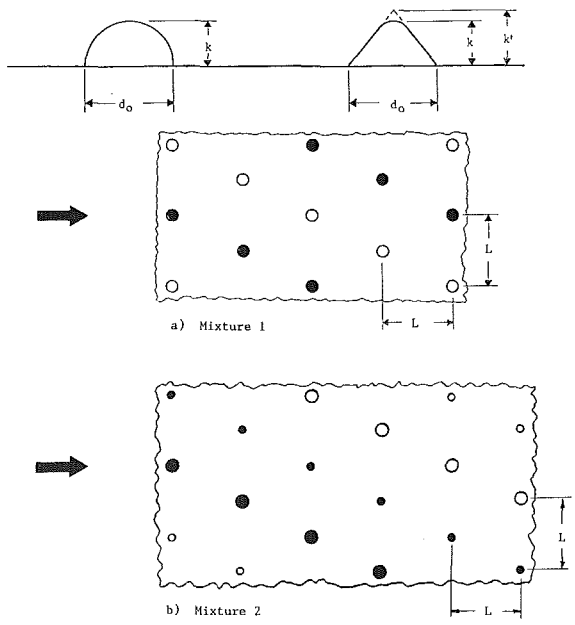

Fig. 1 Surface roughness geometries

Table 1 Nominal and measured geometries of the nonuniform rough surfaces

Surface	Test section diameter (mm)	Base diameter d_0 (mm)		Element spacing L (mm)		Element height k (mm)		Projected height k' (mm)
		nominal	measured	nominal	measured	nominal	measured	nominal
Mixture 1:	51.46			10.16	10.10			
hemispheres		2.54	2.50			1.27	1.20	--
cones		2.54	2.55			1.27	1.30	1.52
Mixture 2:	51.61			10.16	10.15			
Large Hemispheres		2.54	2.50			1.27	1.25	--
Large Cones		2.54	2.50			1.27	1.32	1.52
Small Hemispheres		1.27	1.25			0.64	0.65	--
Small Cones		1.27	1.30			0.64	0.60	0.76

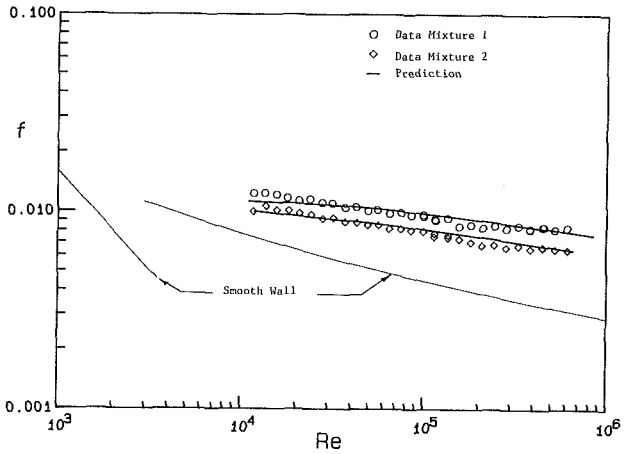

Fig. 2 Comparison of friction factor data and predictions

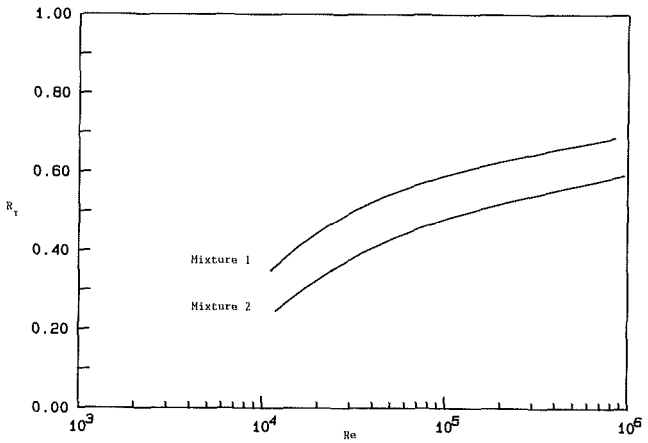

Fig. 3 Roughness parameter, R_T, computed for the surfaces with mixed roughness elements

Results and Discussion

The geometrical parameters describing the shapes and spacings of the hemispherical and conical roughness elements which make up the two nonuniform surfaces are shown in Fig. 1. The nominal and measured values of these geometrical parameters are presented in Table 1.

The surface denoted as Mixture 1 was roughened with hemispheres and cones. Both types of roughness element had a nominal base diameter $d_0 = 2.54$ mm (0.100 in) and a nominal height $k = 1.27$ mm (0.050 in). The roughness elements were spaced 4 base diameters apart. This surface, therefore, had constant roughness element size and spacing, with shape as a variable.

The surface denoted as Mixture 2 was roughened with two sizes of hemispheres and two sizes of cones. The large elements had the same nominal base diameters and heights as those of Mixture 1. The small elements had a nominal base diameter $d_0 = 1.27$ mm (0.050 in) and a nominal height $k = 0.64$ mm (0.025 in). The elements were spaced 10.16 mm (0.400 in) apart. This surface, therefore, contained variations of roughness element size, nondimensional spacing L/d_0, and shape.

The friction factor data for the two surfaces are presented in Fig. 2 and compared with the predictions of the discrete element model and with standard smooth wall correlations. At the higher Reynolds numbers, the data for these surfaces are about 2 to 2 1/2 times smooth wall values. The agreement of the predictions and the data is excellent. This is particularly encouraging for the case of Mixture 2, where variations of shape, height, and nondimensional spacing were involved.

The values of the roughness parameter, $R_T = \tau_R/\tau_T$, calculated from the discrete element model are shown in Fig. 3 for both surfaces. This parameter was recommended by Taylor et al. (1985) as a delimiter for aerodynamically smooth, transitionally rough and fully rough flow regimes. Scaggs et al. (1988a) suggest a value of $R_T = 0.60$ as an appropriate boundary between the transitionally and fully rough regimes. Using this criterion, the data for Mixture 1 with Re > 100,000 would be in the fully rough regime, while all other data would be in the transitionally rough regime.

Acknowledgments

This work was supported by the U. S. Air Force Wright Aeronautical Laboratories, Contract F33615-84-K-3014. The experimental apparatus was constructed with the support of the U. S. Air Force Office of Scientific Research, Grant AFOSR-85-0075. The authors thank Mr. Melvin Buck and Dr. Tony Fiore of the Wright Aeronautical Laboratories and Dr. James Wilson of the Air Force Office of Scientific Research for their support and encouragement.

References

Acharya, M., Bornstein, J., and Escudier, M. P., 1986, "Turbulent Boundary Layers on Rough Surfaces," *Experiments in Fluids*, Vol. 4, pp. 33–47.

Adams, J. C., and Hodge, B. K., 1977, "The Calculation of Compressible Transitional Turbulent and Relaminarization Boundary Layers over Smooth and Rough Surfaces Using an Extended Mixing-Length Hypothesis," AIAA Paper 77-682.

Bammert, K., and Sandstede, H., 1976, "Influences of Manufacturing Tolerances and Surface Roughness of Blades on the Performance of Turbines," ASME *Journal of Engineering for Power*, Vol. 98, pp. 29–36.

Berg, D. E., 1977, "Surface Roughness Effects on the Hypersonic Turbulent Boundary Layer," Ph.D. Dissertation, Graduate Aeronautical Laboratories, Cal. Tech.

Cebeci, T., and Chang, K. C., 1978, "Calculation of Incompressible Rough-Wall Boundary-Layer Flow," *AIAA Journal*, Vol. 16, pp. 730–735.

Christoph, G. H., 1984, "Skin Friction and Heat Transfer for Combined Roughness and Mass Addition," in *Laminar Turbulent Boundary Layers*, ASME Publication, FED-Vol. 11.

Christoph, G. H., and Pletcher, R. H., 1983, "Prediction of Rough-Wall Skin Friction and Heat Transfer," *AIAA Journal*, Vol. 21, pp. 509–515.

Coleman, H. W., Hodge, B. K., and Taylor, R. P., 1984, "A Reevaluation of Schlichting's Surface Roughness Experiment," ASME JOURNAL OF FLUIDS ENGINEERING, Vol. 106, pp. 60–65.

Dirling, R. B., Jr., 1973, "A Method for Computing Rough Wall Heat Transfer Rates on Reentry Nose Tips," AIAA Paper No. 73-763.

Dvorak, F. A., 1969, "Calculation of Turbulent Boundary Layers on Rough Surfaces in Pressure Gradients," *AIAA Journal*, Vol. 7, pp. 1751–1759.

Finson, M. L., 1975, "A Reynolds Stress Model for Boundary Layer Transition with Application to Rough Surfaces," AFOSR-TR-0322.

Finson M. L., 1982, "A Model for Rough Wall Turbulent Heating and Skin Friction," AIAA Paper 82-0199.

Finson, M. L., and Clark, A. S., 1980, "The Effect of Surface Roughness Character on Turbulent Reentry Heating," AIAA Paper 80-1459.

Finson, M. L., and Wu, P. K. S., 1979, "Analysis of Rough Wall Turbulent Heating with Applications to Blunted Flight Vehicles," AIAA Paper 79-008.

Kays, W. M., and Crawford, M. E., 1980, *Convective Heat and Mass Transfer*, 2nd edition, McGraw-Hill, New York, NY.

King, M. J., Chuah, K. B., Olszowski, S. T., and Thomas, T. R., 1981, "Roughness Characteristics of Plane Surfaces Based on Velocity Similarity Laws," ASME Paper 81-FE-34.

Koch, C. L., and Smith, L. H., 1976, "Loss Sources and Magnitudes in Axial-Flow Compressors," ASME *Journal of Engineering for Power*, Vol. 98, pp. 411–424.

Lewis, M. J., 1975, "An Elementary Analysis for Predicting the Momentum- and Heat-Transfer Characteristics of a Hydraulically Rough Surface," ASME *Journal of Heat Transfer*, Vol. 97, pp. 249–254.

Liepmann, H. W., and Goddard, F. E., 1957, "Note on the Mach Number Effect Upon the Skin Friction of Rough Surfaces," *J. Aeronautical Sci.*, Vol. 24, p. 784.

Ligrani, P. M., 1979, "The Thermal and Hydrodynamic Behavior of Thick Rough-Wall, Turbulent Boundary Layers," Ph.D. Dissertation, Dept. Mech. Eng., Stanford Univ.; Report HMT-29.

Lin, T. C., and Bywater, R. J., 1980, "The Evaluation of Selected Turbulence Models for High-Speed Rough-Wall Boundary Layer Calculations, AIAA Paper 80-0132.

Nikuradse, J., 1933, "Stromungsgesetze in Rauhen Rohren," VDI-Forchungsheft 361. (Also, "Laws of Flow in Rough Pipes," NACA TM 1292.)

Scaggs, W. F., Taylor, R. P., and Coleman, H. W., 1988a, "Measurement and Prediction of Rough Wall Effects on Friction Factors in Turbulent Pipe Flow," Mechanical and Nuclear Engineering Department, Mississippi State University, Report TFD-88-1.

Scaggs, W. F., Taylor, R. P., and Coleman, H. W., 1988b, "Measurement and Prediction of Rough Wall Effects on Friction Factor—Uniform Roughness Results," ASME JOURNAL OF FLUIDS ENGINEERING, published in this issue pp. 385–391.

Schlichting, H., 1936, "Experimentelle Untersuchungen Zum Rauhigkeits-Problem," *Ingenieur-Archiv.*, Vol. VII, No. 1, pp. 1–34. (Also "Experimental Investigation of the Problem of Surface Roughness," NACA TM 823).

Simpson, R. L., 1973, "A Generalized Correlation of Roughness Density Effects on the Turbulent Boundary Layer," *AIAA Journal*, Vol. 11, pp. 242–244.

Tarada, F., 1987, "Prediction of Heat Transfer to Rough Turbine Blading Using a Two-Equation Model of Turbulence—Part 6: Topographical Models of Stochastic Roughness," Thermo-Fluid Mechanics Research Centre, University of Sussex, Report 87/TFMRC/104.

Taylor, R. P., Coleman, H. W., and Hodge, B. K., 1984, "A Discrete Element Prediction Approach for Turbulent Flow Over Rough Surfaces," Mechanical and Nuclear Engineering Department, Mississippi State University, Report TFD-84-1.

Taylor, R. P., Coleman, H. W., and Hodge, B. K., 1985, "Prediction of Turbulent Rough-Wall Skin Friction Using a Discrete Element Approach," ASME JOURNAL OF FLUIDS ENGINEERING, Vol. 107, No. 2, pp. 251–257.

Townsin, R. L., Spencer, D. S., Mosaad, M., and Patience, G., 1985, "Rough Propeller Penalties," Presented at the Annual Meeting of the Society of Naval Architects and Marine Engineers, New York, Nov. 13–16, Paper No. 7.

W. F. Scaggs[1]

R. P. Taylor

H. W. Coleman

Thermal & Fluid Dynamics Laboratory,
Mechanical and Nuclear Engineering
Department,
Mississippi State University,
Mississippi State, MS 39762

Measurement and Prediction of Rough Wall Effects on Friction Factor—Uniform Roughness Results

The results of an experimental investigation of the effects of surface roughness on turbulent pipe flow friction factors are presented and compared with predictions from a previously published discrete element roughness model. Friction factor data were acquired over a pipe Reynolds number range from 10,000 to 600,000 for nine different uniformly rough surfaces. These surfaces covered a range of roughness element sizes, spacings and shapes. Predictions from the discrete element roughness model were in very good agreement with the data.

Introduction

Given the geometry of an object immersed in a flowfield, a specification of the freestream flow conditions, and a geometrical description of the roughness of the system surfaces, an analyst or designer would like at least to be able to predict the surface shear distribution, the heat transfer distribution and the total drag. In the past, most of the research effort has been directed at the development of computational methods for various geometries with smooth surfaces, and the roughness problem has received relatively little attention. However, many systems of engineering interest have surfaces which are aerodynamically rough. Therefore, if the flow parameters mentioned above are to be predicted, computational procedures to model the effects of rough surfaces must be developed and proven by comparison with well-documented data sets.

Schlichting (1936) experimentally investigated the fluid dynamics of this type of problem. He related his skin friction results on a range of well-described rough surfaces to the previous results obtained by Nikuradse (1933) for sand-roughened pipes through definition of an equivalent sandgrain roughness, k_s. In subsequent surface roughness effects investigations, workers used these results of Schlichting and the equivalent sandgrain roughness concept in analyzing their experimental data and in developing analytical models for use in predictive methods. Over the years, several correlations (Dvorak, 1969; Simpson, 1973; Dirling, 1973) were developed which produced a value of k_s for a rough surface when certain geometrical descriptors were known. These correlations were all intimately tied to the original k_s results of Schlichting.

An important data set of somewhat limited range was reported by Chen (1971), who determined the skin friction in 0.19 m diameter pipes roughened with hemispherical roughness elements at three spacings. The most interesting part of Chen's work was the segregation of the two components of the apparent wall shear stress. He did this by measuring the total force on one roughness element and determining the total apparent wall shear stress from pressure drop measurements.

Over the past decade or so, a predictive approach called the discrete element method, which does not use the equivalent sandgrain roughness concept, has been used with varying degrees of rigor by several groups of researchers (Finson, 1975; Adams and Hodge, 1977; Finson and Wu, 1979; Finson and Clark, 1980; Lin and Bywater, 1980; Finson, 1982; Taylor, Coleman and Hodge, 1983; Taylor, Coleman and Hodge, 1985). Such approaches rely on empirical input in order to calibrate the roughness models.

Until the present time, the experimental results of Schlichting (1936) have remained the only data sets which included the effects of well-defined roughness element shape, size and spacing on skin friction. However, Coleman, Hodge and Taylor (1984) showed that Schlichting had made erroneous assumptions during his data reduction which had significant effects on the data which he reported. It was shown that his skin friction results were too large by amounts ranging up to 73 percent and that his reported values of k_s were too high by amounts ranging from 26 to 555 percent. These findings caused some consternation since practically all work since the 1930's on surface roughness effects relied significantly on either the skin friction or k_s results as originally reported by Schlichting.

As a result of the research efforts discussed above, it became apparent that there exists a need for accurate, precise, comprehensive data sets on the fluid dynamics in turbulent flow over well-defined rough surfaces. The research discussed in this paper was designed to investigate the effects of surface roughness element size, spacing and shape on friction factor in fully developed flow over a wide range of Reynolds numbers.

[1]Now with the Computational Fluid Dynamics Group, General Dynamics, Fort Worth, TX.

Contributed by the Fluids Engineering Division for publication in the JOURNAL OF FLUIDS ENGINEERING. Manuscript received by the Fluids Engineering Division January 11, 1988.

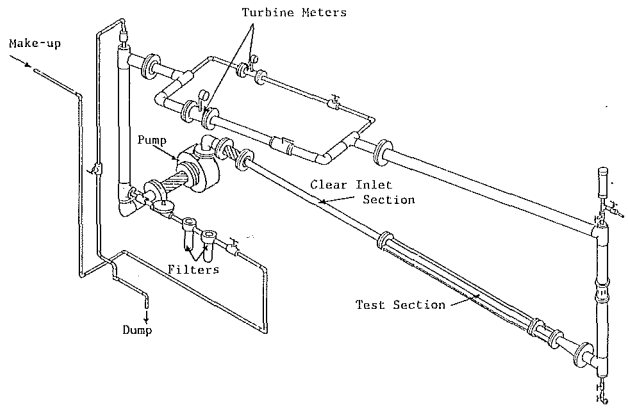

Fig. 1 Schematic of water tunnel facility

Experimental Apparatus

The closed loop water tunnel, shown in Fig. 1, was constructed to experimentally investigate the effects of surface roughness on friction factors in fully developed pipe flow. The system can be operated over a range of pipe Reynolds numbers from about 10,000 to 600,000.

The pump, motor, and eddy current clutch assembly (which allows a variable pump speed) are located on a spring-mounted concrete base to isolate induced vibrations. The inlet and outlet of the pump are connected to flexible hoses in a further attempt to isolate the pump and motor vibrations from the rest of the system.

After exiting the pump the water enters a 2.44 m (8 ft) long, 50 mm (2 in.) diameter clear pipe. In this clear section the flow was visually inspected to insure that there was no swirl superimposed on the flow. This inspection was done as the air was bled from the tunnel after initially filling it with water.

Connected to the clear pipe is the 2.44 m (8 ft) long test section. There was one test section for each surface tested. Each section has a nominal diameter of 50 mm (2 in.) and is made of two fiberglass halves. In each half, molded silicone sheet test surfaces containing the desired roughness pattern are glued into the test section. So that the pressure drop can be measured, there are 12 pressure taps evenly spaced at 203.2 mm (8 in.) along the test section. These taps are brass tubing with an outside diameter of 1.59 mm (1/16 in.) and an inside diameter of 0.79 mm (1/32 in.). Using a specially designed guide and cutter, techniques were developed so that very repeatable holes were cut in the silicone sheets to finish the pressure taps. With the pressure tap holes cut, the two halves were bolted together and the test section was ready to be placed in the water loop.

The silicone skins mentioned above are the means by which a rough surface is created for each test section. These skins are precision molded 203 mm (8 in.) by 81 mm (3.2 in.) by 0.25 mm (.010 in.) thick silicone sheets. The desired roughness pattern, say hemispheres spaced four diameters apart, is molded on the skin at the same time that the skin is molded. This process allows a large number of roughness elements to be precisely and easily attached to the test section wall. All skins used in this project were manufactured according to the procedures described by Holden (1983).

After exiting the test section the flow passes through one of two turbine meters. The turbine meters measure the volumetric flowrate of the water. The meters are valved manually and chosen depending on the desired Reynolds number range.

The flow then returns to the inlet of the pump; however, since the temperature of the water tends to increase from the pump work, a portion of the flow is dumped and cooler make-up water is added. The make-up water passes through a pressure regulator and a 50 micron particulate filter before entering the system.

Experimental Procedure

The wall shear stress for steady incompressible fully developed pipe flow can be written as

$$\tau_w = \frac{\Delta P}{4}\frac{D}{\Delta X}. \tag{1}$$

Defining the friction factor as

$$f = \frac{\tau_w}{\rho u_{\text{avg}}^2/2} \tag{2}$$

and recalling that for pipe flow the average velocity is $u_{\text{avg}} = 4Q/\pi D^2$, the data reduction equation for this experiment can be written as

$$f = \frac{\pi^2}{32}\frac{\Delta P}{\rho}\frac{D^5}{\Delta X}\frac{1}{Q^2}. \tag{3}$$

The procedure used to obtain a data point (f and Re) was as follows. Considering $\text{Re} = 4\rho Q/\pi\mu D$ and equation (3) for f, it can be seen that five measurements are required: water temperature, to obtain ρ and μ; test section diameter, D; flow rate, Q; pressure drop, ΔP; and distance, ΔX. Temperature was measured using a thermistor, and flow rate was measured using the turbine meters discussed above. The diameters of the

Nomenclature

C_D = roughness element drag coefficient, equation (9)
d_0 = roughness element base diameter
$d(y)$ = local roughness element diameter
D = pipe diameter
f = friction factor, equations (3) and (6)
k = roughness element height
k' = projected height of conical roughness elements
k^+ = nondimensional roughness height, ku^*/ν
k_s = equivalent sandgrain roughness
L = roughness element spacing
l_m = Prandtl mixing length, equation (7a)
P = pressure
Q = volumetric flowrate
r = radial coordinate
R = pipe radius
R^+ = nondimensional R; Ru^*/ν
R_τ = roughness parameter, τ_R/τ_T
Re = Reynolds number based on test section diameter
Re_d = Reynolds number based on local roughness element diameter, equation (8)
Re_{k_s} = roughness Reynolds number; $k_s u^*/\nu$
$u(y)$ = velocity at y-location
u^* = friction velocity; $u_{\text{avg}}\sqrt{f/2}$
u_{avg} = average velocity in pipe
y = coordinate normal to the surface
y^+ = nondimensional y; yu^*/ν
β_x = blockage factor
β_y = blockage factor
ΔP = pressure drop
ΔX = distance over which ΔP is measured
μ = dynamic viscosity
μ_T = eddy viscosity
ν = kinematic viscosity
ρ = density
τ_R = apparent wall shear stress due to form drag on elements
τ_T = total wall shear stress
τ_w = wall shear stress

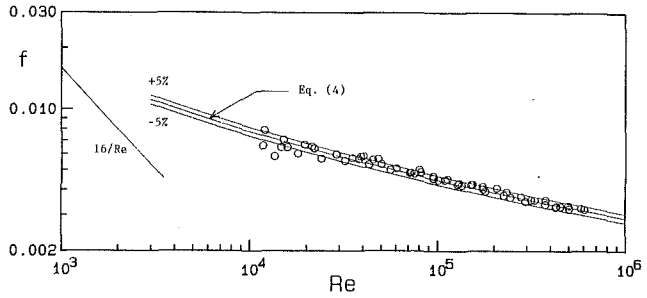

Fig. 2 Friction factor data for smooth, bare wall test section

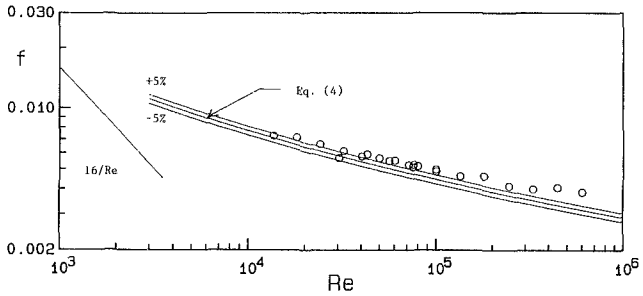

Fig. 3 Friction factor data for smooth, silicone skin test section

test sections were measured with a micrometer. Pressure drop was determined by measuring the pressure difference between every other static tap—$\Delta X = 406.4$ mm (16 in.). The test section was divided into ten of the these ΔX's by plumbing a fluid switch wafer to place across the differential pressure transducer tap 1 versus 3, tap 2 versus 4, tap 3 versus 5, etc.

Although fully developed smooth wall pipe flow exists at the junction of the inlet section and the test section, slight misalignments could cause an entry effect. In addition, the flow requires several diameters to adjust to the test section roughness. Therefore, the first two ΔP's (the first 500 mm or 10 diameters) were not used in determining friction factors. Using the remaining downstream ΔP's, eight values of f were computed and averaged to give the reported value.

The uncertainties associated with the measurements are estimated at 95 percent coverage as:

temperature	±0.2°C
flowrate	±1.25 percent
pressure drop	±1.5 percent
diameter	±0.74 percent
length ΔX	±0.05 mm

These uncertainties are essentially all bias. Precision errors were determined to be negligible relative to the bias error estimates. The resulting uncertainty in the friction factor is ±4.7 percent. The uncertainty in the diameter is the major cause of the uncertainty in the friction factor. This is caused by the dependence of the friction factor on the fifth power of the diameter as shown in equation (3). The uncertainty in the Reynolds number is ±1.5 percent. The data points plotted in the figures correspond approximately in size to the measurement uncertainty in the friction factor. Details of the uncertainty analysis, calibration procedures, tabular data listings, etc. have been presented in Scaggs et al. (1988).

Test Rig Qualification

To qualify this experimental apparatus, a bare wall test section and a test section with smoooth silicone skins were tested so that the smooth wall data obtained might be compared to accepted smooth wall data.

An excellent source of smooth wall pipe data is the exhaustive compilation of data prepared and presented by Drew, Koo, and McAdams (1932). In all 1328 data points were reported, with all but a few points scattering within a ±5 percent band. They reported the best line through the friction factor data to be

$$f = 0.00140 + \frac{0.125}{\mathrm{Re}^{0.32}}. \tag{4}$$

The data obtained in the Mississippi State University (MSU) water tunnel for the bare wall test section are plotted in Fig. 2. These data fall primarily within the ±5 percent data scatter exhibited in the compilation of Drew et al. (1932), This close agreement with such a large volume of accepted smooth wall data indicated the validity of the MSU instrumentation and data reduction procedures, thus moving the experimental program through the qualification phase and into the production phase of the research project.

The runs plotted in Fig. 2 and the other runs presented in this work include replications made on different days as well as replications made with the test section reversed. That is, the exit end of the test section was made the entrance end for the reverse run. One of these orientations was arbitrarily labeled north while the other was labeled south. With the flow entrance noted as north, friction factor data were taken for a series of Reynolds numbers. The section was then reversed, the flow entrance now being south, and data were taken at Reynolds numbers that would fall between those of the northern replication. No preference should be assumed for the north or south designations.

The data obtained using the test section with the smooth silicone skins are plotted in Fig. 3. The data of these replications fall above the ±5 percent band of the accepted smooth wall data. This was not surprising, since the addition of the glue and the silicone sheets to the test section produced a surface that was not as smooth as the surface finish of the bare fiberglass section. Also, seams resulted at the joints between two silicone sheets. This created small transverse ridges every 203 mm (8 in.) down the test section. The effects of this added roughness on the friction factors is more pronounced at the higher Reynolds numbers as seen in Fig. 3.

The Discrete Element Model for Uniform Roughness

The discrete element model presented in this work is formulated for roughness elements with three dimensional shapes (as opposed to transverse ribs, for example) for which the element cross section can be approximated as circular at every height, y. The physical effects of roughness on the flow field are modeled by considering the blockage effect of the roughness elements and the drag forces which the roughness elements exert on the fluid. In the following, attention is restricted to roughness elements of uniform shape and spacing. The case of axisymmetric fully developed internal flow in a pipe of radius R as presented below is a simplified extension of the equations for steady (Reynolds-averaged), two-dimensional turbulent boundary layer flow over a rough surface as derived by Taylor, Coleman, and Hodge (1984, 1985). The momentum equation is

$$0 = \frac{\mu}{R-y}\frac{d}{dy}\left[(R-y)\beta_y\left(1+\frac{\mu_T}{\mu}\right)\frac{du}{dy}\right] - \beta_x\frac{dP}{dx} - \frac{1}{2}\rho C_D\frac{u^2 d(y)}{(R-y)L^2/R}, \tag{5}$$

where $\beta_x = \beta_y = 1 - \pi d^2(y)/[4(R-y)L^2/R]$.

The parameters β_x, β_y and $d(y)$ are determined solely from the roughness element geometry with no empirical input required. For uniform arrays the cross-sectional diameter, $d(y)$, is the same for all of the elements at a given y-location.

As in Taylor et al. (1984, 1985), the "wall shear stress" is

defined as the sum of the shear and form drag forces on the wall in the mean flow direction divided by the plan area of the wall. The corresponding friction factor can then be written as

$$f=\frac{(\beta_y)_w\mu\left.\frac{du}{dy}\right|_w+\frac{1}{2}\int_0^k\frac{1}{L^2}(\rho dC_D u^2)dy}{\frac{1}{2}\rho u_{\text{avg}}^2}. \tag{6}$$

In order to solve equation (5) an eddy viscosity turbulence model for μ_T and a roughness model for C_D were required. Turbulence closure was achieved using the Prandtl mixing length formulation with van Driest damping as suggested by Kays and Crawford (1980). That is, near the wall

$$\mu_T=\rho l_m^2\left|\frac{du}{dy}\right| \tag{7a}$$

where

$$l_m=0.40y[1-\exp(-y^+/26)]$$

and

$$\mu_T=0.40\mu R^+/6 \tag{7b}$$

in the core region. The boundary between equations (7*a*) and (7*b*) is taken to be where they give the same value of μ_T. This model was not modified to include roughness effects since the physical effects of the roughness on the flow are included explicitly in the differential equations.

Taylor et al. (1984, 1985) chose to formulate the C_D model as a function of the local element Reynolds number

$$\text{Re}_d=\frac{u(y)d(y)}{\nu} \tag{8}$$

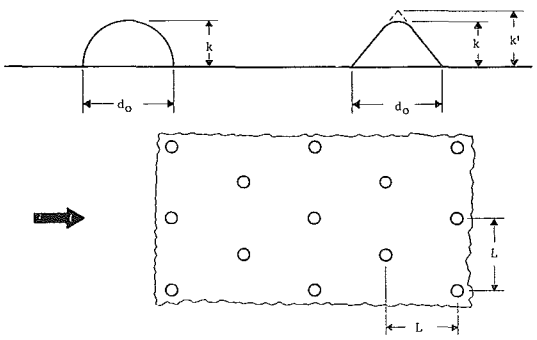

Fig. 4 Surface roughness geometry

which includes roughness element size and shape information through $d(y)$. This model (as calibrated using the corrected Schlichting data sets for surfaces with spherical, spherical segment and conical roughness elements) is given by

$$\log_{10} C_D = -0.125\log_{10}(\text{Re}_d)+0.375;\text{Re}_d<6\times10^4$$

$$C_D = 0.6 \qquad ;\text{Re}_d\geq 6\times10^4. \tag{9}$$

For the conditions covered in this experimental program, the largest predicted value of Re_d was about 17,000 as calculated from equation (5) for the densest spacing of the large hemispheres.

With the closure models formulated, equation (5) was solved using an iterative, implicit finite difference technique. Details of this procedure are presented by Taylor et al. (1984).

Results and Discussion

The geometrical parameters describing the shapes and spacings of the hemispherical and conical roughness elements which make up the nine uniform rough surfaces are shown in Fig. 4. The nominal and measured values of these geometrical parameters are presented in Table 1. The descriptors A-1, B-2, etc. assigned to each surface as given in Table 1 are used for convenience. Actually three parameters (element shape, size, and spacing) distinguish the surfaces.

Three surfaces with large hemispherical roughness elements were tested. Each surface was made up of hemispheres with a nominal base diameter $d_0=2.54$ mm (0.100 in.) and a nominal height $k=1.27$ mm (0.050 in.). The roughness elements of the three surfaces were spaced 2, 4, and 8 base diameters apart, respectively. The friction factor data for the three spacings can be seen in Fig. 5. At the larger Reynolds numbers, the A-1 ($L/d_0=2$) data are about 5 times greater than the smooth wall correlation values, the A-2 ($L/D_0=4$) data about 2.7 times, and the A-3 ($L/d_0=8$) data about 1.5 times. The A-1 surface produced the largest friction factors of this experimental study.

Unlike the A-1 and A-2 data, the A-3 data indicate a sensitivity to test section orientation. As shown in Fig. 5, the friction factors produced by the northern replications (open symbols) are about 12 percent greater at the larger Reynolds numbers than those of the southern (solid symbols) replications. This general trend was observed to a lesser degree for the sparsest element density ($L/d_0=8$) of both the cones and the small hemispheres. The 12 percent difference between the northern and southern replications, attributed to the sensitivity of the data to the test section orientation, adds an additional bias error to the data uncertainty at the larger Reynolds

Table 1 Nominal and measured geometries of the uniform rough surfaces

Surface	Test section diameter	Base diameter d_0 (mm)		Element spacing L (mm)		Element height k (mm)		Projected height k' (mm)
	(mm)	nominal	measured	nominal	measured	nominal	measured	nominal
Large Hemispheres								
A-1	51.46	2.54	2.55	5.08	5.10	1.27	1.25	—
A-2	51.46	2.54	2.55	10.16	10.20	1.27	1.25	—
A-3	51.54	2.54	2.55	20.32	20.25	1.27	1.15	—
Cones								
A-4	51.31	2.54	2.50	5.08	5.05	1.27	1.30	1.52
A-5	51.40	2.54	2.55	10.16	10.10	1.27	1.30	1.52
A-6	51.46	2.54	2.50	20.32	20.25	1.27	1.25	1.52
Small Hemispheres								
B-1	51.88	1.27	1.25	2.54	2.50	0.64	0.65	—
B-2	51.54	1.27	1.25	5.08	5.05	0.64	0.60	—
B-3	51.63	1.27	1.30	10.16	10.10	0.64	0.55	—

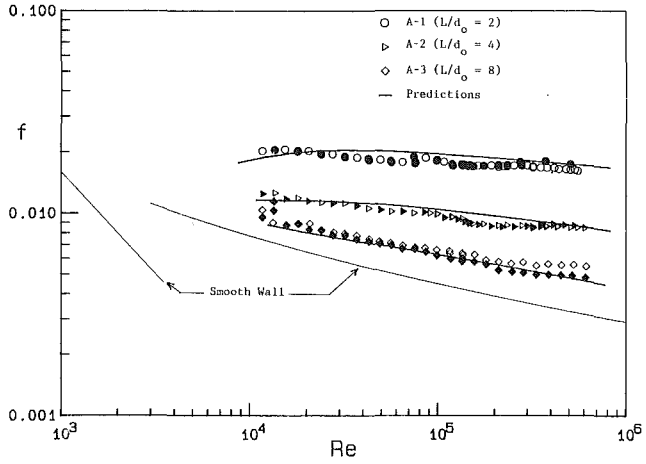

Fig. 5 Comparison of data for the large hemispherical roughness elements with predictions. (Test section orientation: open symbols, northern; solid symbols, southern.)

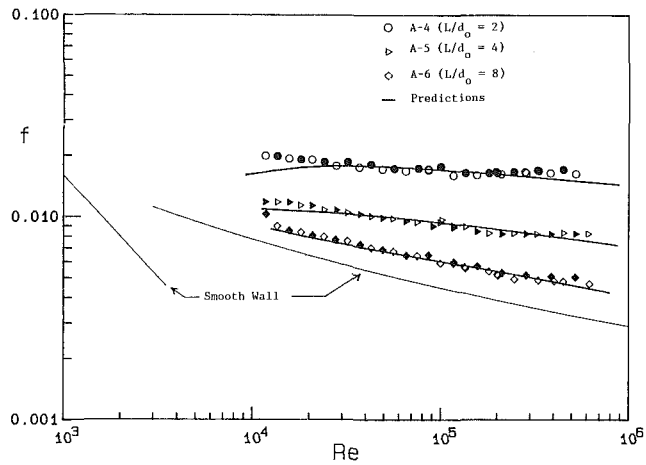

Fig. 6 Comparison of data for the conical roughness elements with predictions. (Test section orientation: open symbols, northern; solid symbols, southern.)

numbers. If an additional bias error of ±4 percent is assumed to exist because of this flow effect, then combining this error with the measurement uncertainty (±4.7 percent) by the root sum square results in a total data uncertainty of ±6 percent for this surface.

The silicone surfaces of all of the test sections were carefully inspected to insure that none of the individual roughness elements were obstructing a pressure tap. This particular test section did not appear to be any different from the other test sections. Although not fully explained, this phenomenon was very repeatable. The A-3 data plotted in Fig. 5 are made up of two northern replications, each taken one month apart, and two southern replications, each also taken one month apart. There is no discernible difference between the northern replications and none between the southern replications.

The nondimensional roughness height $k^+ = ku^*/\nu$ is a measure of the height of the element in the inner region coordinates commonly used in turbulent flow analyses. For the three surfaces with large hemispherical roughness, the values of k^+ ranged from 20 to 750 for surface A-3, from 25 to 1000 for surface A-2 and from 30 to 1250 for surface A-1. The thickness of the viscous sublayer is usually taken to be about $y^+ = 5$ in these coordinates.

Comparisons of the predictions using the discrete element model discussed previously with the friction factor data are also shown in Fig. 5. Inspection of the figure shows very good agreement for the three element spacings. The predicted values of friction factor are slightly high over most of the range of data for surfaces A-1 and A-2 ($L/d_0 = 2$ and 4, respectively). The measurement uncertainty of ±4.7 percent associated with the experimental friction factors is approximately represented by the size of the data point symbols in the figures presented in this work. Using this reference, it can be seen that the maximum disagreement between the predicted and measured friction factors is about 10 percent. The prediction of the friction factor data for surface A-1 trails off slightly at the very low range of reported Reynolds numbers. This was typical behavior of the predictions for the densest element spacing, $L = 2d_0$, of the surfaces presented in this work.

Three surfaces with truncated conical roughness elements were tested. Each of these surfaces was made up of truncated cones with a nominal base diameter $d_0 = 2.54$ mm (0.100 in.) and a nominal height $k = 1.27$ mm (0.050 in.). The roughness elements of the three surfaces were spaced 2, 4, and 8 base diameters apart, respectively. The friction factor data for the three conical spacings are plotted in Fig. 6. At the larger Reynolds numbers, the A-4 ($L/d_0 = 2$) data are approximately 5 times greater than the smooth wall correlation values, the A-5 ($L/d_0 = 4$) data about 2.6 times, and the A-6 ($L/d_0 = 8$) data about 1.6 times.

The difference between the data of the northern and southern replications of surface A-6 is the same order as the measurement uncertainty. This is less than that demonstrated by the large hemispherical roughness.

For the three surfaces with conical roughness, the nondimensional roughness height, k^+, ranged from 20 to 725 for surface A-6, from 25 to 1000 for surface A-5 and from 30 to 1200 for surface A-4.

Figure 6 also shows the comparison between the predicted and the measured friction factor data for the conical roughness elements. Overall, the agreement is excellent. Again, the predicted trend for surface A-4 ($L/d_0 = 2$) tends to trail off at the low end of reported Reynolds numbers.

Three surfaces with small hemispherical roughness elements were tested. Each of these surfaces was made up of hemispheres with a nominal base diameter $d_0 = 1.27$ mm (0.050 in.) and a nominal height $k = 0.64$ mm (0.025 in.). The roughness elements of the three surfaces were spaced 2, 4, and 8 base diameters apart, respectively. The friction factor data for the three small hemisphere spacings can be seen in Fig. 7. At the larger Reynolds numbers, the B-1 ($L/d_0 = 2$) data are about 4.5 times greater than the smooth wall correlation values, the B-2 ($L/d_0 = 4$) data about 2.3 times, and the B-3 ($L/d_0 = 8$) data about 1.4 times. The B-3 surface produced the smallest friction factors of the rough surfaces tested in this experimental study.

The B-3 surface does exhibit a difference between the northern and southern replications, as was the case with the two other $L/d_0 = 8$ surfaces (A-3 and A-6). The northern replication produced friction factors approximately 10 percent greater (at the higher Reynolds numbers) than those of the southern replication.

For the three surfaces with small hemispherical roughness, the nondimensional roughness height, k^+, ranged from 10 to 300 for surface B-3, from 10 to 425 for surface B-2 and from 15 to 575 for surface B-1.

The friction factor data from the small hemispherical elements are also compared to the discrete element predictions in Fig. 7. Overall the agreement is again excellent. The trend predicted for surface B-1 ($L/d_0 = 2$) at the lowest Reynolds numbers behaves like that for surfaces A-1 and A-4 shown in Figs. 5 and 6, respectively.

In each of the three previous figures (5–7), the effects of the roughness spacing were shown for a constant element size and shape. In Fig. 8, the effect of element size is shown for constant element density (number of elements/unit area) and

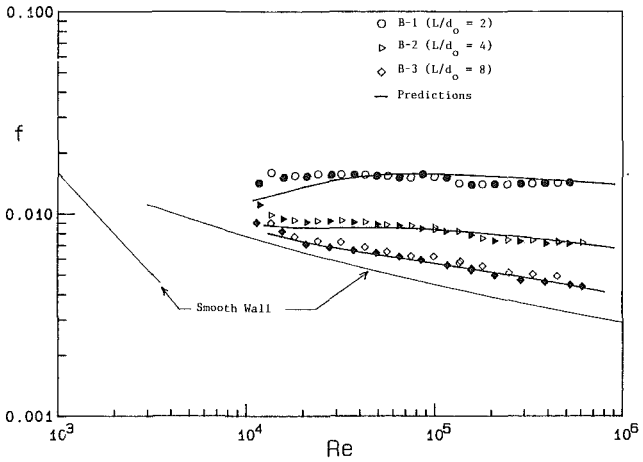

Fig. 7 Comparison of data for the small hemispherical roughness elements with predictions. (Test section orientation: open symbols, northern; solid symbols, southern.)

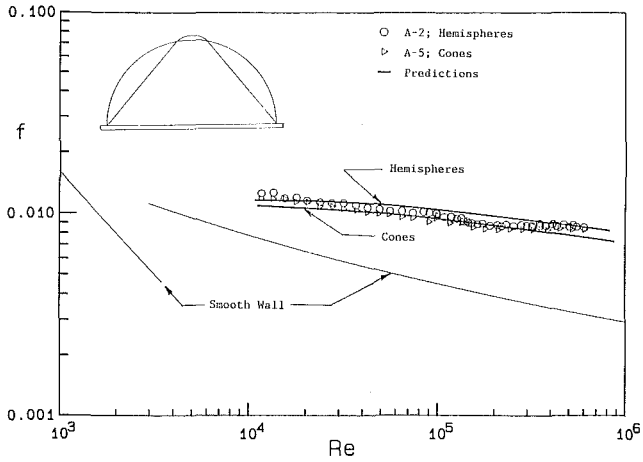

Fig. 9 Comparison of predictions and data for the conical and large hemispherical elements at $L/d_0 = 4$

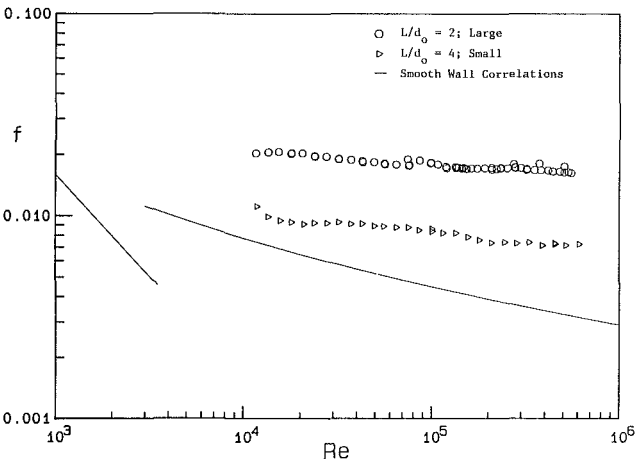

Fig. 8 Comparison of friction factor data for the large and small hemispherical roughness at the same element densities

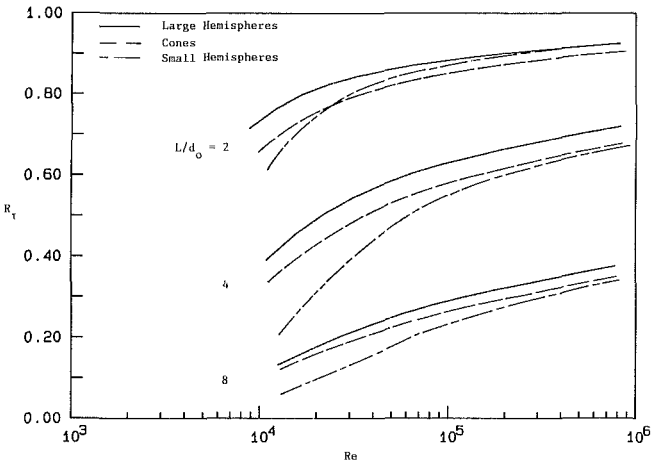

Fig. 10 Roughness parameter, $R_\tau = \tau_R/\tau_T$.

shape. Data presented are for the large hemispherical elements at $L/d_0 = 2$ and the small hemispherical elements at $L/d_0 = 4$—on both of these surfaces, the elements are at a spacing $L = 5$ mm. Comparison of these two data sets shows that doubling the size of the elements increased the friction factor by a factor of 2.5.

The effect of roughness element shape can be isolated by comparing the data for the large hemispherical elements with that for the conical elements at a constant L/d_0, since both elements had $d_0 = 2.5$ mm. Such a comparison is shown in Fig. 9 for the A-2 hemispherical element surface and the A-5 conical element surface, both with $L/d_0 = 4$. As was the case for all L/d_0 values, the conical roughness data and the large hemispherical roughness data are identical within the measurement uncertainty. This result is somewhat surprising to the authors. While the large hemispheres and the cones have essentially the same height and aspect ratio (d_0/k), their projected areas differ by 35 percent as shown in the inset of Fig. 9.

Also shown in Fig. 9 are the friction factor predictions. Inspection of the figure reveals that the predictions for the conical roughness are somewhat lower than those for the hemispherical roughness. However, the difference between the predictions is of the order of uncertainty in the data and is certainly within the fidelity of the prediction technique.

For pipe flow the traditional definition of a fully rough flow is one for which the friction factor is no longer a function of Reynolds number, but is only a function of the roughness. For boundary layer flows and other developing flows this definition is no longer applicable, and some other character of the roughness must be used to delimit aerodynamically smooth, transitionally rough, and fully rough flows. In the past, the value of the so-called roughness Reynolds number, $\mathrm{Re}_{k_s} = u^* k_s/\nu$, was used. However, the equivalent sandgrain roughness is a somewhat contrived single-length-scale roughness discriptor, and it has been abandoned in the discrete element approach.

An alternate candidate suggested by Taylor et al. (1985) is R_τ, the ratio of the apparent wall shear stress due to form drag on the roughness elements to the total wall shear stress. They proposed, based on data available at the time, that

$$R_\tau < 0.05 - 0.10, \text{ aerodynamically smooth}$$

$$0.05 - 0.10 < R_\tau < 0.80 - 0.90, \text{ transitionally rough}$$

$$R_\tau > 0.80 - 0.90, \text{ fully rough.}$$

The values of R_τ calculated from the predictions presented earlier are shown in Fig. 10. Based on these calculations and the friction factor data presented earlier, the authors suggest that a value of $R_\tau \approx 0.60$ might be considered an appropriate boundary between the transitionally and fully rough regimes.

Acknowledgments

This work was supported by the U.S. Air Force Wright Aeronautical Laboratories, Contract F33615-84-K-3014. The experimental apparatus was constructed with the support of

the U.S. Air Force Office of Scientific Research, Grant AFOSR-85-0075. The authors thank Mr. Melvin Buck and Dr. Tony Fiore of the Wright Aeronautical Laboratories and Dr. James Wilson of the Air Force Office of Scientific Research for their support and encouragement.

References

Adams, J. C., and Hodge, B. K., 1977, "The Calculation of Compressible Transitional Turbulent and Relaminarizational Boundary Layers over Smooth and Rough Surfaces Using an Extended Mixing-Length Hypothesis," AIAA Paper 77-682.

Chen, C. K., 1971, "Characteristics of Turbulent Flow Resistance in Pipes Roughened with Hemispheres," Ph.D. Dissertation, Washington State University.

Coleman, H. W., Hodge, B. K., and Taylor, R. P., 1984, "A Reevaluation of Schlichting's Surface Roughness Experiment," ASME JOURNAL OF FLUIDS ENGINEERING, Vol. 106, pp. 60–65.

Dirling, R. B., Jr., 1973, "A Method for Computing Rough Wall Heat Transfer Rates on Reentry Nose Tips," AIAA Paper No. 73-763.

Drew, T. B., Koo, E. C., and McAdams, W. H., 1932, "The Friction Factor for Clean Round Pipes," *Transactions of the AIChE*, Vol. 28, pp. 56–72.

Dvorak, F. A., 1969, "Calculation of Turbulent Boundary Layers on Rough Surfaces in Pressure Gradients," *AIAA Journal*, Vol. 7, pp. 1751–1759.

Finson, M. L., 1975, "A Reynolds Stress Model for Boundary Layer Transition with Application to Rough Surfaces," AFOSR-TR-76-0322.

Finson, M. L., 1982, "A Model for Rough Wall Turbulent Heating and Skin Friction," AIAA Paper 82-0199.

Finson, M. L., and Clark, A. S., 1980, "The Effect of Surface Roughness Character on Turbulent Reentry Heating," AIAA Paper 80-1459.

Finson, M. L., and Wu, P. K. S., 1979, "Analysis of Rough Wall Turbulent Heating with Applications to Blunted Flight Vehicles," AIAA Paper 79-008.

Holden, M. S., 1983, "Studies of Surface Roughness Effects in Hypersonic Flow," Calspan Report, No. 7018-A-2, Advanced Technology Center, Buffalo, NY.

Kays, W. M., and Crawford, M. E., 1980, *Convective Heat and Mass Transfer*, 2nd edition, McGraw-Hill, New York, NY.

Lin, T. C., and Bywater, R. J., 1980, "The Evaluation of Selected Turbulence Models for High-Speed Rough-Wall Boundary Layer Calculations," AIAA Paper 80-0132.

Nikuradse, J., 1933, "Stromungsgesetze in Rauhen Rohren," VDI-Forchungsheft 361. (Also "Laws of Flow in Rough Pipes," NACA TM 1292.)

Scaggs, W. F., Taylor, R. P., and Coleman, H. W., 1988, "Measurement and Prediction of Rough-Wall Effects on Friction Factors in Turbulent Pipe Flow," Mechanical and Nuclear Engineering Department, Mississippi State University, Report TFD-88-1.

Schlichting, H., 1936, "Experimentelle Untersuchungen Zum Rauhigkeits-Problem," *Ingenieur-Archiv.*, Vol. VII, No. 1, pp. 1–34. (Also "Experimental Investigation of the Problem of Surface Roughness," NACA TM 823).

Simpson, R. L., 1973, "A Generalized Correlation of Roughness Density Effects on the Turbulentf Boundary Layer," *AIAA Journal*, Vol. 11, pp. 242–244.

Taylor, R. P., Coleman, H. W., and Hodge, B. K., 1984, "A Discrete Element Prediction Approach for Turbulent Flow Over Rough Surfaces," Mechanical and Nuclear Engineering Department, Mississippi State University, Report TFD-84-1.

Taylor, R. P., Coleman, H. W., and Hodge, B. K., 1985, "Prediction of Turbulent Rough-Wall Skin Friction Using a Discrete Element Approach," ASME JOURNAL OF FLUIDS ENGINEERING, Vol. 107, No. 2, pp. 251–257.

Shiro Akaike
Professor.

Mitsumasa Nemoto
Assistant.

Kanagawa Institute of Technology,
Atsugi, 243-02, Japan

Potential Core of a Submerged Laminar Jet

This study is intended to clarify the flow pattern in the flow developing region of an axisymmetric laminar water jet issuing into the surrounding calm water. The jet, initially having a potential core region of some extent at the nozzle exit, was studied. The numerical solution of the Navier-Stokes equations in the developing region was obtained using a finite-difference approximation. The velocity profile was measured using a miniature cone-type hot probe. Flow visualization by the hydrogen bubble method was also performed. Experiments were carried out for the jet Reynolds number ranging from 100 to 600. The flow pattern in the developing region was made clear. The experimental results were compared with the numerical solution.

Introduction

The mixing of two raw materials in reaction injection molding, a manufacturing process used to make plastic parts, is performed by coaxial impingement of opposing jets in the mixing chamber. The jet Reynolds number Re based on the diameter d of the nozzle and the mean velocity $\bar{u}_0$ is about 300 and the jets are impinged upon each other at a distance of about $5d$. Therefore, the jets may be laminar. In order to design the mixing chamber, it is important to know the flow pattern near the nozzle exit.

Although Schlichting's exact solution [1] to the boundary layer equations for the axisymmetric laminar jet has been experimentally verified at large distance from the nozzle exit where the jet developed fully, there were a few studies on the velocity profile of the jet with a potential core near the nozzle exit. Approximate solutions in the flow developing region for the jet issuing into the same fluid with a uniform velocity profile at the nozzle exit were made by Okabe [2], Hatta and Nozaki [3], and Rankin and Sridhar [4]. Fox et al. presented a numerical finite difference method [5], but only a few examples of solutions were given.

For the experiment on the laminar jet with an initially uniform profile at the nozzle exit, Greene and Brink presented a method of producing a low Reynlods number jet by using a porous plate nozzle [6]. Greene's experimental data were also referred in Rankin and Sridhar's [4], but his data were not published, therefore we could not learn the details of his experiment. On the other hand, a few experimental studies were performed on the jet issuing from the long pipe with a fully developed laminar flow with a parabolic velocity profile [7]. Few studies on the jet initially having a potential core region to some extent have been carried out. Actually, it may be impossible to establish a complete uniform profile at the nozzle exit except by using a special nozzle as the porous plate nozzle [6], because a boundary layer develops along the nozzle wall.

This study is intended to clarify the flow pattern in the flow developing region of an axisymmetric laminar water jet issuing into the surrounding calm water. The numerical solution of steady state Navier-Stokes equations in the developing region was obtained by a finite-difference approximation. The velocity profile near the nozzle exit was measured using a miniature cone-type hot film probe. The supply nozzle was commonly used for the above mixing chamber. Flow visualization by the hydrogen bubble method was also performed.

Experiments were carried out for the jet Reynolds number Re ranging from 100 to 600. The experimental results were compared with the numerical solution. The flow pattern in the flow developing region was clarified and the extent of the developing region was discussed.

Numerical Solution

Governing Equations. The velocity profile in the flow developing region of a submerged axisymmetric laminar jet is analyzed. The jet is issued from the nozzle of radius r_0 into the fluid of infinite extent as shown in Fig. 1 and the flow is axisymmetric. By substituting the stream function ψ and vortici-

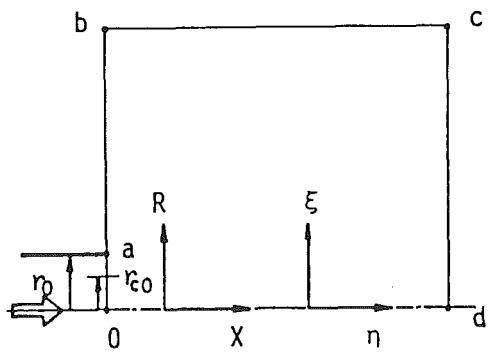

Fig. 1 Coordinates and boundaries

Contributed by the Fluids Engineering Division for publication in the JOURNAL OF FLUIDS ENGINEERING. Manuscript received by the Fluids Engineering Division January 30, 1986.

ty ϕ as the dependent variables, the Navier-Stokes equations and the vorticity equation reduce to [8]

$$\frac{\mathrm{Re}\cdot R^2}{2}\left[\frac{\partial}{\partial X}\left(\bar{\phi}\frac{\partial\bar{\psi}}{\partial R}\right)-\frac{\partial}{\partial R}\left(\bar{\phi}\frac{\partial\bar{\psi}}{\partial X}\right)\right]$$

$$-\frac{\partial}{\partial X}\left(R^3\frac{\partial\bar{\phi}}{\partial X}\right)-\frac{\partial}{\partial R}\left(R^3\frac{\partial\bar{\phi}}{\partial R}\right)=0 \quad (1)$$

$$\frac{\partial}{\partial X}\left(\frac{1}{R}\frac{\partial\bar{\psi}}{\partial R}\right)+\frac{\partial}{\partial X}\left(\frac{1}{R}\frac{\partial\bar{\psi}}{\partial X}\right)+\bar{\phi}R=0 \quad (2)$$

Here,

$$\bar{\phi}=\frac{\phi}{R(\bar{u}_0/r_0)}=\frac{1}{R}\frac{\partial\bar{V}}{\partial X}-\frac{1}{R}\frac{\partial\bar{U}}{\partial R} \quad (3)$$

$$\bar{\psi}=\frac{\psi}{\bar{u}_0 r_0^2},\ \bar{U}=\frac{1}{R}\frac{\partial\bar{\psi}}{\partial R},\ \bar{V}=-\frac{1}{R}\frac{\partial\bar{\psi}}{\partial X} \quad (4)$$

Boundary Conditions. The solution of the problem consists of solving differential equations (1) and (2) by applying the boundary conditions at a finite but sufficiently large distance from the nozzle exit.

(1) Nozzle exit $(0-a)$,

It is assumed that the potential core extends to a radius r_{c0} and the boundary layer with a quadratic profile develops along the wall between r_{c0} and r_0 at the nozzle exit. Then, the assumed velocity profile may be written nondimensionally as follows

$$U_0 = \frac{u_0}{u_{\max 0}}=1 (R\le R_{c0})$$

$$U_0 = 1-\frac{(R-R_{c0})^2}{(1-R_{c0})^2}(R>R_{c0}) \quad (5)$$

Here, the relation between the mean velocity $\bar{u}_0$ and the maximum velocity $u_{\max 0}$ is

$$\bar{u}_0=u_{\max 0}(1-A),\ A=\frac{2}{(1-R_{c0})^2}\left(\frac{1}{4}-\frac{2R_{c0}}{3}+\frac{R_{c0}^2}{2}-\frac{R_{c0}^4}{12}\right) \quad (6)$$

(2) Jet axis $(0-d)$

Because of axial symmetry

$$\bar{\psi}=0,\ \bar{\phi}=0 \quad (7)$$

(3) On the axis $(a-b)$

Assuming no flow through the boundary $a-b$

$$\bar{\psi}=\bar{\psi}_a=0.5,\ \bar{\phi}=0 \quad (8)$$

(4) Outer boundary $(c-b-d)$

Schlichting's velocity profile is assumed at the outer boundary. The profile is [1]

$$u=\frac{3J}{8\pi\mu}\frac{1}{x'}\frac{1}{(1+\bar{\xi}^2)^2} \quad (9)$$

$$v=\left(\frac{3J}{4\pi\rho}\right)^{1/2}\frac{1}{x'}\frac{\bar{\xi}-\bar{\xi}^3}{(1+\bar{\xi}^2)^2} \quad (10)$$

Here,

$$\bar{\xi}=\frac{1}{8\nu}\left(\frac{3J}{\pi\rho}\right)^{1/2}\frac{r}{x'}$$

The kinematic momentum J in equations (9) and (10) is decided from the assumed velocity profile at the nozzle exit. The virtual origin upstream of the nozzle exit is decided as follows.

The entrainment volume rate Q' is expressed by the Reynolds number Re

$$Q'=8\pi\nu x'=\frac{16}{\mathrm{Re}}(\pi\bar{u}_0 r_0^2)X'=Q_0\frac{16}{\mathrm{Re}}(X+X_v) \quad (11)$$

Here, Q_0 is the flow rate at the nozzle exit. When $X=0$, $X'=X_v$ and $Q'=Q_0$. Therefore, $X_v=\mathrm{Re}/16$ is assumed. By using J and X_v, $\bar{\psi}$ and $\bar{\phi}$ on the outer boundary are obtained.

Numerical Solution. A coordinate transformation is used which gives closely spaced intervals in the physical space near the axis and near the nozzle. The transformations used are

$$\xi=\tanh(k_1 R),\ \eta=\tanh(k_2 X) \quad (12)$$

$$\frac{\partial\xi}{\partial R}=k_1(1-\xi^2)=M,\frac{\partial\eta}{\partial X}=k_2(1-\eta^2)=N,\ K=M/N \quad (13)$$

where k_1 and k_2 are constants. The governing equations (1) and (2) are transformed to

$$\frac{\partial}{\partial\xi}\left(KR^3\frac{\partial\bar{\phi}}{\partial\xi}\right)+\frac{\partial}{\partial\eta}\left(\frac{R^3}{K}\frac{\partial\bar{\phi}}{\partial\eta}\right)$$

$$-\frac{\mathrm{Re}R^2}{2}\left[\frac{\partial}{\partial\eta}\left(\bar{\phi}\frac{\partial\bar{\psi}}{\partial\xi}\right)-\frac{\partial}{\partial\xi}\left(\bar{\phi}\frac{\partial\bar{\psi}}{\partial\eta}\right)\right]=0 \quad (14)$$

Nomenclature

$B=r_c/d$, $B_2=r_2/\mathrm{d}$ = nondimensional radii
d = nozzle diameter
J = kinematic momentum
Q = flow rate
$R=r/r_0$, $R_2=r/r_2$,
$R_{c0}=r_{c0}/r_0$ = nondimensional radii
$\mathrm{Re}=(\bar{u}_0 d)/\nu$,
$\mathrm{Rem}=(\bar{u}_{\max 0}d)/\nu$ = Reynolds numbers
r = radius measured from the jet axis
r_2 = half-radius
r_c = potential core radius
$U=u/u_{\max}$, $\bar{U}=u/\bar{u}_0$, $U_a=u_{\max}/u_{\max 0}$ nondimensional axial velocities
u = axial velocity
$\bar{u}_0$ = mean velocity at nozzle exit
$u_{\max}$ = maximum velocity at measuring section
$\bar{V}=v/\bar{u}_0$ = nondimensional radial velocity
v = radial velocity
$X=x/r_0$, $\bar{X}=X_d/\mathrm{Re}$, $X_d=x/d$, $X_m=X_d/\mathrm{Rem}$, $X_v=x_v/r$, $X'=x'/r_0$ = nondimensional axial distances
x = axial distance from nozzle exit
x' = axial distance from virtual origin
x_v = virtual origin
Z = variable defined by equation (16)
ν = kinematic viscosity
ρ = density
ϕ = vorticity
ψ = stream function

Subscripts

0 = nozzle exit
2 = half-radius
c = poential core

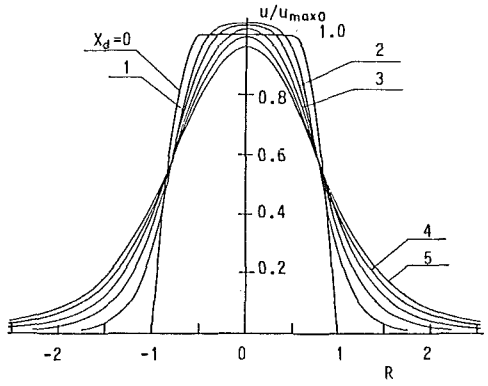

Fig. 2 Velocity profiles near the nozzle (Re = 200, $R_{c0} = 0.5$)

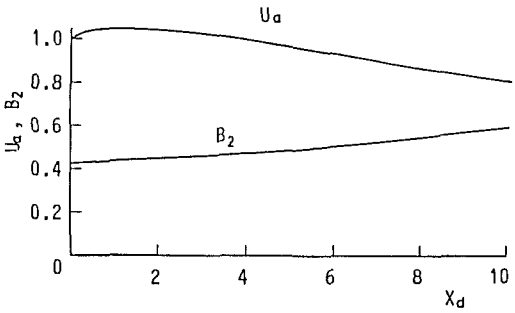

Fig. 3 Variation of the centerline velocity U_a and half-radius B_2 Re = 200, $R_{c0} = 0.5$)

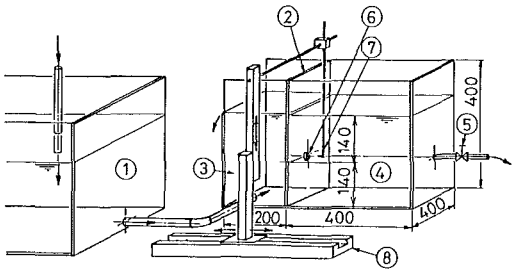

Fig. 4 Skeleton view of equipment (unit mm)

$$\frac{\partial}{\partial \xi}\left(\frac{K}{R}\frac{\partial \dot{\bar{\psi}}}{\partial \xi}\right)+\frac{\partial}{\partial \eta}\left(\frac{1}{KR}\frac{\partial \bar{\psi}}{\partial \eta}\right)+\frac{R}{KN^2}\bar{\phi}=0 \qquad (15)$$

The transformed equations (14) and (15) together with the boundary conditions are solved numerically using the finite difference scheme and an iterative scheme with $k_1 = 0.10034$ and $k_2 = 1.8/\mathrm{Re}$. ξ and η are 0.005. Convergence is tested by comparing the values of $\bar{\psi}$ and $\bar{\phi}$ from successive iterations and ensuring that the maximum change in $\bar{\psi}$ and $\bar{\phi}$ to the preceding values are within 10^{-3} for every grid point. The velocity profiles are calculated from the stream function obtained.

Figure 2 shows a numerical example of the velocity profiles in the flow developing region of Re = 200 and $R_{c0} = 0.5$. The velocity near the jet axis increases immediately after the nozzle exit and thereafter decreases. Figure 3 shows the variation of the nondimensional centerline velocity U_a and the nondimensional half-radius B_2 with X_d.

Experimental Equipment and Procedures

Experiments were carried out for the water jet issuing into the surrounding calm water. Figure 4 shows a skeleton view of the equipment. Water in the supplement reservoir ① which had a sufficiently wide water surface, was supplied from city water. The overflow was made at the overflow reservoir ③ connected to the supplement reservoir and the constant head was maintained. The parting plate ② divided the measuring reservoir ④ from the overflow reservoir. Head difference between the reservoirs ③ and ④ was adjusted by the valve ⑤ and the steady laminar jet was issued into the measuring reservoir from the nozzle ⑥ which was installed on the parting plate.

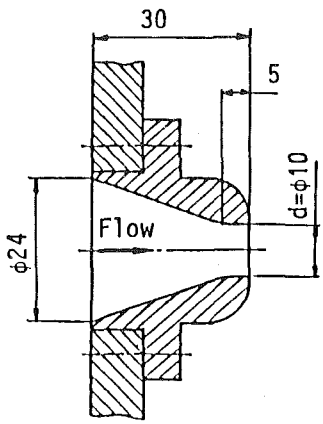

Fig. 5 Cross section of the supply nozzle (unit mm; Uncertainty in $d = \pm 0.01$ mm)

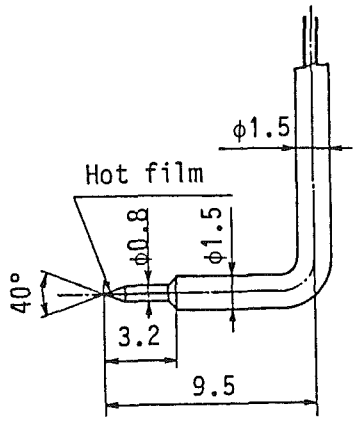

Fig. 6 Miniature hot film probe (unit mm; KANOMAX Type 1264W)

Figure 5 shows the cross section of the supply nozzle. The inner diameter of the exit was $\phi 10$ mm and the nozzle had a straight section with a length of 5 mm. For a preliminary experiment, a pipe with an inner diameter $\phi 10$ mm and a length of 320 mm was used for the nozzle. They were made of acrylic plastic.

By using a miniature cone-type hot film probe as shown in Fig. 6, the velocity profiles were measured in the developing region near the nozzle, where a potential core remained. The probe ⑦ was traversed by the differential apparatus ⑧. Flow rate was measured at the valve exit by the weighing method. Flow visualization by the hydrogen bubble method was also conducted. Photographs were taken by a 36 mm camera.

Experiments were carried out for the Reynolds number Re ranging from 100 to 600 (Uncertainty in Re = ±2).

Experimental Results and Discussion

Flow Visualization. Figure 7 shows photographs which visualize the flow pattern in the developing region of the submerged laminar jet by the hydrogen bubble. The flow pat-

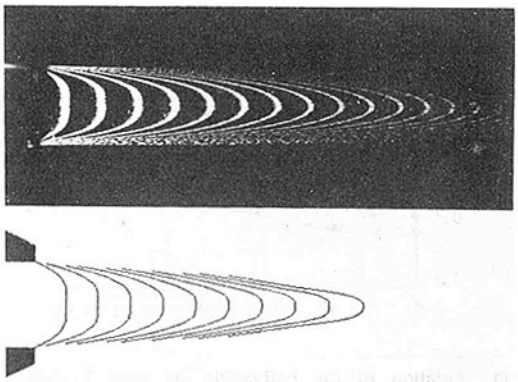

Fig. 7(a) Re = 147

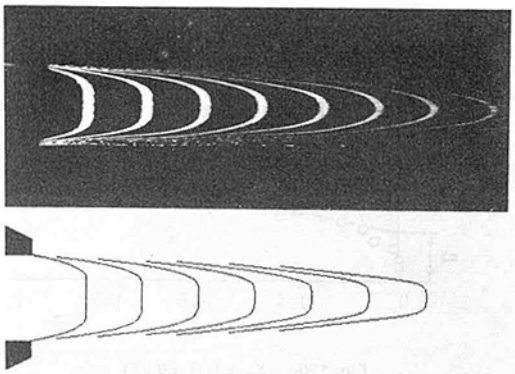

Fig. 7(b) Re = 221

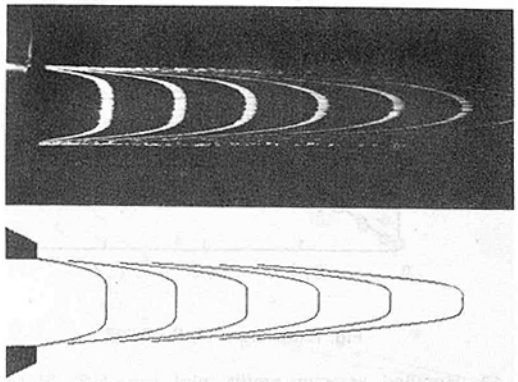

Fig. 7(c) Re = 302

Fig. 7 Flow pattern near the nozzle (pulse frequency $T = 0.2$ s)

terns obtained from the numerical solution are also shown. The figures show clearly the existence of a potential core near the nozzle exit.

The velocity profile can be determined from these photographs, however, there are some problems with measurement accuracy. Therefore, the flow in the developing region will be discussed on the basis of the results obtained from the hot probe measurement.

Velocity Profile. Figure 8 shows the variation of the axial velocity profiles in the downstream direction of the jets issued from the pipe and the nozzle. For the pipe jet in Fig. 8(*a*), the velocity profile at the exit ($X_d = 0$) agrees well with a parabolic

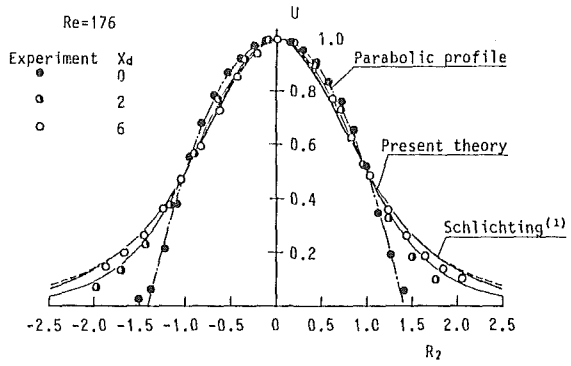

Fig. 8(a) Pipe jet (Re = 176)

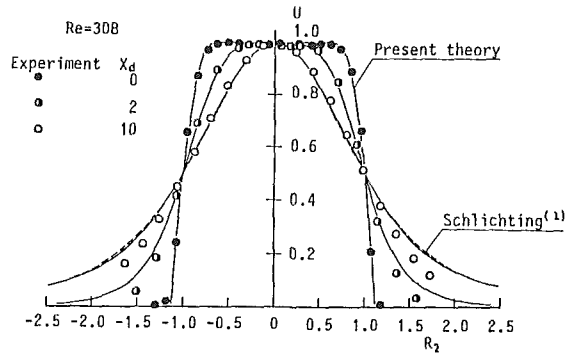

Fig. 8(b) Nozzle jet (Re = 308)

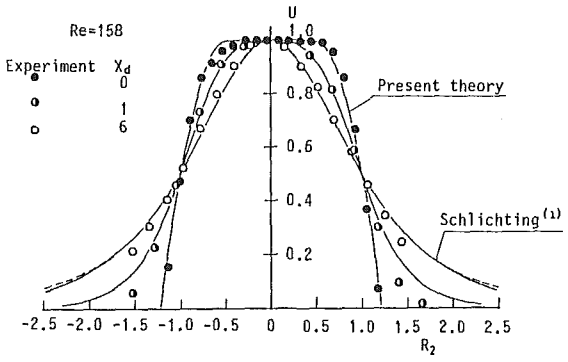

Fig. 8(c) Nozzle jet (Re = 158)

Fig. 8 Variation of the velocity profiles and comparison with theories (Uncertainties in $U = \pm 0.02$, in $R_2 = \pm 0.01$)

profile for the fully developed laminar pipe flow. The profile approaches Schlichting's profile of equation (9) for the fully developed laminar jet according to the increase of the distance from the nozzle exit and, at $X_d = 6$ ($\bar{X} = 0.034$), is almost equal to Schlichting's one. This result also agrees with the result obtained by Rankin et al. [7]. They showed that the distance from the nozzle at which the pipe jet became a fully developed condition was $\bar{X} = 0.036$. The solid lines in the figure are the numerical results. They agree well with the experiment.

For the nozzle jet in Fig. 8(*b*) of Re = 308, the potential core remains around the jet axis at $X_d = 2$, where a uniform velocity region is observed. The velocity profile becomes close to Schlichting's at $X_d = 10$. The agreement between the theory and the experiment seems to become slightly less in the outer region of the jet axis. The same tendency can be seen in Fig. 8(*c*) of Re = 158.

Figure 9 shows the initial conditions of the nondimensional

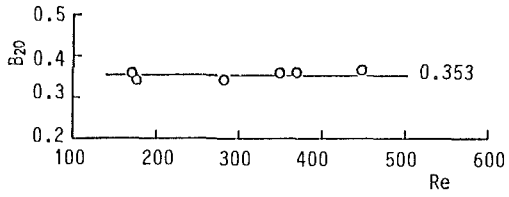

Fig. 9(*a*) Pipe jet

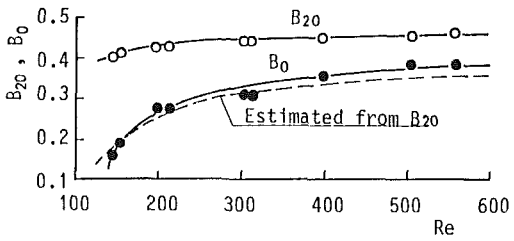

Fig. 9(*b*) Nozzle jet

Fig. 9 Initial condition of the jet at the nozzle exit (Uncertainty in $B_{20} = \pm 0.02$, in $B_0 = \pm 0.005$)

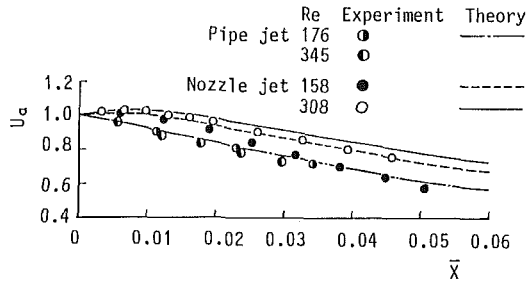

Fig. 10 Variation of the centerline velocity U_α with $\bar{X}$ (Uncertainty in $U_\alpha = \pm 0.02$, in $\bar{X} = \pm 0.0001$)

half-radius B_{20} and the nondimensional potential core radius B_0 at the nozzle exit. The core radius B_0 is obtained in the same manner described later. The half-radius of the pipe jet in Fig. 9(*a*) is almost equal to 0.353 calculated from the parabolic velocity profile. B_{20} of the nozzle jet in Fig. 9(*b*) is affected by the Reynolds number Re. It becomes small according to the decrease of Re.

It may be impossible to obtain a complete uniform exit velocity profile with a normal nozzle. For the supply nozzle, the core radius B_0 at the exit is less than 0.5 and decreases with the Reynolds number. The broken line in the figure is the result calculated from the assumed velocity profile of equation (5) using the experimental value of B_{20}. The theoretical results presented for the comparison with the experiment are obtained using this initial value B_0 at the nozzle exit.

Centerline Velocity and Half-Radius. Figure 10 shows the variation of the nondimensional centerline velocity U_a with the nondimensional axial distance $\bar{X}$. U_a for the pipe jet decrease immediately after the exit, although U_a for the nozzle jet increases near the exit and thereafter begins to decrease as shown in the theoretical example of Fig. 3. For the jet issuing from a long pipe with a fully developed laminar profile, it is known that the variation of a centerline velocity and a half-radius depend on $\bar{X}$ [7]. The same result is also obtained from the present theory and the experiment.

On the other hand, for the jet which has a potential core at the nozzle exit, the variation of U_a does not depend only on $\bar{X}$. It may be seen that U_a near the exit increases as the core radius B_0 increases, and U_a downstream has the same tendency.

The agreement between the experiment and the theory is good for the pipe jet, but the decay of the experimental U_a for the nozzle jet is faster than the theoretical one.

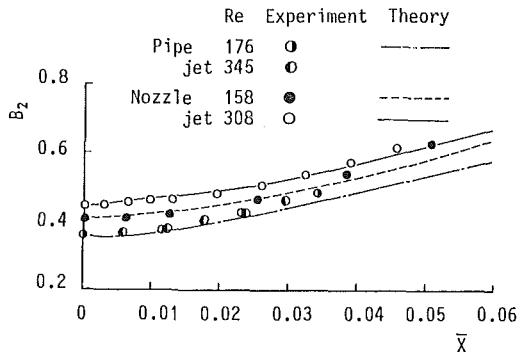

Fig. 11 Variation of the half-radius B_2 with $\bar{X}$ (Uncertainty in $B_2 = \pm 0.02$, in $\bar{X} = \pm 0.0001$)

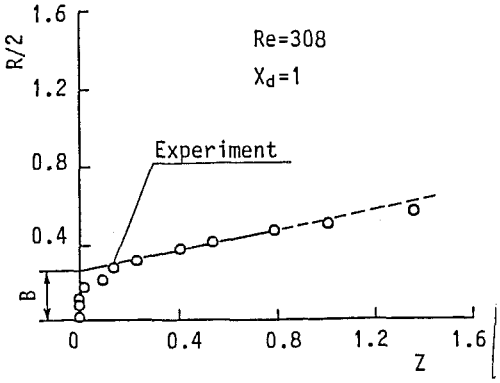

Fig. 12(*a*) $X_d = 1$, $B = 0.271$

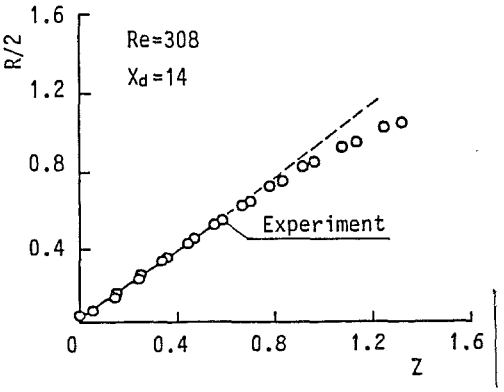

Fig. 12(*b*) $X_d = 14$, $B = 0.002$

Fig. 12 Modified velocity profile plot (Re = 308) (Uncertainty in $R = \pm 0.01$, in $Z = \pm 0.02$)

Figure 11 shows the variation of the nondimensional half-radius B_2 with $\bar{X}$. Contrary to the centerline velocity case, the increase of experimental B_2 is larger than the theoretical one with increasing downstream distance.

Potential Core Radius. In the case of a turbulent jet, the potential core radius is determined at the outer edge where the exit uniform velocity remains. The core radius r_c of a laminar jet, however, cannot be determined in the same manner as the turbulent jet, because the velocity in the core region accelerates immediately after the nozzle exit. Therefore, in this study, r_c is determined at the outer radius of a uniform velocity existing around the jet axis.

Since it is difficult to determine experimentally the potential core radius r_c, the method of Rankin and Sridhar [4] is used to

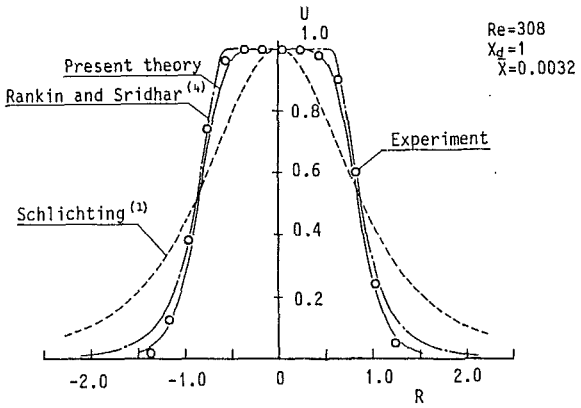

Fig. 13(*a*) $X_d = 1$, $B = 0.271$

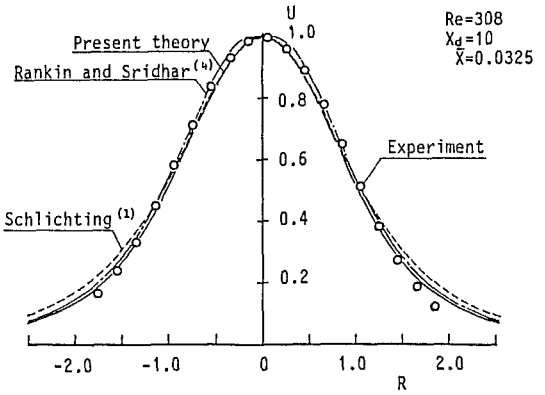

Fig. 13(*b*) $X_d = 10$, $B = 0.056$

Fig. 13 Comparison of velocity profiles between the experiment and theories (Re = 308, Uncertainty in U = ±0.02, in R = ±0.01)

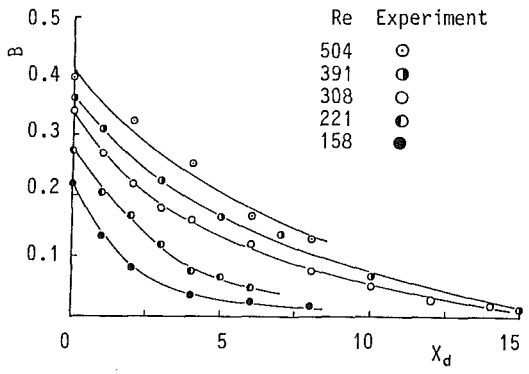

Fig. 14 Variation of the potential core radius B with X_d (Uncertainty in $B = \pm 0.02$, in $X_d = \pm 0.01$)

determine r_c. If the free shear layer in the outer region of the core is assumed by Schlichting's profile, the following linear equation is obtained.

$$R = kZ + 2B,\ Z = (U^{-1/2} - 1)^{1/2} \tag{16}$$

Here, k is constant. If the experimental values of R are plotted against Z, such a figure as shown in Fig. 12 is obtained. Figure 12(*a*) is the result of Re = 308 and $X_d = 1$ in the flow developing region and the nondimensional potential core radius B is determined from the value of R at $Z = 0 (U = 1)$. Figure 12(*b*) shows the result of $X_d = 14$ in the developed flow region. In this case, the line almost intercepts the origin ($R \doteqdot 0$, $Z = 0$).

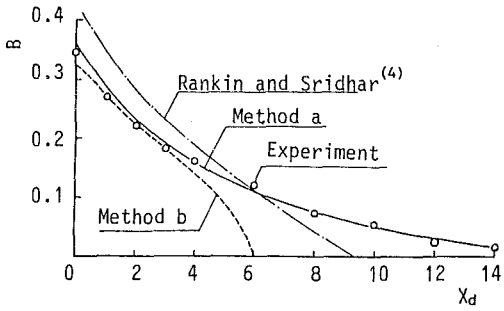

Fig. 15 Comparison of B between the experiment and theories (Uncertainty in $B = \pm 0.02$, in $X_d = \pm 0.01$)

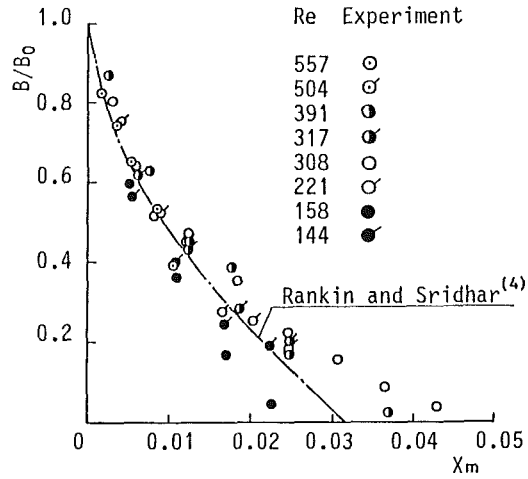

Fig. 16(*a*) Variation with X_m

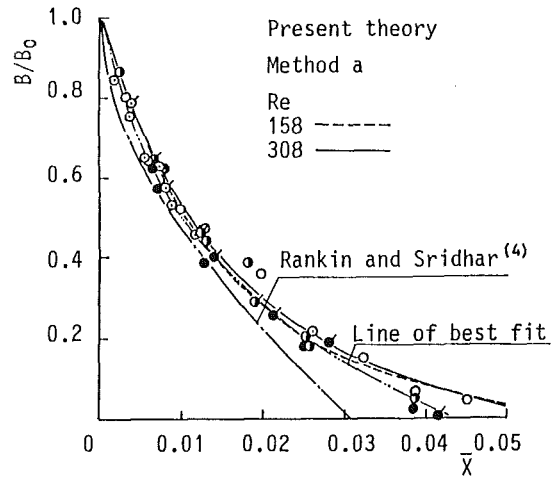

Fig. 16(*b*) Variation with $\bar{X}$

Fig. 16 Variation of B/B_0 (Uncertainty in $B/B_0 = \pm 0.008$, in $\bar{X} = \pm 0.0001$, in $X = \pm 0.0001$)

When the potential core radius is large, the above method has a tendency to estimate B a little large. The agreement between the experiment and the estimated profile is not as good as shown in Fig. 13(*a*). In the last portion of the flow developing region where B becomes small, the experimental profile is estimated well by this method as shown in Fig. 13(*b*). For the comparison, the present theoretical profile and the Schlichting's one which agrees with the experiment at the half-radius are also given in the figure.

Figure 14 shows the variation of B with X_d. The core radius of the turbulent jet vanishes at $X_d \doteqdot 11$ independent of the

Reynolds number [3], although it appears that the variation of B of the laminar jet with X_d depends on Re. The flow developing region is extended according to the increase of Re.

The comparison between the theory and the experiment is given in Fig. 15. The theoretical values are determined by the following two methods. Method (a) is similar to the experimental procedure and B is calculated from equation (16) using the three point velocities of $U=0.25$, 0.5, 0.75 ($Z=1.0$, 0.6436, 0.3933). This is given by the solid line. B by method (b) is obtained from the radius at which u becomes 0.99 of the maximum velocity u_{max0} of the nozzle exit. The broken line shows this value. The experimental values do not agree with that of method (b) and have a tendency to agree with that of method (a) in the limits of this experiment. As mentioned above, the axial extent of the flow developing region may not be determined by method (b) for the laminar jet. The result of Rankin and Sridhar [4] for $B_0=0.5$ of course does not agree with the experiment.

In this experiment, the core radius at the nozzle exit is dependent upon the Reynolds number, so that the ratio B divided by the initial value B_0 is discussed as follows.

Figure 16 shows the variation of B/B_0 with X_m and $\bar{X}$. The flow development of the laminar jet with a fully developed exit velocity has been presented using the nondimensional distance $X_m=X_d/\mathrm{Rem}$ [7], where the Reynolds number Rem is based on the maximum velocity u_{max0} at the exit. As shown in Fig. 16(a), scatter of B/B_0 with X_m is considerable. B/B_0 with $\bar{X}$ as shown in Fig. 16(b) has only a small amount of scatter. Therefore, it is reasonable to expect similarity of B/B_0 by $\bar{X}$. The broken and the solid lines in Fig. 16(b) are the theoretical values obtained from method (a) for $\mathrm{Re}=158$ and 308. As there is a little difference between them near $\bar{X}\fallingdotseq 0.02$, an agreement between the experiment and the theory is comparatively good except for the flow region, where the jet is approaching the developed flow.

The result by Rankin and Sridhar [4] for the jet of $B_0=0.5$ is also given in the figure. In the region close to the nozzle where $\bar{X}$ is small, it nearly agrees with the experiment and the present theory, but it becomes smaller than these results in the region where $\bar{X}$ is large. Hatta and Nozaki also calculated the variation of B with $\bar{X}$ [3]. Their result is less than that of Rankin and Sridhar.

It is concluded that the axial distance $\bar{X}$, at which the core vanishes and the jet reaches a developed flow region, is about 0.04 in the limits of this experiment, although the result of Rankin and Sridhar is $\bar{X}\fallingdotseq 0.03$.

Conclusions

In this study, the flow developing region of the laminar jet with the potential core is discussed theoretically and experimentally.

The results obtained are as follows.

1. For the laminar jet, the variation of the potential core in the flow developing region does not only depend on the nondimensional distance X_d.
2. The variation of the ratio B/B_0 is dependent on the nondimensional distance $\bar{X}$.
3. The distance $\bar{X}$, at which the core vanishes, is $\bar{X}\fallingdotseq 0.04$.
4. The flow variation in the developing region is estimated well by the present theory.

References

1 Schlichting, H., *Boundary Layer Theory*, 7th ed., McGraw-Hill, 1979, p. 230.

2 Okabe, J., "Approximate Calculations of Laminar Jets," Rep. Res. Inst. Fluid Eng., Kyushu Univ., Vol. 5, 1948, p. 1.

3 Hatta, K., and Nozaki, T., "Two-Dimensional and Axisymmetric Jet Flows with Finite Initial Cross Section," *Bulletin of JSME*, Vol. 18, No. 118, 1975, p. 349.

4 Rankin, G. W., and Sridhar, K., "Developing Region of Laminar Jets With Uniform Exit Velocity Profiles," ASME JOURNAL OF FLUIDS ENGINEERING, Vol. 100, No. 1, 1978, p. 55.

5 Fox, H., et al., "An Implicit Finite Difference Solution for Jets and Wake Problems," *Astronautica Acta*, Vol. 17, 1972, p. 265.

6 Greene, G. C., and Brink, D. F. "Methods for Producing a Uniform, Low Reynolds Number Jet," *J. Spacecraft and Rockets*, Vol. 11, No. 8, 1974, p. 604.

7 Rankin, G. W., et al., "An Experimental Investigation of Laminar Axisymmetric Submerged Jets," *J. Fluid Mech.*, Vol. 133, 1983, p. 217.

8 Deshpande, M. D., and Vaishnav, R. N., "Submerged Laminar Jet Impingement on a Plane," *J. Fluid Mech.*, Vol. 114, 1982, p. 213.

Adiabatic and Diabatic Flow Studies by Shear Stress Measurements in Annuli With Inner Cylinder Rotation

Y. A. G. Abdallah
Assistant Professor,
Department of Mechanical Engineering,
Bahrain University

J. E. R. Coney
Senior Lecturer,
Department of Mechanical Engineering,
University of Leeds, Leeds LS2 9JT,
England

The shear stress, occurring at the outer surface of a vertical annular gap formed by a stationary outer cylinder and a rotatable inner cylinder, was measured for a wide range of conditions, using a flush mounted probe. For annular gaps of radius ratio 0.8 and 0.9, axial flows of Reynolds numbers 100, 165, 200, and 300 were imposed under adiabatic and diabatic upflow and also diabatic downflow conditions. Under these conditions, the shear stress was determined over a range of Taylor numbers approaching 10^7, the flow being fully developed. Diabatic conditions were achieved by the isothermal heating of the outer surface of the gap. A primary regime, in which Taylor vortices are absent or exist away from the outer surface of the gap was identified. Secondary, tertiary and quaternary regimes, in which the vortex flow is in contact with that surface ensued. The contrast between the results for diabatic upflow and diabatic downflow gives an understanding of the effect of natural convection in these regimes.

Introduction

In the past, the determination of the shear stress occurring at the outer wall of an annular gap, formed by a stationary outer cylinder and a rotating inner cylinder, has proved of value in the study of the characteristics of a combined axial laminar and Taylor vortex flow. In [1], Coney and Simmers describe a method of shear stress measurement using a flush-mounted hot film probe attached to the outer surface of a vertical annular gap, the working fluid being air. In [2], they describe the application of this method to the study of fully developed laminar axial flow and Taylor vortex flow, the range of the axial Reynolds number being from 300 to 1600. In their investigations, they noted three flow regimes. In the primary regime, Taylor vortex flow was either absent or insignificant and the shear stress was invariant with the Taylor number.

In the secondary regime, the shear stress increased exponentially with the Taylor number, the exponent of the Taylor number being constant. In this regime, the flow is dominated by Taylor vortices. However, for the two lowest values of axial Reynolds number investigated, viz. 300 and 400, a tertiary regime was found to exist. As in the secondary regime, an exponential relationship between the shear stress and the Taylor number was found, but with a higher constant exponent. This phenomenon could not be explained at the time, but reasons for it are offered in the present work.

References [1] and [2] were restricted to adiabatic flow, but the authors have extended their investigations to diabatic flow, these conditions being achieved by the isothermal heating of the outer surface of the annular gap. Because of the low axial Reynolds numbers under consideration, viz. 100, 165, 200, and 300, the effects of natural convection could not be ignored in the diabatic case. Hence, tests were performed with the imposed axial flow being in the upward direction, natural convection aiding, and in the downward direction, natural convection opposing it. In addition, temperature profiles were taken across the annular gap for the above conditions.

Apparatus

The apparatus is described in detail in [3]. It consisted, in essence, of a vertical concentric annular gap, having a stationary outer cylinder and rotating inner cylinder, with an axial length of 1820 mm. The outer cylinder could be heated isothermally by wet steam flowing through a jacket. The inner cylinder was of an insulating material, Tufnol, to minimize heat transfer through the inner surface of the annular gap. Two interchangeable inner cylinders of radius 55.9 mm and 62.9 mm were used to provide narrow and wide gap radius ratios of 0.8 and 0.9, respectively, the radius of the inner surface of the stationary outer cylinder being 69.85 mm. The working fluid was air, values of the axial Reynolds number being determined by means of orifice plates.

To permit the insertion of measuring probes into the annular gap, 29 measuring stations were provided. These sta-

Contributed by the Fluids Engineering Division for publication in the JOURNAL OF FLUIDS ENGINEERING. Manuscript received by the Fluids Engineering Division August 29, 1986.

tions were arranged in four vertical lines at 90 degree intervals along the length of the gap. Three of the lines had seven stations, while the fourth had eight. The stations were not equispaced but were concentrated at either end of the annular gap to facilitate study of entry conditions.

For the determination of the shear stress at the outer surface of the annular gap, two types of probe were considered. The glue-on probe DISA Type 55R47 used in [1] and [2] had the advantage of low cost but was designed to be permanently fixed to a given point on the surface; also the two wires, through which electrical connections were made, could disturb the boundary layer, thus causing erroneous measurements. The flushmounted probe, DISA type 55R46, which was ultimately chosen has the advantage of portability, only one probe being required for taking measurements at any station along the annular gap. Also, because of its cylindrical form and flat head, it could be positioned easily and accurately. It was also sensitive in all directions. Because of the small diameter of the head (3 mm) compared with the radius of the inner surface of the outer cylinder (34.93 mm), the deviation from the curved surface was negligible.

The temperature at the outer surface of the annular gap was determined by nine chromel-alumel thermocouples, arranged in three equal and equispaced groups at each end and at the middle of the annular gap. Since a suitable thermocouple probe was not available for measuring the variation of the air temperature across the gap, it was necessary to develop a fine wire probe for this purpose.

Shear Stress Probe Calibration

In order to calibrate the probe, it must be subjected to a known flow from which a theoretical shear stress may be obtained. In the present apparatus, the simplest flow obtainable is Couette flow, which gives a straight line distribution across the annular gap. However, this type of flow is unreliable for calibration purposes because, in the absence of an imposed axial flow, vortices occur at low inner cylinder rotational speeds; at such speeds, the change in shear stress is small. Hence, Poiseuille flow, induced by a pressure gradient along the length of the annular gap was employed. The calibration was performed by subjecting the probe to this type of flow in the range of the axial Reynolds numbers to be used in the investigation.

By assuming a parabolic axial velocity profile for fully developed axial flow in an annular gap, an expression for the axial velocity at any radial position may be obtained (4), from which it may be shown that

$$\tau_w = \frac{2\mu^2 \mathrm{Re}_a}{\rho d_e \left[1 + N^2 + \frac{1-N^2}{\ln N}\right] R_2} \left[2 + \frac{1-N^2}{\ln N}\right] \quad (1)$$

In [4], the results of Rothfus [5] are quoted, who compared experimental velocities for laminar flow in plain annuli with theoretical values, as used in the formulation of equation (1). He showed that, for an annular gap of $N = 0.65$ with $\mathrm{Re}_a = 1250$, there was good agreement between the theoretical and experimental values. However, at $\mathrm{Re}_a = 1820$, there was some deviation between theory and experiment. In the present study, the values of Re_a are much lower, than either of these values.

Under adiabatic conditions, the probe output voltage was read for seven values of Re_a. The wall shear stress was calculated from (1) and a calibration of the form

$$\tau_w^{\frac{1}{3}} = AV^2 + B \quad (2)$$

was plotted, as proposed by Geremia [6].

In the case of diabatic flow, with the outer surface of the annular gap heated isothermally, it was noted that, at a given axial Reynolds number, the shear stress in upflow was greater than that in downflow, which in turn was greater than that for adiabatic flow. The probe, therefore, was calibrated for all three flow conditions. However, the calibration in the diabatic condition applies to a particular temperature difference prevailing between the probe and the air flowing past it. Hence, the values of A and B in (2) are dependent on the temperature difference and differ, as between the upflow and downflow conditions. Within the experimental range, these differences were found to be very small. For a given value of V^2, the value of $\tau_w^{1/3}$ for the upflow calibration was between 0 and 4 percent of that given by the downflow calibration. In consequence, an equation, having mean values of A and B was used, covering both upflow and downflow conditions.

Results

Experimental Procedure. The variation of shear stress was obtained over a wide range of Taylor numbers, at each of four low axial Reynolds numbers, viz. 100, 165, 200, and 300 in annular gaps of radius ratio 0.9 and 0.8, and for three conditions, viz. adiabatic, diabatic upflow and diabatic downflow. For the latter two conditions, the temperature of the outer surface of the annular gap was held constant at 102°C ± 0.5°C. The axial Reynolds number of 300 was chosen to enable comparison of the present results with those of Coney and Sim-

Nomenclature

A, B = constants
b = annular gap width $(R_2 - R_1)$
c = constant
d_e = equivalent diameter of annular gap $(2b)$
g = acceleration due to gravity
Gr = Grashof of number $\left[\frac{g\beta d_e^3 \Delta T}{\nu^2}\right]$
N = annular radius ratio (R_1/R_2)
n = constant
R_1 = radius of inner cylinder
R_2 = radius of outer cylinder
Re_a = axial Reynolds number $\left(\frac{U_a d_e}{\nu}\right)$
T = temperature
T_m = mean temperature of air at a given section
T_w = temperature of outer wall
ΔT = temperature difference
Ta = Taylor number $\left[\frac{2\Omega_1^2 R_1^2 b^3}{(R_1 + R_2)\nu^2}\right]$
Ta_c = apparent critical Taylor number (at onset of secondary regime)
$\mathrm{Ta}^{\#}$ = Taylor number at onset of tertiary regime
U_a = mean axial velocity component
V = probe output voltage
β = coefficient of thermal expansion
μ = dynamic viscosity of fluid
ν = kinematic viscosity of fluid (μ/ρ)
ρ = density of fluid
τ_w = shear stress at outer surface of annular gap
Ω_1 = angular velocity of inner cylinder

mers [2]. To ensure that the probe was in the fully developed regime, the required minimum axial distance from the entrance of the annular gap was determined from [7]. Radial temperature profiles were obtained for the two radius ratios for Re_a = 100 and 165, in upflow and downflow.

The mean air temperature, used to determine viscosity for the calculation of Re_a and Ta, was taken as the mid-gap temperature. When compared with the mean temperature obtained from the radial temperature profiles, it was found that the difference was negligible.

Adiabatic Conditions. The plots shown in Fig. 1 for $N=0.9$ and in Fig. 2 for $N=0.8$ are similar in form. They exhibit three distinct regimes, the first of which is characterized by a constant shear stress up to a certain value of the Taylor number at which Taylor vortex flow shows a marked effect. In this primary regime, the shear stress, although constant with Taylor number, increases with axial Reynolds number. It is also higher in the narrow gap than the wide gap for the same axial Reynolds number.

In the secondary regime, there is an increase of shear stress with Taylor number and, in the tertiary regime, this increase continues more sharply. Taking the intersection between the primary and secondry regimes as marking the point at which the effect of spiral Taylor vortex flow reaches the outer surface, apparent critical Taylor numbers Ta_c have been estimated from Figs. 1 and 2 and are given in Table 1.

In the secondary and tertiary regimes, the plots take the form:

$$\tau_w^{\frac{1}{3}} = n \ln \mathrm{Ta} + c$$

where n and c are constants. Ascribing suffix 2 to the secondary regime and suffix 3 to the tertiary regime, Table 1 also gives values of n and the Taylor numbers $Ta^{\#}$ at the discontinuities between these two regimes for the four axial Reynolds numbers under consideration.

From Table 1, it can be seen that axial flow has a stabilizing effect; for both radius ratios, Ta_c increases with Re_a. Also, for a given radius ratio, n_2, n_3 and $Ta^{\#}$ vary little over the range of Re_a under consideration. However, it should be noted from Fig. 2 that for $N = 0.8$, a quarternary regime is evident at $T_a > 2\times10^6$.

Diabatic Conditions. Figure 3 shows the experimental results for downflow through an annular gap of $N=0.9$, the outer surface of the gap being heated isothermally. The form of these plots is similar to those for adiabatic flow, shown in Fig. 1; the primary, secondary and tertiary regimes are present and the transitions between them clear. Figure 4 shows results under identical conditions to those of Fig. 3 but for an annular gap of $N=0.8$. Here again, there is a similarity to the adiabatic results of Fig. 2 but the quaternary regime evident in Fig. 2 is much more developed. The consequent reduction of the tertiary regime made it impossible to estimate values of n_3.

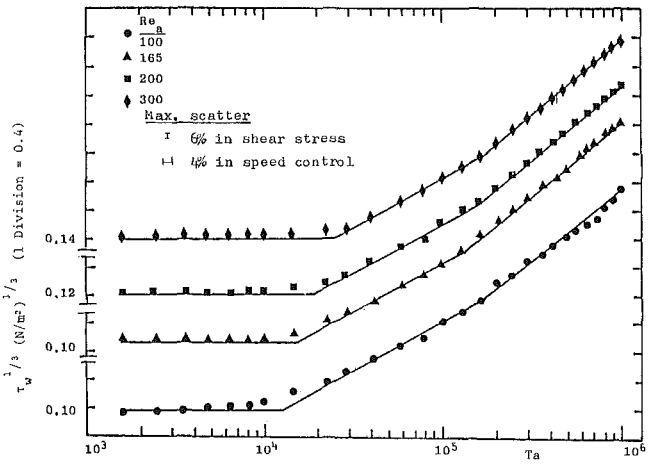

Fig. 1 Variation of τ_W 1/3 with Ta for N = 0.9 (adiabatic conditions)

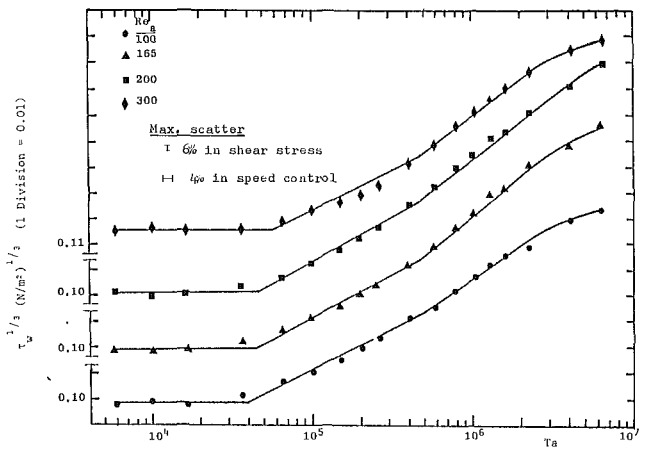

Fig. 2 Variation of τ_W 1/3 with Ta for $N = 0.8$ (adiabatic conditions)

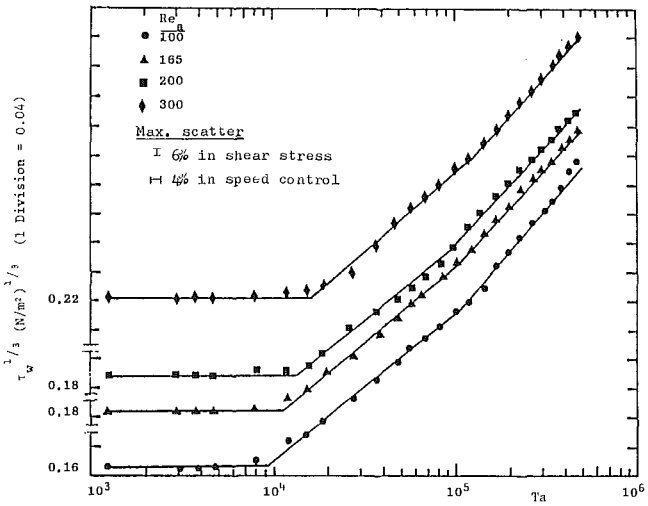

Fig. 3 Variation of τ_W 1/3 with Ta for $N = 0.9$ (diabatic conditions: downflow)

Table 1 Values of Ta_c, n_2, n_3 and $Ta^{\#}$ for various axial Reynolds numbers (adiabatic conditions)

	$N=0.8$				$N=0.9$			
Re_a	Ta_c	n_2	n_3	$Ta^{\#}$	Ta_c	n_2	n_3	$Ta^{\#}$
100	3.9×10^4	0.499	0.700	4.3×10^5	1.3×10^4	0.563	0.800	1.7×10^5
165	4.5×10^4	0.521	0.795	4.7×10^5	1.6×10^4	0.556	0.800	1.3×10^5
200	4.8×10^4	0.532	0.781	4.8×10^5	1.9×10^4	0.556	0.808	1.6×10^5
300	5.8×10^4	0.532	0.754	5.0×10^5	2.5×10^4	0.556	0.800	1.6×10^5

Table 2 Values of Ta_c, n_2, n_3 and $Ta^{\#}$ for various axial Reynolds numbers and for $N = 0.9$ (diabatic conditions)

	Downflow				Upflow			
Re_a	Ta_c	n_2	n_3	$Ta^{\#}$	Ta_c	n_2	n_3	$Ta^{\#}$
100	9.0×10^3	0.857	1.143	1.1×10^5	8.4×10^3	1.026	1.212	1.7×10^5
165	1.1×10^4	0.833	1.111	1.1×10^5	1.2×10^4	1.053	1.176	1.6×10^5
200	1.3×10^4	0.833	1.100	1.1×10^5	1.5×10^4	1.053	1.212	1.2×10^5
300	1.5×10^4	0.833	1.111	1.2×10^5	1.7×10^4	1.026	1.176	1.3×10^5

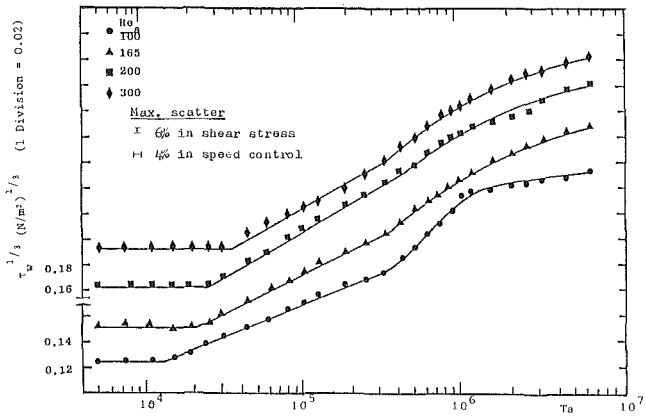

Fig. 4 Variation of $\tau_W{}^{1/3}$ with Ta for $N = 0.8$ (diabatic conditions: downflow)

A similar series of experiments was performed for upflow through the annular gap. Because the form of the plots do not differ greatly from their downflow counterparts, they are not given here. The results for this series of experiments are given in Tables 2 and 3. Radial temperature profiles across the annular gaps of $N = 0.9$ and 0.8 for $Re_a = 165$ (downflow) are given in Fig. 5. The profiles for upflow are not given here since they vary little from those for downflow except for $T_a = 0$.

Discussion of Results

Primary Regime. In this regime, for both adiabatic and diabatic flow, where Taylor vortices are absent or ineffective, the shear stress remains constant for a given Re_a and is identical to that which results from Poiseuille flow alone. It may be concluded that, when the inner cylinder is rotated at a speed insufficient to generate Taylor vortices energetic enough to reach the outer surface, there is no measurable effect on the shear stress; this confirms the findings of Coney and Simmers [2] and Yamada [8].

For both the narrow and wide gaps, at a given axial Reynolds number, the diabatic shear stress in upflow is greater than that in downflow which, in turn, is greater than that in adiabatic flow. These differences, while they exist, are not significant. However, the annular gap radius ratio affects the results considerably. In the narrow gap, for both adiabatic and diabatic conditions, higher shear stresses are experienced than in the wide gap at a given axial Reynolds number. This effect is reflected in Fig. 5 where, for $Ta = 0$, the dimensionless temperature gradient at the outer wall is less for $N = 0.9$ than for $N = 0.8$.

Apparent Critical Taylor Number. Tables 1, 2, and 3 show the stabilizing effect of an imposed axial flow; they also suggest that flow in a wide gap is more stable than that in a narrow gap. However, Sorour and Coney [9] found flow to be more stable in a narrow gap and this contradiction should be resolved. To do this, the concept of critical Taylor number

Table 3 Values of Ta_c, n_2, and $Ta^{\#}$ for various axial Reynolds numbers and for $N = 0.8$ (diabatic conditions)

	Downflow			Upflow		
Re_a	Ta_c	n_2	Ta#	Ta_c	n_2	Ta#
100	1.35×10^4	0.425	3.4×10^5	1.45×10^4	0.442	1.8×10^5
165	2.2×10^4	0.506	3.5×10^5	2.7×10^4	0.571	1.5×10^5
200	2.5×10^4	0.580	4.0×10^5	3.6×10^4	0.667	1.9×10^5
300	3.6×10^4	0.625	3.6×10^5	3.8×10^4	0.741	1.8×10^5

used in [9] and in the present study must be compared. In [9], measurements were made at mid-gap, near to the origin of the vortices. Now, for a given axial Reynolds number, the mid-gap axial velocity is greater in a narrow gap than in a wide gap and the effect of the higher velocity will be to stabilize the flow. In the present study, the first evidence of criticality was when the shear stress began to rise above the constant value of the primary regime. This increase occurs only when the effect of the vortices extends to the outer surfaces of the annular gap and not at their first appearance in mid-gap. Hence, the apparent critical Taylor number at which the vortices reach the outer surface will be greater than that at which the vortices first form near the mid-gap, the true critical Taylor number. Considering the differences in gap width, it is not surprising that in the present study, the critical Taylor number for the wide gap is greater than that for the narrow gap.

Figure 6 compares the results of the present adiabatic narrow gap study with the results of similar studies by Sorour and Coney [9], Snyder [10], and Gravas and Martin [11]. In the three latter investigations, the first appearance of the vortices was detected in mid-gap, the region of maximum instability, unlike in the present investigation.

The apparent critical Taylor numbers for diabatic conditions are given in Tables 2 and 3, the stabilizing effect of the imposed axial flow being evident. Also, for a given Re_a, the apparent critical Taylor numbers are greater for an imposed upflow, when natural convection is aiding, than for downflow, when it is opposing.

This effect is consistent with the flow mechanism taking place at the outer heated surface. When natural convection aids the imposed flow, the axial velocity near the outer surface will increase, enhancing the stabilizing effect of the imposed flow. The values of the apparent critical Taylor number for $N = 0.8$ are higher than those for $N = 0.9$, for the same reason given for the adiabatic condition. These values are plotted against the axial Reynolds number in Fig. 7. For both radius ratios, the values of Ta_c for imposed downward and upwards flows approach each other, as Re_a increases, implying the diminution of the effect of natural convection. The ratio of buoyancy forces to inertia forces (Gr/Re^2_a) at $Re_a = 300$ is 1.04 for $N = 0.8$ and 0.13 for $N = 0.9$. In the former case, there is still some effect of natural convection present, whereas, in the latter, it is of little importance. However, for both radius ratios, the effect of natural convection diminishes rapidly for $Re_a > 300$.

Figure 8 compares the present results with those of Coney

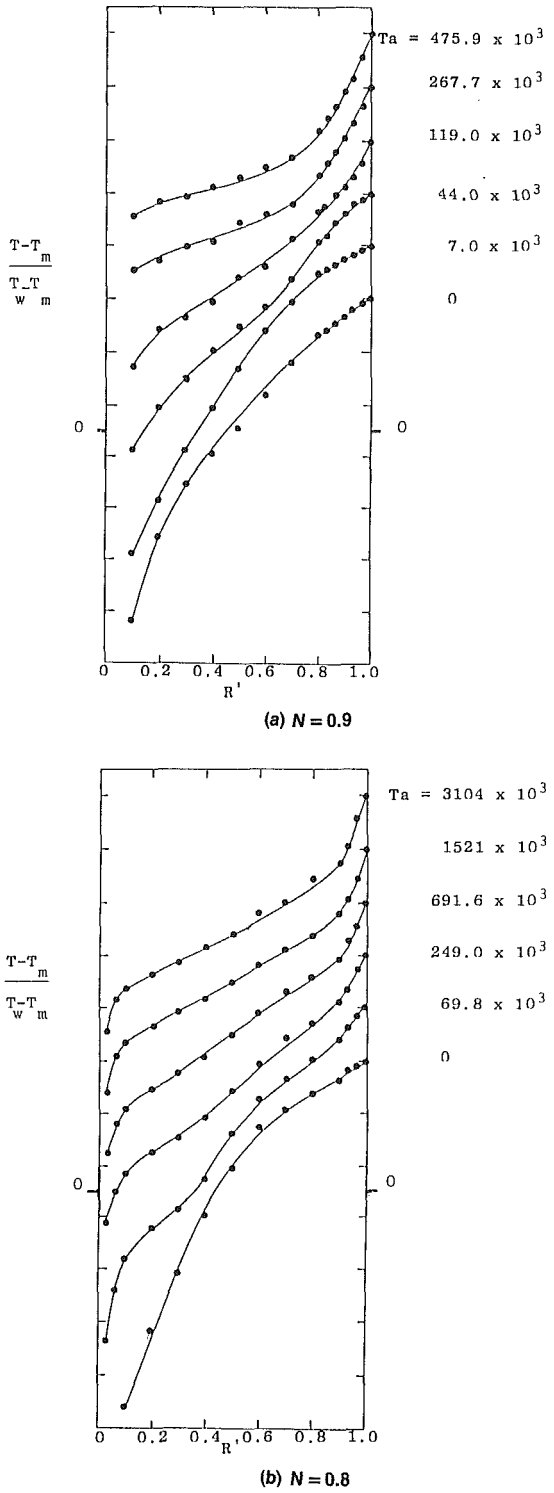

Fig. 5 Radial temperature profiles (downflow)

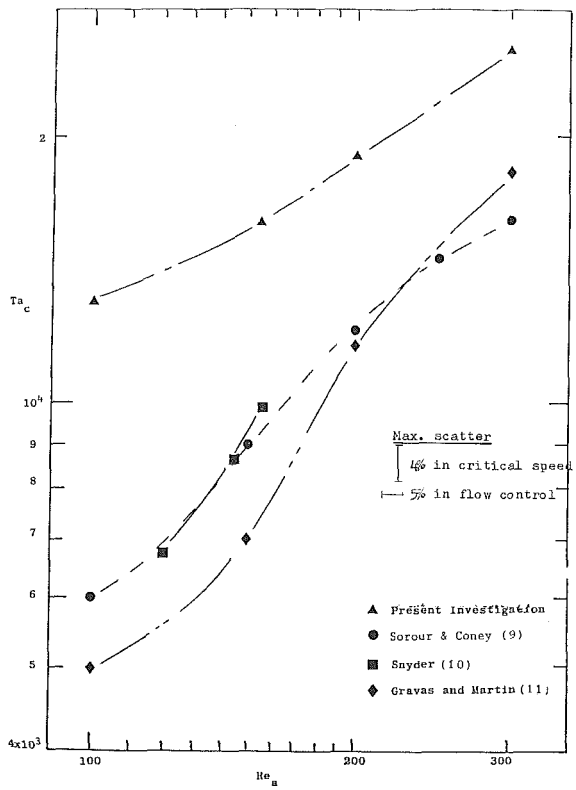

Fig. 6 Variation of Ta_c with Re_a (adiabatic conditions). (Comparison of present results with other investigations.)

and Sorour [9]. While values of Ta_c for an imposed downflow show close agreement, the present study gives higher values for upflow. This deviation suggests that natural convection stabilizes the flow near the outer surface, when aiding the imposed axial flow, but may destabilize the flow in the mid-gap region, where the measurements of [9] were taken.

Secondary and Tertiary Regime. The present study confirms the existence of a tertiary regime first observed by Coney and Simmers [2]. Table 1 gives the Taylor number ($Ta^{\#}$) at which the change from the secondary to the tertiary regime occurs. There is little change in $Ta^{\#}$ with Re_a for a given radius ratio, but a considerable difference as between radius ratios.

In [12], Wan and Coney report the results of a spectral and visual investigation using an annular gap of $N = 0.848$ and an axial Reynolds number of 250, with oil as the working fluid. After the onset of spiral vortex flow at the critical Taylor number, they noted a progressive breakdown into chaotic flow. However, at a Taylor number of 260,000, the flow developed into large vortices which were detected both spectrally and visually. Of interest, the above value of Taylor number at $N=0.848$ is approximately half way between the values of $Ta^{\#}$ at $N=0.8$ and $N = 0.9$ given in Table 1, thus suggesting that the onset of the tertiary regime occurs at the transition of the flow from the chaotic to the large vortex form. A confirmatory investigation of the visual results of (12) was performed by Abdallah (13). From Table 1 and from the results of (12), it may be concluded that $Ta^{\#}$ increases with N in the range $0.8 \leq N \leq 0.9$.

Referring to the secondary regime, Table 1 shows n_2 to be almost invariant with Re_a; this finding is in accord with (2) but with different values of n_2. This constancy also occurs in the tertiary regime. However, it is noted from Fig. 2 and 4 that a quarternary regime exists at very high values of Ta. Both phenomena may be attributed to the large vortices formed at $Ta^{\#}$, which are present under both adiabatic and diabatic conditions.

Under diabatic conditions, Tables 2 and 3 show the values of $Ta^{\#}$ are largely independent of Re_a, but dependent on N and the direction of the imposed flow. As in the adiabatic case, the wider the annular gap, the more stable is the flow in terms of transition between secondary and tertiary regimes. However, an imposed upflow is seen to be slightly more stable than a downflow, in these terms for diabatic flow in a narrow gap (Table 2), but in a wide gap, it is considerably less stable (Table 3). It is suggested, therefore, that, when aiding an imposed flow, natural convection assists strongly in the formation of the large vortices.

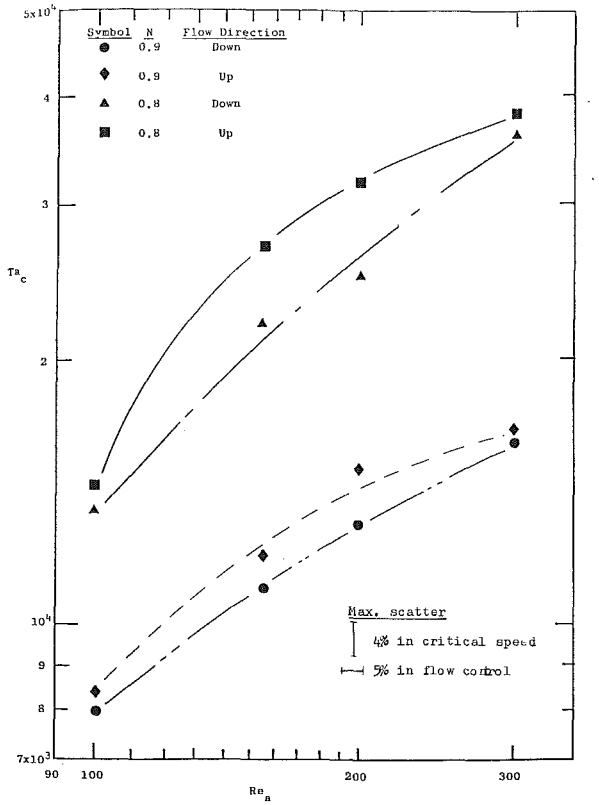

Fig. 7 Variation of Ta_c with Re_a for $N = 0.8$ and 0.9 (diabatic conditions: upflow and downflow)

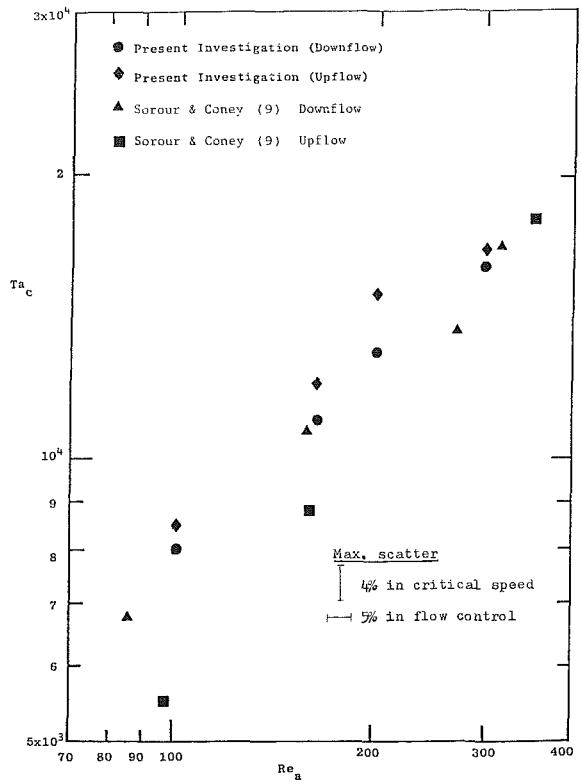

Fig. 8 Variation of Ta_c with Re_a (diabatic conditions). (Comparison of present results with those of (9).)

The values of n_2 and n_3 for diabatic conditions are almost constant for $N = 0.9$ (Table 2) and greater than the corresponding adiabatic values (Table 1). Moreover, the values of n_2 and n_3 obtained from the upflow experiments are higher than those from downflow. For $N = 0.8$, n_2 and n_3, under adiabatic, and n_2, under diabatic conditions, are not constant but increase with Re_a. Furthermore, n_2 has a greater value in upflow than downflow.

In Fig. 5, the dimensionless temperature gradient at the outer wall is seen to increase, as Ta increases through the secondary and tertiary regimes.

Quaternary Regime

From Figs. 2 and 4, it may be inferred that for $Ta > 10^6$, there exists a quarternary regime, the gradient of the plot of $\tau_w^{1/3}$ against Ta being less than for the tertiary regime, especially at $Re_a = 100$. This regime was detected, also, in upflow in the same annular gap of $N = 0.8$ for $Ta > 10^6$ and $100 < Re_a < 300$. The results of Figs. 1 and 3 show that this regime was not detected in the tests on the annular gap of $N = 0.9$. However, in these tests, it was not possible to achieve a Taylor number greater than 10^6.

Using the present apparatus, Wan and Coney [14] showed that a drop in Nusselt number occurred at $Ta > 10^6$. They termed this a tertiary regime because in their tests, they were not able to separate this secondary regime into a secondary and tertiary, as in the present investigation.

In investigating the variation of turbulence intensity across an annular gap of $N = 0.8$ for $Re_a = 500$, Wan and Coney [15] noted that, near to the outer surface, a sharp fall occurred at $Ta = 2 \times 10^6$, for both adiabatic and diabatic conditions. Power spectra and auto-correlograms were also taken, which indicated near to the annular boundaries a low frequency periodic disturbance. However, considering the dimensionless temperature profiles for $Ta > 10^6$ in Fig. 5(*b*), the effect of the quaternary regime is not discernible.

Conclusions

The results of a shear stress investigation into adiabatic and diabatic flow in an annular gap at low axial Reynolds numbers show four regimes. In the primary regime, Taylor vortices are absent or exist away from the outer surface of the gap without affecting the probe, which is flush with that surface. The shear stress remains constant with Taylor number in this regime. The shear stress in the diabatic experiments is higher than the adiabatic value at a given axial Reynolds number. It is also shown that the narrow gap always gives, for both adiabatic and diabatic conditions, higher values of wall shear stress in a wide gap. In this regime, also the shear stress increases when natural convection aids the imposed flow, while it decreases when it opposes it.

The apparent critical Taylor number was defined as that at which the shear stress begins to rise from the constant value of the primary regime. Since the measurements were taken at the outer surface, higher values of critical Taylor numbers were obtained in this investigation than by previous workers. The results also show, in the case of a wide gap, that a higher Taylor number is needed for the vortices to spread to the outer wall than in the narrow gap. It is of interest that the critical Taylor number is higher for imposed upflow, when natural convection is aiding, than for downflow, when natural convection is opposing the flow. The results suggest that natural convection stabilizes the flow in the region of outer surface, when aiding the imposed axial flow, but destabilizes it in the mid-gap region.

The secondary regime is considered to be one of spiral vortex flow, breaking down into a chaotic flow with increase in Taylor number. It is succeeded by a tertiary regime, the

change being attributed to large vortices appearing in the flow at the very high Taylor numbers.

The succeeding quaternary regime is typified by a fall in the rate of increase of shear stress with Taylor number. Because it was not possible to reach sufficiently high Taylor numbers in the narrow gap, this regime was observable only in the wide gap.

References

1 Coney, J. E. R., and Simmers, D. A., "The Determination of Shear Stress in Fully Developed Laminar Axial Flow and Taylor Vortex Flow, Using a Flush-Mounted Hot Film Probe," *Disa Information*, Vol. 24, 1979, pp. 9–14.

2 Coney, J. E. R., and Simmers, D. A., "A Study of Fully-Developed Laminar, Axial Flow and Taylor Vortex Flow by Means of Shear Stress Measurements," *J. Mech. Engng. Sci.*, Vol. 21, No. 1, 1979, pp. 19–24.

3 Simmers, D. A., and Coney, J. E. R., "A Reynolds Analogy Solution for the Heat Transfer Characteristics of Combined Taylor Vortex and Axial Flows," *Int. J. Heat Mass Transfer*, Vol. 22, 1979, pp. 679–689.

4 Knudsen, I. G., and Katz, D. L., "Fluid Dynamics and Heat Transfer," McGraw-Hill, New York, 1958.

5 Rothfus, R. R., "Velocity Gradients and Friction in Concentric Annuli, Ph.D. thesis, Carnegie I.T., 1948.

6 Geremia, J. O., "Experiments on the Calibration of Flush-Mounted Film Sensors," *Disa Information*, Vol. 13, 1971, pp. 5–10.

7 Simmers, D. A., and Coney, J. E. R., "The Effect of Taylor Vortex Flow on the Development Length in Concentric Annuli," *J. Mech. Engng. Sci.*, Vol. 21, No. 2, pp. 59–64.

8 Yamada, Y., "Resistance of Flow through an Annulus with an Inner Rotating Cylinder," *Bulletin Jap. Soc. Mech. Engrs.*, Vol. 15, No. 18, 1962, pp. 302–310.

9 Sorour, M. M., and Coney, J. E. R., "An Experimental Investigation of the Stability of Spiral Vortex Flow," *J. Mech. Engng. Sci.*, Vol. 21, No. 6, 1979, pp. 397–402.

10 Snyder, M. A., "Experiments on the Stability of Spiral Flow at Low Axial Reynolds Numbers," *Proc. Roy. Soc. Series*, A265, 1962, pp. 150–226.

11 Gravas, N., and Martin, B. W., "Instability of Viscous Axial Flow in Annuli Having a Rotating Inner Cylinder," *Journal Fluid Mech.*, Vol. 86, 1978, pp. 385–394.

12 Wan, C. C., and Coney, J. E. R., "An Investigation of Adiabatic Spiral Vortex Flow in Wide Annular Gaps by Visualisation and Digital Analysis," *Int. J. Heat and Fluid Flow*, Vol. 3, No. 1, 1982, pp. 39–44.

13 Abdallah, Y. A. G., "A Study of Natural Convection on Flow in An Annular Gap with Inner Cylinder Rotation," Ph.D. thesis, Leeds University, 1983.

14 Wan, C. C., and Coney, J. E. R., "An Experimental Study of Diabatic Spiral Vortex Flow," *Int. J. Heat and Fluid Flow*, Vol. 3, No. 1, pp. 31–38.

15 Wan, C. C., and Coney, J. E. R., "Radial Variation of Adiabatic and Diabatic Spiral Flow in a Wide Annual Gap," *Int. J. Heat and Fluid Flow*, Vol. 3, No. 2, 1982, pp. 101–112.

The Mean Flow Structure Around and Within a Turbulent Junction or Horseshoe Vortex—Part I: The Upstream and Surrounding Three-Dimensional Boundary Layer

J. D. Menna
Process Engineer,
E.I. DuPont Company at Savannah River,
Aiken, SC 29808-0001
Assoc. Mem. ASME

F. J. Pierce
Professor of Mechanical Engineering,
Virginia Polytechnic Institute and State University,
Blacksburg, VA 24061
Fellow ASME

The mean flow structure upstream, around, and in a turbulent junction or horseshoe vortex is reported for an incompressible, subsonic flow. This fully documented, unified, comprehensive, and self-consistent data base is offered as a benchmark or standard case for assessing the predictive capabilities of computational codes developed to predict this kind of complex flow. Part I of these papers defines the total flow being documented. The upstream and surrounding three-dimensional turbulent boundary layer-like flow away from separation has been documented with mean velocity field and turbulent kinetic energy field measurements made with hot film anemometry, and local wall shear stress measurements. Data are provided for an initial condition plane well upstream of the junction vortex flow to initiate a boundary layer calculation, and freestream or edge velocity, as well as floor static pressure, are reported to proceed with the solution. Part II of these papers covers the flow through separation and within the junction vortex flow.

Introduction

The 1981-1982 Stanford Conference on Complex Turbulent Flows [1] has clearly revealed that however one may categorize and subdivide the broad class of flows generally designated as turbulent and complex, in virtually any particular category there is a severe shortage of experimentally studied flows that are sufficiently unified, comprehensive, and detailed to allow for an unbiased test of the predictive capabilities of computational codes. This lack of completeness in experiments allows, or even requires, code developers to make assumptions in their work that could have very large effects on their computed results, and clouds the objectivity in evaluating the predictive capability of such computer codes.

This fully documented, unified, comprehensive, and self-consistent database for a total complex flow should be valuable in providing for an unbiased evaluation of the predictive capabilities of computational codes developed to predict either portions of, or the total flow documented. This database should also provide insight in the development of flow and turbulence models.

The complex turbulent flow documented is the three-dimensional separated turbulent flow centered about a junction or horseshoe vortex system. This flow is generated by placing a streamlined cylinder with circular leading edge normal to a flat surface in a thick turbulent boundary layer as shown in Fig. 1.

The total flow system is arbitrarily divided into four regions, the first of which is presented in Part I, the second presented in Part II, and the last two of which will be covered in subsequent publications. These regions include:

I. The three-dimensional pressure-driven turbulent boundary layer-like flow upstream and around the body but excluding the separated flow.

II. The three-dimensional separated region including the separation sheet/envelope and the three-dimensional horseshoe or junction vortex system which is contained between the separation sheet and the body itself, including the flow forward of and around the body sides to the trailing edge.

III. The near-wake flow dominated by the strong mixing of the tails of the horseshoe vortex system coming off the two sides of the body, as well as the wake from the boundary layers developed on the body sides and mixing with the adjacent, more remote, boundary layer-like floor flow.

IV. The far-wake flow where the various complex turbulent flows in region III continue to mix and homogenize to some extent toward a more typical boundary layer-like downstream flow.

This type of flow occurs in a wide variety of real world flow circumstances such as in the flow around bridge piers in rivers,

Contributed by the Fluids Engineering Division for publication in the JOURNAL OF FLUIDS ENGINEERING. Manuscript received by the Fluids Engineering Division October 29, 1986.

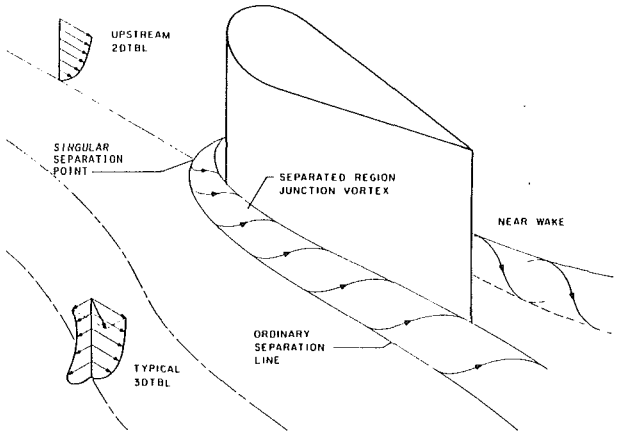

Fig. 1 The overall complex separated three-dimensional turbulent flow centered around a junction vortex

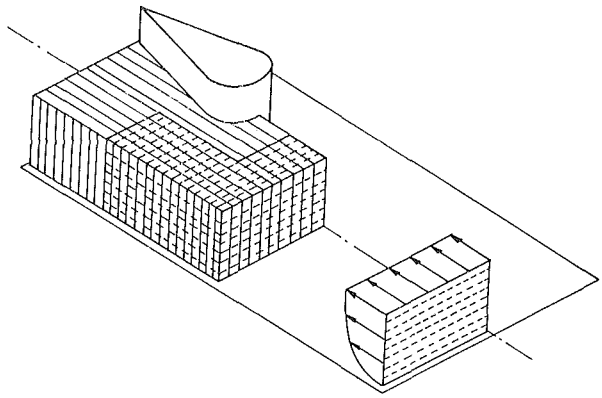

Fig. 2 Measurement regions

around buildings and structures in an atmospheric boundary layer, at wing-fuselage junctions, at strut-surface junctions, control surface-body junctions, at strut-surface junctions in turbomachine flow passages, at the leading edge junction between turbomachine blades and end walls, around submarine sail-hull junctions, and in and around ship hull-strut intersections.

The 1981-1982 Stanford Conference [1] recommended four out of some sixteen candidate flows to serve as standard test cases in the three-dimensional turbulent boundary layer (3DTBL) flow category. These included the studies of van den Berg and Elsenaar [2] and Elsenaar and Boelsma [3], Bissonnette and Mellor [4], Dechow and Felsh [5], and Lohmann [6]. The experiments of Bissonnette and Mellor, and Lohmann are shear driven flows in which a developing 2DTBL flowing axially over a stationary cylinder is suddenly skewed by the transverse motion of a rotating cylinder. The studies of van den Berg, Elsenaar, and Boelsma were made in a quasi two-dimensional turbulent boundary layer flow on a flat plate under infinite swept wing and adverse pressure gradient conditions. The only work similar in some respects to the present study is that reported by Dechow and Felsh. This is an excellent study; however, it provides initial condition data along a line rather than a plane and only limited edge condition data. More recently, Shabaka and Bradshaw [6], McMahon, Hubbartt, and Kubendran [8, 9], Dickinson [10], Hsing and Teng [11], and Moore and Forlini [12] have reported work on mean flow and some turbulence properties in junction vortex flows. At least the first two studies offer measurements of sufficiently high quality to warrant consideration as benchmark studies and should prove valuable to flow and turbulence modelers. However, none of the others cited appears to be sufficiently comprehensive so as to permit the computational fluid dynamicist an unbiased test of the predictive capability of a solver for such a complex flow.

For the 3DTBL-like flow upstream and around the body and generally away from the separation sheet, region I, documentation includes: (1) the mean velocity and turbulent kinetic energy (TKE) on an initial condition plane well upstream of the separated flow and junction vortex, (2) the freestream or edge velocity, (3) the floor surface static pressure, (4) the mean velocity field and the turbulent kinetic energy field for the strongly three-dimensional flow around the body, and (5) local wall shear stress measurements made with a Preston tube and compared to earlier wall shear measurements made with a direct force sensing shear meter responding simultaneously to local shear magnitude and direction.

Figure 2 summarizes the regions where flow measurements were made. The initial condition plane and the 3DTBL flow of region I are shown as a plane and volume marked with broken lines. The junction vortex flow of region II, reviewed in a companion paper, is shown marked with solid lines. There is substantial overlap of some of the region II measurements into the region I flow.

Since the flow in region I is a 3DTBL-like flow which is usually posed as a mixed mode, upstream initial condition-edge condition problem, the test case includes 1) measured upstream initial conditions, 2) measured local freestream or edge velocity conditions, along with the floor surface pressure, and 3) measured mean velocity field, turbulence properties, and wall shear field data at selected downstream positions where comparisons can be made between the measured quantities and corresponding computed quantities. For a code using a higher order closure model the upstream initial condition plane provides measured values of the turbulent kinetic energy field to initiate a calculation.

Since the flow in region II is a fully three-dimensional turbulent flow likely requiring a fully elliptic, turbulent, Navier-Stokes solver, flow measurements are required to provide boundary conditions on all surfaces of any solution domain.

The paper provides an overview and summary of Pierce,

Nomenclature

C_f = skin friction coefficient
C_P = pressure coefficient
P = local static pressure
P_{T*} = total pressure at tunnel inlet throat
Q = dynamic pressure based on local freestream speed $\rho U_{FS}^2/2$
Q^* = dynamic pressure at tunnel inlet throat $\rho V_*^2/2$
TKE = turbulent kinetic energy
UFS = local mean freestream speed
$U_1U_2U_3$ = local mean velocity components, tunnel coordinates
$u_1u_2u_3$ = fluctuating velocity components, tunnel coordinates
u_i' = rms fluctuation component
$\overline{u_iu_i}$ = normal turbulent stress
u^* = shear velocity $\sqrt{\tau_w/\rho}$
V_* = speed at tunnel inlet throat
δ = boundary layer thickness
ρ = density
τ_w = local wall shear stress
ν = kinematic viscosity

Harsh, and Menna [13] which contains more complete details, fully tabulated data, and uncertainty estimates for all measured quantities for this flow. That report itself is a condensation of the very extensive and detailed work reported in Menna [14] and Harsh [15] or Harsh and Pierce [16].

Facilities

The pressure-driven 3DTBL flow in Region I was generated by a streamlined cylinder with a circular leading edge placed normal to a flat plate floor. The cylinder has a leading edge diameter of nominally 127 mm, is 229 mm high, and tapers to a sharp trailing edge with an overall length of 298 mm.

A right-hand orthogonal $x_1x_2x_3$ coordinate system is used. The origin of the coordinate system is at the intersection of the floor centerline with the leading edge of the faired cylinder. The tunnel centerline in the flow direction defines the x_1 axis, the x_2 axis coincides with the stagnation line on the body, and the x_1x_3 plane defines the flat floor of the wind tunnel. Probes were traversed across the flow field in the x_2 direction. For convenience, the x_1 and x_3 directions will be referred to as the streamwise and spanwise or transverse directions, respectively.

The separated flow experiments were conducted in the open circuit, subsonic wind tunnel dedicated to this project. Air is drawn through a rectangular inlet 3.66 m wide and 2.44 m high containing a series of filter cloth, screens, and flow straighteners. A 16:1 contraction follows this inlet into the rectangular tunnel. Menna [14] conducted an extensive experimental investigation of this inlet section and chose the present arrangement to minimize flow nonuniformities far downstream of the inlet.

The boundary layer is tripped on all four sides of the exit nozzle or tunnel throat with 2.8-mm diameter rods. The boundary layer growth on the tunnel walls imposed a slight favorable streamwise pressure gradient of approximately 5.66 Pa/m on the nominal 2DTBL floor flow. At the tunnel operating speed, this amounted to an approximately 2 percent increase in the core velocity over approximately 5 m distance leading to the test section. The freestream turbulence intensity at the test section was measured at about 0.5 percent. The tunnel operates in a suction mode with the flow exhausting into the laboratory.

Dynamic similarity was achieved by maintaining a constant unit Reynolds numbers, V_*/ν, of 1.34×10^6/m $\pm$0.5 percent at the wind tunnel throat.

Methods

For the three-dimensional turbulent boundary layer-like flow in region I, measurements included: (1) mean velocity and turbulent kinetic energy on an initial condition plane, (2) mean velocity and turbulent kinetic energy at selected stations in the downstream 3DTBL flow, (3) freestream or edge velocity measurements over the 3DTBL flow field, (4) floor static pressure measurements, and (5) local wall shear measurements at select floor stations made with a Preston tube and compared with earlier direct force shear measurements.

Figures 3 and 4 show the stations for the initial condition plane, for the freestream or edge velocity measurements, and for the downstream region I 3DTBL flow. While most dimensions are reported in SI units, the original floor grid was arranged in a pattern on 2 inch centers. Data stations are typically identified by an (x_1, x_3) pair, where these numbers give the floor station coordinates in inches.

The initial condition plane is 610 mm upstream of the body leading edge. Mean velocity profiles were taken at five stations and TKE profiles were taken at four stations.

The freestream velocity magnitude and direction were measured at 47 stations, 127 mm from the floor, beginning with the initial plane and extending downstream to the forward quadrant of the pressure-driven 3DTBL. Six

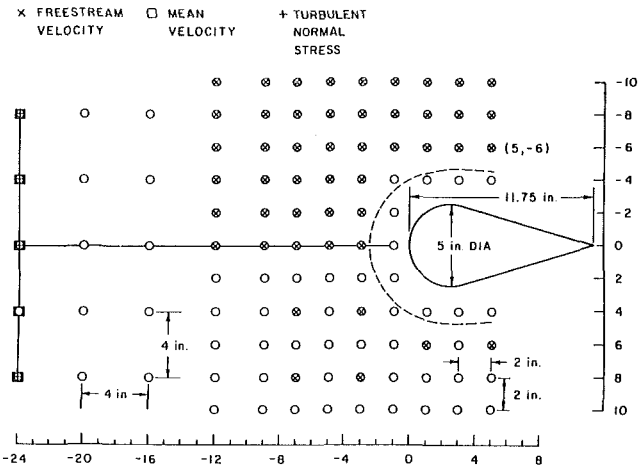

Fig. 3 Flow data stations for the initial condition plane and edge condition measurements of region I flow

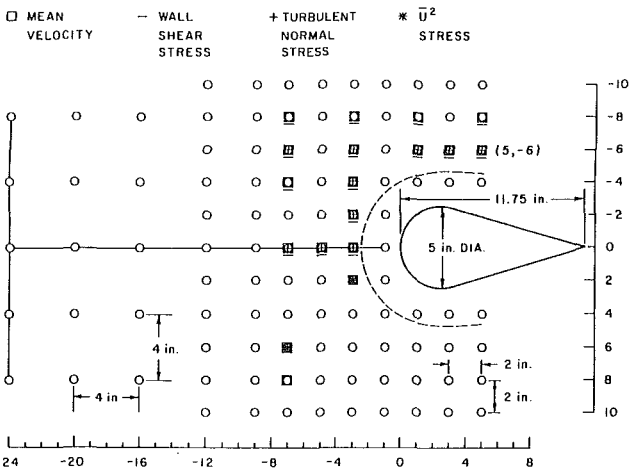

Fig. 4 Flow data stations for the three-dimensional turbulent boundary layer measurements in region I flow

measurements of the edge condition were taken in the adjacent quadrant to determine the degree of symmetry of the freestream flow. The edge condition was measured by two different methods. The magnitude and direction of the mean velocity were obtained with a single hot film, and subsequently, a three-hole yaw probe measured the flow angle and a Pitot-static probe measured the magnitude of the freestream velocity.

Measurements of mean velocity and wall shear magnitude and direction were made at 15 stations. In addition, 3 mean velocity profiles were taken in the adjacent forward quadrant of the flow to determine the degree of symmetry of the flow. The Preston tube results are compared to the direct force wall shear measurements reported in McAllister, Pierce, and Tennant [17].

The turbulent kinetic energy profiles were measured at 10 stations. The measurement of the TKE required two traverses at each station with two x-array sensors. In the actual data acquisition, two additional traverses were made with a slant x-array in two distinct positions for redundancy.

Mean velocity and turbulence quantities were measured, as necessary, with two channels of a DISA 55M modular linearized CTA system, with a DISA 55B25 turbulence processor.

Three quartz coated hot film x-array probes and a single hot film probe were used to measure the turbulent normal stresses and mean velocity fields, respectively. A standard TSI model 1240-20 horizontal x-array and a standard TSI model 1210-20

single film probe were used, with a TSI model 1241BA-20 vertical and model 1240AG-20 slant x-array probes. The latter two arrays were specifically designed with the sensor support prongs offset to ensure a clear line of sight for each sensor, minimizing aerodynamic interference from the sensor supports.

Wire sensors are much smaller than film sensors, with wires typically 5μm in diameter, while films are typically 25 or 51 μm in diameter. Cylindrical films overcome some of the deficiencies of hot wires which are more susceptible to strain, breakage, and shifts in calibration due to environmental contamination, while the films are more stable, rugged and less sensitive to contamination. Films exhibit inferior frequency response characteristics when compared to wires [18, 19] with this effect attributed to the substrate or backing material [20]. However, for -20 cylindrical films, the extensive study by Taslim, Kline, and Moffat [21] has shown that a 51-μm diameter cylindrical film gave $\overline{u_1u_1}$ normal stress values essentially identical with, and $\overline{u_1u_2}$ shear stress values within 2 percent of a 5-μm diameter wire in a fully developed channel flow. These are relatively small errors in light of the strength and stability of the cylindrical film sensors.

The probes were mounted vertically in a traversing mechanism located on the roof of the tunnel. A protractor with vernier scale permitted angular measurements to the nearest 0.2 deg. The uncertainty of the vertical positioning procedure in locating the wall reference distance was estimated at ± 51-μm at 19/1 odds. Since the size of the tunnel and magnitude of volume flow rate created sufficient suction to slightly displace the roof and floor of the tunnel, the reference point was determined with the tunnel operating and the body in place for all the profiles taken.

To examine the effects of self-induced turbulence by the probe due to vortex shedding or vibration of the probe components, output voltage signals from individual sensors were fed to an FFT analyzer with the sensors at different positions in the flow field. Frequency spectra showed no significant contributions at frequencies identified with the probe geometry.

Yaw angles in planes parallel to the tunnel flow were measured with a single hot film probe. Repeated measurements suggested a yaw angle uncertainty of ± 0.5 deg.

The magnitudes of the mean velocities and TKE were measured with the probes aligned with these local yaw directions where in local streamline coordinates the transverse components are zero. The local pitch angle and normal velocity component were obtained by using the calibrated sensor sensitivities of the vertical x-array as in Müller [22, 23].

Preston tube and pressure probe measurements were made with Datametrics model 1400 electronic manometers. These units were calibrated periodically throughout the study using a Microtector Electronic Point Gage manometer manufactured by Dwyer Instruments Inc. which served as a laboratory secondary pressure standard.

The floor static pressure was measured in earlier work using a 48 port Scanivalve unit with a Setra 237 bidirectional differential capacitance type pressure transducer.

The mean velocity profiles measured by the single film ranged from y of 0.51 to 127 mm. Measurements of TKE and mean velocity using the x-arrays ranged from 1.27 mm near the wall to 127 mm where the smallest distance from the wall was dictated by the physical size of the probe. The measuring point was assumed to be at the geometric center of each x-array.

Static velocity calibrations were performed on the sensors of each probe in the potential core of the tunnel flow before and after each traverse was taken. Both the initial and final calibration data were used to obtain the probe calibration curve using a least squares algorithm. The combined processing of these data gave scatter usually to within a standard error 1 percent about the estimated mean line. Data sessions typically lasted from four to twelve hours with each profile requiring approximately four hours to complete. The final calibration served as a means of detecting and quantifying the amount of drift that may have occurred during the profile run. With the laboratory temperature held essentially constant and continuous operation of the instruments, electronic drift was usually not a problem. The linearizers did however appear to be very sensitive to small changes in the ambient temperature conditions. Whenever any detected drift was judged unacceptable, measured by a corresponding change in the sensors' velocity calibration, the profile was repeated.

A detailed yaw calibration was made for each individual sensor of the three x-array probes used and in each of two positions for the slant x-array probe for a total of eight sensor yaw calibrations. For the popular Hinze [24] or Jorgensen [25] cooling law, in terms of the local yaw angle α, where $f=\cos^2\alpha+k^2\sin^2\alpha$, the problem is to determine the value of the parameter k and the possible dependence of k on yaw angle and/or velocity.

An innovative yaw calibration procedure was used which utilized a wide range of both velocity and yaw angle data for estimating the parameter k. The development was motivated by the use of cross flow x-array probes where the flow vector is normal to the probe stem or support. For an x-array in a plane normal to the probe stem and with straight sensor supports, the inner sensor is in the wake of a sensor support when oriented normal to a calibration flow vector. This precludes calibration of the probe in the usual manner with the sensor normal to the calibration flow vector. The new method calibrates the sensor over a range of velocities and at various yaw positions in a window avoiding the specific yaw positions where obvious sensor support interference occurs. A calibration curve is obtained at distinct yaw locations in the plane of the x-array which contains the calibration flow vector, to generate a family of curves in the neighborhood of the intended measurement position. For x-array probes, the measurement position is typically $\alpha=45$ deg. The yaw calibrations were performed over a yaw interval of approximately 35 to 55 deg, a reasonable interval for even moderate turbulence levels.

For a lineraized bridge circuit where the bridge output, E, is

$$E=A+BfU$$

the calibration procedure, which uses parameter estimation procedures, returns values of A, B, and the cooling law parameter k in the cooling law function f.

The credibility of the turbulence measurement process, including instrumentation, data acquisition, and data reduction, was established by comparison of current results with the classic Klebanoff [26] 2DTBL flow data. The present degree of agreement with the Klebanoff data was judged equivalent to the level of agreement shown by Dechow and Felsch [5], Elsenaar and Boelsma [3], and Löfdhal and Larsson [27], all of whom used wire sensors and made similar measurements in nominally two-dimensional flows as part of their measurements in 3DTBL flows.

Figure 5 shows the three normal turbulent stresses which define the TKE for a nominally two-dimensional flow (station $-24, 0$). The $\overline{u_1u_1}$ stress distributions show very good agreement with the present data falling off for $x_2/\delta<0.1$, earlier than the fall-off reported by Klebanoff. The $\overline{u_2u_2}$ stress shows excellent agreement. The $\overline{u_3u_3}$ stress shows good qualitative agreement but is lower in value than the Klebanoff data, with the difference increasing toward the wall to a value of about 10 percent near the wall. This behavior is also seen in the work cited above [5, 3, 27].

Several repeated measurements of edge condition velocity, wall shear stress, and mean velocity and TKE profiles in the upstream and downstream regions of the flow were taken with very good repeatability. Flow yaw angle measurements were generally repeatable to within ± 0.5 deg. The uncertainty in

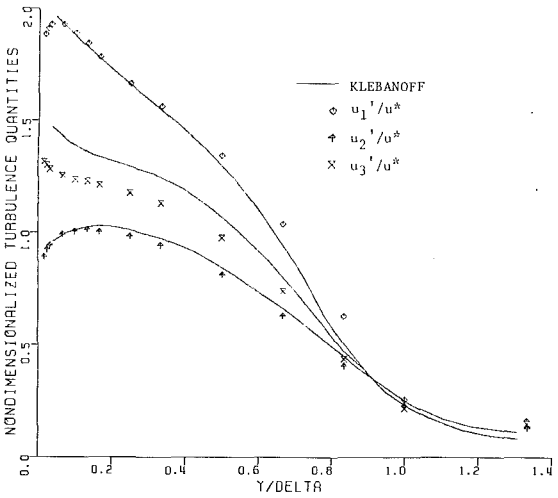

Fig. 5 Comparison of the nominally two-dimensional turbulent normal stresses at (−24, 0) with the Klebanoff [26] results. For $y/\delta < 2/3$, the uncertainty in the reported normal stress is estimated at 4 percent.

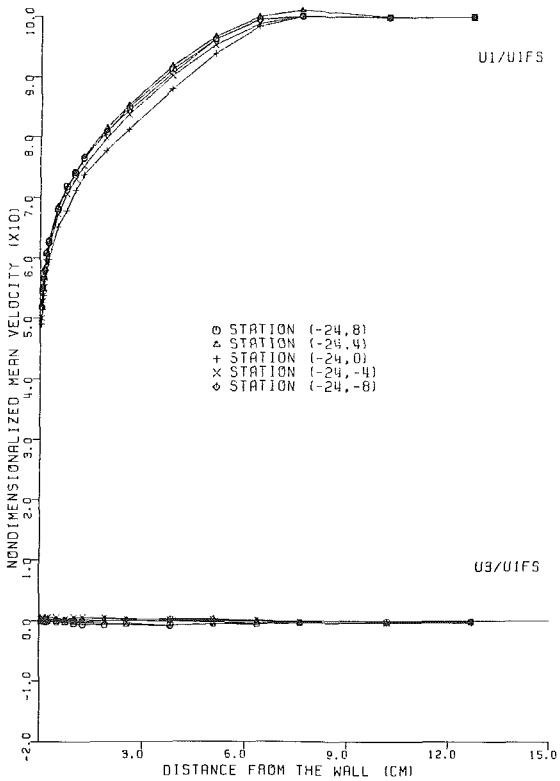

Fig. 6 Mean velocity profiles along the initial condition plane. The uncertainties in the speed and yaw angles are estimated at 0.5 percent and 0.5 degree, respectively.

mean velocity was estimated at ±0.5 percent in the outer region of the boundary layer, and increasing to ± 2 percent at the wall. Generally, the normal stresses were repeatable to within ± 3 to 4 percent in the lower two-thirds of the boundary layer where significant magnitudes were measured. In the absence of fixed errors, this would imply an experimental uncertainty of equal range. Additionally, redundant u_1u_1 stresses measured with the horizontal, vertical, and the slant x-array used in two positions, were in very good agreement.

The surface static pressure was measured at 681 points on the flat floor for the region I flow using an instrumented pressure plate with an array of 0.51 mm diameter pressure taps. A 48 port Scanivalve unit with a Setra 237 bidirectional differential capacitance type pressure transducer was used.

The pressure coefficient is defined as

$$C_P = \frac{P - P_{T*}}{Q_*}$$

where P_{T*} is the total pressure and Q_* is the dynamic pressure at the throat of the tunnel inlet nozzle.

The wall pressure field for this region I, boundary layer-like flow was uneventful, and not unexpectedly resembled the static pressure field for the potential flow about a circular cylinder. The region I floor pressure field is shown together with that for the separated flow in region II in Fig. 6 of the companion paper.

The use of indirect wall shear diagnostic devices such as Preston tubes to infer wall shear stress in three-dimensional flows, assumes a priori the validity of a two-dimensional-like similarity law in a three-dimensional flow in the wall flow layer wherein the probe face lies. For modestly skewed profiles with an approximate upper limit of 15-20 deg, as well as a plane of symmetry, the results of Pierce et al. [28, 29] indicate that indirect devices such as Preston tubes, which are not highly sensitive to yaw angles, could give reasonably good approximations (within 5 to 10 percent) of the *magnitude* of the wall shear stress using a two-dimensional calibration. The indirect devices however would be relatively poor in indicating the local wall shear stress or limiting wall streamline direction due to their insensitivity to yaw. Pierce et al. suggest that for modestly skewed flows, the combination of an indirect device such as a Preston tube with a well-established flow visualization technique could do a reasonably satisfactory job in mapping a wall shear field.

The Preston tube consisted of a 0.457 mm OD stainless steel tube mounted on a 12.7 mm diameter aluminum disk with the tube opening at the center of the disk. Static pressure taps were located 0.635 and 1.27 mm from the tube opening on a line perpendicular to the tube axis.

To account for the transverse pressure gradients present in this flow, the static pressure was measured at both ports with a first order or linear static pressure correction used to calculate the dynamic pressure at the tube opening. The Preston tube was algined at an angle obtained from a linear interpolation between the limiting wall stream-line direction, taken from an oil streak flow visualization, and the measured flow direction nearest to the wall at $x_2 = 0.51$ mm.

The wall shear stress results are presented as skin friction coefficients with

$$C_f = \frac{\tau_w}{Q}$$

where Q is the dynamic pressure based on the local freestream speed. This usage of local freestream speed is universal practice in two-dimensional flows and it has been extended to three-dimensional flows as well. One should recognize the differences in these two cases since the freestream direction in a three-dimensional flow can be skewed relative to the wall shear direction. Such usage does not assume collateral wall shear and freestream mean velocity vectors. The wall shear stress magnitudes were obtained from Patel's [30] calibration equations.

Uncertainty Estimates

Representative values of uncertainty estimates are noted in this text and in figure captions. Complete and more detail uncertainty estimates are included with the full data in Pierce, Harsh, and Menna [13].

Results and Discussion

For the flow in region I, the 3DTBL-like flow upstream and

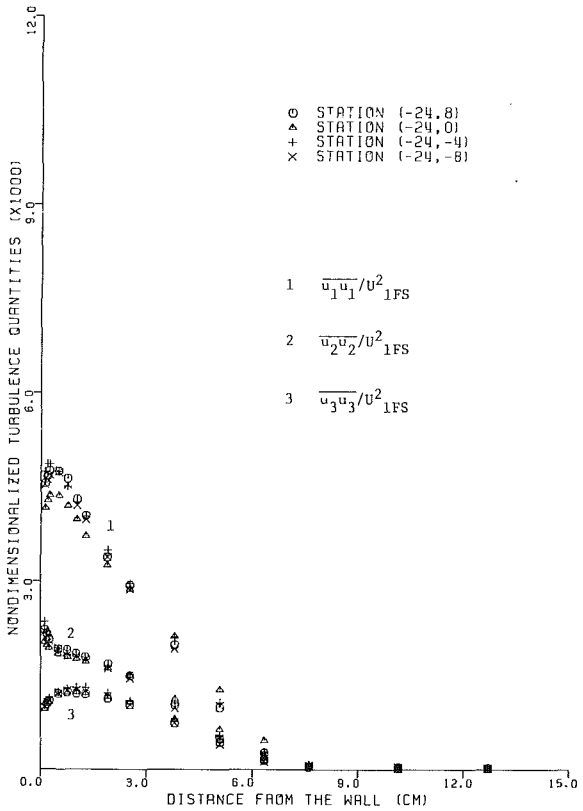

Fig. 7 Normal turbulent stresses along the initial condition plane. For $y/\delta < 2/3$, the uncertainty in the reported normal stress is estimated at 4 percent.

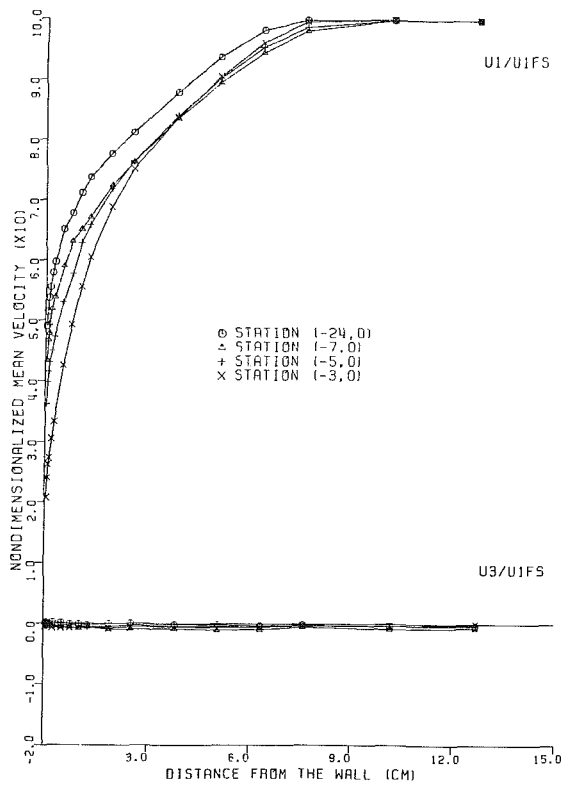

Fig. 8 Mean velocity profiles along the plane of symmetry. The uncertainties in the speed and yaw angles are estimated at 0.5 percent and 0.5 degree, respectively.

around, but generally away from the separated flow, results include:

1. The mean velocity and turbulent kinetic energy (TKE) on an upstream initial condition plane.
2. The mean velocity profiles and TKE profiles for the strongly three-dimensional boundary layer-like flow around the body.
3. The freestream or edge velocity.
4. The floor surface static pressure.
5. Local wall shear stress measurements made with a Preston tube and compared to earlier data when force magnitude and direction were measured simultaneously with a mechanical, direct force sensing meter.

Mean flow velocities, turbulent normal stresses, and the TKE were measured on the initial condition plane at stations shown in Fig. 3. Mean velocity profiles taken with a single horizontal film sensor and uncorrected for turbulence effects are shown in Fig. 6. Turbulent normal stress and TKE profiles are shown in Fig. 7, where TKE is defined as

$$\text{TKE} = \frac{1}{2}(\overline{u_1u_1} + \overline{u_2u_2} + \overline{u_3u_3}).$$

The mean velocities and normal stress components are in the laboratory or tunnel $x_1x_2x_3$ coordinates and the nondimensionalizing velocity is the boundary layer edge or freestream velocity component along x_1.

Figure 6 shows the slightly retarded mean velocity profile on the symmetry plane. This profile shape is not due to the presence of the body. Extensive studies on the character of the flow by Fitts [31] identified this profile shape with a small convergence of the floor boundary layer flow (1/12 deg per transverse inch across an 18-in. tunnel half width), and identified with the side wall boundary layer growth of the relatively long flow section upstream of the test section area. Measurements of both the mean velocity field and the TKE

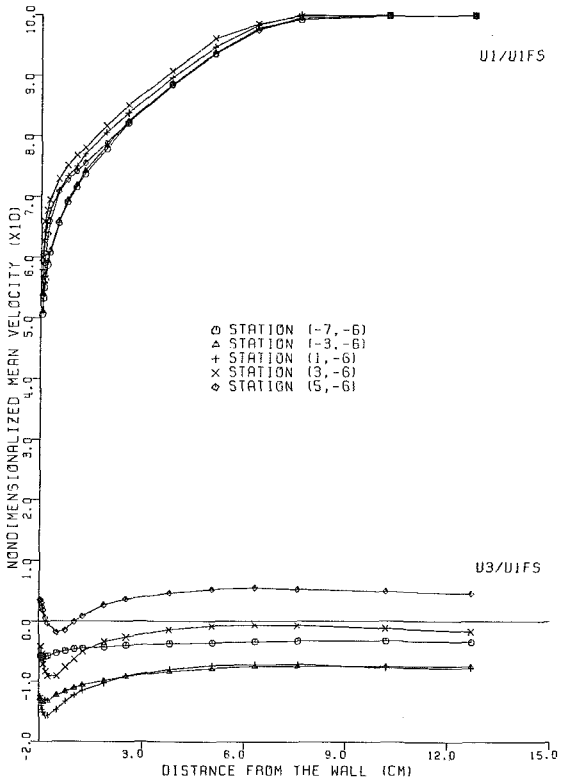

Fig. 9 Mean velocity profiles along the plane $x_3 = -6$ in. The uncertainties in the speed and yaw angles are estimated at 0.5 percent and 0.5 degree, respectively.

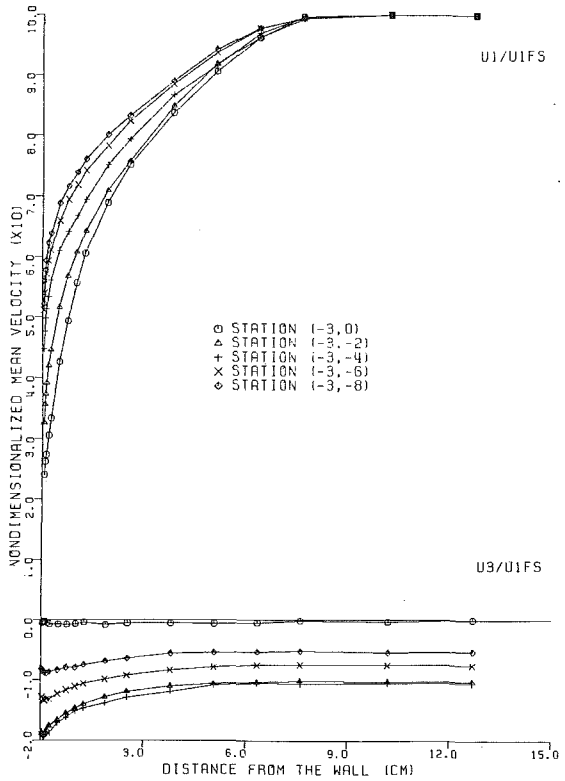

Fig. 10 Mean velocity profiles along the plane $x_1 = -3$ in. The uncertainties in the speed and yaw angles are estimated at 0.5 percent and 0.5 degree, respectively.

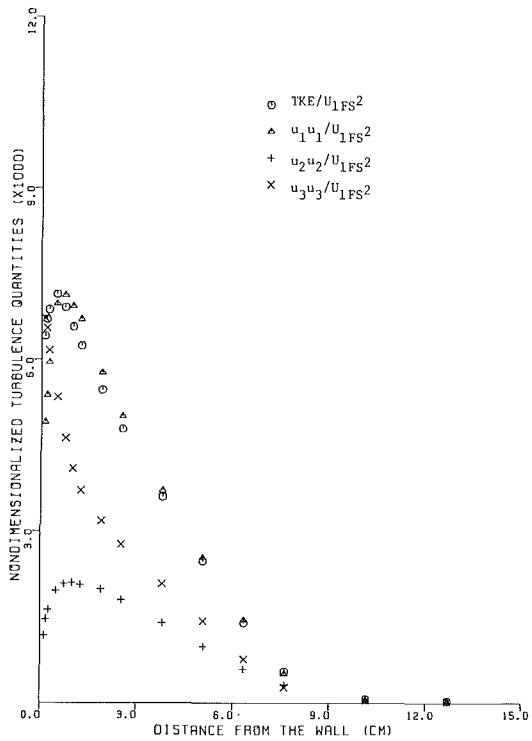

Fig. 12 Normal turbulent stresses and turbulent kinetic energy at station (−3, −2). For $y/\delta < 2/3$, the uncertainty in the reported normal stress is estimated at 4 percent.

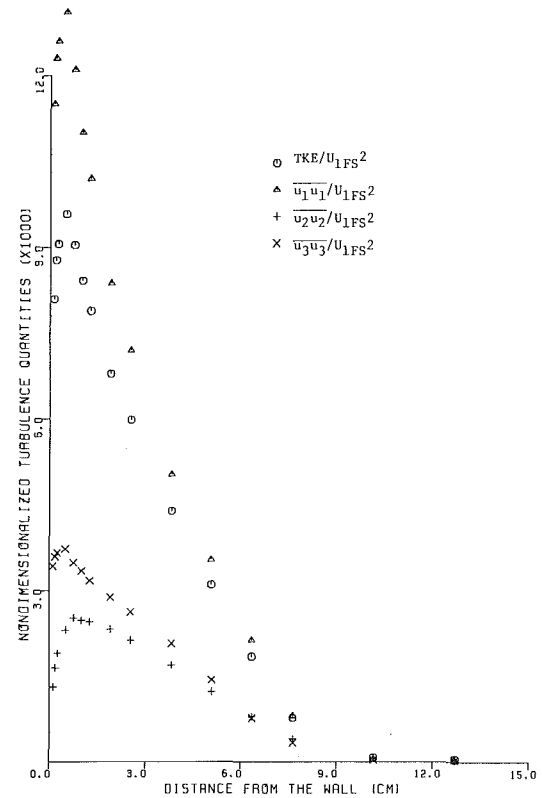

Fig. 11 Normal turbulent stresses and turbulent kinetic energy at station (−3, 0). For $y/\delta < 2/3$, the uncertainty in the reported normal stress is estimated at 4 percent.

show that the initial condition plane was sufficiently far upstream so as to not be affected by the presence of the body.

Mean velocities, turbulent normal stresses, and turbulent kinetic energy were measured in the 3DTBL flow field at the stations shown in Fig. 4. Representative mean velocity profiles uncorrected for turbulence are shown in Figs. 8 through 10 for the symmetry plane, $x_3 = 0$, along the streamwise plane at $x_3 = -6$ in., and along the transverse or spanwise plane at $x_1 = -3$ in. The degree and spatial extent of the effect of the body and the vortex system is shown in these figures. It is noted that in general, the presence of the body in this relatively thick undisturbed 2DTBL does not change the boundary layer thickness significantly. The upstream boundary layer fluid accelerates around the body approximately within the undisturbed boundary layer thickness.

Figures 11 through 13 show the turbulent normal stress and TKE development in the 3DTBL at representative locations for stations (−3, 0), (−3, 2), and (3, −6). The very large increase in the turbulent normal stresses and TKE along the symmetry plane in Figs. 7 and 11 is consistent with the increased fluctuations seen in the sensor response as the stagnation line of the body was approached. Figure 12 shows a large decrease in the nondimensionalized normal stresses and TKE away from the body in the spanwise direction, although the distributions at the most remote station are noticeably different than those on the essentially 2DTBL initial condition plane. Figure 13 shows a small decrease in the TKE in the streamwise direction, 152 mm from the body centerline, with a clear second local maximum appearing in the TKE and the streamwise turbulent normal stress, and a less distinct but similar character in the $\overline{u_2u_2}$ turbulent normal stress as well. This distribution with two local maxima in the $\overline{u_1u_1}$ stress is similar to that found in the end wall boundary layer of the curved channel flow in Francis and Pierce [32].

The edge conditions for the region I flow were obtained in the freestream at the locations shown in Fig. 3. Two complete

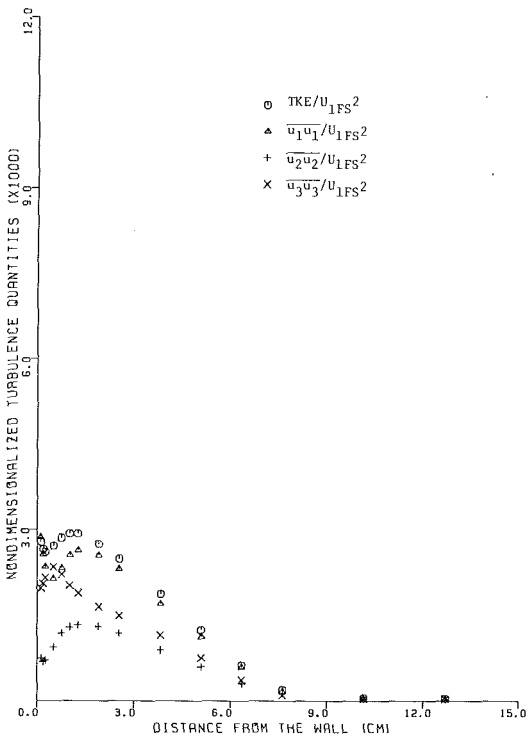

Fig. 13 Normal turbulent stresses and turbulent kinetic energy at station (3, −6). For $y/\delta < 2/3$, the uncertainty in the reported normal stress is estimated at 4 percent.

and independent sets of freestream data were taken. The freestream mean direction and velocity magnitude measured by a single film, and by the combined use of a Pitot static and a 3-hole yaw probe show overall good agreement between the two methods. The uncertainty in the edge condition was estimated at ±0.5 deg for the flow angle measurements and ±0.5 percent for the mean velocity magnitudes. The freestream measurements made at the end of each single film mean velocity traverse agreed very closely with edge condition data taken after all the 3DTBL profiles were measured.

The floor static pressure field results are presented as pressure coefficients. Floor static pressure measurements were taken on a 12.7 mm grid which spanned ±254 mm laterally from the plane of symmetry, beginning 178 mm upstream of the body, and extending 305 mm longitudinally to 127 mm downstream of the body leading edge.

The wall shear stress measurements by the Preston tube were taken at the floor stations shown in Fig. 4. The results are presented in Table 1 as skin friction coefficients.

The Preston tube arrangement used in measuring wall shear stress magnitudes is described earlier. The two static pressure taps adjacent to the side of the tube opening allowed for a correction of the static pressure to account for the transverse pressure gradients. Substantially poorer results were obtained without these corrections for the transverse pressure gradients.

As shown in Table 1, the nearest wall velocity direction can differ significantly from the local oil streak or wall shear stress direction. These results are consistent with those of Pierce, McAllister, and Tennant [28] and in Pierce and McAllister [33], who used a 3-hole yaw probe for local flow direction, and indicate that the velocity vector generally changes direction continuously to the wall in a pressure-driven flow.

Table 1 compares the local skin friction coefficients from the McAllister, Pierce, and Tennant [17] direct force wall shear measurements with the Preston tube results of this study. Two of the 15 pairs compared show exceptionally large differences, with both these data stations in very close proximity to the separation line caused by the junction vortex as shown in the flow visualizations. Omitting these two points on the assumption that either or both the Preston tube measurement or the shear meter measurement were inaccurate due to the close proximity of the separation line, the remaining 13 pairs of C_f values compare reasonably well. These data show a range of differences between −7.1 to +5.3 percent, with an average difference of just under 1 percent and a variance of 4.2 percent. With the usual assumption of normality, this suggests that the Preston tube and mechanical meter data are within ±8 percent at about 19:1 odds. The results support the suggested use of a relatively simple device such as a Preston tube (correcting for transverse pressure gradients as necessary) together with a good flow visualization technique as a means of mapping the shear field in a 3DTBL flow without excessive skew and away from separation.

Summary

The mean flow structure upstream and around a turbulent junction or horseshoe vortex are reported for an incompressible, subsonic flow. The flow is generated by placing a streamlined cylinder normal to a flat surface in a relatively thick boundary layer, where the boundary layer thickness is of the order of the cylinder thickness or width.

The upstream and surrounding 3DTBL-like flow away from separation has been documented with mean velocity field and TKE field measurements made with hot film anemometry. For use in validating predictive codes for the boundary layer-like portion of the flow, mean velocity and TKE data are also provided for an initial condition plane well upstream of the junc-

Table 1 Comparison of skin friction coefficients and wall flow angles

Station	$c_f \times 10^3$ Preston Tube	Shear Meter	Wall flow angles Shear Meter	Oil Flow	Film Probe#
−7,0	1.94	1.92	−0.9	0.5	−0.4
−5,0	1.54	1.47	−1.8	0.5	
−3,0	0.71	0.295		1.3	
−3,−2	1.57	2.01	52.3	47.0	30.0
−7,−4	2.19	2.08	10.1	10.0	7.6
−3,−4	2.37	2.55	31.7	31.5	22.6
−7,−6	2.36	2.32	9.4	10.5	6.5
−3,−6	2.58	2.69	16.9	16.5	14.1
1,−6	3.19	3.04	3.9	5.5	12.1
3,−6	3.13	3.07	−6.9	−4.0	4.0
5,−6	2.58	2.74	−11.9	−10.5	−3.7
−7,−8	2.42	2.40	6.4	7.0	6.1
−3,−8	2.62	2.61	9.3	9.0	8.9
1,−8	2.90	2.78	1.5	4.0	5.8
7,−8	2.72	2.62	−8.1	−7.0	−3.0

#Single film sensor at $y = 0.508$ mm.

tion vortex flow, and freestream or edge velocity, as well as floor static pressure are reported. Additionally, local wall shear stress values are also reported for the 3DTBL-like flow.

For the upstream and surrounding 3DTBL-like flow the TKE shows a sharp increase as the flow approaches the separation sheet on the plane of symmetry, with a sharp drop from these larger values in the transverse direction away from the symmetry plane. Along a streamwise plane slightly away from the body, the TKE develops a distinct second local maximum near the floor.

For the flow away from separation, the floor pressure distribution resembles that of a potential flow for an infinite body of the same cross section.

Acknowledgments

The results reported here are from a long-term, ongoing project. Initial support from the National Science Foundation provided for most of the physical facilities, some early instrumentation, and the initial work on the project. Subsequent support from the NASA-Ames Research Laboratory provided for additional instrumentation, the development of the automated data acquisition system, and the bulk of the results reported here. Recent support from the David W. Taylor Naval Ship Research and Development Center provided for the continuation of the documentation of the total flow, focusing on boundary conditions for the elliptic vortex region II flow, and the documentation of the near and far wake of the downstream flow.

References

1 Kline, S. J., Cantwell, J. B., and Lilley, G. M., *1980-1981 AFOSR-HTTM-Stanford Conference on Complex Turbulent Flows*, Vols. I, II, III, Stanford University, 1981.

2 Van den Berg, B., and Elsenaar, A., "Measurements in a Three-Dimensional Incompressible Turbulent Boundary Layer in an Adverse Pressure Gradient Under Infinite Swept Wing Conditions," NRL TR 72092 U, 1972.

3 Elsenaar, A., and Boelsma, H. S., "Measurements of the Reynolds Stress Tensor in a Three-dimensional Turbulent Boundary Layer Under Infinite Swept-Wing Conditions," National Aerospace Laboratory, NRL, The Netherlands, NRL TR 74095 U, 1974.

4 Bissonnette, L. R., and Mellor, G. L., "Experiments on the Behavior of an Axisymmetric Turbulent Boundary Layer with Sudden Circumferential Strain," *Journal of Fluid Mechanics*, Vol. 63, Part 2, 1974, pp. 369-413.

5 Dechow, R., and Felsch, K. O., "Measurements of the Mean Velocity and of the Reynolds Stress Tensor in a Three-Dimensional Turbulent Boundary Layer Induced by a Cylinder Standing on a Flat Wall," *Symposium on Turbulent Shear Flows*, Vol. 1, American Society of Mechanical Engineers, University Park, Pa., Apr. 18-20, 1977, pp. 9.11-9.20.

6 Lohmann, R. P., "The Response of a Developed Turbulent Boundary Layer to Local Transverse Surface Motion," ASME Paper 76-FE-3, 1976.

7 Shabaka, I. M. M. A., and Bradshaw, P., "Turbulent Flow Measurements in an Idealized Wing/Body Junction," *AIAA Journal*, Vol. 19, No. 2, February, 1981, pp. 131-132.

8 McMahon, H., Hubbartt, J., and Kubendran, L., "Mean Velocities and Reynolds Tresses in a Juncture Flow," NASA Contractor Report No. 3605, National Aeronautics and Space Administration, Langley Research Center, Hampton, Virginia, 1982.

9 McMahon, H., Hubbartt, J., and Kubendran, L., "Mean Velocities and Reynolds Tresses Upstream of a Simulated Wing Fuselage Juncture," NASA Contractor Report No. 3695, National Aeronautics and Space Administration, Langley Research Center, Hampton, Virginia, 1983.

10 Dickinson, S. C., "Flow Visualization and Velocity Measurements in the Separated Region of an Appendage-Flat Plate Junction," *Proceedings of the Ninth Biennial Symposium on Turbulence*, University of Missouri-Rolla, Rolla, Mo., Oct. 1-3, 1984.

11 Hsing, T. D., and Teng, H. Y., "Experimental Study of the Behavior of 3D-Turbulent Boundary Layer in a Simplified Wing/Body Junction," Paper No. AIAA-84-1529, presented at the American Institute of Aeronautics and Astronautics 17th Fluid Dynamics, Plasma Dynamics, and Lasers Conference, Snowmass, Colorado, June 25-27, 1984.

12 Moore, J., and Forlini, T. J., "A Horseshoe Vortex in a Duct," Paper No. 84-GT-202, presented at the American Society of Mechanical Engineers 29th International Gas Turbine Conference and Exhibit, Amsterdam, The Netherlands, June 4-7, 1984.

13 Pierce, F. J., Harsh, M. D., and Menna, J. D., "The Mean Flow Structure Around and Within a Turbulent Junction or Horseshoe Vortex," Report VPI-E-85-19, Mechanical Engineering, Virginia Polytechnic Institute and State University, Blacksburg, Va., Sept., 1985 (available NTIS).

14 Menna, J. D., "A Three-Dimensional Turbulent Boundary Layer Upstream and Around a Junction Vortex Flow," Dissertation, Mechanical Engineering, Virginia Polytechnic Institute and State University, Blackburg, Va., May 1984.

15 Harsh, M. D., "An Experimental Investigation of a Turbulent Junction Vortex," Dissertation, Mechanical Engineering, Virginia Polytechnic Institute and State University, Blacksburg, Va., Jan. 1985.

16 Harsh, M. D., and Pierce, F. J., "An Experimental Investigation of a Turbulent Junction Vortex," Rpt. VPI-E-85-4, NASA Grant NSG 2301, Mechanical Engineering, Virginia Polytechnic Institute and State University, Blacksburg, Va., Feb. 1985. (Availabel NTIS.)

17 McAllister, J. E., Pierce, F. J., and Tennant, M. H., "Direct Force Wall Shear Measurements in a Pressure-Driven Three-Dimensional Turbulent Boundary Layer," ASME JOURNAL OF FLUIDS ENGINEERING, Vol. 104, June 1982, pp. 150-155.

18 Anderson, O. K., "Time Resolution Power in Correlation Measurements with DISA Type 55A01 Hot-Wire and Hot Film Anemometers," *DISA Information*, No. 4, 1966, pp. 3-16.

19 Freymuth, P., and Fingerson, L. M., "Electronic Testing of Frequency Response for Thermal Anemometers," TSI Incorporated.

20 Bellhouse, B. F., and Rasmussen, C. G., "Low-Frequency Characteristics of Hot-Film Anemometers," *DISA Information*, No. 6, Feb. 1968, pp. 3-10.

21 Taslim, M. E., Kline, S. J., and Moffat, R. J., "Calibration of Hot Wires for Velocity Fluctuations," Rpt. TMC-4, Thermosciences Division, Dept. of Mech. Eng., Stanford University, Aug. 1978.

22 Müller, U. R., "Measurement of the Reynolds Stresses and the Mean-Flow Field in a Three-Dimensional Pressure-Driven Boundary Layer," *Journal of Fluid Mechanics*, Vol. 119, 1982, pp. 121-153.

23 Müller, U. R., "On the Accuracy of Turbulence Measurements with Inclined Hot Wires," *Journal of Fluid Mechanics*, Vol. 119, 1982, pp. 155-172.

24 Hinze, J. O., *Turbulence*, 2nd edition, McGraw-Hill, 1975.

25 Jorgensen, F. E., "Directional Sensitivity of Wire and Fiber-Film Probes," *DISA Information*, No. 11, May 1971, pp. 31-37.

26 Klebanoff, P. S., "Characteristics of Turbulence in a Boundary Layer with Zero Pressure Gradient," NACA Rpt. 1247, 1955.

27 L%ofdahl, L., and Larsson, L., "Measurements of Reynolds-Stress Profiles in the Stern Region of a Ship Model," IUTAM Symposium, Berlin, Germany, 1982, pp. 66-78.

28 Pierce, F. J., McAllister, J. E., and Tennant, M. H., "Near-Wall Similarity in a Pressure-Driven Three-Dimensional Turbulent Boundary Layer," ASME JOURNAL OF FLUIDS ENGINEERING, Vol. 105, Sept. 1983, pp. 257-262.

29 Pierce, F. J., and McAllister, J. E., "Near-Wall Similarity in a Shear-Driven Three-Dimensional Turbulent Boundary Layer," ASME JOURNAL OF FLUIDS ENGINEERING, Vol. 105, Sept. 1983, pp. 263-269.

30 Patel, V. C., "Calibration of the Preston Tube and Limitations on Its Use in Pressure Gradients," *Journal of Fluid Mechanics*, Vol. 23, Part 1, 1965, pp. 185-208.

31 Fitts, D. O., "A Study of Two- and Three-Dimensional Turbulent Boundary Layer Data Sets Using Momentum Integral Techniques," Thesis, Mechanical Engineering, Virginia Polytechnic Institute and State University, Blacksburg, Va, Mar. 1982.

32 Francis, G. P., and Pierce, F. J., "The Experimental Study of Skewed Turbulent Boundary Layers in Low Speed Flows," ASME *Journal of Basic Engineering*, Vol. 89, Sept. 1967, pp. 597-608.

33 Pierce, F. J., and McAllister, J. E., "Measurements in a Pressure-Driven and a Shear-Driven Three-Dimensional Turbulent Boundary Layer," in *Three-Dimensional Turbulent Boundary Layers, IUTAM-Symposium Proceedings*, Springer-Verlag, Berlin, 1982.

The Mean Flow Structure Around and Within a Turbulent Junction or Horseshoe Vortex—Part II. The Separated and Junction Vortex Flow

F. J. Pierce
Professor of Mechanical Engineering,
Virginia Polytechnic Institute and State University,
Blacksburg, VA 24061
Fellow ASME

M. D. Harsh
Staff Engineer,
Hercules Inc. at Allegany Ballistics Laboratory,
Cumberland, MD 21502
Mem. ASME

The mean flow structure upstream, around, and in a turbulent junction or horseshoe vortex are reported for an incompressible, subsonic flow. This fully documented, unified, comprehensive, and self-consistent data base is offered as a benchmark or standard test case for assessing the predictive capabilities of computational codes developed to predict this kind of complex flow. The three-dimensional turbulent boundary layer-like flow upstream and around the separated junction vortex flow is described in a companion paper, Part I. Part II of these papers covers the flow through the separation region and in the vortex system. This portion of the flow has been documented with mean velocity, static pressure, and total pressure measurements using a very carefully calibrated five-hole probe. The streamwise vorticity field is calculated from the measured velocity field. Extensive floor static pressure measurements emphasizing the region of the vortex system, and static pressure measurements on the cylinder surface are also reported. Flow visualizations on the floor and cylinder surface show unusual detail and agree well both qualitatively and quantitatively with the various flow field measurements.

Introduction

As reviewed in Part I [1] of these papers, the 1981–1982 Stanford Conference on Complex Turbulent Flows [2] focused on the lack of unified, coherent, comprehensive, and self-consistent databases needed for the validation of flow and turbulence models and particularly for the objective and unbiased evaluation of the capabilities of computer codes offered to solve various complex turbulent flows.

These papers report on the results of an experimental program designed to produce a benchmark or standard test database for a complex flow. This fully documented, unified, comprehensive, and self-consistent experimental study should be valuable in assessing the capabilities of computational codes developed to predict such complex flows, as well as in the development of turbulence and flow models.

The particular flow documented in this report is the three-dimensional separated turbulent flow centered about a junction or horseshoe vortex system. This flow is generated by placing a streamlined cylinder with a circular leading edge normal to a flat surface in a thick turbulent boundary layer as shown in Fig. 1 of Part I [1].

The total flow system is arbitrarily divided into four regions, the first two of which are reported on in these two papers. The remaining regions will be covered in subsequent publications. The four regions include:

I. The pressure-driven three-dimensional turbulent boundary layer-like (3DTBL) flow upstream and around the body but excluding the separated flow.

II. The three-dimensional separated region including the separation sheet/envelope and the three-dimensional horseshoe or junction vortex system which is contained between the separation sheet and the body itself, including the flow forward of and around the body sides to the trailing edge.

III. The near-wake flow dominated by the strong mixing of the tails of the horseshoe vortex system coming off the two sides of the body, as well as the wake from the boundary layers developed on the body sides and mixing with the adjacent, more remote, boundary layer-like floor flow.

IV. The far-wake flow where the various complex turbulent flows in region III continue to mix and homogenize to some extent toward a more typical boundary layer-like downstream flow.

As described in Part I [1], this type of flow occurs in a wide variety of real world circumstances.

Measurements reported here include:

1. Flow visualizations for the floor of the total flow.
2. Flow visualizations of the body surface (region II).

For the fully three-dimensional turbulent junction vortex flow, region II, measurements of time-mean values include:

Contributed by the Fluids Engineering Division for publication in the JOURNAL OF FLUIDS ENGINEERING. Manuscript received by the Fluids Engineering Division October 29, 1986.

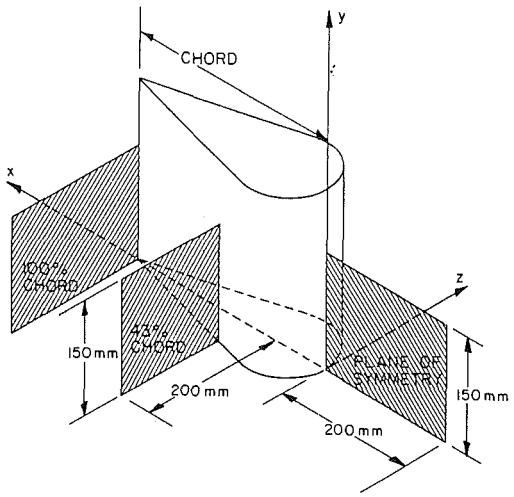

Fig. 1 Five-hole probe measurement planes for region II flow

3. The floor surface static pressure coefficient.
4. The body surface static pressure coefficient.
5. The velocity field.
6. The total pressure field.
7. The static pressure field.
8. The computed vorticity field.

Figure 2 of Part I [1] summarizes the regions where flow measurements were made. The initial condition plane and the 3DTBL flow of region I, reviewed in Part I, are shown as a plane and volume marked with broken lines. The junction vortex flow of region II, reviewed here (with overlap into the 3DTBL flow of region I) is shown marked with solid lines.

Since the flow in region I is a 3DTBL-like flow which is usually posed as a mixed mode, upstream initial condition-edge condition problem, the test case includes 1) measured upstream initial conditions, 2) measured local freestream or edge velocity conditions along with the floor surface pressure, and 3) measured mean velocity field, turbulence properties, and wall shear field data in a downstream region where comparisons can be made between the measured quantities and corresponding computed quantities. In particular, if a code is to model the turbulent kinetic energy, the upstream initial condition plane provides measured values of the turbulent kinetic energy field to initiate the calculation.

Since the flow in region II is a fully three-dimensional turbulent flow likely requiring a fully elliptic, turbulent, Navier-Stokes solver, flow measurements are required as boundary conditions on all surfaces of the solution domain.

These papers provide an overview and summary of Pierce, Harsh, and Menna [3] which contains more complete details and fully tabulated data for this flow. That report itself is a condensation of the very extensive and detailed work reported in Menna [4] and Harsh [5] or Harsh and Pierce [6].

Facilities

The pressure-driven 3DTBL flow in Region I was generated by a streamlined cylinder with a circular leading edge placed normal to a flat floor. The cylinder has a leading edge diameter of nominally 127 mm, is 229 mm high, and tapers to a sharp trailing edge with an overall length of 298 mm.

For the flow in region II the righthand orthogonal coordinate directions are labeled x, y, and z. The origin of the coordinate system is at the intersection of the floor center line with the leading edge of the cylinder. The tunnel centerline in the flow direction defines the x axis, the y axis coincides with the stagnation line on the body, while the xz plane defines the flat floor of the wind tunnel. Probes were traversed across the flow field in the y direction. For convenience, the x and z directions will be referred to as the streamwise and spanwise or transverse directions, respectively. Floor data stations are given in millimeters as an x, z pair.

The separated flow experiments were conducted in the open circuit, subsonic wind tunnel described in Part I. Dynamic similarity for the low speed, three-dimensional flow study was achieved by maintaining a constant with Reynolds number, V_*/ν, of $1.34 \times 10^6/\text{m} \pm 0.5$ percent, at the wind tunnel throat.

Methods

The surface flows on the flat floor of the wind tunnel and on the body were made visible using an oil-film technique described by Squire et al. [7], using a mixture of titanium dioxide (TiO_2), diesel fuel, and oleic acid. Both the flat wind tunnel floor and the body were covered with removable coatings to preserve the limiting streamline patterns. The tunnel floor was covered with a thin piece of tempered aluminum sheet metal with a hand finished leading edge blended into the tunnel floor in an attempt to minimize the roughness effect on the boundary layer. The body was covered with a cellulose acetate sheet. After a test was completed, these sheets were removed from the model surfaces and painted with clear acrylic lacquer to preserve them for later consideration.

For the flow in the separated region and including the junction vortex, measurements included: (1) the floor static pressure field, (2) the body surface static pressure field, (3) the mean velocity field, (4) the total pressure field, and (5) the static pressure field.

For the measurements in this region an automated traverse and data acquisition system was used for vertical probe movement and data acquisition. This system allowed for the systematic accumulation of a large body of data. The subsequent application of rigorous statistical methods in the calibration of probes and in the subsequent data reduction of all measurements resulted in formally calculated and statistically meaningful uncertainties for all of the results for the flow in region II.

The two degree-of-freedom, multi-channel, data acquisition system was designed by Herwig [8]. Probe motion is affected by two stepper motors. The physical limitations on the vertical movement include a minimum displacement of 5 μm and a range of 180 mm. The minimum angular displacement is 0.036 deg.

Nomenclature

C_P = pressure coefficient
D_p = probe diameter
f_i = 5-hole probe calibration functions
P = local static pressure
P_{T_*} = total pressure at tunnel inlet throat
Q^* = dynamic pressure at tunnel inlet throat $\rho V_*^2/2$
Q = local dynamic pressure $\rho V^2/2$
Re_p = probe Reynolds number VD_p/ν
$U_1U_2U_3$ = local mean velocity components in tunnel coordinates
V_* = speed at tunnel inlet throat
V = local speed sensed by probe
α = local pitch angle sensed by probe
β_i = coefficient in probe calibration function
ρ = density
ν = kinematic viscosity

The surface pressure distributions on the flat floor in the vicinity of the leading edge and on the vertical sides of the body were measured with 0.51-mm in diameter pressure taps distributed on both surfaces in anticipation of high pressure gradients. Pressures were read using a Datametrics Model 5900 digital micromanometer.

Three hundred sixty-three pressure taps were machined into a removable aluminum test plate in the wind tunnel floor with forty-three taps included to check the flow symmetry.

A hollow, cast, polyester resin body with one side of the body instrumented with six rows of thirteen pressure taps was used for the body surface pressure measurements. An additional, symmetrically disposed row of twelve taps was included at approximately 120 mm from the floor to check for flow symmetry.

Distributions of three-dimensional velocity, total pressure, and static pressure were measured in three planes as shown in Fig. 1 using a 3.18 mm diameter, United Sensor Corporation, type DC, five-hole, biconic, Prandtl type pressure probe shown in Fig. 2. For the data in the planes normal to the streamwise direction, the probe was pointed into the wind by rotating it in the yaw sense until the pressure difference, $P_2 - P_3$, was zero. The flow pitch angle with respect to the probe at this yaw orientation, the speed, the total pressure, and the static pressure were then determined from three measured pressure differences and three calibration curves. For the plane of symmetry data, the probe was traversed in the y direction at two fixed yaw orientations, one with the probe facing the freestream flow direction and one with the probe rotated 180 deg from this freestream orientation. The correct orientation of the probe was then obtained by maximizing the total pressure response (from hole 1 in Fig. 2) of the probe.

The probe was rotated into the wind at each vertical position using a simple least squares control algorithm in the microcomputer. At the first vertical position in each traverse, the probe was nulled manually and an initial yaw orientation was fed into the microcomputer. The microcomputer then moved the probe a small increment in the y direction to the next vertical position with a yet undetermined but slightly different flow yaw angle. The new yaw position was predicted with three yaw pressure differences, which bracketed this new yaw position, using a yaw calibration curve. This simple approach produced good results because of the linear behavior of the yaw pressure coefficient about the null point.

The five-hole probe was calibrated for pitch angle in the free jet of a calibration tunnel. Three calibration functions were considered, including a pitch pressure coefficient,

$$f_3(\alpha, \mathrm{Re}_P) = \frac{P_4 - P_5}{P_1 - P_2},$$

a dynamic pressure coefficient,

$$f_4(\alpha, \mathrm{Re}_P) = \frac{Q}{P_1 - P_2},$$

and a total pressure coefficient,

$$f_5(\alpha, \mathrm{Re}_P) = \frac{P_1 - P_T}{Q},$$

where Re_p is the probe Reynolds number. Data required to evaluate these functions were acquired over a large range of pitch angles (± 15 deg) and a range of Reynolds numbers greater than those anticipated in the three-dimensional flow measurements. Thirty-two candidate models were considered for each calibration function, including all polynomial models through fourth-degree in pitch and first-degree in probe Reynolds number. Coefficients in the models for these data were evaluated using weighted least squares [9–13] with the weights equal to the inverse of the squared estimated uncertainties in the calibration data. The final choice for each of these models represents a trade-off between goodness of fit,

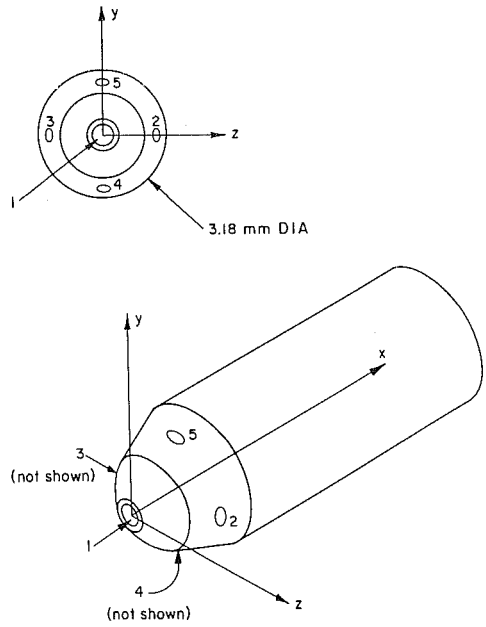

Fig. 2 Five-hole pressure probe

predictive capability, and parsimony. Only the dynamic pressure coefficient was found to have a significant Reynolds number dependency. The optimized models for the calibration functions are given by:

$$f_3(\alpha) = B_2 + B_3\alpha,$$

$$= -0.0139 + 0.033\alpha,$$

$$f_4(\alpha, \mathrm{Re}_P) = B_4 + B_5\alpha + B_6\alpha^2 + B_7\mathrm{Re}_P,$$

$$= 0.912 + 0.00131\alpha - 5.7(10^{-5})\alpha^2 - 1.9(10^{-6})\mathrm{Re}_P,$$

$$f_5(\alpha) = B_8 + B_9\alpha + B_{10}\alpha^2 + B_{11}\alpha^4,$$

$$= -0.0065 - 6.3(10^{-4})\alpha - 1.57(10^{-4})\alpha^2 - 7.2(10^{-7})\alpha^4.$$

At each vertical position typically 36 sets of the three pressure differences, $P_4 - P_5$, $P_1 - P_2$, and $P_1 - P_T$*, were recorded. These data sets were processed by the microcomputer to provide mean and variance values. Using these results and the calibration functions, the pitch, the local dynamic pressure, the speed, the total pressure coefficient, and the static pressure coefficient were computed.

Uncertainty estimates for the region II flow were obtained by the Kline and McClintock method [14, 15, 16]. This method estimates the uncertainty in a result R, which is a function of k uncertain observations, x_i, $i = 1, 2, 3, \ldots k$, by:

$$w_R = \left[\sum_{i=1}^{k} \sum_{j=1}^{k} \left(r_{x_i x_j} w_{x_i} w_{x_j} \frac{\partial R}{\partial x_i} \frac{\partial R}{\partial x_j} \right) \right]^{1/2},$$

where the uncertainty estimates, w_R and w_{x_i} for all i, are at the same level of significance. A common situation is one in which the errors in the observations are independent. In this case, the estimated correlation coefficient, $r_{x_i x_j}$, is:

$$r_{x_i x_j} = \begin{cases} 0, & i \neq j \\ 1, & i = j \end{cases}$$

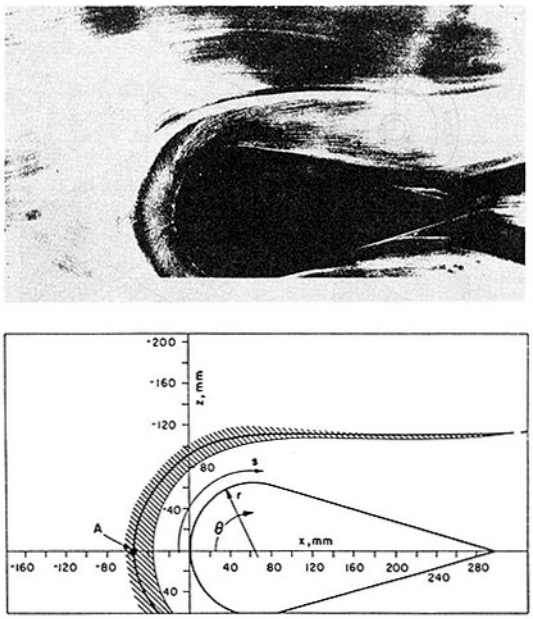

Fig. 3 Surface flow visualization on the flat floor of the wind tunnel

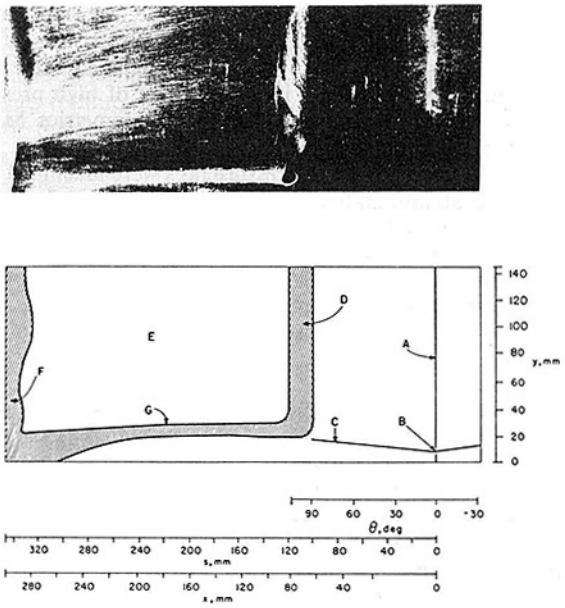

Fig. 4 Surface flow visualization on one side of the body

and the estimated uncertainty becomes:

$$w_R = \left\{ \sum_{i=1}^{k} \left[\left(w_{x_i} \frac{\partial R}{\partial x_i} \right)^2 \right] \right\}^{1/2}.$$

For this general case, $k/2(k+3)$ pieces of information are required to estimate the uncertainty in a result. The required information includes k sensitivities (partial derivatives) of the result to the various observations, k estimated uncertainties in the observations, and $k/2(k-1)$ estimated correlation coefficients. The k sensitivities can be evaluated explicitly using the data reduction equations or approximated with finite differences. Both approaches were used to obtain the reported results. The k estimated uncertainties in the observations were at the 5 percent significance level (95 percent confidence interval, 19 to 1 odds).

The estimated uncertainties in the calibration coefficients were obtained from the least squares analysis of the calibration data [9–12]. Only the correlations between the calibration coefficients were recognized. All other correlation coefficients were assumed to be zero.

Results and Discussion

The flow visualization for the floor of the total flow (regions I, II, III, and IV), and of the body surface (region II) are presented first. These are followed by the results for the fully three-dimensional junction vortex flow in region II, including: (1) the floor surface static pressure, (2) the body surface static pressure, (3) the velocity field, (4) the computed vorticity field, (5) the total pressure field, and (6) the static pressure field. Some of these results are shown in contour plots generated using the Surface II graphics package [17], incorporating some of the estimation and smoothing capabilities of this software.

Figure 3 is a view of the floor flow visualization, showing only the two quadrants over which the three-dimensional flow was measured. A schematic of the photograph emphasizes the major features of the floor surface flow. Point A, approximately 60 mm upstream of the leading edge, on the tunnel centerline, and difficult to locate precisely in the photographs, is a singular separation point where the streamwise flow in the plane of symmetry meets with the reversed flow in the junction vortex. Emanating from point A are two rays, one on each side of the centerline and just as difficult to precisely locate as point A, corresponding to the loci of ordinary separation points around the junction. This line of ordinary separation divides the floor into an interior region and an exterior region. Just downstream of point A and approximately 38 mm upstream of the leading edge, a distinct line crosses the tunnel centerline in a near circular arc. Other investigators [18–21] have reported that this distinct line corresponds to the projection of the vortex center line on the flat floor. Surface pressure measurements to be described indicate that this line corresponds to a relative minimum in the wall pressure distribution. During the flow visualization studies it was observed that the portion of the floor between this distinct line and the body dried much more rapidly than the floor in the exterior region. The inference to be made from this observation is that the highest wall shear stresses on the floor occur in the interior region near the leading edge of the body. The lowest wall shear stress on the floor should occur at the singular separation point. The accumulation of white titanium dioxide particles in the vicinity of the singular separation point is a result of the low wall shear stresses and pressure gradients in the area. These hypotheses about the wall shear stress distribution on the floor are supported by the direct-force wall shear measurements reported by McAllister, Pierce, and Tennant [20].

The developed surface corresponding to one vertical side of the bluff body is shown in Fig. 4. A schematic of this photograph emphasizes the major features of the body-surface flow visualization. Three horizontal scales are shown, one for the cylinder angle defined in Fig. 3, one for the distance along the developed surface also shown in Fig. 3, and one nonlinear scale showing the streamwise distance. The leading edge attachment line is shown coincident with the origins of theses axes. The total pressure gradient near the leading edge produces the downwash on the surface near the leading edge junction with the floor. This downwash meets with a small region of reversed flow at the singular separation point marked B. The ordinary separation line marked C divides the boundary layer-like flow on the leading edge from a small junction vortex deep in the corner. The area marked D, beginning at approximately 90 deg from the attachment line and extending for about 20 mm on the surface, is believed to be a laminar separation bubble. Early in the flow visualization process, a large amount of titanium dioxide-diesel fuel

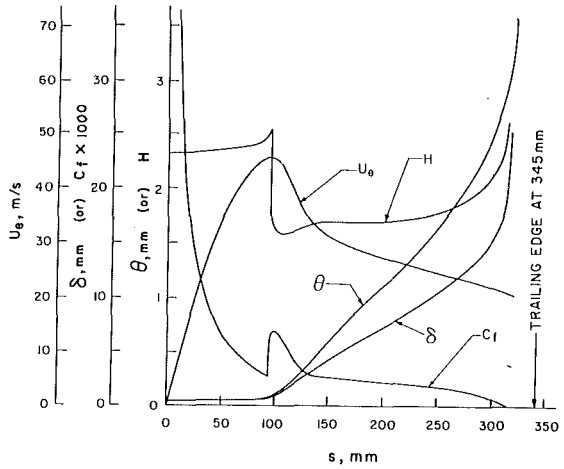

Fig. 5 Predicted two-dimensional boundary layer parameters

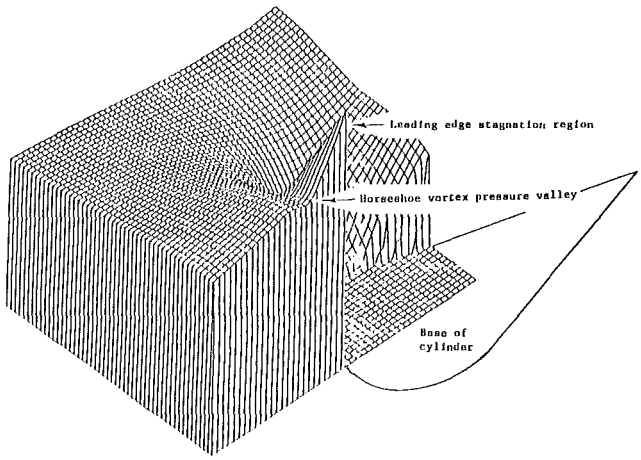

Fig. 6 Floor pressure coefficient topological map

paint accumulated in this region and slowly sank to the floor under its own weight. Near the floor, the excess mixture exited the bubble and streamed back along the straight side of the body in the region marked G. A turbulent boundary layer reattached to the body surface downstream of the bubble and appears to have flowed markedly downward on the surface. This turbulent boundary layer was not able to overcome the adverse pressure gradient on the rearward portion of the body and separated near the trailing edge leaving the stalled region marked F. Additional interpretations of these floor and body flow visualizations are made in Pierce and Harsh [23].

A two-dimensional boundary layer analysis was performed for the idealized boundary layer flow over the sides of the bluff body. The Pohlhausen-Holstein-Bohlen, laminar, one-parameter integral method [24] and Moses' turbulent, two-parameter integral method [25] were used to perform the analysis. The freestream edge condition for these calculations was the surface pressure distribution resulting from a two-dimensional potential flow solution for the bluff body geometry. The laminar calculation was started at the stagnation point. Transition was assumed to occur at 85 deg from the stagnation point. The calculation was continued from this point using the turbulent integral method. The initial conditions required by the turbulent integral calculation were obtained by equating the laminar momentum thickness to the turbulent momentum thickness at the point of transition and, somewhat arbitrarily, increasing the skin friction coefficient by a factor of two. This later assumption had little effect on the turbulent boundary layer calculations after a few millimeters downstream of the transition point. In fact, the skin friction coefficient was systematically varied from 95 percent to 300 percent of the laminar prediction at the transition point, and it was observed that the solutions converged to within 2 percent just 10 mm ($\approx$ 10 deg) downstream of the initial condition.

The predicted boundary layer parameters are shown in Fig. 5. The abscissa in this figure is distance measured along the surface of the body, as shown in Fig. 4. These results indicate separation of the thick turbulent boundary layer from the flat sides of the body 314 mm from the leading edge (90 percent chord), in general agreement with the results of the flow visualization study.

Measurements in Regions II and III represent the highest degree of refinement in the evolution of the data acquisition system in data reduction. For these data, there was no body repositioning. All data was acquired with the automated, microcomputer-controlled data acquisition system. Data reduction included a formal and rigorous statistical treatment, providing for statistically meaningful estimates in the uncertainty of reported quantities at the 5 percent significance level (95 percent confidence intervals or at 19 to 1 odds).

The pressure distributions on the flat floor near the leading edge and on the vertical side of the body are reported in terms of a pressure coefficient defined as:

$$C_P = \frac{P - P_{T^*}}{Q_*}.$$

where P_{T_*} is the total pressure and Q_* is the dynamic pressure, both at the throat of the tunnel inlet nozzle. While the reported pressure coefficients are referenced to the tunnel inlet nozzle, sufficient data is available in the tabulated results of reference [6] to allow the interested user to redefine these coefficients to better suit individual preferences.

The measured pressure distribution on the floor around the body is shown in Fig. 6 as a three-dimensional topographic figure. Two notable features of this figure are a result of the three-dimensional nature of the junction vortex. These three-dimensional effects are the relative maximum on the line of symmetry approximately 56 mm upstream of the stagnation point, and the locus of relative minima crossing the line of symmetry in a near circular arc approximately 40 mm upstream of the stagnation point. The local maximum in pressure near the separation point followed by the local minimum under the junction vortex on the plane of symmetry are clearly seen in the figure on the right. These extreme points coincide with the singular separation point and the distinct line bounding the relatively high wall shear stress area shown in Fig. 3. A lesser local minimum on the downstream side is also seen in this figure, and this also occurs under the junction vortex.

The pressure distribution on the surface body, plotted in s-y coordinates so that it corresponds to the developed surface, is shown in Fig. 7. The isobars shown are nearly one-dimensional over a large portion of the body surface. Near the point of maximum body thickness (90 deg from the stagnation line or 100 mm downstream of the stagnation line measured along the surface), the isobars are strongly two-dimensional in the body-floor junction region and indicate that the surface pressure increases in the negative y direction.

The five-hole probe yielded the three-dimensional velocity field, the total pressure field, and the static pressure field in the three planes as shown in Fig. 1. Due to space limitations only the results at the 100 percent chord transverse plane will be presented.

The three-dimensional velocity distributions are shown in Figs. 8 and 9. Figure 8 shows the y-z, or secondary component of the mean velocity vector.

A number of observations are worthy of recognition. These

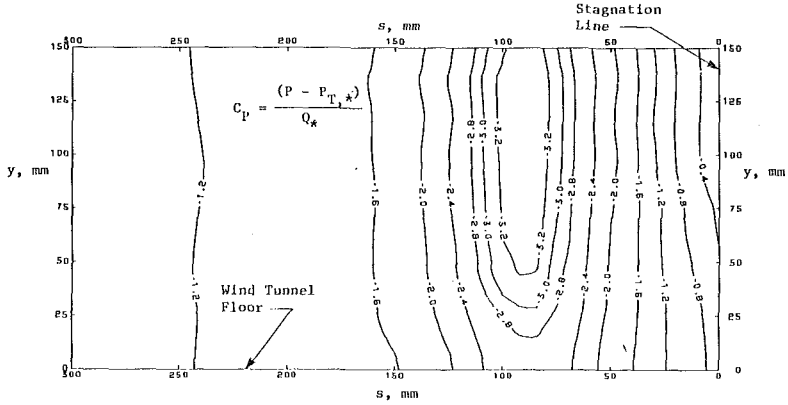

Fig. 7 Measured pressure distribution on the vertical side of the body. Typical uncertainty range is from ±0.005 to ±0.020.

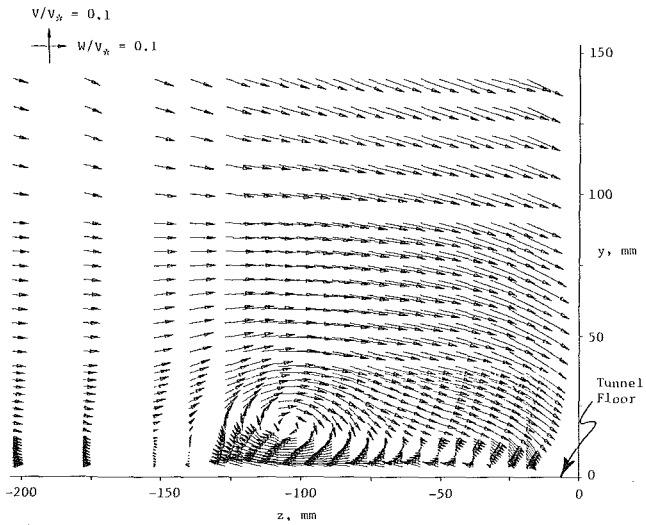

Fig. 8 Secondary velocity distribution at 100 percent cord. Typical uncertainty range is from ±0.001 to ±0.0007.

figures show only one vortex clearly. Other vortices may be present but were not resolved by the data grid. Figure 9 shows that the vortex consists of lower streamwise momentum fluid. The corner between the flat floor and the vertical side of the body is filled with relatively high streamwise momentum fluid, probably induced into the corner by the vortex motion. The negative y component of velocity near the side of the body in Fig. 8 is consistent with the flow visualization shown in Fig. 4 where is was noted that the surface flow on the side of the body was markedly downward.

An attempt was made to quantify the streamwise vorticity,

$$\Omega = \frac{\partial W}{\partial y} - \frac{\partial V}{\partial z},$$

apparent in Fig. 8 using finite difference approximations for the required partial derivatives with the experimental data. The average of forward and backward difference approximations was used, with approximations at the corners and sides of the data grid consisting of forward or backward differences only, as appropriate. The computed vorticity in s^{-1} at nominal laboratory conditions is shown in Fig. 10. At 43 percent chord, the mean streamwise vorticity at the center of the principal vortex is on the order of 120 s^{-1}. At 100 percent chord, the vortex has decreased in strength and increased in cross sectional area with vorticity in the core on the order of 45 s^{-1}. Figure 10 can be interpreted to suggest the existence of at least two additional smaller vortices, both closer to the floor and nearer to the body than the principal vortex. A small corner vortex can be envisioned at the body-floor junction, and a second small vortex may exist close to the floor and centered along $z \cong -45$ mm.

The total pressure distributions and the static pressure distributions in the transverse plane at 100 percent chord are shown in Figs. 11 and 12. These figures indicate that the vortex core consists of both low total pressure and low static pressure fluid. The total pressure distribution in Fig. 11 shows the total pressure defect resulting from the rapid boundary layer growth on the straight sides of the body. This defect appears near the centerline as a layer with a thickness in excess of 25 mm, in fair agreement with the idealized boundary layer analysis described earlier. The total pressure distribution shown in Fig. 11 also agrees with extensive Kiel probe data not reported here. Unlike a boundary layer flow, in the region of the large vortex Fig. 12 shows a considerable variation in the static pressure normal to the floor. This is also seen at the 43 percent chord position. These figures suggest the need to consider the three-dimensional static pressure variation in the vortex core flow.

In the regions away from the junction vortex, the static pressure measurements support the pressure variation model identified with a recurving or S-shaped freestream streamline. At the 43 percent chord position, with the freestream streamlines concave toward the body in an xz plane, there is a static pressure gradient away from the body. At the 100 percent chord position, when the freestream streamlines experience some recurvature in following the reduced body thickness, the static pressure gradient is toward the body, consistent with the freestream streamlines concave away from the body.

The velocity distribution, the total pressure distribution, and the static pressure distribution on the plane of symmetry are qualitatively similar to those at the two transverse planes. Only one relatively small and tightly wound vortex is apparent in the velocity vector diagram. Figure 13 presents a summary of several observations made from the different kinds of measurements on the plane of symmetry. The mean velocity measurements show the dominant vortex to extend from the floor to about the height of the surrounding boundary layer and up to about 47 mm upstream of the body leading edge. In this region, the mean velocity vectors show definite upward or downward components of velocity identified with the principle vortex structure. The mean velocity field also shows the vortex center to be about 40 mm ahead of the body leading edge and very close to the floor at about 8 mm above the floor. The vortex structure shows a high degree of asymmetry. From the velocity field on the symmetry plane in Fig. 13, the Maskell

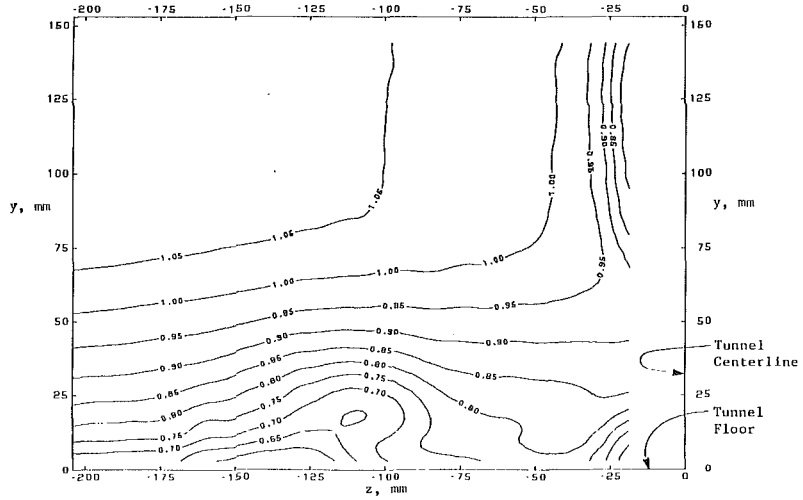

Fig. 9 Streamwise velocity distribution at 100 percent cord. Typical uncertainty is ±0.007.

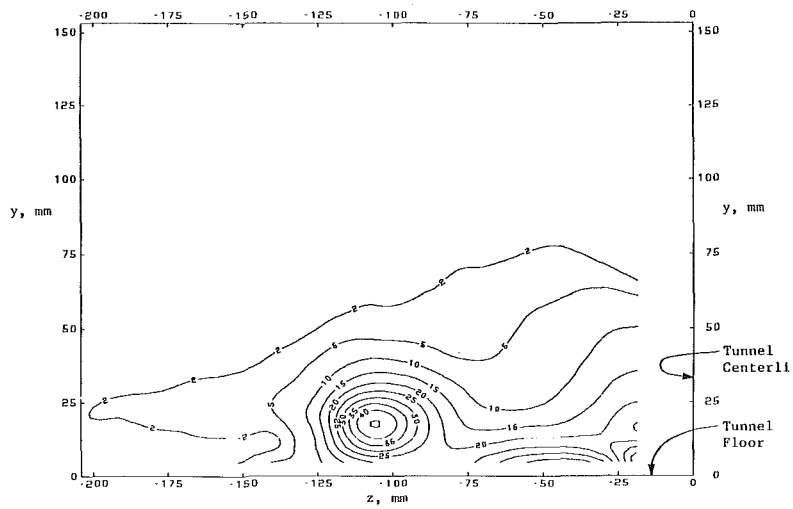

Fig. 10 Streamwise vorticity distribution at 100 percent cord

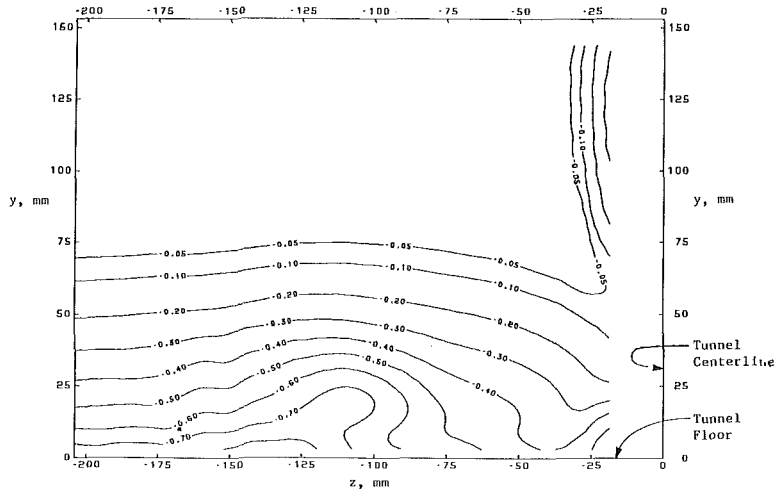

Fig. 11 Total pressure coefficient at 100 percent cord. Typical uncertainty is ±0.01.

model of this junction vortex flow would have a very tightly wound and short separation sheet. The floor flow visualizations show a singular separation point at about −60 mm and the clear line of the visualization is at about −38 mm. The floor pressure contours show a local maximum at about −56 mm, approximately coincident with the location of the singular separation point shown by the flow visualization. A local pressure minimum occurs at about −40 mm, and this is

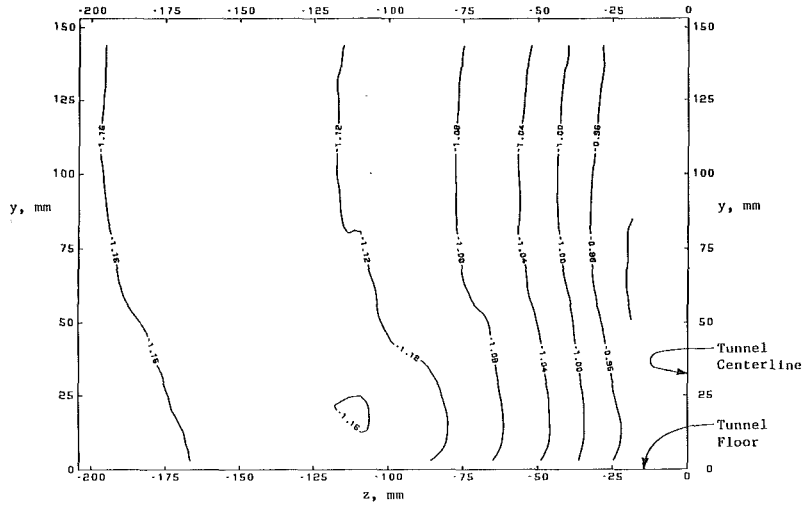

Fig. 12 Static pressure coefficient at 100 percent cord. Typical uncertainty is ±0.02.

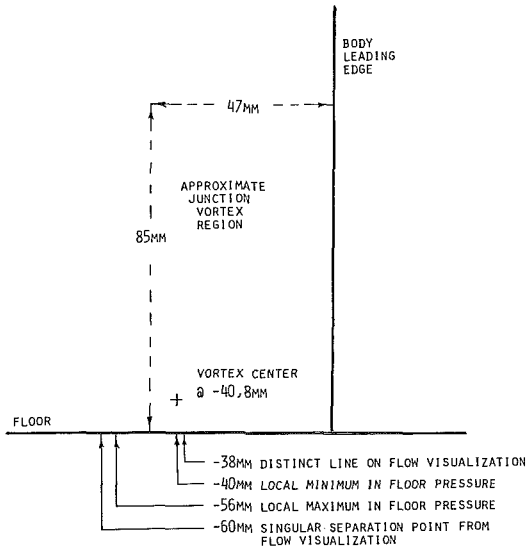

Fig. 13 Junction vortex flow details on the plane of symmetry as estimated from the different measurements

approximately coincident with the sharp line of the flow visualization and just below the estimated center of the vortex, as reported in Steinheuer [18], Belik [19], and Baker [20, 21]. The velocity field on the symmetry plane can be interpreted to indicate the singular separation point to be at about 50 mm ahead of the body leading edge. It should be noted, however, that no velocity measurements were obtained closer than 3.7 mm from the floor, and additionally, the velocity measurements in the high pitch region close to the separation point are typically outside the range of the calibration functions of the five-hole probe and hence with the largest uncertainties. Kiel probe profiles, not included here but which were as close as 0.8 mm to the floor, indicate the separation point to be at about 55 mm before the body leading edge and in closer agreement with the floor flow visualizations.

Summary

The mean flow structure within a turbulent junction or horseshoe vortex is reported for an incompressible, subsonic flow. The flow is generated by placing a streamlined cylinder normal to a flat surface in a relatively thick boundary layer, where the boundary layer thickness is of the order of the cylinder thickness or width.

The flow through separation and in the vortex has been documented with mean velocity field, static pressure field, and total pressure field using a very carefully calibrated five-hole probe. The measured velocity field was used to calculate the vorticity field. In addition, extensive floor static pressure measurements emphasizing the region of the vortex system, and static pressure measurements on the cylinder surface are also reported.

Flow visualizations on the floor and cylinder surface show unusual detail and agree well both qualitatively and quantitatively with the various flow field measurements.

The oil-film surface flow visualizations defined the extent of the three-dimensional separation and gave good indication of flow direction at the tunnel floor. The prominent features of the floor surface visualization include a singular separation point on the floor center-line about 58–60 mm upstream of the leading edge and a line of ordinary separation emanating from this point. The floor flow visualization process also gave some indication of high wall shear stresses deep in the corner between the obstacle and the flat floor. The body surface visualizations showed an additional separation point on the stagnation line near the intersection between the leading edge and the floor centerline.

Extensive surface pressure measurements also showed the extent of the junction vortex. On the floor centerline, a relative maximum pressure was observed at a position approximately corresponding to the singular separation point on the floor. This high pressure region was identified with the stagnating flow resulting from the streamwise flow meeting with the reversed flow at the singular separation point. Downstream of the singular separation point and about 40 mm upstream of the body leading edge, a relative minimum pressure was observed. This relative minimum was associated with the center of the vortex core. This pressure minimum is also approximately coincident with the sharp or distinct line on the floor flow visualization and also identifies as below the vortex center. The velocity field measurements above the floor suggest a vortex center at about $x = -40$ mm and $y = 8$ mm. It is noted that the velocity measurements in this region have the highest uncertainties.

The mean, three-dimensional flow field was surveyed with the five-hole probe in three planes. On the plane of symmetry, the mean flow results indicated that the three-dimensional separation and subsequent junction vortex were confined to a region very near the floor. The vortex in the plane of sym-

metry was, in fact, too close to the floor for accurate mean flow measurements in the region of reversed flow. One dominant vortex was observed in the other planes, downstream of the stagnation line. The computed vorticity field at the 100 percent chord position can be interpreted to show two smaller vortices, both closer to the floor and closer to the body than the horseshoe vortex which dominates the flow.

Acknowledgments

The results reported here are from a long-term, ongoing project. Initial support from the National Science Foundation provided for most of the physical facilities, some early instrumentation, and the initial work on the project. Subsequent support from the NASA-Ames Research Laboratory provided for additional instrumentation, the development of the automated data acquisition system, and the bulk of the results reported here. Support from the ONR General Hydromechanics Research Program Administrated by the David W. Taylor Naval Ship Research and Development Center provided for the completion of the documentation of the total flow, focusing on boundary conditions for the elliptic vortex Region II flow, and the documentation of the near wake of the downstream flow.

References

1 Menna, J. D., and Pierce, F. J., "The Mean Flow Structure Around and Within a Turbulent Junction or Horseshoe Vortex—Part I: The Upstream and Surrounding Three-Dimensional Boundary Layer," ASME JOURNAL OF FLUIDS ENGINEERING, Vol. 110, published in this issue, pp. 406–414.

2 Kline, S. J., Cantwell, B. J., and Lilley, G. M., *1980–1981 AFOSR-HTTM-Stanford Conference on Complex Turbulent Flows*, Vols. I, II, III, Stanford University, 1981.

3 Pierce, F. J., and Harsh, M. D., and Menna, J. D., "The Mean Flow Structure Around and With a Turbulent Junction or Horseshoe Vortex," Report VPI-E-85-19, Mechanical Engineering, Virginia Polytechnic Institute and State University, Blacksburg, Va., Sept, 1985, (available NTIS).

4 Menna, J. D., "A Three-Dimensional Turbulent Boundary Layer Upstream and Around a Junction Vortex Flow," Dissertation, Mechanical Engineering, Virginia Polytechnic Institute and State University, Blacksburg, Va., May 1984.

5 Harsh, M. D., "An Experimental Investigation of a Turbulent Junction Vortex," Dissertation, Mechanical Engineering, Virginia Polytechnic Institute and State University, Blacksburg, Va., Jan. 1985.

6 Harsh, M. D., and Pierce, F. J., "An Experimental Investigation of a Turbulent Junction Vortex," Rpt. VPI-E-85-4, NASA Grant NSG 2301, Mechanical Engineering, Virginia Polytechnic Institute and State University, Blacksburg, Va., Feb. 1985. (Available NTIS).

7 Squire, L. C., Maltby, R. L., Keating, R. F. A., and Stanbrook, A., "The Surface Oil Flow Technique," *Flow Visualization in Wind Tunnels Using Indicators*, NATO Agardograph No. 70, North Atlantic Treaty Organization Advisory Group for Aerospace Research and Development, Apr. 1962, pp. 1–74.

8 Herwig, N. L., "Design of a Data Acquisition System to Control and Monitor a Velocity Probe in a Fluid Flow Field," Thesis, Mechanical Engineering, Virgina Polytechnic Institute and State University, Blacksburg, Va., Dec. 1982.

9 Draper, N., and Smith, H., *Applied Regression Analysis*, 2nd edition, Wiley, New York, 1981.

10 Montgomery, D. C., and Peck, E. A., *Introduction to Linear Regression Analysis*, Wiley, New York, 1982.

11 Walpole, R. E., and Myers, R. E., *Probability and Statistics for Engineers and Scientists*, 2nd edition, Macmillan, New York, 1978.

12 Beck, J. V., and Arnold, K. J., *Parameter Estimation in Engineering and Science*, Wiley, New York, 1977.

13 Junkins, J. L., *An Introduction to Optimal Estimation of Dynamical Systems*, Sijthoff and Noordhoff, Alphen aan den Rijn, The Netherlands, 1978.

14 Kline, S. J., and McClintock, F. A., "Describing Uncertainties in Single-Sample Experiments," *Mechanical Engineering*, Jan. 1953, pp. 3–8.

15 Moffat, R. J., "Contributions to the Theory of Single-Sample Uncertainty Analysis," ASME JOURNAL OF FLUIDS ENGINEERING, Vol. 104, No. 2, June 1982, pp. 250–260.

16 Schenck, H., *Theories of Engineering Experimentation*, 3rd edition, McGraw-Hill, New York, 1979, pp. 53–79.

17 Sampson, R. J., *Surface II Graphics System*, Kansas Geological Survey, Lawrence, Kan., 1978.

18 Steinheuer, J., "Three-Dimensional Boundary Layers on Rotating Bodies and in Corners," *Recent Developments in Boundary Layer Research*, Part II, NATO Agardograph No. 97, North Atlantic Treaty Organization Advisory Group for Aerospace Research and Development, May 1965, pp. 567–612.

19 Belik, L., "The Secondary Flow About Circular Cylinders Mounted Normal to a Flat Plate," *Aeronautical Quarterly*, Vol. 26, Feb. 1973, pp. 47–54.

20 Baker, C. J., "The Laminar Horseshoe Vortex," *Journal of Fluid Mechanics*, Vol. 95, Part 2, Nov. 1979, pp. 347–368.

21 Baker, C. J., "The Turbulent Horseshoe Vortex," *Journal of Wind Engineering and Industrial Aerodynamics*, Vol. 6, No. 1–2, July 1980, pp. 9–23.

22 McAllister, J. E., Pierce, F. J., and Tennant, M. H., "Direct Force Wall Shear Measurements in a Pressure-Driven Three-Dimensional Turbulent Boundary Layer," ASME JOURNAL OF FLUIDS ENGINEERING, Vol. 104, June, 1982, pp. 150–155.

23 Pierce, F. J., and Harsh, M. D., "Three-Dimensional Turbulent Boundary Layer Separation at the Junction of the Streamlined Cylinder with a Flat Plate," *Proceedings of the Third International Symposium on Flow Visualization*, Sept. 1983, pp. 59–63.

24 Schlicting, H., *Boundary-Layer Theory*, 7th edition, McGraw-Hill, New York, 1979, pp. 206–214.

25 Moses, H. L., "A Strip-Integral Method for Predicting the Behavior of Turbulent Boundary Layers," *Computation of Turbulent Boundary Layers—1968 AFOSR-IFP-Stanford Conference*, Vol. I, Thermosciences Division, Department of Mechanical Engineering, Stanford University, Stanford, Calif., 1968, pp. 76–82.

Shuichiro Hirai
Research Associate.

Toshimi Takagi
Professor.

Department of Mechanical Engineering,
Faculty of Engineering,
Osaka Univ., Suita,
Osaka, 565, Japan

Masaharu Matsumoto
Engineer,
Sanyo Electric Company,
Tottori, 680, Japan

Predictions of the Laminarization Phenomena in an Axially Rotating Pipe Flow

Numerical predictions are compared with the experiments of swirling turbulent flows in a pipe where the swirl is driven by the pipe wall rotating around the pipe axis. The laminarization phenomena, that is, the deformation of the axial velocity profile into a shape similar to the laminar one and the decrease of the friction factor, caused by the pipe rotation can be predicted by the calculations applying the stress equation turbulence model. However, calculations applying two types of the k-ϵ two-equation models with and without the modification by the Richardson number, cannot predict the laminarization phenomena and the characteristic behaviors due to the swirl. The interpretations of the laminarization phenomena and the applicability of the turbulence models are presented.

1 Introduction

The turbulent swirling flows are often encountered in many furnaces and combustors as well as in rotating machinery. In these flow fields, the interaction between turbulence and the centrifugal force induced by the swirl has influence on the characteristics of the turbulent transfer of momentum, heat and mass. Numerous studies have been conducted to obtain a better understanding of these phenomena and to establish the prediction procedures for the swirling flows.

The experimental results on the turbulent swirling flows in stationary pipes by Wolf et al. [1] and Seno and Nagata [2] indicate that there are two distinct regions; the one is near the central axis where the tangential velocity component is that of the solid-body rotation and the other is at the outer region where the velocity component is that of the free-vortex.

The swirl at the region of the solid-body rotation near the central axis is supposed to have stabilizing effects, which suppress the turbulent exchange of momentum, heat and mass. The swirl in the axially rotating pipe flow has this stabilizing effect, in which the decrease of the wall friction, heat transfer rate and the deformation of the axial velocity profile into a shape similar to the laminar one were observed by White [3], Murakami et al. [4], Cannon and Kays [5], and Kikuyama et al. [6], [7]. And, the phenomena are concerned with the retardation of mixing and combustion in swirling flames in a tube as shown by Takagi et al. [8].

On the contrary, the swirl of the free-vortex results in destabilizing the flow and in enhancing the turbulent exchange. These phenomena seem to have concern with the Taylor vortices [9] and with the increase of the wall friction and the heat transfer rate in the swirling flow in the annulus with a rotating inner cylinder by Becker and Kaye [10] and Hirai et al. [11].

In this paper, however, attention is restricted to the turbulent flow stabilized by the swirl of the solid-body rotation. This kind of swirling flow excluding the free vortex region can be obtained in the pipe flow rotating around its axis.

Experimental studies have been made of the effects of the swirl driven by the rotating pipe wall on the turbulent flow characteristics. The decrease of the wall friction due to the swirl was pointed out [3]–[7] and the axial velocity components tend to deform into laminar-like velocity profiles with the increase of the swirl strength [4]–[7]. These experimental results indicate the laminarization phenomena of turbulent flow due to the swirl.

As for the predictions of the turbulent swirling flows, Bradshaw [12] proposed several Richardson numbers to take account of the effects of the curvature or the rotation. Koosinlin, Launder, and Sharma [13] applied the mixing length model modified by the Richardson number to predict successfully the flows over spinning cones, discs and cylinders. Launder, Priddin and Sharma [14] introduced the effects of the curvature or the rotation into the k-ϵ two equation turbulence model in terms of the Richardson number. They applied the model successfully to the boundary layer flows developing over curved and spinning surfaces. Kikuyama [7] applied the mixing length model modified by the Richardson number to predict the laminarization phenomena of the swirling flow in an axially rotating pipe. But, the Richardson number was calculated by the measured tangential velocity.

The swirling turbulent flow produced in a rotating pipe is one of the fundamental flows to investigate the applicability of the turbulent model to the swirling flows because (1) the flow configuration is relatively simple due to the absence of any free vortex region, (2) the fully developed swirling flow is obtained, and (3) the phenomena peculiar to the swirling flow such as the flow laminarization are remarkable.

In the present study, numerical computations were made applying three kinds of turbulence models, i.e., k-ϵ two equa-

Contributed by the Fluids Engineering Division for publication in the JOURNAL OF FLUIDS ENGINEERING. Manuscript received by the Fluids Engineering Division November 21, 1986.

tion model with [14] and without [15] modification by the Richardson number, and stress equation model [16]. The computations were compared with the experiments [17] on the swirling flow drived by a rotating pipe wall to examine the applicability of the turbulence models to the swirling flow, putting the check points on the laminarization phenomena and the axial and tangential velocity profiles. The causes of the laminarizations due to the swirl were also discussed.

2 Analysis

A. Basic Equations. The analysis is based on the time-averaged conservation equations of mass and momentum in an axisymmetric cylindrical coordinate system, with and without swirl. There is no recirculating zone due to the swirl and the boundary layer approximation is applied. The basic equations are

$$\frac{\partial}{\partial x}(r\rho U)+\frac{\partial}{\partial r}(r\rho V)=0 \tag{1}$$

$$\rho\left(U\frac{\partial U}{\partial x}+V\frac{\partial U}{\partial r}\right)=-\frac{\partial p}{\partial x}-\frac{1}{r}\frac{\partial}{\partial r}(r\rho\overline{uv})+\frac{1}{r}\frac{\partial}{\partial r}\left(r\mu_l\frac{\partial U}{\partial r}\right) \tag{2}$$

$$\rho\left(U\frac{\partial W}{\partial x}+V\frac{\partial W}{\partial r}+\frac{VW}{r}\right)=-\frac{1}{r^2}\frac{\partial}{\partial r}(r^2\rho\overline{vw})+\frac{1}{r^2}\frac{\partial}{\partial r}\left\{\mu_l r^3\frac{\partial}{\partial r}\left(\frac{W}{r}\right)\right\} \tag{3}$$

$$\frac{\partial p}{\partial r}=-\frac{\partial}{\partial r}\rho\overline{v^2}+\frac{\rho}{r}(W^2+\overline{w^2}-\overline{v^2}) \tag{4}$$

where x, r, θ are the coordinates in the axial, radial and tangential directions, respectively. U, V, W and u, v, w are the time-mean and fluctuating velocity components in the three directions, respectively. ρ is the fluid density, μ_l the laminar viscosity and p the pressure. ρ and μ_l are assumed to be constant. $(\overline{\ })$ denotes the time average. The correlations of velocity fluctuations (the Reynolds stresses) in equation (2), (3), and (4) are evaluated from the turbulence models.

B. The Turbulence Models. The turbulence modes applied to the present calculations in order to estimate the Reynolds stresses are the conventional k-ϵ two equation model [15], the k-ϵ model modified by the Richardson number [14] and the stress equation model [16].

In the conventional k-ϵ two equation model, kinetic energy of turbulence k and its dissipation rate ϵ are calculated from the following transport equations [15].

$$\rho\left(U\frac{\partial k}{\partial x}+V\frac{\partial k}{\partial r}\right)=\frac{1}{r}\frac{\partial}{\partial r}\left(r\frac{\mu_{\text{eff}}}{\sigma_k}\frac{\partial k}{\partial r}\right)+\mu_t\left[\left\{r\frac{\partial}{\partial r}\left(\frac{W}{r}\right)\right\}^2+\left(\frac{\partial U}{\partial r}\right)^2\right]-\rho\epsilon \tag{5}$$

$$\rho\left(U\frac{\partial \epsilon}{\partial x}+V\frac{\partial \epsilon}{\partial r}\right)=\frac{1}{r}\frac{\partial}{\partial r}\left(r\frac{\mu_{\text{eff}}}{\sigma_\epsilon}\frac{\partial \epsilon}{\partial r}\right)+\frac{\epsilon}{k}\left[C_1'\mu_t\left\{\left(r\frac{\partial}{\partial r}\left(\frac{W}{r}\right)\right)^2+\left(\frac{\partial U}{\partial r}\right)^2\right\}-C_2'\rho\epsilon\right] \tag{6}$$

The turbulent viscosity μ_t is determined from the relation, assuming an isotropic eddy viscosity

$$\mu_t=C_D\rho k^2/\epsilon \tag{7}$$

The empirical constants in equations (5)–(7) are adopted from Jones and Launder [15], Launder and Spalding [17], and Takagi and Koto [18] and are listed as follows. $C_D=0.09$, $C_1'=1.45$, $C_2'=1.95$, $\sigma_k=1.0$, $\sigma_\epsilon=1.3$. The Reynolds shear stress terms $\rho\overline{uv}$ and $\rho\overline{vw}$ in equation (2) and (3) are modelled by the turbulent viscosity and the velocity gradient as

$$-\rho\overline{uv}=\mu_t\left(\frac{\partial U}{\partial r}\right) \tag{8}$$

$$-\rho\overline{vw}=\mu_t r\frac{\partial}{\partial r}\left(\frac{W}{r}\right) \tag{9}$$

In equation (4), $\overline{w}^2-\overline{v}^2$ is neglected with respect to W^2.

Launder et al. [14] have proposed a modification of the k-ϵ two equations model, correcting the source term in the dissipation rate equation by the Richardson number (R). The modified transport equation of dissipation rate ϵ is

Nomenclature

C_1', C_2', C_D = constants in k-ϵ turbulence model
$C_1, C_2, C_s, C_{\epsilon 1}, C_{\epsilon 2}, C_\epsilon$ = constants in stress equation turbulence model
d = internal diameter of pipe
D = diffusion terms in stress equation model
k = turbulent kinetic energy $=\frac{1}{2}(\overline{u^2}+\overline{v^2}+\overline{w^2})$
N = dimensionless parameter of swirl strength $= W_0/U_0$
p = time-mean pressure
P_i = production terms in stress equation model
R_i = redistribution terms in stress equation model
R = Richardson number
U_0 = mean axial velocity
U, V, W = time-mean velocity components in x, r, θ directions
U^+ = nondimensional velocity $= U/U^*$
U^* = friction velocity
u, v, w = fluctuating components in x, r, θ directions
W_0 = tangential velocity of pipe wall
x, r = coordinates
y^+ = nondimensional wall distance
α, β, γ = constants in stress equations turbulence model
ϵ = dissipation rate of k
μ_l = laminar viscosity
μ_t = turbulent viscosity
μ_{eff} = turbulent effective viscosity $=\mu_l+\mu_t$
ν_l = kinematic viscosity
ρ = density
$\sigma_{k,\epsilon}$ = diffusion constants in k, ϵ equations
τ_w = wall shear stress

Subscripts

l = laminar
t = turbulent
w = wall

Overbars

$\overline{\ }$ = time averaging

$$\rho\left(U\frac{\partial\epsilon}{\partial x}+V\frac{\partial\epsilon}{\partial r}\right)=\frac{1}{r}\frac{\partial}{\partial r}\left(r\frac{\mu_{\text{eff}}}{\sigma_\epsilon}\frac{\partial\epsilon}{\partial r}\right)$$
$$+\frac{\epsilon}{k}\left[C_1'\mu_t\left\{\left(r\frac{\partial}{\partial r}\left(\frac{W}{r}\right)\right)^2+\left(\frac{\partial U}{\partial r}\right)^2\right\}-C_2'(1-\beta R)\rho\epsilon\right] \tag{10}$$

where

$$R=\frac{k^2}{\epsilon^2}\frac{W}{r^2}\frac{\partial}{\partial r}(rW) \tag{11}$$

and the value of coefficient $\beta=0.005$ is adopted in the present calculations. A positive gradient of the angular momentum rW tends to produce a positive Richardson number, which increases the dissipation rate ϵ and decreases the turbulent viscosity. In the present swirling flow field, where the swirl is drived by the pipe wall rotating around the axis, the tangential velocity component has a stabilizing effect on the flow.

The stress equation model solves the transport equations of correlations of the velocity fluctuations in order to evaluate the Reynolds stresses in equations (2)–(4). The stress equation model adopted for the present study is that proposed by Launder, Reece and Rodi [16] (LRR). But for the diffusive transport term (the triple velocity correlation), the present work applies the simple form approximated by Daly and Harlow [19]. The stress equation model to evaluate six correlations of the velocity fluctuations ($\overline{u^2}$, $\overline{v^2}$, $\overline{w^2}$, $\overline{uv}$, $\overline{uw}$, $\overline{vw}$) and the dissipation rate ϵ is described as below in the axisymmetric cylindrical coordinate system, applying the boundary layer approximation.

$$U\frac{\partial\overline{u^2}}{\partial x}+V\frac{\partial\overline{u^2}}{\partial r}=-2\overline{uv}\frac{\partial U}{\partial r}$$
$$-C_1\frac{\epsilon}{k}\left(\overline{u^2}-\frac{2}{3}k\right)+2\alpha\overline{uv}\frac{\partial U}{\partial r}$$
$$+\frac{2}{3}(\alpha+\beta)P+\frac{C_s}{r}\frac{\partial}{\partial r}\left(\frac{rk\overline{v^2}}{\epsilon}\frac{\partial\overline{u^2}}{\partial r}\right)-\frac{2}{3}\epsilon \tag{20}$$

$$U\frac{\partial\overline{v^2}}{\partial x}+V\frac{\partial\overline{v^2}}{\partial r}-2\overline{vw}\frac{W}{r}=2\overline{vw}\frac{W}{r}$$
$$-C_1\frac{\epsilon}{k}\left(\overline{v^2}-\frac{2}{3}k\right)-2\alpha\overline{vw}\frac{W}{r}$$
$$+2\beta\left(\overline{vw}\frac{\partial W}{\partial r}+\overline{uv}\frac{\partial U}{\partial r}\right)+\frac{2}{3}(\alpha+\beta)P$$
$$+\frac{C_s}{r}\frac{\partial}{\partial r}\left\{\frac{rk}{\epsilon}\left(\overline{v^2}\frac{\partial\overline{v^2}}{\partial r}-2\frac{\overline{vw^2}}{r}\right)\right\}$$
$$-2\frac{C_s}{r}\frac{k}{\epsilon}\left\{\overline{vw}\frac{\partial\overline{vw}}{\partial r}+\frac{\overline{w^2v^2}-\overline{w^2})}{r}\right\}-\frac{2}{3}\epsilon \tag{21}$$

$$U\frac{\partial\overline{w^2}}{\partial x}+V\frac{\partial\overline{w^2}}{\partial r}+2\overline{vw}\frac{W}{r}=-2\overline{vw}\frac{\partial W}{\partial r}$$
$$-C_1\frac{\epsilon}{k}\left(\overline{w^2}-\frac{2}{3}k\right)+2\alpha\overline{vw}\frac{\partial W}{\partial r}$$
$$-2\beta\overline{vw}\frac{W}{r}+\frac{2}{3}(\alpha+\beta)P$$
$$+\frac{C_s}{r}\frac{\partial}{\partial r}\left\{\frac{rk}{\epsilon}\left(\overline{v^2}\frac{\partial\overline{w^2}}{\partial r}+2\frac{\overline{vw^2}}{r}\right)\right\}$$
$$+2\frac{C_sk}{r\epsilon}\left\{\overline{vw}\frac{\partial\overline{vw}}{\partial r}+\frac{\overline{w^2}(\overline{v^2}-\overline{w^2})}{r}\right\}-\frac{2}{3}\epsilon \tag{22}$$

$$U\frac{\partial\overline{uv}}{\partial x}+V\frac{\partial\overline{uv}}{\partial r}-\overline{uw}\frac{W}{r}$$
$$=-\overline{v^2}\frac{\partial U}{\partial r}+\overline{uw}\frac{W}{r}-C_1\frac{\epsilon}{k}\overline{uv}$$
$$+\alpha\left(\overline{v^2}\frac{\partial U}{\partial r}-\overline{uw}\frac{W}{r}\right)$$
$$+\beta\left(\overline{u^2}\frac{\partial U}{\partial r}+\overline{uw}\frac{\partial W}{\partial r}\right)-\gamma k\frac{\partial U}{\partial r}$$
$$+\frac{C_s}{r}\frac{\partial}{\partial r}\left\{\frac{rk}{\epsilon}\left(\overline{v^2}\frac{\partial\overline{uv}}{\partial r}\right.\right.$$
$$\left.\left.-\frac{\overline{vw}\,\overline{uw}}{r}\right)\right\}-\frac{C_sk}{r\epsilon}\left(\overline{vw}\frac{\partial\overline{uw}}{\partial r}+\overline{w^2}\frac{\overline{uv}}{r}\right) \tag{23}$$

$$U\frac{\partial\overline{uw}}{\partial x}+V\frac{\partial\overline{uw}}{\partial r}+\overline{uv}\frac{W}{r}=-\left(\overline{uv}\frac{\partial W}{\partial r}+\overline{vw}\frac{\partial U}{\partial r}\right)-C_1\frac{\epsilon}{k}\overline{uw}$$
$$+\alpha\left(\overline{uv}\frac{\partial W}{\partial r}+\overline{vw}\frac{\partial U}{\partial r}\right)-\beta\overline{uv}\frac{W}{r}$$
$$+\frac{C_s}{r}\frac{\partial}{\partial r}\left\{\frac{rk}{\epsilon}\left(\overline{v^2}\frac{\partial\overline{uw}}{\partial r}+\frac{\overline{vw}\,\overline{uv}}{r}\right)\right\}$$
$$+\frac{C_s}{r}\frac{k}{\epsilon}\left\{\overline{vw}\frac{\partial\overline{uv}}{\partial r}-\overline{w^2}\frac{\overline{uw}}{r}\right\} \tag{24}$$

$$U\frac{\partial\overline{vw}}{\partial x}+V\frac{\partial\overline{vw}}{\partial r}+(\overline{v^2}-\overline{w^2})\frac{W}{r}$$
$$=-\left(\overline{v^2}\frac{\partial W}{\partial r}-\overline{w^2}\frac{W}{r}\right)-C_1\frac{\epsilon}{k}\overline{vw}$$
$$+\alpha\left(\overline{v^2}\frac{\partial W}{\partial r}-\overline{w^2}\frac{W}{r}\right)-\beta\left(\overline{v^2}\frac{W}{r}-\overline{uw}\frac{\partial U}{\partial r}-\overline{w^2}\frac{\partial W}{\partial r}\right)$$
$$-\gamma k\left(\frac{\partial W}{\partial r}-\frac{W}{r}\right)+\frac{C_s}{r}\frac{\partial}{\partial r}\left\{\frac{rk}{\epsilon}\left(\overline{v^2}\frac{\partial\overline{vw}}{\partial r}\right.\right.$$
$$\left.\left.+\overline{vw}\frac{(\overline{v^2}-\overline{w^2})}{r}\right)\right\}$$
$$+\frac{C_sk}{r\epsilon}\left\{\overline{vw}\frac{\partial}{\partial r}(\overline{v^2}-\overline{w^2})-4\overline{w^2}\frac{\overline{vw}}{r}\right\} \tag{25}$$

$$U\frac{\partial\epsilon}{\partial x}+V\frac{\partial\epsilon}{\partial r}=C_{\epsilon1}\frac{\epsilon P}{k}-C_{\epsilon2}\frac{\epsilon^2}{k}+\frac{C_\epsilon}{r}\frac{\partial}{\partial r}\left(\frac{rk\overline{v^2}}{\epsilon}\frac{\partial\epsilon}{\partial r}\right) \tag{26}$$

where

$$P=-\overline{uv}\frac{\partial U}{\partial r}-\overline{vw}r\frac{\partial}{\partial r}\left(\frac{W}{r}\right)$$

Six empirical constants in the transport equations (20)–(26) are adopted from Launder et al. [16], Hanjalic and Launder [20] and Morse [21] and are listed as follows.

$$C_1=1.5,\ C_2=0.4,\ C_s=0.22,\ C_{\epsilon1}=1.45,\ C_{\epsilon2}=1.90,\ C_\epsilon=0.15$$

C. The Boundary Conditions and the Calculation Procedure. The boundary conditions are needed on the axis, near the wall region and at the inlet region for the calculations applying the conventional k-ϵ two equation model, the modified k-ϵ model and the stress equation model.

At the near wall boundaries, the boundary conditions are determined for the grid points in a turbulent region one mesh inside the wall. Near the wall region, the nondimensional velocity U^+ $(=U/U^*)$ and the nondimensional distance from

the wall y^+ ($=U^*y/\nu_l$) are supposed to obey a universal relation $U^+ = f(y^+)$ in a fully developed turbulent flow. Here, U^* denotes the friction velocity ($=(\tau_w/\rho)^{0.5}$), τ_w the wall shear stress, y the distance from the wall. The Karman's universal velocity distribution [22] is applied for the relations, $U^+ = f(y^+)$. In the swirling flows, the composed velocity of the axial velocity component U and the tangential velocity component W is used instead of U and in this case, τ_w becomes a composed wall shear stress. From these relations, the boundary conditions of U and W near the wall region are evaluated and the wall shear stress is calculated simultaneously. In the calculations applying the conventional k-ϵ two equation model and the modified k-ϵ model, the boundary condition for the turbulent kinetic energy near the wall region is evaluated from the relation $k = \tau_w/(\rho C_D{}^{0.5})$, which is obtained from the assumption that the production term and the dissipation term are in the local equilibrium near the wall region. The boundary condition for the dissipation rate ϵ near the wall region is obtained from the assumption of the local equilibrium of equation (5) and from the boundary condition for k. In the calculation applying the stress equation model, the boundary conditions for the turbulent kinetic energy k and for the velocity fluctuations correlations $\overline{u^2}$, $\overline{v^2}$, $\overline{w^2}$ and $\overline{uw}$ near the wall region are evaluated from the equations (23), (20), (21), (22), (24) respectively, with the approximation of $\partial/\partial x << \partial/\partial r$, $V \fallingdotseq 0$, $\overline{vw} \fallingdotseq 0$ (the reason is described in Section 3.B) in a fully developed turbulent boundary layer and of neglecting the diffusive transport. The boundary condition for the dissipation rate ϵ near the wall region is evaluated from the assumption that it is in equilibrium with the production term in the transport equation of k. The boundary conditions for the velocity fluctuations correlations $\overline{uv}$ and $\overline{vw}$ near the wall region are evaluated from the wall shear stress of the axial direction component $(\tau_{xr})_w$ and of the tangential direction component $(\tau_{r\theta})_w$, respectively, which are the components of the composed wall shear stress τ_w. As for the boundary conditions on the axis, the gradients of U, k, ϵ, $\overline{u^2}$, $\overline{v^2}$, $\overline{w^2}$ in the radial direction are zero. In addition, to ensure the equality of $\overline{v^2}$ and $\overline{w^2}$ on the axis because of the rotational symmetry, $\overline{u^2}$, k ($=(\overline{u^2}+\overline{v^2}+\overline{w^2})/2.0$) and $(\overline{w^2}-\overline{v^2})$ are solved as the dependent variables instead of solving equations (20), (21), (22) of $\overline{u^2}$, $\overline{v^2}$ and $\overline{w^2}$ directly. Then, $\overline{w^2}-\overline{v^2}$ and the gradients of k, $\overline{u^2}$ are zero on the axis. W, uv, vw, uw are also zero on the axis.

The inlet profile of the dependent variables are determined referring to a fully developed turbulent pipe flow profile. For the swirl flow rotating around the tube axis, the tangential velocity W at the inlet section is set to zero, except on the tube wall.

The above differential equations are solved numerically using a finite difference method based on the procedure developed by Patanker and Spalding [23]. 30 grid points are located in the radial direction at nonuniform intervals.

3 Discussions of Numerical Predictions

A. Nonswirling Turbulent Pipe Flows. Prior to the predictions applying the stress equation model to a turbulent swirling flow, calculations are compared with Laufer's experiment [24], which is a nonswirling turbulent pipe flow. Laufer measured the radial profiles of $\overline{u^2}$, $\overline{v^2}$, $\overline{w^2}$, and $\overline{uv}$ at a fully developed region. The internal diameter of the pipe was 247 mm and the Reynolds number was 500,000. In Fig. 1, points are the Laufer's experimental results and solid lines are the calculations applying the stress equation model. The predictions estimate $\overline{u^2}$, $\overline{v^2}$, and $\overline{w^2}$ to be a little larger near the axis. However, the experimental results were predicted fairly well on the whole. It is also ascertained that the radial profile of the time-mean axial velocity U is well predicted. The prediction of $\overline{v^2}$ have a tendency to increase near the wall, where the experimental value tends to decrease. This decrepancy is caused by the boundary condition of $\overline{v^2}$ near the wall region. In the present calculations, $\overline{v^2}$ near the wall is estimated by the relation $\overline{v^2}/k = (-30C_2+2)/33C_1+2/3 = 0.465$ which gives a littel larger value than that of the Laufer's experimental result. It is confirmed that the calculation, applying the boundary conditions near the wall region being adjusted to the Laufer's experiment, can predict the experimental tendency that $\overline{v^2}$ decreases near the wall. Altering the boundary conditions of $\overline{v^2}$ as mentioned above does not make significant change for the profiles of the Reynolds shear stress and the time-mean axial velocity.

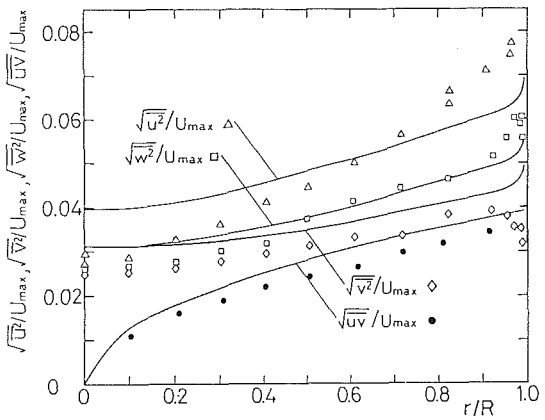

Fig. 1 Radial profile of the correlations of velocity fluctuations in a developed nonswirling pipe flow. Plots: Laufer's experimental results, Solid lines: Calculations applying stress equation model.

B. Turbulent Flows in an Axially Rotating Pipe. Kikuyama [7] introduced a fully developed turbulent flow into a pipe rotating around its axis and studied the effects of the pipe rotation on the time-mean axial and tangential velocities and on the friction factors at the fully developed region. This flow field gives fully developed swirling flow which can not be obtained in a stationary pipe. In addition, the swirling flow obtained in the rotating pipe is simple because the tangential velocity component increases monotonously from the axis to the wall, where the swirl is supposed to have only the effects of stabilizing the turbulence.

According to the experimental results, pipe rotation deforms the fully developed turbulent profile of the axial velocity U into a laminar-like velocity profile and decreases the friction factor. These phenomena are so called "the laminarization phenomena." The calculations applying the conventional k-ϵ two equation model [15], the k-ϵ model modified by the Richardson number [14] and the stress equation model [16] are performed to investigate which model is applicable to predict the characteristics of the swirling flow and to get the interpretations of the phenomena.

In Fig. 2, the experimental and the predicted radial profiles of the axial velocity U are compared, varying the strength of the swirl. Points in Fig. 2(a) are the Kikuyama's experimental results [7], where the Reynolds number, defined as $U_0 d/\nu_l$, is 10^4. U_0 denotes the mean axial velocity and d the internal diameter of the pipe. The solid lines in Fig. 2(a), (b) and (c) are the predictions applying the stress equation model [16], the conventional k-ϵ two equation model [15] and the k-ϵ model modified by the Richardson number [14], respectively. r is the distance from the axis. The internal radius of the rotating pipe R is 10 mm. N is a parameter, which represents the strength of the swirl, defined as $N = W_0/U_0$, where W_0 is the tangential velocity of the pipe wall.

Increasing the swirl strength, the experimental values of the axial velocities U near the centerline are increased and the axial velocity profile deforms into a laminar-like flow profile.

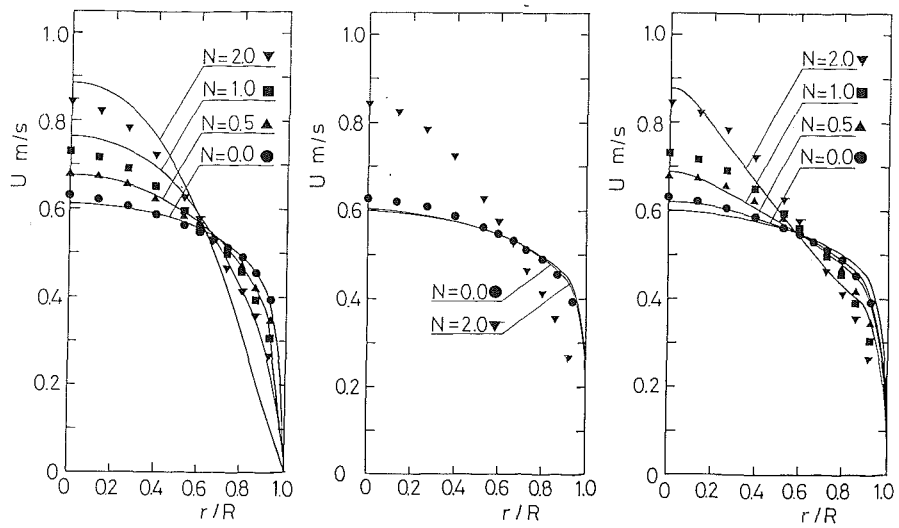

Fig. 2(a) Stress equations model Fig. 2(b) Conventional k-ε model Fig. 2(c) k-ε model with modification

Fig. 2 Axial velocity profile at an axially rotating pipe flow. Plots: Kikuyama's experimental results. Solid lines: Calculations applying (a) stress equation model; (b) conventional k-ε two equation model; (c) k-ε model modified by the Richardson number.

Table 1 Comparison of experimented and calculated wall friction factor at an axially rotating pipe flow. Kikuyama's experimental results and calculations applying the stress equation model.

N	Experiment	Calculation
0.0	0.032	0.031
0.5	0.026	0.027
1.0	0.020	0.020
2.0	0.014	0.017

The calculations applying the conventional k-ϵ two equation model (Fig. 2(b)) can not predict the tendency of the experimental results, where the axial velocity profile show a nearly similar profile between the flow with strong swirl ($N=2.0$) and the flow without swirl $N=0.0$). This is caused by the fact that the predicted tangential velocity profile becomes solid rotational profile ($W \propto r$), and so the terms containing the swirl effect in the transport equations of k and ϵ become negligibly small. Then, the turbulent viscosity μ_t, evaluated from k and ϵ, is not affected by the swirl.

In the calculations applying the k-ϵ model modified by the Richardson number [14] (Fig. 2(c)), the axial velocity U increases near the centerline, with increase of swirl strength. The predicted radial profile of U, however, becomes rectilinear when the swirl is strong ($N=2.0$) and can not predict the experimental results of the curvilinear laminar-like velocity profile.

The calculation applying the stress equation model [16] (Fig. 2(a)) can predict the tendency of the measured axial velocity profile which becomes closer to the laminar-like velocity profile for higher strength of the swirl.

The friction factors obtained by the experiments are compared with those of the calculations applying the stress equation model [16] in Table 1. The calculation can predict the experimental tendency, that is, the friction factor decreases with increase of the strength of the swirl.

The phenomena that the axial velocity U gets closer to the laminar-like velocity profile and the friction factor decreases with increase of the strength of the swirl are supposed to be

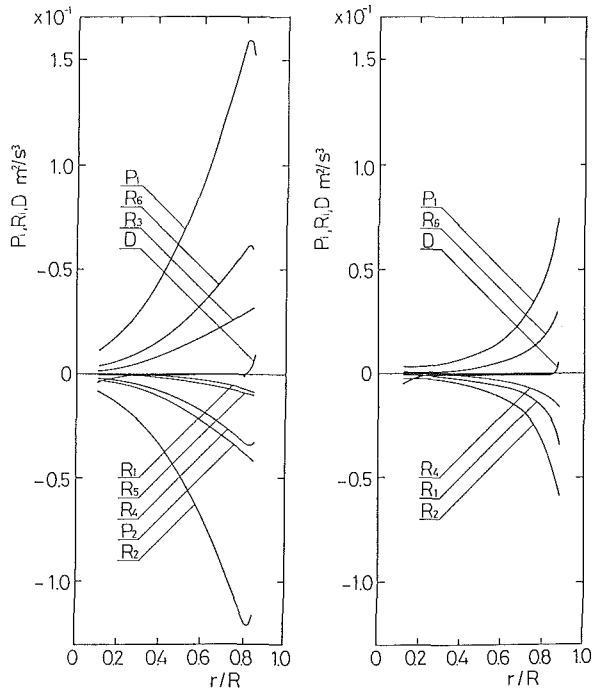

Fig. 3(a) Swirling flow ($N=1.0$) Fig. 3(b) Nonswirling flow ($N=0.0$)

Fig. 3 Calculated radial profile of the magnitude of the terms P_i, R_i, and D in transport equations of $\overline{uv}$ applying stress equations model at an axially rotating pipe flow. P_1: $-\overline{v^2}\partial U/\partial r$, P_2: $\overline{uw}W/r$, R_1: $-C\epsilon\overline{uv}/R_2$: $\alpha\overline{v^2}\partial U/\partial r$, R_3: $-\alpha\overline{uw}W/r$, R_4: $\beta\overline{u^2}\partial U/\partial r$, R_5: $\beta\overline{uw}\partial W/\partial r$, R_6: $-\gamma k\partial U/\partial r$, D: $C_s/r\cdot\partial/\partial r\ \{r(k/\epsilon)(\overline{v^2}\partial\overline{uv}/\partial r-\overline{vw}\cdot\overline{uw}/r)\}-C_s\ (k/r\epsilon)\ (\overline{vw}/\partial\overline{uw}/\partial r+\overline{w^2}\overline{uv}/r)$

caused by the suppression of the turbulent momentum exchange $\rho\overline{uv}$ due to the swirl. The causes for these phenomena can be investigated by the magnitude of the terms in the transport equation (23) of $\overline{uv}$. *The radial profile of the* magnitude of the terms in equation (23) are indicated in Fig. 3(a) and (b) for the flow with the swirl ($N=1.0$) and without swirl ($N=0.0$), respectively. The conditions of the Fig. 3(a) and (b) correspond to those of $N=1.0$ and 0.0 in Fig. 2(a) for the calculation by the stress equations model. The marks in

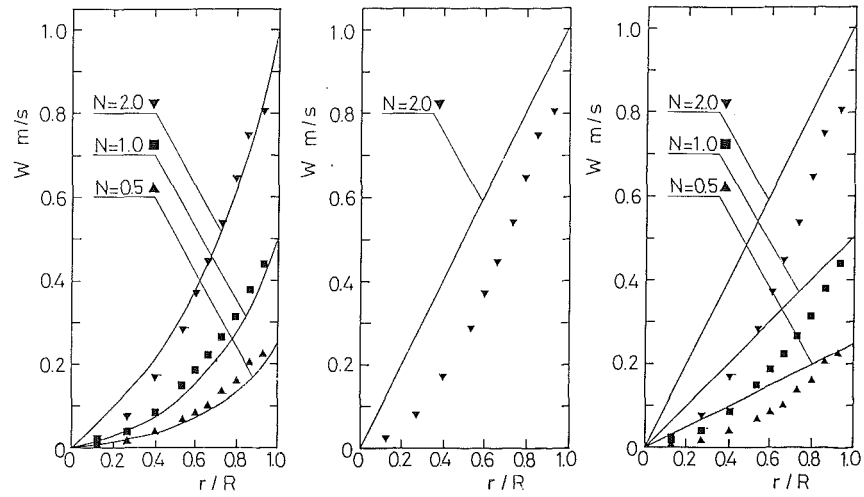

Fig. 4(a) Stress equations model Fig. 4(b) Conventional k-ϵ model Fig. 4(c) k-ϵ model with modification

Fig. 4 Tangential velocity profile at an axially rotating pipe flow. Plots: Kikuyama's experimental results. Solid lines: Calculations applying (a) stress equations model; (b) conventional k-ϵ two equations model; (c) k-ϵ model modified by the Richardson number.

the figure P_i, R_i, D indicate the terms of the right-hand side of equation (23), which are shown under Fig. 3, respectively.

P_i are the production terms. $P_1 (= -\overline{v^2}\partial U/\partial r)$ contributes significantly to the production of $\overline{uv}$ in both cases with and without swirl. Particularly, in the case with swirl, P_2 $(=\overline{uw}W/r)$ becomes a negative production term, which reduces the magnitude of $\overline{uv}$. The redistribution terms, R_3 and R_5 also include the effect of W. R_3 $(= -\alpha\overline{uw}\ W/r)$ has an effect to increase $\overline{uv}$. But, the coefficient α takes the value 0.76 and so it never overcomes the effect of P_2 to decrease $\overline{uv}$. R_5 $(=\beta\overline{uw}\ \partial W/\partial r)$ also has an effect on $\overline{uv}$ to decrease. Since the coefficient β takes a small value $(=0.11)$, R_5 is smaller than P_2. The diffusion term D is negligibly small except near the wall region and has no large effect on $\overline{uv}$. From these considerations, the reduction of $\overline{uv}$ due to the swirl is caused by the negative production term P_2 $(=\overline{uw}W/r)$ in the $\overline{uv}$ transport equation (23). The convection terms also contain $\overline{uw}W/r$, which has the same effect of P_2. $\overline{uw}$ is nearly zero in a nonswirling flow. In the present swirling flow, $\overline{uw}$ becomes negative which introduces negative $\overline{uw}W/r$. The negative $\overline{uw}$ is caused mainly by the two terms of $-\overline{uv}\partial W/\partial r$ and $\overline{uv}\ W/r$ in the transport equation (24) of $\overline{uw}$. These two terms have an effect for negative production and to make $\overline{uw}$ negative in the present swirling flow.

In Fig. 4, the experimented and the predicted radial profiles of the tangential velocity W are compared, varying the strength of the swirl. Points in Fig. 4(a) are the experimental results. The conditions of the experiments and the calculations correspond to the case in Fig. 2. The solid lines in Fig. 4(a), (b), (c) are the calculations applying the stress equation model [16], the conventional k-ϵ two equation model [15] and the k-ϵ model modified by the Richardson number [14]. The experimental values are nearly parabolic, which are well predicted by the stress equation model [16] (Fig. 4(b)). The predictions applying the conventional k-ϵ two equation model (Fig. 4(b)) and the modified k-ϵ model (Fig. 4(c)) show straight line profiles, which deviate from the experimental results.

The reason is explained as follows why the two equation model with the assumption of gradient-type turbulent diffusion for momentum transfer yield the straight line profiles of tangential velocity component W. From the conservation equation of momentum in the tangential direction, which prescribes the radial profile of the tangential velocity W, the condition $\overline{vw} \fallingdotseq 0$ is obtained, if we put $V \fallingdotseq 0$, $\partial/\partial x = 0$ in a fully developed region and the momentum transfer by laminar viscosity is negligibly small. If we apply gradient model, $\rho\overline{vw}$ is expressed in terms of the turbulent viscosity coefficient μ_t and the velocity gradient in equation (9). Combining equation (9) and $\overline{vw} \fallingdotseq 0$, $\partial(W/r)/\partial r$ becomes zero, which means the tangential velocity W is directly proportional to the distance from the axis r (see Fig. 4(b), (c)). That is to say, the gradient-type model can not predict the experimental tendency of the parabolic tendency velocity profiles.

In the calculations applying the stress equation model [16], the correlation of velocity fluctuations (the Reynolds stresses) are evaluated from the transport equations respectively without the assumption of the effective viscosity, which make possible to predict the present swirling flow field that can not be predicted by the k-ϵ two equation model.

4 Summary

Computations on the turbulent flows in a pipe rotating around its axis were conducted to investigate the applicability of the turbulent models and to study the phenomena of the laminarization of the turbulence due to the swirl.

Three kinds of the turbulence models of the conventional k-ϵ two equation model, the k-ϵ model modified by the Richardson number and the stress equation model were applied and the computations were compared with the experiments [7]. The results obtained are as follows.

(1) The stress equation model can predict the experimental facts that the axial velocity profile deforms into a laminar-like velocity profile and the wall friction factor decreases in the swirling flow driven by the rotation of the pipe wall.

(2) These laminarization phenomena are supposed to be caused by the reduction of the turbulent momentum flux $\rho\overline{uv}$ due to the swirl. The reduction of the $\rho\overline{uv}$ is caused mainly by the negative production term $\overline{uw}W/r$ in the transport equation of $\overline{uv}$.

(3) On the other hand, the conventional k-ϵ two equation model does not predict the experimental tendencies such as the laminarization phenomena mentioned above. The reason is that the terms associated with the swirl velocity component include $\partial(W/r)/\partial r$ in the k and ϵ equations and become negligibly small because W becomes proportional to r in the calculation of the developed pipe flow.

(4) The modification of the k-ϵ model by the Richardson number can improve the prediction of the axial velocity com-

ponent as compared with the conventional k-ϵ model. But, the prediction is not as good as that by the stress equations model.

(5) The conventional and modified k-ϵ models fail to predict the parabolic profiles of the tangential velocity component W because the gradient models applying turbulent effective viscosity yield inherently linear velocity profiles of W in the developed flow in a pipe. On the other hand, the stress equation model can predict the experimental tendency of the parabolic profiles of tangential velocity component.

Acknowledgment

The author wishes to thank Professor K. Kikuyama for offering the valuable experimental data.

References

1 Wolf, Jr., L., Lavan, Z, and Fejer, A., "Measurements of the Decay of Swirl in Turbulent Flow," *AIAA Journal*, Vol. 7, 1969, pp. 971–973.

2 Senoo, Y., and Nagata, T., "The Swirl Flow in Long Pipes with Different Roughnesses," *Bull. Japan Soc. Mech. Engng.*, Vol. 15, 1972, pp. 1514–1521.

3 White, A., "Flow of a Fluid in an Axially Rotating Pipe," *Journal Mechanical Engineering Science*, Vol. 6, 1964, pp. 47–52.

4 Murakami, M., and Kikuyama, K., "Turbulent Flow in Axially Rotating Pipes," ASME JOURNAL OF FLUIDS ENGINEERING, Vol. 102, 1980, pp. 97–103.

5 Cannon, J., and Kays, W., "Heat Transfer to a Fluid Flowing Inside a Pipe Rotating About Its Longitudinal Axis," ASME *Journal of Heat Transfer*, Vol. 91, 1969, pp. 135–139.

6 Kikuyama, K., Murakami, M., and Nishibori, K., "Development of Three-Dimensional Turbulent Boundary Layer in an Axially Rotating Pipe," ASME JOURNAL OF FLUIDS ENGINEERING, Vol. 105, 1983, pp. 154–160.

7 Kikuyama, K., Murakami, M., Nishibori, K., and Maeda, K., "Flow in a Rotating Pipe (A Calculation of Flow in the Saturated Region) *Bull. Japan Soc. Mech. Engng.*, Vol. 26, 1983, pp. 506–513.

8 Takagi, T., and Okamoto, T., and Yamada, M., "Phenomena of the Retardation of Mixing and Combustion in Swirling Flows," ASME-JSME Thermal Engineering Joint Conference, Vol. 4, 1983, pp. 131–136.

9 Schlichting, H., *Boundary Layer Theory*, 4th ed., McGraw-Hill, 1968, pp. 500–504.

10 Becker, K. M., and Kaye, J., "Measurements of Diabatic Flow in an Annulus with an Inner Rotating Cylinder," ASME *Journal of Heat Transfer*, Vol. 84, 1962, pp. 97–104.

11 Hirai, S., Takagi, T., Tanaka, K., and Mori, N., "Turbulent Heat Transfer to the Flow in a Concentric Annulus with a Rotating Inner Cylinder," 8th International Heat Transfer Conference, Vol. 3, 1986, pp. 895–900.

12 Bradshaw, P., "The Analogy between Streamline Curvature and Buoyancy in Turbulent Shear Flow," *Journal of Fluid Mechanics*, Vol. 36, 1969, pp. 177–191.

13 Koosinlin, M. L., Launder, B. E., and Sharma, B. I., "Prediction of Momentum, Heat and Mass Transfer in Swirling, Turbulent Boundary Layers," ASME *Journal of Heat Transfer*, Vol. 96, 1974, pp. 204–209.

14 Launder, B. E., Priddin, C. H., and Sharma, B. I., "The Calculation of Turbulent Boundary Layers on Spinning and Curved Surfaces," ASME JOURNAL OF FLUIDS ENGINEERING, Vol. 99, 1977, pp. 231–239.

15 Jones, W. P., and Launder, B. E., "The Calculation of Low-Reynolds-Number Phenomena with a Two-Equation Model of Turbulence," *International Journal of Heat and Mass Transfer*, Vol. 16, 1973, pp. 1119–1130.

16 Launder, B. E., Reece, G. J., and Rodi, W., "Progress in the Development of a Reynolds-Stress Turbulence Closure," *Journal of Fluid Mechanics*, Vol. 68, 1975, pp. 537–566.

17 Launder, B. E., and Spalding, D. B., *Mathematical Models of Turbulence*, Academic Press, 1972, pp. 90–110.

18 Takagi, T., and Kotoh, S., "Computation and Its Comparison with Experiments of Time-Mean and Fluctuating Properties in Round Jets with and without Flame," *Proceeding 3th Symposium Turbulent Shear Flows*, 1981, pp. 3.21–3.26.

19 Daly, B. J., and Harlow, F. H., "Transport Equations in Turbulence," *Physics of Fluids*, Vol. 13, 1970, pp. 2634–2649.

20 Hanjalic, K., and Launder, B. E., "A Reynolds Stress Model of Turbulence and its Application to Thin Shear Flows," *Journal of Fluid Mechanics*, Vol. 52, 1972, pp. 609–638.

21 Morse, A., "Axisymmetric Free Shear Flows with and without Swirl," Ph.D. Thesis, Univ. of London, 1980, pp. 122–209.

22 Schlichting, H., *Boundary Layer Theory*, 4th ed., McGraw-Hill, 1968, pp. 553–558.

23 Patanker, S. V., and Spalding, D. B., *Heat and Mass Transfer in Boundary Layers*, Interext Book, 1970, pp. 28–46.

24 Hinze, J. O., *Turbulence*, 2nd ed., McGraw-Hill, 1975, pp. 724–726.

Determination of Incompressible Flow Friction in Smooth Circular and Noncircular Passages: A Generalized Approach Including Validation of the Nearly Century Old Hydraulic Diameter Concept

N. T. Obot
Associate Professor,
Fluid Mechanics, Heat and Mass Transfer Laboratory,
Department of Chemical Engineering,
Clarkson University,
Potsdam, New York 13676
Mem. ASME

It has been demonstrated conclusively that the widely observed differences in data for frictional pressure coefficient between circular and noncircular passages derive from the inseparably connected effects of transition and the choice of a length scale. A relatively simple approach, the critical friction method (CFM), has been developed and when applied to triangular, rectangular, and concentric annular passages, the reduced data lie with remarkable consistency on the circular tube relations. In accordance with the theory of dynamical similarity, it has also been shown that noncircular duct data can be reduced using the hydraulic diameter or any arbitrarily defined length scale. The proposed method is what is needed to reconcile such data with those for circular tubes. With the hydraulic diameter, the critical friction factor almost converges to a universal value for all passages and the correction is simply that required to account for the difference in critical Reynolds number. By contrast, with any other linear parameter, two corrections are needed to compensate for variations in critical friction factor and Reynolds number. Application of the method to roughened passages is discussed.

1 Introduction

Determination of friction in flow passages, be it due to single-phase or two-phase flow, is of considerable importance in numerous engineering applications, and the problem has been studied to the point that a complete review of the available literature, even that dealing with single phase flows, would be of itself a major undertaking. Despite this extensive literature, no generally valid method is available for handling single phase data obtained on ducts of arbitrary shapes. Two reasons can be provided for this unsatisfactory situation. First, the origin of the differences in frictional pressure coefficient between circular and noncircular passages is not well understood. In fact, from much that has been written on the subject in many standard texts, one might wrongly conclude that these discrepancies are due to the inadequacy of the hydraulic diameter, $D_e = 4A/P_w$, for laminar and turbulent flows. And, secondly, the role of the hydraulic diameter has not been thoroughly examined. Hence, no sound evidence has been established in support of the wide use of D_e in friction and heat transfer calculations except, of course, for the fact that this definition asserts that the hydraulic diameter of a cylindrical passage is its diameter.

One is confronted with a difficulty. For if D_e is not the correct length scale, how is one to explain the remarkable consistency in fully rough turbulent friction factors obtained on circular, rectangular and triangular passages (Webb et al., 1971; Han et al., 1978, 1979; Obot et al., 1987) especially since the noncircular duct data were reduced using D_e, or how can one justify the widely recommended use of fully rough circular tube data for noncircular passages by simply replacing the tube diameter with D_e? It seems very unlikely that either of these somewhat related questions could be addressed satisfactorily without definite conclusions concerning the disagreement among the results obtained on smooth channels.

Several suggestions toward an explanation of the discrepancy with smooth channels present themselves. In the first place, transition which is a unique phenomenon of virtually all channel flows would play an important role, due to the well known differences in the flow field between circular and noncircular passages. According to Reynolds (1883), for each critical velocity (Reynolds number), itself a function of the initial flow conditions and flow geometry, there exists a corresponding

Contributed by the Fluids Engineering Division and presented at the Winter Annual Meeting, Chicago, Ill., November 28-December 2, 1988 of THE AMERICAN SOCIETY OF MECHANICAL ENGINEERS. Manuscript received by the Fluids Engineering Division November 6, 1987. Paper No. 88-WA/FE-1.

critical pressure (friction factor). From the theory of dynamical similarity, also advanced by Reynolds, it is natural to suppose that laminar and turbulent friction factors obtained on noncircular passages would agree or deviate from those on circular tubes according to whether the critical variables are the same or different. Even for geometrically similar ducts, it is to be expected that laminar and turbulent friction factors would be different when the critical variables vary with geometric details (smooth or abrupt entrance) or with initial flow conditions. And, secondly, with knowledge of the attendant physical phenomenon, it should be possible to generalize friction data for all ducts provided the conditions for dynamic similarity are met, whether the length scale is the hydraulic diameter or any other linear parameter.

The main objective of this study was to test the above suggestions. Fortunately, there is a very extensive data base and it has been possible to complete this phase of the analysis without additional experiments.

2 Review of Relevant Literature

Of the early experiments, virtually all of which were performed on circular tubes, the most comprehensive were carried out by Darcy (1858) and Reynolds (1883). Darcy considered the flow of water through fairly rough tubes. For certain types of roughness his data indicate that friction factor is independent of Re. Reynolds investigated the general cause for the change from steady to eddying motion (i.e., transition) as well as the change in the law of resistance. As noted in the introductory section, he established the existence of a critical velocity and pressure for transition. This work undoubtedly forms the basis for the subsequent development of the subject of turbulence (Reynolds, 1895).

Subsequent studies on circular tubes were undertaken by numerous researchers (Saph and Schoder, 1903; Gibson, 1909; Stanton, 1911; Carothers, 1912; Stanton and Pannell, 1914; and Lees, 1915), and these results did not differ materially from those of Reynolds. Other investigations not cited here, notably those carried out by Brix and by Stockalper, are discussed in detail elsewhere (Gibson, 1909; Stanton and Pannell, 1914). Based on tests with steam and water, Lander (1916) concluded that the general form of the resistance formula is applicable to saturated vapors. From these studies several conclusions can be made. First, the resistance laws for smooth circular tubes were thoroughly and satisfactorily established by 1920. Second, the onset of transition or the critical point for the change from steady to eddying motion is almost definite in character and in value, occurring at a Reynolds number (Re) of about 2,100, irrespective of the numerical value for the diameter of the smooth tube. It is, of course, by now well known that transition can be delayed to much larger Re if the necessary precautions (no disturbance at inlet, no pipe vibration, etc.) are taken.

For noncircular passages, there is very extensive literature beginning from around 1908 when Grindley and Gibson, at the suggestion of Osborne Reynolds, carried out experiments with air flow in coiled tubes. The objective in this study was to determine the viscosity of air. No definite conclusion could be drawn from the very limited pressure drop data that were given for turbulent flow. A few years later, Eustice (1910, 1911) studied the flow of water in curved pipes. In the first work, the procedure used for coiling caused the pipe cross-section to become oval to a considerable degree. To compensate for the reduction in area due to coiling, the ingenious approach of Eustice was to compare the resistance of the pipe in its coiled state with that when compressed to an oval form between straight boards. Much later, White (1929) made a more extensive investigation of the resistance in curved pipes. Depending on the degree of curvature, the critical Re was found to be higher than for a straight circular tube. Also, he observed that, for large disturbances, flow in curved pipes was more stable than in straight pipes. These observations are consistent with the increased resistance with curvature as has been documented by numerous researchers. A common problem faced by these authors was the choice of the length scale for data reduction and this will be considered later.

In 1910, Gibson carried out a very comprehensive study using twenty-five pipes of circular, square and rectangular cross-sections. The ducts had the same angle of convergence or divergence with identical initial and final areas. His results indicated that the head loss was highest for a square duct, being 20-30% larger than the lowest values obtained on a circular geometry, with intermediate values for the rectangular channel. Further, for pipes of the same initial and final areas and of the same length, the head loss was much greater with a rectangular than with either a square or circular geometry.

In 1923, very painstaking tests on rectangular passages were performed by Schiller; Hopf; and Fromm; all of whom used the hydraulic radius or diameter (A/P_w or $4A/P_w$) to reduce the data to nondimensional form. Later, similar studies were conducted by Nikuradse (1926) and in 1928 by Cornish; Fritsch; and Davies and White. Since these and subsequent studies were reviewed by other researchers (see, for example, Jones, 1976), a further elaboration here is unnecessary. Suffice it to state that Cornish provided the first indication that the critical Re for transition increases with increasing aspect ratio.

Systematic investigations on concentric annular passages

Nomenclature

A = cross-section flow area, m^2
AR = aspect ratio, w/s
b = base of triangular duct, m
D, D_e = diameter, equivalent (hydraulic) diameter, m
d_i = inner diameter of annular space, m
d_o = outer diameter of annular space, m
e = rib height, m
e^+ = roughness Reynolds number, $(e/D_e)\mathrm{Re}(f/2)^{1/2}$
f = Fanning friction factor
$\bar{f}$ = modified friction factor, equation (4)
h = height of triangular duct, m
L_e = entrance length, m
L_t = length between pressure taps in test section, m
m = mass flow rate, kg/s
P_w = wetted perimeter, m
p = rib pitch, m
Δp = pressure drop, Pa
Re = Reynolds number
$\overline{\mathrm{Re}}$ = modified Reynolds number, equation (3)
Re^+ = roughness function, equation (5)
s = channel spacing, m
V = average velocity, m/s
w = channel width, m
α = apex angle, deg
β = diameter ratio, d_i/d_o
μ = fluid viscosity, Pa•s
ν = kinematic viscosity, m^2/s
ρ = fluid density, kg/m^3
ψ_f = ratio of smooth duct critical f, equation (2)
ψ_R = ratio of smooth duct critical Re, equation (2)

Additional Subscripts

c = circular tube
n = noncircular passage
c,c = circular tube critical variable
n,c = noncircular duct critical variable
fR = critical f ratio for roughened duct
RR = critical Re ratio for roughened duct

were carried out by Lea and Tadros, 1931; Rothfus et al., 1950; Walker et al., 1957; Koch and Feind, 1958; to mention but a few. The general conclusion is that the critical Re increases with increasing diameter ratio. The interested reader may wish to consult the very thoughtful analysis which was presented not too long ago (Jones and Leung, 1983). In sharp contrast to the trends noted above for rectangular or concentric annular flow passages, careful tests with isosceles triangular ducts (Carlson, 1959; Hanks and Cope, 1970; Cope and Hanks, 1972) indicated that the smaller the apex angle, the lower the critical Re. Consequently, triangular duct friction factors are generally lower than those for circular or rectangular passages.

For circular tubes, the specification of the length scale in the definition of friction factor and Reynolds number is quite obvious. By contrast, for noncircular passages, the problem always arises of what to use as the correct length scale. Although it is customary to use the hydraulic diameter, this choice is widely believed to be incorrect. This view, which is not necessarily correct, appears to be the result of the general expectation that, since Re is a similarity parameter, two channel flows having the same Re should be dynamically similar to one another and, hence, should have almost identical friction factors. This is indeed the case for smooth circular pipes and, in this case, the critical Re for tests on tubes of sufficient entrance length assumes almost a constant value, as was first observed by Reynolds (1883). The closeness with which the Re similarity can be applied to circular tubes while entirely failing to reconcile data for noncircular ducts with divergent trends for the critical Re, affords strong presumption that there is a fundamental phenomenon of fluid motion in ducts, as well as boundary layer flows, of which due account has not been given.

In connection with the above discussion of the Reynolds number similarity criterion, it is of interest to note that this concept was formulated even before the most celebrated experiments of Reynolds (1883). In 1873, Helmholtz, in a paper to the Royal Prussian Academy (Berlin) presented a more general treatment of the problem by considering two pipe flows with $\rho_1, \mu_1, V_1, P_1, L_1$ and $\rho_2, \mu_2, V_2, P_2, L_2$, where L_1 and L_2 are the length scales. He showed that the two flows may be similar if the conditions $L_2 = (\nu_2 V_2/\nu_1 V_2)L_1$ or $V_1 L_1/\nu_1 = V_2 L_2/\nu_2$ and $P_1/\rho_1 V_1^2 = P_2/\rho_2 V_2^2$ are satisfied simultaneously. Much later, following the theoretical and experimental study by Reynolds which established that transition occurs when Re has a definite value, Rayleigh (1892, 1899) used the theory of dynamical similarity to arrive at a conclusion similar to that of Helmholtz. Specifically, he showed that the resistance per unit area, R, could be expressed definitely by the simple mathematical formula:

$$R/\rho V^2 = f(VD/\nu) \tag{1}$$

Thereafter, the Re similarity criterion has been used universally for both friction and heat transfer analysis. To the best knowledge of this author, the role of transition in determining the general validity of the Reynolds number similarity has hitherto not been considered.

Finally, it seems appropriate to comment briefly on the historical use of the hydraulic diameter. Long before any systematic studies of friction in closed conduits were made, scientists did establish, in connection with hydraulic research on river basins and open channel flows, that the ratio of the frictional area to the volume of the stream is an important parameter that governs friction loss. For friction calculations, the hydraulic mean depth, defined as the area divided by the wetted perimeter was widely used. Tracing of the exact origin of the hydraulic mean depth concept was hampered by translation difficulties and the fact that many of the original papers are difficult to obtain.

As noted earlier, the choice of a length scale with noncircular passages has been a perennial problem. Although Grindley and Gibson (1908) showed that the hydraulic mean depth, A/P_w, entered directly into the force balance equation, they chose to use the mean radius in their data analysis. Later, in Gibson (1909), the definition of this mean depth was given as $D/4$. Eustice (1910) correlated his data using the hydraulic mean radius, the definition of which was not provided. From a re-analysis of his data, by this author, it was concluded that this was the mean radius of the coiled tubes. Interestingly, Eustice concluded this paper by noting that he "is also investigating the effect of the ratio of area to perimeter in oval tubes on the flow and critical velocity." The subsequent publication (Eustice, 1911) contained much valuable information of a qualitative nature for a range of curvature, with no definite conclusions on the effect of A/P_w.

Much later, Schiller (1923) undertook a full scale study in which the hydraulic radius was used to reduce pressure drop data for a well defined geometry. Hopf made some tests at about the same time as Schiller. The choice of a rectangular configuration was made in order to determine the effect of varying the hydraulic radius for a given roughness geometry. This study was extended by Fromm (1923). Thereafter, the usual practice has been, when working with noncircular passages, to use the hydraulic diameter for friction and heat transfer calculations.

3 Formulation of the Critical Friction Method (CFM)

The formulation of the CFM is based on the following observations:

1. Transition from laminar to turbulent flow is the controlling phenomenon.
2. For each critical velocity, there exists a corresponding critical pressure, as was first enunciated by Reynolds (1883). Expressed as nondimensional parameters, these correspond respectively to the critical Reynolds number and friction factor and will be denoted symbolically by $(\mathrm{Re}_{c,c}, f_{c,c})$ and $(\mathrm{Re}_{n,c}, f_{n,c})$, where the subscripts c,c and n,c refer to circular and noncircular passages.
3. The values for the critical variables depend on the entrance length, duct geometry and on the initial flow conditions (Reynolds, 1883), an observation that has been verified by numerous researchers.
4. The fact that the hydraulic diameter of a given noncircular flow area is not numerically equal to the diameter of a circular pipe of the same area makes it perfectly clear that, even if the values for the critical velocity and pressure were the same for both cases, the nondimensional critical variables, in particular the critical Re, will be different. This rather unique situation is a direct consequence of the transformation from physical to dimensionless parameters.

When fluid is transported through passages, critical Reynolds number and friction factor exist such that for $f_{n,c} > f_{c,c}$ and $\mathrm{Re}_{n,c} > \mathrm{Re}_{c,c}$ transition occurs at a Reynolds number that is greater than that for a circular pipe and the noncircular duct data can be expected to lie above those for circular tubes. This is indeed the case with increasing aspect ratio of a rectangular channel as well as diameter ratio of the concentric annulus. Conversely, for $f_{n,c} < f_{c,c}$ and $\mathrm{Re}_{n,c} < \mathrm{Re}_{c,c}$, the point of transition on the familiar logarithmic plot of f versus Re lies behind that for circular tubes, the noncircular duct data being generally lower than those with the cylindrical geometry. Again, this is almost the consistent trend for triangular passages. Conceivably, if $f_{n,c} = f_{c,c}$ and $\mathrm{Re}_{n,c} = \mathrm{Re}_{c,c}$, conditions that should be satisfied simultaneously, it is to be expected that no differences in friction factor would occur between circular and noncircular passages. This equality of the critical parameters, a clear statement of the dynamic similarity criterion for all pipes, is the basis of the present method.

From the above discussion, and considering that the difficult mathematics of transition is not amenable to an elegant treatment, a relatively simple and straightforward generalization of friction data can still be formulated by introducing the following scale factors:

$$\psi_R = \mathrm{Re}_{c,c}/\mathrm{Re}_{n,c};\ \psi_f = f_{c,c}/f_{n,c} \tag{2}$$

Using equation (2) the expressions for the modified or reduced Reynolds number ($\overline{\mathrm{Re}}$) and friction factor ($\bar{f}$) for isothermal conditions become:

$$\overline{\mathrm{Re}} = \psi_R \mathrm{Re}_n = (m_n/m_{n,c})\mathrm{Re}_{c,c} \tag{3}$$

$$\bar{f} = \psi_f f_n = (\Delta p_n/\Delta p_{n,c})(m_{n,c}/m_n)^2 f_{c,c} \tag{4}$$

where the subscripts n and n,c refer to the noncircular passage.

From equations (3) and (4) it is unmistakably clear that $\bar{f}$ or $\overline{\mathrm{Re}}$ is independent of the characteristic length of the noncircular passage. The implication here is that the noncircular duct data, when reduced using the D_e or any arbitrarily selected length scale, would collapse on the circular tube curves, provided that equations (2)-(4) are used to account for the inseparably connected effects of transition and choice of length scale as dictated by the dynamic similarity criterion. Clearly, $\psi_f > 1$ and $\psi_R > 1$ when noncircular duct transition occurs at a lower Reynolds number than is the case for a circular tube, while $\psi_f < 1$ and $\psi_R < 1$ corresponds to the situation where the onset of transition is at a higher Re relative to that for a tube.

4 Effect of Duct Geometry on Critical Parameters

Prior to the discussion of the usefulness (if any) of the hydraulic diameter concept, it is instructive to examine the general trends for critical values of f and Re, typical results of which are presented in Tables 1-4. The critical point or the onset of transition as used here coincided effectively with the location of the minimum in the familiar logarithmic plot of f versus Re. Accurate determination of these critical values turned out to be a more time consuming task than was envisaged initially, requiring, in addition to log-log plots of f versus Re, linear plots of some of the data in the forms $f \cdot \mathrm{Re}$ versus Re and/or $1/\sqrt{\bar{f}}$ versus $\log_{10}\mathrm{Re}\sqrt{\bar{f}}$. Since the general shapes of these curves are clearly of a universal nature, it was possible to reconstruct the critical point from the available literature data to a high degree of accuracy and consistency.

Table 1 Summary of circular tube critical data

Author(s)	$f_{c,c} \times 10^3$	$\mathrm{Re}_{c,c}$
Reynolds (1883)	7.81	2,120
Stanton and Pannell (1914)	7.46	2,170
Nikuradse (1933)	7.69	2,125
Rothfus et al. (1950)	7.61	2,140
Walker et al. (1957)	8.40	2,086
Koch and Feind (1958)	8.83	2,719
Dodge and Metzner (1959)	8.49	2,080
Hanks and Cope (1970)	7.74	2,084

Table 2 Summary of rectangular duct critical data

Author(s)	aspect ratio, AR	$f_{n,c} \times 10^3$	$\mathrm{Re}_{n,c}$	
Cornish (1928)	2.92	8.60	2,225	
Allen and Grunberg (1937)	3.92	7.89	2,315	(2,400)+
Washington and Marks (1937)	20.0	8.30	3,300	
	40.0	7.31	3,550	
Walker et al. (1957)	20.0	8.17	2,954	
Whan and Rothfus (1959)	20.0	8.89	2,938	
Hartnett et al. (1962)	1.0	7.98	2,147	(2,200)
	10.0	7.81	2,470	(2,500)
	20.0	8.14	2,495	(2,500)
Jones (1976)	13.0	8.36	2,591	
	26.0	8.18	2,899	
	$31.0(\Delta P_{1-8})$	9.0	2,590	
	$31.0(\Delta P_{2-8})$	8.4	2,773	

+ Values in brackets correspond to those reported by the authors.

Examination of the data in these tables reveals several important trends. First, for circular, rectangular and triangular cross-sections, the critical friction factor could be stated as 0.00819 ± 0.0005, 0.0080 ± 0.0005 and 0.0080 ± 0.0003 successively, indicating that this parameter almost converges to a common value for all these geometries. Considering the rather unique nature of each laboratory experiment, this degree of convergence is indeed remarkable. For triangular ducts, the data of Hanks and Cope (1970) for 2.5 and 7.5 deg apex angles were excluded from this analysis, for the reason that these were probably in error because transition is not an abrupt process as can be inferred from their data. There is, of course, no reason that the critical friction factor for the concentric annuli should not approach the same common value, and this expectation is confirmed by some of the data of Koch and Feind (1958). By contrast, the detailed studies by Rothfus and his students gave values that were substantially greater than the base value of 0.008. The implications of this disagreement will be considered in Section 6.

Another important trend, that for the critical Re, is also quite evident from Tables 1-4. For circular pipes, a logical conclusion, based on all but the data of Koch and Feind, is that this value could be stated as $\mathrm{Re}_{c,c} = 2115$, with an error of no more than 3 percent. The data of Koch and Feind are associated with an indeterminate amount of error. For rectangular, triangular and concentric annular passages, $\mathrm{Re}_{n,c}$ increases with increasing aspect ratio (AR), apex angle or with

Table 3 Summary of triangular duct critical data

Author(s)	apex angle, α, deg.	h/b	$f_{n,c} \times 10^3$	$\mathrm{Re}_{n,c}$
Carlson (1959)	4.01	14.26	8.91	1,389
	7.96	7.21	7.96	1,613
	12.0	4.75	8.45	1,549
	22.3	2.54	7.77	1,712
	38.8	1.42	7.90	1,775
Hanks and Cope (1970)	5.0	11.44	9.80	1,249
	15.0	3.80	1.06	1,272
	30.0	1.99	8.51	1,646
	45.0	1.21	8.23	1,770
	60.0	0.87	8.06	1,880
	75.0	0.65	8.05	2,000
	90.0	0.50	8.05	1,925
Cope and Hanks (1972)	30.0	1.87	8.65	1,619
	60.0	0.87	8.15	1,782
Tung and Irvine (1978)	11.5	4.94	8.10	1,414
Chegini and Chaturvedi (1986)	38.8	1.41	8.57	2,000
	60.0	0.87	7.5	2,000
Obot and Adu-Wusu (1985)	Scalene	0.46	9.4	1,816

Table 4 Summary of critical data for tubes of annular section

Author(s)	diameter ratio, β	$f_{n,c} \times 10^3$	$\mathrm{Re}_{n,c}$
Rothfus et al. (1950)	0.162	10.0	2,213
	0.650	10.5	2,534
Walker et al. (1957)	0.026	9.77	2,461
	0.067	10.3	2,619
	0.125	10.5	2,392
	0.165	10.9	2,442
	0.331	10.7	2,498
	0.499	10.1	2,545
Koch and Feind (1958)	0.212	8.2	2,873
	0.409	8.1	3,014
	0.60	7.5	3,239
	0.698	7.1	3,398
	0.793	7.6	3,037
	0.838	-	-

decreasing height-to-base and diameter ratio (β), successively. For the latter, the results of Koch and Feind indicate a marked variation with β, while very moderate effect with increasing β can be inferred from the results of Rothfus and co-workers.

In the case of rectangular and triangular passages for which there are moderate differences among the various results, the effects of duct geometry on $\mathrm{Re}_{n,c}$ are illustrated graphically on Figs. 1 and 2, respectively, where ψ_R (the ratio of $\mathrm{Re}_{c,c}$ to $\mathrm{Re}_{n,c}$ using the rounded value of 2,100 for $\mathrm{Re}_{c,c}$) is plotted against the appropriate geometric parameter. Figures 1 and 2 were prepared using the data in Tables 2 and 3, respectively. For the isosceles cross-section, it is customary to correlate friction factor in terms of the apex angle. However, since this approach introduces some ambiguity when applied to scalene passages, it seems more appropriate to select the abscissa as the height-to-base ratio. It is pertinent to note that, for isosceles ducts, the larger the height-to-base ratio, the smaller the apex angle and the lower the critical Re; resulting in the trend depicted in Fig. 2. For the concentric annuli, there are significant quantitative differences in the calculated ψ_R values, hence these results are not shown graphically.

It is well known that the general cause of the change from steady to eddying motion or transition from laminar to turbulent flow is that, under certain circumstances, the steady motion becomes unstable. Since the influence of duct geometry on transition manifests itself through a change in the critical Re, fluid flow in rectangular channels of large aspect ratio can be expected to be more stable than those with small aspect ratios under identical entrance conditions, while use of isosceles triangular passages of small apex angles (or large height-to-base ratios) should give flows that are less stable relative to those in ducts of small h/b. For the latter cross-section, this instability may be the cause for the coexistence of laminar and turbulent flows, as first reported by Eckert and Irvine (1956) and subsequently confirmed by Bandopadhayay and Hinwood (1973). In passing, it should be emphasized that the concept of stable and unstable flows, as discussed above, refers specifically to the onset of transition or eddying motion and, as such, should not be confused with the theory of stability for laminar flows subjected to small disturbances.

5 How Good is the Hydraulic Diameter Concept?

In view of the observation in Section 3 concerning the arbitrary choice of a length scale for data reduction, one may wish to enquire on the real advantage to using the hydraulic diameter especially since its validity has long been a very contentious issue. From the results in Tables 1-4 and the discussion in the preceding section, the near convergence of the critical friction factor to a universal value can be considered, at least for the moment, to be the most important advantage.

A more definite conclusion is perhaps most easily reached by considering the alternative representations of the triangular duct data ($\alpha = 38.8$ deg) of Carlson (1959) which are given in Figs. 3 and 4. The choice of the results of Carlson for the purpose of this illustration was made for several reasons. First, his results have been verified by numerous researchers. Second, the magnitudes of the deviation between circular and noncircular passage friction factors are probably largest for the triangular geometry. Hence, this represents the worst case analysis. Third, the test conditions and results were documented in sufficient detail, and it was possible to reanalyze the results and to present them in the forms which are given in Fig. 3 where, beginning from top to bottom, the length scales used correspond to the height, base and D_e successively. The circular pipe relations are also included in Fig. 3 for the purpose of comparison. To arrive at the ψ_f and ψ_R values that are given in Fig. 3, the by now well known values of 0.008 and 2,100 were used for $f_{c,c}$ and $\mathrm{Re}_{c,c}$, respectively. This figure highlights one of the observations (#4) made in

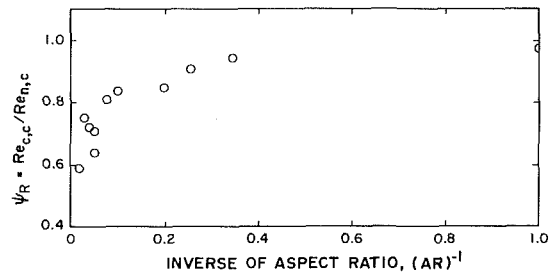

Fig. 1 Variation of rectangular duct critical Re with aspect ratio

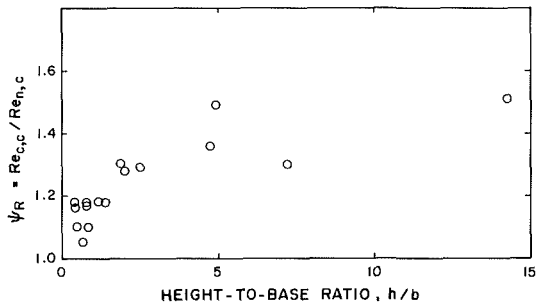

Fig. 2 Variation of triangular duct critical Re with height-to-base ratio

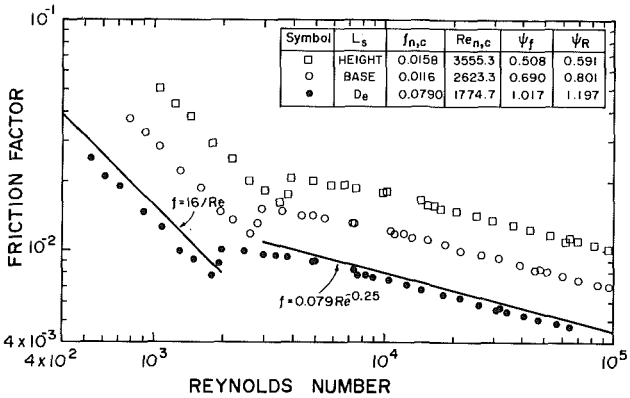

Fig. 3 Alternative representations of Carlson's triangular duct data

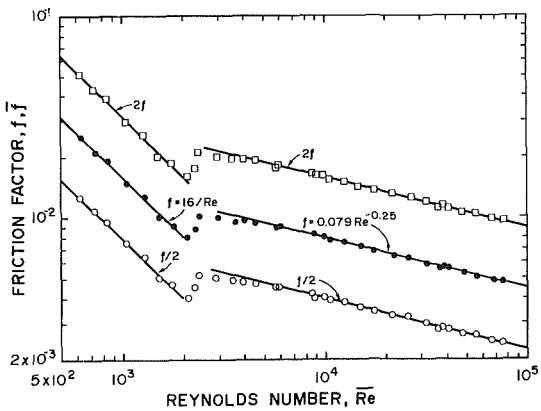

Fig. 4 The corrected data of Carlson

Section 3; that is, for the same critical velocity and pressure, the corresponding nondimensional variables vary with the selected length scale.

Figure 4 is a plot of $f, \bar{f}$ versus $\overline{\mathrm{Re}}$ using the data of Fig. 3, along with the appropriate ψ_f and ψ_R values. With D_e, the correction was applied only to the Reynolds number, in line with the observation that $f_{c,c} \simeq f_{n,c}$. The solid lines correspond to the appropriately scaled circular tube relations. It is especially

noticeable from Fig. 4 that, when D_e is used as the linear parameter, the correction is simply that needed to account for the shift in the critical Re. By contrast, when an arbitrary choice of a length scale is made (such as the base or height in the case of a triangular passage, Figs. 3 and 4) ψ_f and ψ_R will be lower or greater than unity according to whether $f_{n,c}$ and and $\mathrm{Re}_{n,c}$ are greater or less than the corresponding values for a circular tube. In this case, $\bar{f}$ and $\overline{\mathrm{Re}}$ must be computed using equations (2)-(4), and the reduced data should lie with remarkable consistency on the curves for circular tubes as indicated here on Fig. 4. This figure fully demonstrates that D_e or any linear parameter can be used for reduction of frictional pressure drop and flowrate data, the proposed method being what is needed to bring the results in line with those for tubes.

In summary, the above illustration and discussion highlight one practical advantage of using D_e, that is, it eliminates an additional step of the data reduction. The present observation is in complete agreement with the findings of other researchers (Carlson, 1959; Jones, 1976; Jones and Leung, 1981; to mention but a few). Specifically, these authors have reported that, with D_e, a modified Reynolds number was all that was needed to reconcile the differences in friction factor between circular and several noncircular cross-sections.

6 Validation of the CFM

Having illustrated and discussed the choice of a length scale, attention will now be directed to application of the proposed method to some of the available data for triangular, rectangular and concentric annular passages. It should be mentioned from the outset that the criteria for data selection were that they satisfy the conditions outlined in Section 3.

Of the six sets of independent data that are considered here, two (Carlson, 1959; Cornish, 1928) were obtained from the complete tabulation provided in the original work, while the remaining were taken from published journal articles (Allen and Grunberg, 1937, Koch and Feind, 1958; Hartnett et al., 1962 and Jones, 1976). For the latter, the painstaking exercise of extracting the data from the plots resulted in reading errors that were generally within 2 percent. This was verified for five isosceles passages from comparisons of the extracted data (Carlson and Irvine, 1961) with the complete tabulation obtained subsequently from the original thesis (Carlson, 1959).

For triangular and rectangular channels, the reduced data are given in Figs. 5 and 6, respectively. In accordance with the discussion in Sections 4 and 5, the friction factor based on D_e is plotted against the modified Reynolds number, $\overline{\mathrm{Re}}$. For the triangular geometry, the analysis has been carried out for the most extensive data available to date (Carlson, 1959). The results of Hanks and co-workers, while they covered a wide range of apex angles or height to base ratios as can be inferred from Table 3, were unfortunately confined to the laminar and transition regions. For clarity, the results for rectangular channels have been broken into three separate plots (Fig. 6) which, taken together, show the general trend with increasing aspect ratio (AR) over the range of values between AR = 2.92 and AR = 31. In each case, the solid lines represent the appropriately scaled ($2f$, f, $f/2$) circular tube relations.

It is quite evident from Figs. 5 and 6 that the proposed method provides very satisfactory representation of the available data within the accuracy of both experimental and reading errors. The results of Carlson for small apex angles deviate consistently and lie slightly above and below the circular tube relations in the laminar and turbulent regions, respectively; trends that are due to the effect of relative entrance length (L_e/D_e) on the critical Re. Also, in that study the physical length of the test section, over which the pressure drop was measured, was fixed, further contributing to the lack of geometrically similar test conditions. As noted in Section 3, the dependence of the critical Re on L_e/D_e was fully

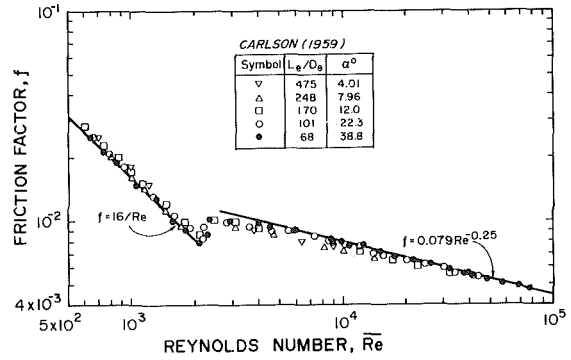

Fig. 5 Friction factor versus $\overline{\mathrm{Re}}$ for isosceles cross-section

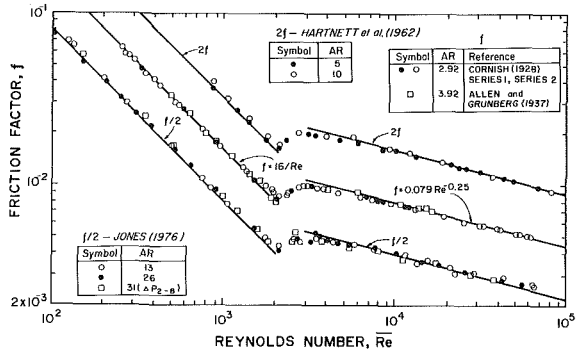

Fig. 6 Friction factor versus $\overline{\mathrm{Re}}$ for rectangular channels

demonstrated by Reynolds (1883). This effect can also be inferred from the AR = 31 results of Jones (1976). Considering that each channel flow laboratory experiment has its own peculiarities and that no two experiments are completely identical in every respect, the most important conclusion amounts to this: no meaningful quantitative assessment of the agreement and/or disagreement between two sets of data can be made without reference to the differences in the critical values for friction factor and Reynolds number.

For square ducts, the available experimental data can be separated into two groups: those that indicate that $\mathrm{Re}_{n,c} > \mathrm{Re}_{c,c}$ (see, for example, Hartnett et al., 1962) and those that show exactly the opposite (Schiller, 1923). The analysis of Jones, which is based on the analytical solution of Cornish (1928), favors the latter trend. Although both trends can be expected to occur depending, of course, on the entrance length and initial flow conditions especially since ψ_R is not much different from unity; a totally unexpected feature of these results and one that is not supported by the present analysis is the general agreement with the circular tube data in the turbulent regime. For this reason, complete agreement of the reduced data with the circular relations over the entire $\overline{\mathrm{Re}}$ range cannot be established from the available data. With the data of Schiller or Hartnett et al., it is worthy of note that, while excellent agreement is obtained in the laminar region, the deviation from the Blasius equation is no more than 8 percent.

It may also be noted that the data of Washington and Marks (1937) for AR = 20 and 40 were associated with an indeterminate amount of error and hence were excluded from this analysis. Further, it was unwise to include the data of Davies and White (1928) obtained on ducts of large aspect ratios, for the reason that in going from AR = 169 to AR = 37 the relative entrance length (L_e/D_e) decreased steadily from $L_e/D_e = 41.9$ to 9.4, a clear indication that fully developed laminar flow was not realized for the Re range tested.

For the concentric annuli, the most extensive data were reported by Lea and Tadros (1931), Walker et al. (1957) and Koch and Feind (1958). Most of the results of Lea and Tadros

were presented differently and, due to insufficient documentation of the test facility and conditions, results for only two of the six β values could be re-analyzed. As noted in Section 4, this author's evaluation of the results of the two remaining studies indicates significant quantitative differences. First, as can be readily established from Table 4, the critical friction factors of Walker et al. are 12-20 percent higher than, while the values of Koch and Feind are (except for $\beta = 0.698$ and 0.838) about the same as, those for circular tubes. Second, the results of Walker et al. indicate a very gradual increase of $\mathrm{Re}_{n,c}$ with β, in contradistinction to the greater sensitivity of $\mathrm{Re}_{n,c}$ to changes in β as can be seen in Table 4.

Although neither of the differences noted above are by themselves sufficient to invalidate either set of data, the decisive factor must be the requirement which (for $\psi_f \leq 1$ and $\psi_R < 1$) asserts that both laminar and turbulent friction factors must lie above the circular tube values, irrespective of the definition of the length scale used to reduce the data to dimensionless form. This requirement is met satisfactorily by the results of Koch and Feind, though the trends with increasing β are marred by a residual effect of L_e/D_e and possible experimental errors. Their data for a circular tube exhibited rather unusual trends in the laminar and transition regions, resulting in a substantially greater value for $\mathrm{Re}_{c,c}$ (Table 1). Also, the results for $\beta = 0.838$ and $L_e/D_e = 123$ show no definite critical friction factor or Reynolds number, a feature that is inconsistent with expectations. The laminar flow results of Walker et al. follow the expected trend, but their turbulent data are effectively coincident with the circular tube relation. The latter trend does not appear to be demonstrative; hence, their data could not be used for the present purpose of validation.

One is left therefore with the data of Koch and Feind which, as far as the present analysis indicates, are acceptable with reservations due to the extraneous effects noted above. Their reduced data are presented in Fig. 7, where f is plotted against $\overline{\mathrm{Re}}$. This figure shows a degree of concurrence with the circular tube relations that is as good as can be expected for tests with varying L_e/D_e and possible measurement errors.

In summary, using the data for three contrasting duct geometries it has been demonstrated that, provided the conditions of dynamic similarity are satisfied, the various test results do lie with remarkable consistency on the circular tubes curves. Small deviations from the relations have been observed for systematic experiments and these are due largely to the dependence of critical Re on L_e/D_e and, to a lesser extent, to errors in measurements and in the determination of the critical Re from the available data.

7 Application to Single Phase Flows in Rough Ducts

Having established that the disagreement among friction factor results obtained in smooth passages is due entirely to the inseparably connected effects of transition and length scale, attention may now be turned to the two related questions raised in the introductory section: how is one to explain the consistency in fully rough friction factors with circular and noncircular passages or how can one justify the wide use of fully rough circular tube data for noncircular channels?

In 1923, Schiller, in a study using threads of various depths and inclinations on the inside surface of circular tubes observed that the critical Re was independent of the type of roughness. Later, Nikuradse (1933) carried out extensive and very painstaking tests from which he concluded that the critical Re for all grades of sand grain roughness occurred at about the same position as for smooth pipes, being in the range of Re between 2,160 and 2,500. Comparison of this range of Re with the nearly constant value of 2,100, already established for transition with smooth tubes, appears to suggest that the presence of roughness may cause a moderate increase in the critical Re, with hardly any effect on the critical friction factor. An extensive study would be required to establish these effects precisely.[1]

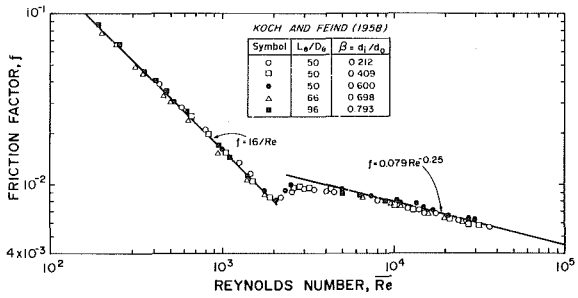

Fig. 7 Friction factor versus $\overline{\mathrm{Re}}$ for tubes of annular section

Based on the law of the wall similarity, Nikuradse showed that experimental data could be correlated adequately using the following friction similarity function:

$$\mathrm{Re}^+(e^+) = (2/f)^{1/2} + 2.5\ln(2e/D_e) + 3.75 \qquad (5)$$

Equation (5) is the basis for nearly all existing correlations for roughened ducts. For arbitrary shapes of roughness, Webb et al. (1971) obtained very close approximation of their fully rough regime data using:

$$\mathrm{Re}^+(e^+) = 0.95(p/e)^{0.53}, \text{ for } e^+ \geq 35,\ p/e \geq 10 \qquad (6)$$

Similar expressions for $e^+ \leq 35$ and $p/e \leq 10$ have been proposed by other investigators (see, for example, Han et al., 1978).

For noncircular rough passages and on the basis of the results obtained with the cylindrical geometry, it is reasonable to suppose that the effect on critical Re or friction factor would parallel that for circular tubes. In other words, the value for the ratio of the critical parameter, ψ_{RR} or ψ_{fR}, would be about the same as that for a smooth channel. Since ψ_{RR} is then the only correction that is needed to account for the differences in critical Reynolds number between circular and noncircular roughened passages and, since such a correction (whether its value is the same or somewhat different from that of the smooth ducts) does not alter the general friction factor trend with increasing Re, due to the fact that friction factor in the fully rough regime is quite independent of Re for all ducts, it must be expected that equations (5) and (6) would be applicable to noncircular geometries.

This expectation is definitely confirmed by the results in Fig. 8 which is reproduced from Obot et al. (1987). These results were obtained with a scalene triangular duct having three roughened ($3R$) sides. It may also be noted that Han et al. (1978) correlated their rectangular duct data using equation (5). Including the effect of p/e, their final correlation for the fully rough regime was in complete agreement with equation (6). A re-analysis of their data using the $\mathrm{Re}^+(e^+)$ expression for the plane geometry (Han et al., 1979), that is, with 4.23 instead of 3.75 in equation (5), resulted in differences in $\mathrm{Re}^+(e^+)$ between their results and those of Webb et al. that were within 10 percent; a degree of concurrence that is perfectly consistent with the fact that 92-96 percent of the channel wetted perimeter was covered with roughness elements.

So, the observation that in the fully rough regime the law of resistance should be of a universal nature for all pipes, as inferred from the critical friction method, has been completely validated for two strikingly different duct geometries. This finding is clearly of considerable importance for two reasons. First, it provides a straightforward method for computation of frictional pressure drop for roughened ducts. Second, it

[1] For internally finned tubes, there are clear indications that the critical Reynolds number, which varies markedly with the relative fin height, is significantly lower than the smooth tube value of 2100 (Masliyah, J. H. and K. Nandakumar, 1976, *Ind. Eng. Chem. Fundam.*, Vol. 15, pp. 144-146).

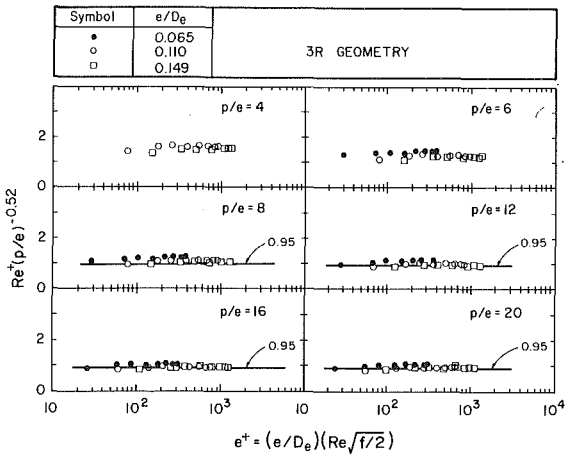

Fig. 8 Correlation of roughened triangular duct data

provides justification for the usual practice of calculating noncircular duct friction factor from circular tube relations.

8 Comparison with the Method of Jones (1976)

The reader is probably aware of the numerous methods that have been proposed for generalization of friction data for various cross-sections (Perry, 1964; Jones, 1976; Jones and Leung, 1981; to mention but a few). Of these, the only one with some physical basis, involving the use of the so-called "laminar equivalent" diameter ($D_L = D_e\phi^*$) for definition of the modified Reynolds number ($\rho V D_L/\mu$), was proposed by Jones and successfully applied to rectangular ducts. Later, the method was extended to smooth concentric annuli (Jones and Leung). It will be demonstrated here that ψ_R and ϕ^* should assume nearly the same values (at least for the $w/s > 2.5$ range), as might have been inferred from the fact that the closeness with which the reduced data of Fig. 6 fit the circular tube relations is remarkably similar to that documented by Jones.

Figure 9 contains the same information as Fig. 1 but with one notable exception, that is, the inclusion of the complete profile (solid line) for ϕ^*, as given by Jones for the rectangular geometry. On the basis of this figure, one can rightly conclude, or at least speculate, that if systematic measurements of the variation of ψ_R with aspect ratio were available, the results for ψ_R and ϕ^* would be satisfactorily consistent.

There is more to be said here about the laminar equivalent diameter (D_L) concept than would at first be supposed, especially in view of the last statement of the preceding paragraph. This concept is used to satisfy the requirement that $\mathrm{Re}_c = \overline{\mathrm{Re}}$ (automatically satisfying the condition $\mathrm{Re}_{c,c} = \overline{\mathrm{Re}}_{n,c}$) for $f_{c,c} \approx f_{n,c}$, and this is consistent with the present method. And, further, since the limiting point with increasing Re on any particular f versus Re profile is the critical point, itself satisfying the exact laminar solution, it follows in accordance with the definition of D_L that $\psi_R \simeq \phi^*$, and this is verified in Figs. 5-7. In this regard it may be noted that, as a rough approximation, the critical point is the intersection of the laminar curve ($f \alpha$ 1/Re) and the normal drawn from the location of the peak value of friction factor. This provides an answer to the question raised by Madsen (1976) in his discussion of the paper by Jones, regarding the applicability of the D_L concept to all uniform ducts for which analytical solutions exist. Jones established quite conclusively that, even with no correction to account for secondary flows, the use of D_L provided remarkable representation of the available data. Since transition is the sole physical phenomenon, such a correction is neither justified nor indeed needed. In conclusion, it is this author's view that the D_L concept is clearly of general validity. It requires verifiable laminar flow data or exact solution, while

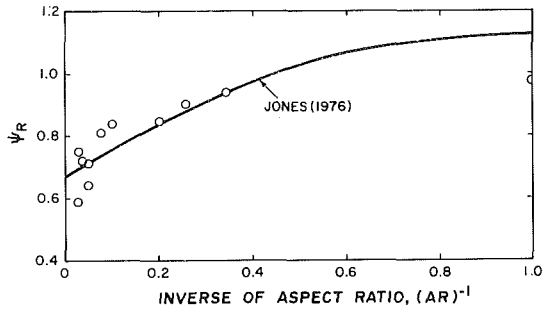

Fig. 9 Comparison with the method of Jones (1976)

the use of the present method is conditioned by the availability of transition data.

9 Discussion

The basic assumptions inherent in the analysis are that friction factor always rises from the minimum or critical value to about the same maximum and that the extent of the transition region, expressed in terms of $V_{c,\max}/V_{c,\min}$, is about the same for all passages. Here, $V_{c,\max}$ and $V_{c,\min}$ refer to the average velocity at the locations within the transition region of the maximum and minimum values for friction factor, respectively. In other words, a single point two-parameter correction (ψ_f, ψ_R) would suffice. A study of the series of plots on Figs. 5-7 reveals that these assumptions are almost satisfied. It is of some interest to note that in the study by Reynolds (1883), $V_{c,\max}/V_{c,\min}$ assumed a nearly constant value of 1.2. The general conclusion itself, that is, transition is the sole physical phenomenon, is certainly not weakened by any departure in the above assumptions; for obviously an analogous two point correction involving $[\psi_f, \psi_R]_{\min}$ and $[\psi_f, \psi_R]_{\max}$ can be similarly formulated and this will certainly produce the same results.

For virtually all of the results so far presented, no special precautions were taken to delay transition and the duct entrance configurations were almost abrupt in design. For a smooth entrance or other situations where transition is delayed artificially, the critical Re is much greater than for an abrupt inlet geometry while the critical friction factor (based on D_e) is significantly lower than the base value of 0.008 (Hartnett et al., 1962). It should be noted as a matter of particular importance to the present consideration that, when transition is delayed artificially, the critical friction factor does not approach a common value; at least no such value could be determined from the available literature. Using the laminar flow data of Hartnett et al. and the critical Re values quoted therein for a smooth entrance, application of equations (2)-(4) provided very satisfactory representation of the reduced data; an indication that the CFM may be applicable to these situations. More definite conclusions must await the availability of results for systematic experiments which cover the laminar, transition and turbulent regimes.

There are indications that, for a given duct geometry, the critical Re may increase or decrease according to whether the fluid is being cooled or heated (Washington and Marks, 1937; Sieder and Tate, 1936), due to the fact that cooling and heating result in stable and unstable boundary layer, respectively (Schlichting, 1968). The proposed method can be used to establish the applicable corrections for a range of duct geometries and operating temperatures. Also, this same approach can be extended to other types of boundary layer flows. Finally, there are important implications of the present development on turbulent heat transfer, and these will be considered in a separate paper.

10 Conclusions and Recommendations

A very thoughtful analysis and discussion of friction in flow

passages has been presented. The most significant observations can be summarized as follows:

1. The differences in laminar and turbulent friction factors between circular and noncircular passages derive from the inseparably connected effects of transition and length scale.
2. According to the criterion for dynamic similarity, passages with the same critical friction factor and critical Re will possess identical laminar and turbulent frictional pressure coefficients.
3. With the hydraulic diameter as a length scale, the critical friction factor almost converges to a universal value for all ducts, requiring only a simple correction to account for the difference in critical Re.
4. The choice of an arbitrary length scale requires two corrections to account for the differences in critical friction factor and Reynolds number between circular and noncircular passages.
5. In the fully rough regime and for geometrically similar roughness, circular tube friction correlations in the form proposed by Webb et al. (1971) are valid for noncircular passages, provided the noncircular duct data are reduced using D_e.

However, there is a definite limitation on the immediate use of the proposed method for friction factor calculations because, as noted in Section 4, a reliable and consistent trend with increasing height-to-base, aspect ratio or diameter ratio could not be established for critical Re from the available literature. In fact, with the exception of the work by Cornish (1928), none of the studies used in the preparation of Figs. 5-7 provided more than three data points within the transition region. There is need for a comprehensive study of transition that will provide very consistent trends for variations of critical Re with duct geometry. For such a study, it would be of utmost importance to maintain geometrically similar conditions for any particular cross-section, i.e., same L_e/D_e and L_t/D_e. For all practical purposes and in order to keep the test facility to manageable size with increasing h/b, AR or β, a value of 60 for L_e/D_e would suffice. Also, a detailed study of the effect of L_e/D_e on the critical Re would constitute a worthwhile contribution to the existing literature. And, further, there is need for a very thorough investigation of the role of roughness on transition.

Acknowledgments

I am indebted to Professor John McLaughlin of our department for his well written comments, to Messrs. T. A. Trabold and E. B. Esen for their comments and help with the manuscript preparation, to Elizabeth Lyman (CU) for excellent typing from the rough draft, and Karen Jenicek (Argonne National Lab., RAS) for typing of the revised manuscript. I am grateful to the reviewers for their suggestions, in particular to Professor O. C. Jones, Jr. (RPI, Troy, NY) for an elaborate open review. Dr. T. J. Rabas (Argonne, EES Div.) and Professor J. N. Cannon (Howard Univ.) provided very valuable comments and additional references.

References

Allen, J., and Grunberg, N. D., 1937, "The Resistance to the Flow of Water Along Smooth Rectangular Passages, and the Effect of a Slight Convergence or Divergence of the Boundaries," *Phil. Mag.*, Vol. 23, Series 7, pp. 490–503.

Bandopadhayay, P. C., and Hinwood, J. B., 1973, "On the Coexistence of Laminar and Turbulent Flow in a Narrow Triangular Duct," *J. Fluid Mech.*, Vol. 59, pp. 775–783.

Carlson, L. W., 1959, "Experimental Friction Factors for Fully Developed Turbulent Flow in Smooth Triangular Ducts," M. S. Thesis, University of Minnesota.

Carlson, L. W., and Irvine, T. F., 1961, "Fully Developed Pressure Drop in Triangular Shaped Ducts," ASME *Journal of Heat Transfer*, Vol. 83, pp. 441–444.

Carothers, S. D., 1912, "Portland Experiments on Flow of Oil in Tubes," *Proc. Roy. Soc. London*, Vol. 87, Series A, pp. 154–163.

Chegini, H., and Chaturvedi, S. K., 1986, "An Experimental and Analytical Investigation of Friction Factors for Fully Developed Flow in Internally Finned Triangular Ducts," ASME *Journal of Heat Transfer*, Vol. 108, pp. 507–512.

Cope, R. C., and Hanks, R. W., 1972, "Transitional Flow in Isosceles Triangular Ducts," *Ind. Eng. Chem. Fundam.*, Vol. 11, pp. 106–117.

Cornish, R. J., 1928, "Flow in a Pipe of Rectangular Cross Section," *Proc. Roy. Soc. London*, Vol. 120, Series A, pp. 691–700.

Darcy, H., 1858, "Recherches Experimentales Relatives au Movement de l'eau dans les Tuyaux," *Memories a l'Academie d. Sciences de l'Institute imperial de France*, Vol. 15, p. 141.

Davies, S. J., and White, C. M., 1928, "An Experimental Study of the Flow of Water in Pipes of Rectangular Section," *Proc. Roy. Soc. London*, Vol. 119, Series A, pp. 92–107.

Dodge, D. W., and Metzner, A. B., 1959, "Turbulent Flow of Non-Newtonian Sytems," *AIChE J.*, Vol. 5, pp. 189–204.

Eckert, E. R. G., and Irvine, T. F., 1956, "Flow in Corners of Passages with Noncircular Cross Sections," *Trans. ASME*, Vol. 78, pp. 709–718.

Eustice, J., 1910, "Flow of Water in Curved Pipes," *Proc. Roy. Soc. London*, Vol. 84, Series A, pp. 107–118.

Eustice, J., 1911, "Experiments on Stream-line Motion in Curved Pipes," *Proc. Roy. Soc. London*, Vol. 85, Series A, pp. 119–131.

Fritsch, W., 1928, "Der Einfluss der Wandrauhigkeit auf die turbulente Geschwindigkeitsverteilung in Rinnen," *Z. Agnew. Math. Mech.*, Vol. 8, pp. 199–216.

Fromm, K., 1923, "Strömungswiderstand in rauhen Rohren," *Z. Agnew. Math. Mech.*, Vol. 3, pp. 339–358.

Gibson, A. H., 1909, "An Investigation of the Resistance to Flow of Air Through a Pipe, with the Deduction and Verification of a Rational Formula," *Phil. Mag.*, Vol. 17, Series 6, pp. 389–402.

Gibson, A. H., 1910, "On the Flow of Water Through Pipes and Passages Having Converging or Diverging Boundaries," *Proc. Roy. Soc. London*, Vol. 83, Series A, pp. 366–378.

Grindley, J. H., and Gibson, A. H., 1908, "On the Frictional Resistances to the Flow of Air Through a Pipe," *Proc. Roy. Soc. London*, Vol. 80, Series A, pp. 114–139.

Han, J. C., Glicksman, L. R., and Rohsenow, W. M., 1978, "An Investigation of Heat Transfer and Friction for Rib-Roughened Surfaces," *Int. J. Heat Mass Transfer*, Vol. 21, pp. 1143–1156.

Han, J. C., Glicksman, L. R., and Rohsenow, W. M., 1979, "Correction to an Investigation of Heat Transfer and Friction for Rib-Roughened Surfaces," *Int. J. Heat Mass Transfer*, Vol. 22, pp. 1587–1588.

Hanks, R. W., and Cope, R. C., 1970, "Laminar-Turbulent Transitional Flow Phenomena in Isosceles Triangular Cross-Section Ducts," *AIChE J.*, Vol. 16, pp. 528–535.

Hartnett, J. P., Koh, J. C. Y., and McComas, S. T., 1962, "A Comparison of Predicted and Measured Friction Factors for Flow Through Rectangular Ducts," ASME *Journal of Heat Transfer*, Vol. 84, pp. 82–88.

Helmholtz, H. L. F., 1873, "Ueber ein Theorem, geometrisch ähnliche Bewegungen flussiger Körper betreffend, nebst Anwendung auf das Problem, Luftballons zu lenken," *Wissenchaftliche Abhandlungen*, Vol. 1, pp. 158–171.

Hopf, L., 1923, "Die Messung der hydraulischen Rauhigkeit," *Z. Agnew. Math. Mech.*, Vol. 3, pp. 329–339.

Jones, O. C., Jr., 1976, "An Improvement in the Calculation of Turbulent Friction in Rectangular Ducts," ASME JOURNAL OF FLUIDS ENGINEERING, Vol. 98, pp. 173–181.

Jones, O. C. Jr., and Leung, J. C. M., 1981, "An Improvement in the Calculation of Turbulent Friction Factor in Smooth Concentric Annuli," ASME JOURNAL OF FLUIDS ENGINEERING, Vol. 103, pp. 615–623.

Koch, R., and Feind, K., 1958, "Druckverlust und Wärmeübergang in Ringspalten," *Chemie-Ing.-Techn.*, Vol. 30, pp. 577–584.

Lander, C. H., 1916, "Surface Friction: Experiments with Steam and Water in Pipes," *Proc. Roy. Soc. London*, Vol. 92, Series A, pp. 337–353.

Lea, F. C., and Tadros, A. G., 1931, "Flow of Water Through a Circular Tube with a Central Core and Through Rectangular Tubes," *Phil. Mag.*, Vol. 11, Series 7, pp. 1235–1247.

Lees, C. H., 1915, "On the Flow of Viscous Fluids Through Smooth Circular Pipes," *Proc. Roy. Soc. London*, Vol. 91, Series A, pp. 46–53.

Madsen, N., 1976, Discussion of "An Improvement in the Calculation of Turbulent Friction in Rectangular Ducts," by O. C. Jones, ASME JOURNAL OF FLUIDS ENGINEERING, Vol. 98, p. 181.

Nikuradse, J., 1926, "Geschwindigkeitsvertleilung in Turbulenten Strömungen," *Zeitschrift-VDI*, Vol. 70, p. 1229.

Nikuradse, J., 1933, "Laws of Flow in Rough Pipes," NACA TM 1292.

Obot, N. T., and Adu-Wusu, K., 1985, "The Flow Pattern in a Scalene Triangular Duct Having Two Rounded Corners," ASME JOURNAL OF FLUIDS ENGINEERING, Vol. 107, pp. 455–459.

Obot, N. T., Esen, E. B., and Adu-Wusu, K., 1987, "Pressure Drop for Rib-Roughened Scalene Triangular Duct Having Two Rounded Corners," *Int. Comm. Heat Mass Transfer*, Vol. 14, pp. 11–20.

Perry, A. E., 1964, "The Concept of Hydraulic Diameter," ASME Paper 64-WA/FE-31.

Rayleigh, L., 1892, "On the Question of the Stability of the Flow of Fluids," *Phil Mag.*, Vol. 34, Series 5, pp. 59–70.

Rayleigh, L., 1899, "Investigation in Capillarity: – The Size of Drops – The Liberation of Gas from Superheated Solutions – Colliding Jets – The Tension of Contaminated Water Surfaces," *Phil Mag.*, Vol. 48, Series 5, pp. 321–337.

Reynolds, O., 1883, "An Experimental Investigation of the Circumstances Which Determine Whether the Motion of Water Shall be Direct or Sinuous, and

of the Law of Resistance in Parallel Channels," *Phil. Trans. Roy. Soc. London*, Vol. 174, Series A, pp. 935–982.

Reynolds, O., 1895, "On the Dynamical Theory of Incompressible Viscous Fluids and the Determination of the Criterion," *Phil. Trans. Roy. Soc. London*, Vol. 186, Series A, pp. 123–164.

Rothfus, R. R., Monrad, C. C., Senecal, V. E., 1950, "Velocity Distribution and Fluid Friction in Smooth Concentric Annuli," *Ind. Eng. Chem.*, Vol. 42, pp. 2511–2520.

Saph, A. V., and Schoder, E. H., 1903, "An Experimental Study of the Resistances to the Flow of Water in Pipes," *Trans. Am. Soc. Civil Eng.*, Vol. 51, pp. 254–330.

Schiller, L., 1923, "Über den Strömungswiderstand von Rohren verschiedenen Querschnitts und Rauhigkeitsgrades," *Z. Agnew. Math. Mech.*, Vol. 3, pp. 2–13.

Schlichting, H., 1968, *Boundary Layer Theory*, Sixth Edition, McGraw-Hill, New York, pp. 494–499.

Sieder, E. N., and Tate, G. E., 1936, "Heat Transfer and Pressure Drop of Liquids in Tubes," *Ind. Eng. Chem.*, Vol. 28, pp. 1429–1435.

Stanton, T. E., 1911, "The Mechanical Viscosity of Fluids," *Proc. Roy. Soc. London*, Vol. 85, Series A, pp. 366–376.

Stanton, T. E., and Pannell, J. R., 1914, "Similarity of Motion in Relation to the Surface Friction of Fluids," *Phil. Trans. Roy. Soc. London*, Vol. 214, Series A, pp. 199–224.

Tung, S. S., and Irvine, T. F., 1978, "Experimental Study of the Flow of Viscoelastic Fluid in a Narrow Isosceles Triangular Duct," in Studies in Heat Transfer: A Festschrift for E. R. G. Eckert, Ed., T. F. Irvine et al., pp. 309–329, Hemisphere Pub. Corp., Washington (D.C.).

Walker, J. E., Whan, G. A., and Rothfus, R. R., 1957, " Fluid Friction in Noncircular Ducts," *AIChE J.*, Vol. 3, pp. 484–489.

Washington, L., and Marks, W. M., 1937, "Heat Transfer and Pressure Drop in Rectangular Air Passages," *Ind. Eng. Chem.*, Vol. 29, pp. 337–345.

Webb, R. L., Eckert, E. R. G., and Goldstein, R. J., 1971, "Heat Transfer and Friction in Tubes with Repeated-Rib Roughness," *Int. J. Heat Mass Transfer*, Vol. 14, pp. 601–617.

Whan, G. A., and Rothfus, R. R., 1959, "Characteristics of Transition Flow Between Parallel Plates," *AIChE J.*, Vol. 5, pp. 204–208.

White, C. M., 1929, "Streamline Flow Through Curved Pipes," *Proc. Roy. Soc. London*, Vol. 123, Series A, pp. 645–663.

A Weakly Compressible Flow Model and Rapid Convergence Methods

Charles C. S. Song
Professor.

Mingshun Yuan
Research Fellow.

St. Anthony Falls Hydraulic Laboratory,
Department of Civil and Mineral Engineering,
University of Minnesota, Minn. 55414

A weakly compressible flow model for small Mach number flows is applied to the computation of steady and unsteady inviscid flows. The equations of continuity and motion are decoupled from the energy equation, but, unlike the equations for incompressible fluids, these equations retain the ability to represent rapidly changing flows such as hydraulic transients and hydroacoustics. Two methods to speed up the process of convergence when an explicit method is used to calculate steady incompressible flows are proposed. The first method which is quite similar to the artificial compressiblity method is to assume an arbitrarily small sound speed (equivalent to large Mach number) to speed up the convergence. Any positive finite number may be used for M. One disadvantage of this method is the contamination of the steady flow solution by acoustic noise that may reverberate in the flow field for some time after the steady flow has been essentially established. The second method is based on the concept of valve stroking or boundary control. Certain boundary stroking functions that will unify the hydroacoustic and hydrodynamic processes can be found by using the inverse method of classical hydraulic transients. This method yields uncontaminated steady flow solution very rapidly independent of the Mach number.

1 Introduction

Unsteady compressible flows at small Mach number are notoriously difficult to compute due to a great disparity between the sound speed and the convective speed. If the fluid is assumed to be incompressible, as frequently done to simplify the governing equations, then the resulting equations can no longer be used to represent highly time-dependent flows such as hydraulic transients and hydroacoustics. Therefore, it is not always possible to approximate a small Mach number flow with an incompressible flow—analogous to the fact that large Reynolds number flow cannot always be approximated by inviscid flow.

It is also well known that the incompressible flow equations are not necessarily easier to solve numerically than the corresponding equations for compressible flow [1, 2]. For that reason, Chorin [3] proposed an artificial compressibility method for the purpose of solving steady incompressible flow problems. More recently, the α-transformation method [4] and pressure gradient scaling method [5] were also proposed for the purpose of speeding up the convergence process when small Mach number flows are to be computed.

Recently, Song et al. [6, 7, 8] have developed a weakly compressible flow model for the purpose of computing both steady and unsteady flows of viscous and inviscid fluids. Although the model is very much like that of the artificial compressibility method when used to calculate steady flow problems, it differs from the latter in that it is also applicable to unsteady flow problems, including hydraulic transients and hydroacoustics, because the concept of the real compressibility is retained.

This paper deals with some aspects of this model, such as rapid convergence and acoustic disturbances, when applied to steady small Mach number flows of inviscid fluid. Although the concept applies as well to viscous fluids, the issue of viscous effect will not be dealt with in this paper.

2 Basic Equations

For a barotropic flow, the governing equations of continuity and motion of inviscid fluid may be written as

$$\frac{\partial p}{\partial t} + (\mathbf{v}\cdot\nabla)p + \rho a^2 \Delta\cdot\mathbf{v} = 0 \tag{1}$$

$$\frac{\partial \mathbf{y}}{\partial t} + (\mathbf{v}\cdot\Delta)\mathbf{v} + \nabla\frac{p}{\rho} + \frac{p}{\rho^2 a^2}\Delta p = 0 \tag{2}$$

where p is pressure, $\mathbf{v}$ is velocity, ρ is density, and a is the speed of sound given by

$$a^2 = \frac{\partial p}{\partial \rho} \tag{3}$$

If the fluid is incompressible, then $a \to \infty$ and the first two terms of equation (1) and the last term of equation (2) drop out. A weakly compressible flow is defined as the flow for which the change in ρ and a are so small that they may be regarded as known constants.

The variables in equations (1) and (2) may be normalized by

Contributed by the Fluids Engineering Division and presented at the Winter Annual Meeting, Chicago, Ill., November 28–December 2, 1988 of THE AMERICAN SOCIETY OF MECHANICAL ENGINEERS. Manuscript received at ASME Headquarters September 19, 1988. Paper No. 88-WA/FE-3.

using $\rho_0 v_0^2$, v_0, ρ_0, a_0, t_0, and l_0 as reference values. The results will be the following dimensionless equations:

$$SM^2\frac{\partial p^*}{\partial t^*}+M^2(\mathbf{v}^*\cdot\nabla^*)p^*+\rho^* a^{*2}\nabla^*\cdot\mathbf{v}^*=0 \tag{4}$$

$$S\frac{\partial \mathbf{v}^*}{\partial t}+(\mathbf{v}^*\cdot\nabla^*)\mathbf{v}^*+\nabla^*\frac{p^*}{\rho^*}+M^2\frac{p^*}{(\rho^* a^*)^2}\nabla^* p^*=0 \tag{5}$$

In these equations, $M=v_0/a_0$ is the Mach number and $S=l_0/(t_0 v_0)$ is the Strouhal number. The asterisk represents the normalized quantity.

The second term in equation (4) and the last term in equation (5) are negligible if M is small. The first term in equation (4) cannot be neglected if S is large, as in the case of hydraulic transients or hydroacoustics. Therefore, for a weakly compressible inviscid flow, the governing equations may be simplified to

$$\frac{\partial p}{\partial t}+K\nabla\cdot\mathbf{v}=0 \tag{6}$$

$$\frac{\partial \mathbf{v}}{\partial t}+(\mathbf{v}\cdot\nabla)\mathbf{v}+\nabla\frac{p}{\rho}=0 \tag{7}$$

where $K=\rho a^2$ is the bulk modulus of elasticity and ρ and a are assumed to be known constants.

The equations for the inviscid weakly compressible flow, equations (6) and (7), are accurate up to the first order of M if M is small. If the flow is steady, then the equation of continuity reduces to that of the incompressible flow, i.e.,

$$\nabla\cdot\mathbf{v}=0 \tag{8}$$

as long as K is not equal to zero. Thus, the weakly compressible flow equations may be used to calculate a steady incompressible flow no matter what values we may assign to K or a. In other words, it is possible to speed up the convergence process by assuming an arbitrarily small a or, equivalently, large M if the objective is to calculate a steady flow. Needless to say, the computed results during the transient process would not represent the real physical process if an arbitrary value is assigned to M.

Equations (6) and (7) represent both hydrodynamic and hydroacoustic process which are nonlinearly coupled through the convective acceleration terms. The two processes may be uncoupled from each other if the acoustic process is much more rapid than the hydrodynamic process. The classical linear hydroacoustic theory assumes that the process is governed by

$$\frac{\partial p'}{\partial t}+K\nabla\cdot\mathbf{v}'=0 \tag{9}$$

$$\frac{\partial \mathbf{v}'}{\partial t}+\nabla\frac{p'}{\rho}=0 \tag{10}$$

where prime represents acoustic quantities. Note that by differentiating equation (9) with respect to t, and eliminating $\partial v'/\partial t$ using equation (10), classical wave equation for p' is obtained.

By the method of characteristics, it can be readily shown that for equations (9) and (10), disturbances travel at the characteristic speed a. Along the characteristics, the magnitude of pressure and speed disturbances are related through the compatibility equation

$$dp'=\pm\rho a dv' \tag{11}$$

In dimensionless form, equation (11) is equivalent to

$$\left|\frac{dv'^*}{dp'^*}\right|=M \tag{12}$$

Equation twelve will be verified by a numerical example.

Separation of hydroacoustic process and hydrodynamic process is impossible if the time scale of two processes are comparable. Under this condition, neither the Euler equations of incompressible flow nor the linear hydroacoustic equations hold. Only the complete compressible flow equations or the weakly compressible flow equations, if M is small, can be used.

When the hydrodynamic transient process is as rapid as the hydroacoustic process, as will be demonstrated later by an example, the time required to generate a steady flow condition is as small as that of the acoustic process. Consequently, the number of computational time steps needed to achieve convergence to a steady flow solution is equivalent to that required to sufficiently resolve a few cycles of sound waves. And, most importantly, the computational requirement is independent of the Mach number and the solution represents the real physical process during the transient stage, as well as the final steady state stage. This is the basic idea behind the rapid convergence method to be presented in this paper.

In the following sections, some two-dimensional flow problems will be used to illustrate the weakly compressible flow theory. Although the theory is equally applicable to two and three-dimensional flows, the former case is selected to save computational costs.

3 Effect of Mach Number on Hydrodynamic and Hydroacoustic Processes

3.1. Numerical Example. The example to be considered here is the flow in a two-dimensional contraction, as sketched in Fig. 1. This contraction is similar to that of a large cavitation channel recently designed for the David Taylor Ship Research and Development Center [9]. Its boundary consists of a flat surface on one side and a fifth order polynomial on the other side. The original objective was to calculate the velocity and pressure fields in the contraction under various given velocity distributions at the upstream end. For the present purpose, only a case when there is a uniform inflow velocity distribution will be considered.

Initially, it is assumed that the velocity is zero and pressure is constant everywhere. Imagine that there is a valve at the downstream end which can be opened instantaneously and the pressure there is dropped to a specified value. Imagine also that there is a large tank at the upstream end so that the total head is maintained constant there. The evolving flow has been calculated by solving equations (6) and (7) numerically until the solution no longer changed with time.

The problem was solved by a finite volume approach using McCormac's predictor-corrector method. A perfect slip condition at the solid walls are used. Constant total head at the upstream end and constant pressure at the downstream end were assumed. In addition to the stated natural boundary conditions, the finite volume approach requires extra boundary conditions, pressure gradient on the wall and velocity gradient at the ends, to be specified. The commonly used zero velocity gradient at the downstream end was chosen. The boundary conditions assumed are:

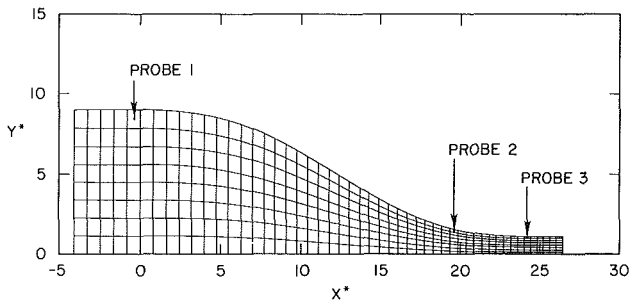

Fig. 1 Half of the symmetric contraction and three locations where pressure and velocity variations are observed

$$\frac{1}{2}\rho u^2 + p = \text{constant and } \frac{\partial u}{\partial x} = v = 0 \tag{13}$$

at the upstream end;

$$p = \text{constant, and } \frac{\partial u}{\partial x} = \frac{\partial v}{\partial x} = 0 \tag{14}$$

at the downstream end; and

$$\mathbf{v}\cdot\mathbf{n} = 0 \text{ and } \frac{\partial p}{\partial n} = \pm\frac{\rho v^2}{r} \tag{15}$$

at a solid boundary, where n is the outward normal to the boundary and r is the radius of curvature. An appropriate sign should be chosen depending on whether the boundary is convex or concave.

3.2. Numerical Results. The simplest way to vary the Mach number is to assume different sound speed. Numerical experiment indicates that the computational requirement is roughly inversely proportional to M. Figure 2 shows the variation of the computed dimensionless pressure with a dimensionless time at three locations when $M = 0.2$. Figure 3 shows the corresponding variation of the dimensionless longitudinal component of velocity. The total number of time steps for this run is 4096. Here the final velocity at the downstream end was chosen as the reference velocity v_0 and the dimensionless time t^* is defined as

$$t^* = \frac{tv_0}{l_0} \tag{16}$$

where l_0 in this example is 1/9th of the width at the entrance.

These two figures show that the hydroacoustic component or the noise persists for a considerable amount of time. The frequency spectrum of the pressure curves are plotted in Fig. 4. The abscissa is the dimensionless frequency defined as the inverse of t^*. The ordinate is the square of the Fourier transform of $2p^*$. Several harmonics, up to eight, are clearly visible. The first harmonic of $f_1 = 0.082$ is equal to the primary frequency of pressure waves reverberating in a pipe of length equal to that of the contraction, 30.5 l_0.

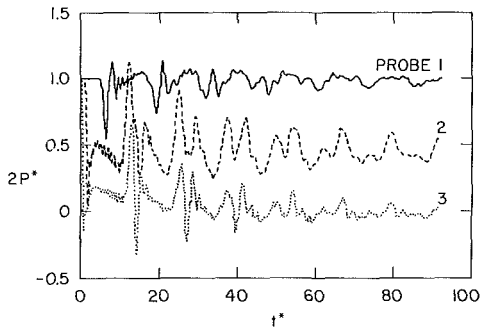

Fig. 2 Variation of dimensionless pressure with dimensionless time, $M = 0.2$

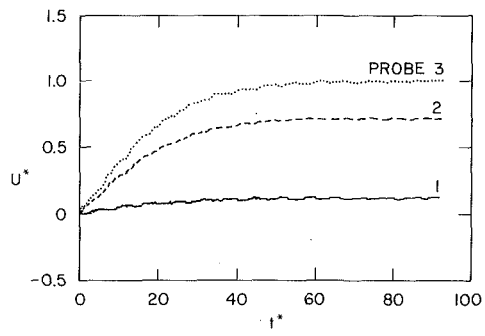

Fig. 3 Variation of dimensionless longitudinal component of velocity with dimensionless time, $M = 0.2$

The transient flow field described above was computed for several values of M ranging from 0.067 to 2.0. The final steady state flow fields for M values smaller than 0.4 agreed among each other very well, thus confirming the theory given in Section 2.

The frequency spectrums of pressure and velocity were computed for the three previously designated locations for all different M cases. The peak values of the first two harmonics of the velocity energy spectrum for probe No. 2 are plotted against M in Fig. 5. Since the flows were generated by dropping the pressure at the downstream end by a constant amount for all cases, according to equation (12), the peaks of velocity-energy spectrum should be proportional to M^2. According to Fig. 5, a power function relationship between S_n and M exists for the range $0 < M < 0.2$. The exponents of this relationship are quite close, but not exactly equal, to 2.0.

4 A Rapid Convergence Method

4.1. The Concept of Valve Stroking. The concept of valve stroking has been used to control one-dimensional transient flows for some time [10]. For a one-dimensional flow, by the method of characteristics, it is relatively easy to solve an inverse problem which is to find a downstream boundary condition required to produce certain predetermined change in flow at any interior point. For an example, it is possible to find the pressure at the downstream end required to change the velocity at the upstream end from zero to a nonzero value smoothly within a specified time interval. This transition can be made without any reverberating acoustic field. The theoretical minimum time interval required for a complete transition is equal to the one round trip time of the acoustic wave. Under this condition, the hydrodynamic and the hydroacoustic processes are identical and cannot be separated from each other.

Inverse problems for unsteady two and three-dimensional flows are extremely difficult to solve and cannot be directly applied at this time. For this reason, the inverse problem for the corresponding one-dimensional flow, taking into account the variable cross-sectional area, was solved first. The one-dimensional equations in characteristic form,

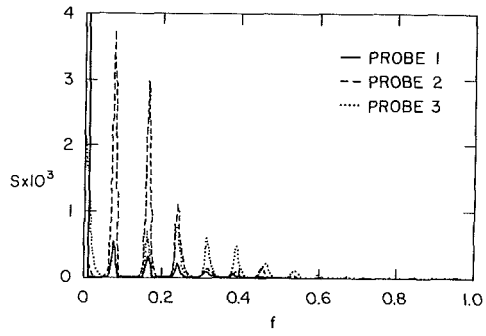

Fig. 4 Frequency spectrums of dimensionless pressure

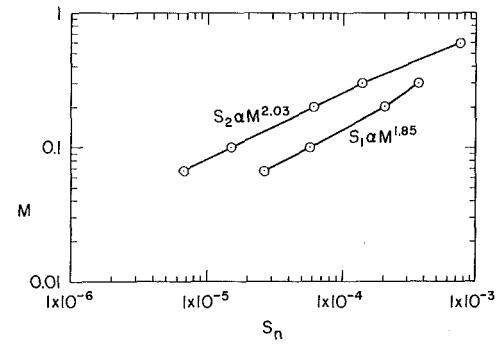

Fig. 5 First two peaks of velocity energy spectrum as functions of Mach number

$$\frac{dH}{dt} \pm \frac{a}{gA}\frac{dQ}{dt} = 0, \qquad \frac{dx}{dt} = \pm a \tag{17}$$

were used for the valve stroking computation. In the above equation, g, A, Q, and H are, respectively, the gravitational-acceleration, the cross-sectional area, the discharge, and the total head. There is, initially, no flow in the pipe. It is desired to find the pressure change necessary at the downstream end in order to cause the discharge at the upstream end to increase smoothly to a predetermined value while the total head is kept constant there.

The following conditions are imposed at the upstream end:

$$H = \frac{1}{2g} \tag{18}$$

$$Q = \begin{cases} 0.0 & t_r \le 0 \\ 3t_r^2 - 2t_r^3 & 0 < t_r < 1.0 \\ 1.0 & t_r \ge 1.0 \end{cases} \tag{19}$$

where

$$t_r = \frac{ta}{2L} - \frac{1}{2} \tag{20}$$

The problem can be solved by the method of characteristics marching the solution from the upstream end to the downstream end. It can be readily shown that, if the pressure at the downstream end just computed and equation (18) are used as the boundary conditions, equation (19) becomes the solution at the upstream end of the direct problem.

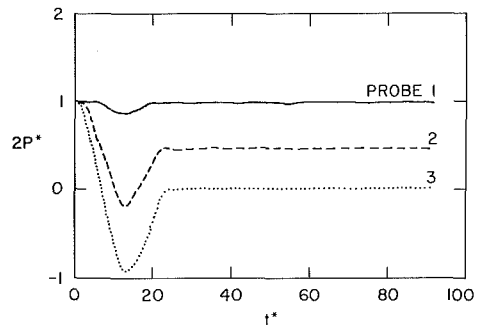

Fig. 6 Variation of pressure in symmetrical contraction, by boundary control rapid convergence method

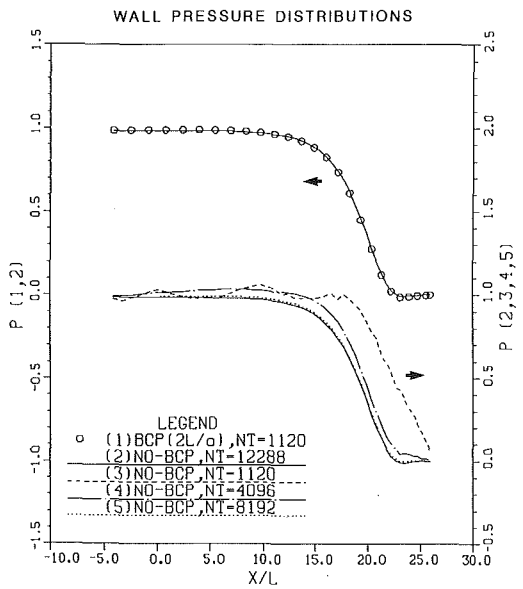

Fig. 7 Comparison of calculated pressure distribution on a wall-conventional method and boundary control method

4.2. Flow in a Symmetrical Contraction. The contraction shown in Fig. 1 which may be regarded as a half of a symmetrical contraction, was reanalyzed using the boundary control type rapid convergence method described above. One of the many possible solutions is obtained by specifying that the transient at the upstream end is to be completed in exactly one natural period (the time required for the sound wave to complete one round trip). The solution to the corresponding one-dimensional inverse flow problem specifies the required pressure stroke at the downstream end. This pressure stroke lasts for two natural periods of transients. At the end of the two natural periods, the flow in the entire field should achieve the desired steady condition.

The calculated pressure variation at three specified locations in the two-dimensional contraction are plotted in Fig. 6. When compared with Fig. 2, it is quite clear that the solution is practically free of noise. In order to compare the rates of conveyances and the converged solutions obtained by the two methods described above, the calculated pressure distribution along a wall at different time steps are shown in Fig. 7. First, the conventional method with M = 0.2 case requires more than 10,000 time steps to converge while the boundary control method requires only 1,120 time steps. Moreover, the number of time steps required for the boundary control method is independent of M, but it is inversely proportional to M for the conventional method. The converged solutions are identical.

4.3. Flow in Nonsymmetrical Fields. The solution described above is remarkably free of noise in spite of the fact that the flow field is two-dimensional with a curved boundary. To test how much the boundaries can be distorted and still yield a clean solution, two other boundary shapes, a nonsymmetrical contraction and a 90 degree bend were considered. A nonsymmetrical contraction was obtained by deforming the straight boundary of Fig. 1 to another fifth order polynomial having half the deflection of the upper boundary. The result, not shown here, indicated that the solution is as noise free as that of the symmetrical case.

The geometry of the 90 degree bend considered herein is shown in Fig. 8. The width of the channel is assumed to be l_0 and the average length is 4.57 l_0. The calculated pressure at the three locations on the outer wall, as indicated in Fig. 8, are plotted in Fig. 9. Clearly, a very rapid convergence is obtained without significant residual noise.

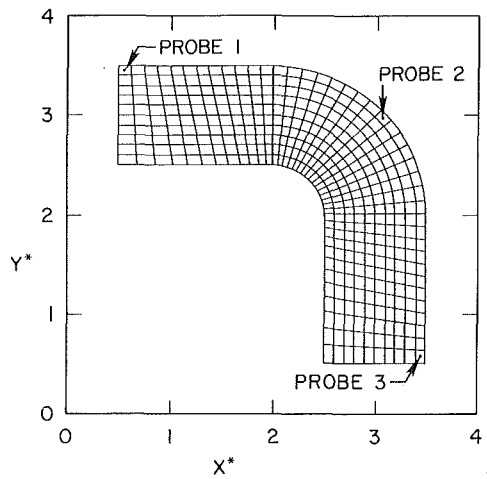

Fig. 8 Flow geometry and computational mesh of 90-degree bend

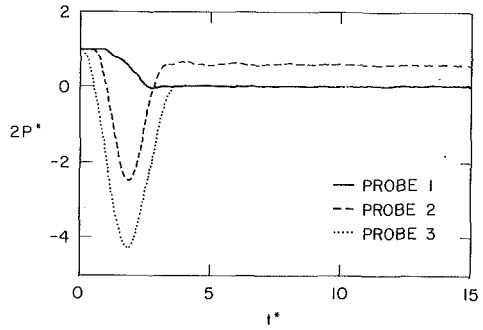

Fig. 9 Variation of pressure in 90-degree bend, by boundary control rapid convergence method

5 Discussions

Although the method presented herein is very much similar to that of Chorin's [3] artificial compressibility method, the two methods are based on somewhat different concepts. The weakly compressible flow equations with or without viscous terms (Eqs. 6 and 7 contain no viscous terms) represent the real flow phenomenon at small Mach number. They are more realistic than the corresponding incompressible flow equations because they retain the most essential term representing acoustic pressure. Because the governing equations are real flow equations for hydrodynamics and hydroacoustics, there is a much wider range of application beyond the solution of steady incompressible flow problems. The boundary control type rapid convergence method is derived from physical considerations.

The fact that an arbitrarily large M can be used when the weakly compressible flow equations are used to calculate a steady incompressible flow may require an explanation. In true compressible flow problems, shock waves that complicate the solution may be generated. In contrast, the weakly compressible flow equations are incapable of generating a supercritical condition no matter how large M may be. This situation is easily explainable by considering the one-dimensional case.

For one-dimensional flow, equations (6) and (7) reduce to

$$\frac{\partial p}{\partial t}+K\frac{\partial u}{\partial x}=0 \tag{21}$$

$$\frac{\partial u}{\partial t}+u\frac{\partial u}{\partial x}+\frac{\partial}{\partial x}\left(\frac{p}{\rho}\right)=0 \tag{22}$$

The characteristic speeds of the above equations are

$$C=\frac{dx}{dt}=\frac{u}{2}(1\pm\sqrt{1+4a^2/u^2}) \tag{23}$$

Clearly, the speed of the negative characteristics is always negative for any finite value of M. In other words, the flow is always subcritical and no shock wave exists.

Because the characteristic speeds, equation (23), are somewhat different from those of the compressible flow, the Courant stability condition will also be slightly different from that of the classical compressible flow computation. The difference becomes greater when larger M is used to speed up the convergence.

Although equations (6) and (7) can capture vorticity, the examples given in this paper yield only potential flows. This is because only uniform boundary conditions have been chosen for these examples. One way to generate a rotational flow is to feed vorticity at the upstream end. Song and Yuan [8] also showed the well known fact that a Kutta-Joukowsky condition may be used to automatically generate vorticity at a flow separation point. Because vorticity moves at a convective speed, a steady flow cannot be achieved in two natural periods. However, the speed of convergence can still be increased by choosing large M. More detailed analysis of rotational flow computations is beyond the scope of this paper.

6 Conclusions

1. When the Euler equations for weakly compressible fluids are used to solve for steady incompressible flow problems, the speed of sound may be arbitrarily reduced or the Mach number increased to speed up the convergence. The resulting solution is independent of the value chosen for M.
2. The transient part of the solution is accurate only when M is equal to or less than 0.2. In this range of Mach number, the acoustic portion of the solution is essentially that of the linear acoustic equations.
3. A very rapid convergence method based on boundary control or a valve stroking concept is proposed for the solution of steady incompressible flow problems. The speed of convergence in this case is independent of the Mach number assumed, and the solution is practically disturbance free.

Acknowledgment

A generous contribution of Cray-2 computer time by the Minnesota Supercomputer Institute which made this study possible is gratefully acknowledged.

References

1 Harlow, F. H., and Welch, J. E., "Numerical Calculation of Time-Dependent Viscous Incompressible Flow with Free Surface," *Physics of Fluids*, Vol. 8, Dec. 1985.

2 Kwak, D., "A Three-Dimensional Incompressible Navier-Stokes Flow Solver Using Primitive Variables," *AIAA Journal*, Vol. 124, No. 23, 1986, pp. 390-396.

3 Chorin, A. J., "A Numerical Method for Solving Incompressible Viscous Flow Problems," *Journal of Computational Physics*, Vol. 2, 1967, pp. 12-26.

4 O'Rourke, P. J., and Bracco, F. V., "Two Scaling Transformations for the Numerical Computation of Multi-Dimensional Unsteady Laminar Flow," *Journal of Computational Physics*, Vol. 33, 1979.

5 Ramshaw, J. D., O'Rourke, P. J., and Stein, L. R., "Pressure Gradient Scaling Method for Fluid Flow with Nearly Uniform Pressure," *Journal of Computational Physics*, Vol. 58, 1985.

6 Song, C. C. S., Yuan, M. and Bobko, G., "Prediction of Vortices," *Proceedings* of Advancements in Aerodynamics, Fluid Mechanics, and Hydraulics, Minneapolis, June 1986.

7 Song, C. C. S., and Yuan, M. "Numerical Modeling for a Vaned Miter Elbow," *Proceedings* of Advancements in Aerodynamics, Fluid Mechanics and Hydraulics," Minneapolis, June 1986.

8 Song, C. C. S., and Yuan, M., "Modeling Large Scale Vortices and Flow Separation," XXII IAHR Congress, Lausanne, Aug. 31-Sept. 4, 1987.

9 Wetzel, J. M., Song, C. C. S., Arndt, R. E. A., "Hydrodynamic Design of Large Cavitation Channel," *Proceedings* of Advancements in Aerodynamics, Fluid Mechanics, and Hydraulics, Minneapolis, June 3-6, 1986.

10 Wylie, E. B. and Streeter, V. L., *Fluid Transients*, McGraw-Hill, New York, 1978.

Details of the Computed Flowfield Over a Circular Cylinder at Reynolds Number 1200

C. L. Rumsey
Research Scientist,
Analytical Methods Branch,
Low-Speed Aerodynamics Division,
NASA Langley Research Center,
Hampton, VA 23665-5225

The application of an upwind-biased implicit approximate factorization Navier-Stokes algorithm to the unsteady impulsive start-up flow over a circular cylinder at Reynolds number 1200 is described. The complete form of the compressible Navier-Stokes equations is used, and the algorithm is second-order accurate in both space and time. The drag on the cylinder is computed for early times in the start-up flow. The value of the local maximum drag as well as the time at which it occurs are predicted and compared to another computational result and experiment. The development with time of the shape and size of the separated vortical flow region is computed, as well as the time-variation of several boundary layer parameters and profile shapes. Computations, in general, show excellent agreement with experiment, although the present method predicts a more rapid onset of reversed flow on the cylinder than evidenced in experiment. The effect of grid density on the development of the unsteady flow is also shown.

Introduction

Unsteady viscous flow problems do not lend themselves easily to computational analysis due to inherent turbulence, massive flow separation, and strong viscous/inviscid interaction. However, it is important to attempt to solve these types of flows since a number of problems of practical importance are unsteady. For example, flows around bluff bodies such as cables, external stores, or airfoils at very high angles-of-attack are generally unsteady and periodic in nature. Code validation for the latter case is difficult because of the scarcity of unsteady experimental results for airfoils.

Extensive experimental results for unsteady periodic flow around circular cylinders are available in the literature. These include the experiments and documentation of Thom [1], Morkovin [2], and Roshko [3]. Cylinders shed alternating vortices with a constant Strouhal number of approximately 0.21 between Reynolds numbers of about 200 to 10^5; Strouhal numbers are lower below this range and higher past Reynolds numbers of 10^5.

Experimental investigations of impulsive start-up flow around circular cylinders are also well-documented. Bouard and Coutanceau [4], Sarapkaya [5], Nagata et al. [6-9], for example, have quantified many parameters associated with this type of flow. Bouard and Coutanceau chiefly investigated the shape and growth rate of the wake region behind the cylinder for Reynolds numbers between 40 and 10^4. The work of Sarapkaya details the wake region development and lift and drag variation with time for cylinders between Reynolds numbers of 15,000 and 120,000. Finally, Nagata et al. investigated start-up flow at Reynolds numbers between 250 and 1200, with the majority of the experiments performed at $Re = 1200$. The authors give detailed results for the time-evolution of the vortical region, boundary layer parameters, and profile shapes at this Reynolds number.

A great number of computational studies have been performed on circular cylinder flow, both in an attempt to reproduce the Strouhal number of the unsteady periodic flow, as well as to accurately predict the wake region shape and growth rate for impulsive start-up flows. Lecointe and Piquet [10] used several compact schemes with the Navier-Stokes vorticity/stream function formulation to solve laminar flows around circular cylinders up to a Reynolds number of 9500. They studied both start-up and unsteady periodic phenomena. Predicted wake region shape as a function of time showed good agreement with experimental flow visualizations. The computations of Ta Phuoc Loc [11] included drag coefficient and wake region size predictions for the start-up computations over a circular cylinder up to $Re = 1000$. The complete Navier-Stokes equations were solved using a combination of second and fourth-order compact finite difference schemes. Rumsey et al. [12] used an upwind implicit approximate factorization Navier-Stokes algorithm to compare wake region growth behind a cylinder with experiment for $Re = 200$. In addition, an extensive study was undertaken at $Re = 174$ to determine the effects of grid density, grid extent, time step, and the thin-layer Navier-Stokes assumption on the resultant Strouhal number and lift variation for unsteady periodic flow.

The present paper details the laminar flow start-up computation around a circular cylinder at $Re = 1200$ using the implicit upwind Navier-Stokes code presented in reference [12]. This Reynolds number was chosen due to the wealth of experimental data available for comparison for this specific case [6-9]. Detailed comparisons between computation and experiment of wake region size, boundary layer parameters, and profile shapes as a function of time are made.

Contributed by the Fluids Engineering Division for publication in the JOURNAL OF FLUIDS ENGINEERING. Manuscript received by the Fluids Engineering Division November 17, 1987.

Governing Equations

The two-dimensional Reynolds-averaged Navier-Stokes equations can be written in generalized coordinates as[13]

$$\frac{\partial \hat{Q}}{\partial t}+\frac{\partial \hat{G}}{\partial \eta}+\frac{\partial \hat{H}}{\partial \zeta}=\overline{\mathrm{Re}}^{-1}\{\partial_\eta[\mathrm{J}^{-1}(\eta_x R+\eta_y S)]+\partial_\zeta[\mathrm{J}^{-1}(\zeta_x R+\zeta_y S)]\} \quad (1)$$

$$\hat{Q}=Q/\mathrm{J} \quad (2a)$$

$$\hat{G}=(\eta_x G+\eta_y H)/\mathrm{J} \quad (2b)$$

$$\hat{H}+(\zeta_x G+\zeta_y H)/\mathrm{J} \quad (2c)$$

$$Q=\begin{bmatrix}\rho\\ \rho u\\ \rho v\\ e\end{bmatrix}\quad G=\begin{bmatrix}\rho u\\ \rho u^2+p\\ \rho uv\\ u(e+p)\end{bmatrix}\quad H=\begin{bmatrix}\rho v\\ \rho uv\\ \rho v^2+p\\ v(e+p)\end{bmatrix} \quad (3)$$

$$p=(\gamma-1)[e-0.5\rho(u^2+v^2)] \quad (4)$$

where η is the coordinate along the body and ζ is the coordinate normal to the body.

The viscous terms on the right-hand side are given by

$$R=\begin{bmatrix}0\\ \tau_{xx}\\ \tau_{xy}\\ R_4\end{bmatrix}\quad S=\begin{bmatrix}0\\ \tau_{xy}\\ \tau_{yy}\\ S_4\end{bmatrix} \quad (5)$$

$$\tau_{xx}=(\lambda+2\mu)(\eta_x u_\eta+\zeta_x u_\zeta)+\lambda(\eta_y v_\eta+\zeta_y v_\zeta) \quad (6a)$$

$$\tau_{yy}=(\lambda+2\mu)(\eta_y v_\eta+\zeta_y v_\zeta)+\lambda(\eta_x u_\eta+\zeta_x u_\zeta) \quad (6b)$$

$$\tau_{xy}=\mu(\eta_y u_\eta+\zeta_y u_\zeta+\eta_x v_\eta+\zeta_x v_\zeta) \quad (6c)$$

$$R_4=u\tau_{xx}+v\tau_{xy}+\mu\mathrm{Pr}^{-1}(\gamma-1)^{-1}[\eta_x(a^2)_\eta+\zeta_x(a^2)_\zeta] \quad (6d)$$

$$S_4=u\tau_{xy}+v\tau_{yy}+\mu\mathrm{Pr}^{-1}(\gamma-1)^{-1}[\eta_y(a^2)_\eta+\zeta_y(a^2)_\zeta] \quad (6e)$$

Stokes hypothesis, $\lambda=-2/3\mu$ is used for bulk viscosity, and viscosity is evaluated with Sutherland's formula assuming a freestream temperature of 460 degrees Rankine. The coordinate transformation Jacobian is given by

$$\mathrm{J}=\eta_x\zeta_y-\eta_y\zeta_x \quad (7)$$

$$\eta_x=\mathrm{J}y_\zeta \qquad \eta_y=-\mathrm{J}x_\zeta$$
$$\zeta_x=-\mathrm{J}y_\eta \qquad \zeta_y=\mathrm{J}x_\eta \quad (8)$$

An implicit, upwind-biased, finite-volume scheme is used to solve (1). The system of equations is approximately factored (see Beam and Warming [14]) and solved in two sweeps:

$$[\frac{(1+\phi)I}{\nu\mathrm{J}\Delta t}+\partial_\eta{}^- A^+ +\partial_\eta{}^+ A^- -\overline{\mathrm{Re}}^{-1}\partial_\eta \mathrm{J}^{-1}N(\eta)]\Delta Q^*$$
$$=\{\frac{\phi}{\nu\mathrm{J}\Delta t}+\overline{\mathrm{Re}}^{-1}[\partial_\eta \mathrm{J}^{-1}N(\zeta)+\partial_\zeta \mathrm{J}^{-1}\mathrm{M}(\eta)]\}\Delta Q^{n-1}-\frac{\mathrm{RHS}}{\nu} \quad (9a)$$

Nomenclature

a = speed of sound
A,B,M,N = Jacobian matrices
b = width of cylinder wake region
c_d = drag coefficient ($=c_{dp}+c_{df}$)
c_{df} = skin friction drag coefficient
c_{dp} = pressure drag coefficient
c_f = coefficient of friction
d = cylinder diameter (=length scale l)
e = total energy per unit volume, nondimensionalized by $\rho_\infty a_\infty{}^2$
G,H = fluxes of mass, momentum and energy
I = identity matrix
J = transformation Jacobian
L = length of cylinder wake region
M = freestream Mach number
n = shedding frequency, nondimensionalized by a_∞/l
p = pressure, nondimensionalized by $\rho_\infty a_\infty{}^2$
Pr = Prandtl number, taken as 0.72
Q = conservation variables
r = distance outward from body
R,S = viscous terms of the Navier-Stokes formulation
Re = Reynolds number, $\rho_\infty u_\infty l/\mu_\infty$
$\overline{\mathrm{Re}}$ = Reynolds number, $\rho_\infty a_\infty l/\mu_\infty$
RHS = right-hand-side term of Navier-Stokes equation
s = thickness of reversed flow region
St = Strouhal number, nd/u_∞
t = time, nondimensionalized by l/a_∞
t^* = time, nondimensionalized by l/u_∞
u,v = Cartesian velocities in x and y directions, respectively, nondimensionalized by a_∞
x,y = Cartesian coordinates
Xc,Yc = location of vortex center
γ = ratio of specific heats, taken as 1.4
δ = boundary layer thickness
ΔQ = $Q^{n+1}-Q^n$
Δt = time step
η,ζ = general curvilinear coordinates
Θ = angle around the cylinder from the point facing upstream, in degrees
λ = coefficient of bulk viscosity
μ = coefficient of molecular viscosity
ρ = density, nondimensionalized by ρ_∞
$\tau_{xx},\tau_{xy},\tau_{yy}$ = viscous shear stress terms
ϕ, ν = time-accuracy parameters

Subscripts

max = maximum
min = minimum
x,y = denotes differentiation in x and y directions, respectively
η,ζ = denotes differentiation in η and ζ directions, respectively
∞ = denotes conditions at infinity

Superscripts

n = denotes time level
$\hat{}$ = denotes quantities in generalized coordinates

$$\left[\frac{(1+\phi)I}{\nu J\Delta t}+\partial_\zeta{}^- B^+ +\partial_\zeta{}^+ B^- - \overline{\mathrm{Re}}^{-1}\partial_\zeta J^{-1}\mathrm{M}(\zeta)\right]\Delta Q=\frac{(1+\phi)\Delta Q^*}{\nu J\Delta t} \tag{9b}$$

$$\mathrm{RHS}=\partial_\eta{}^- \hat{G}^+ +\partial_\eta{}^+ \hat{G}^- +\partial_\zeta{}^- \hat{H}^+ +\partial_\zeta{}^+ \hat{H}^- - \overline{\mathrm{Re}}^{-1}\{\partial_\eta[J^{-1}(\eta_x R+\eta_y S)] + \partial_\zeta[J^{-1}(\zeta_x R+\zeta_y S)]\} \tag{10}$$

The (+) and (−) superscripts indicate positive and negative flux split quantitites, according to the flux vector splittings of Van Leer [15], differenced with fully upwind backward and forward differences, δ^- and δ^+, respectively. All viscous terms are centrally differenced. The A and B matrices are linearizations of the G and H fluxes: $A=\partial\hat{G}/\partial Q$, $B=\partial\hat{H}/\partial Q$. M and N arise from the linearizations of viscous terms in the ζ-direction and η-direction, respectively, with

$$\mathrm{M}=\partial(\zeta_x R+\zeta_y S)/\partial Q \tag{11}$$

$$N=\partial(\eta_x R+\eta_y S)/\partial Q \tag{12}$$

These matrices are split into two parts:

$$\mathrm{M}=\mathrm{M}(\zeta)+\mathrm{M}(\eta) \tag{13}$$

$$N=N(\zeta)+N(\eta) \tag{14}$$

where ζ and η in parentheses indicate that only terms with derivatives in ζ or η, respectively, are retained. The spatial cross-derivative terms, $\partial_\zeta J^{-1}\mathrm{M}(\eta)$ and $\partial_\eta J^{-1}N(\zeta)$ are treated explicitly, lagged in time, while $\partial_\zeta J^{-1}\mathrm{M}(\zeta)$ and $\partial_\eta J^{-1}N(\eta)$ are treated implicitly. Implicit spatial derivatives of the convective and pressure terms are first order accurate, resulting in block tridiagonal inversions for each sweep.

This method is second order accurate in space [12, 16], and can be either first or second order accurate in time, depending on the values of ν and ϕ:

$$\text{1st order time } \nu=1 \quad \phi=0 \tag{15a}$$

$$\text{2nd order time } \nu=1 \quad \phi=1/2 \tag{15b}$$

For all of the applications in this paper, equation (15*b*) is used.

Boundary conditions are applied explicitly. No slip, as well as zero pressure gradient conditions are applied on the body:

$$u=v=0 \tag{16a}$$

$$\frac{\partial p}{\partial \zeta}=0 \tag{16b}$$

Also, specified constant wall temperature, set equal to the freestream total temperature, is imposed on the body. In the farfield, the subsonic freestream boundary conditions are determined through a characteristic analysis normal to the boundary. Details can be found in Thomas and Salas[17].

Results and Discussion

Computations were performed for the flow around a circular cylinder at M = 0.3, Re = 1200. At very low Mach numbers, the compressible Navier-Stokes equations become stiff, and lower time steps are required to advance the solution. The Mach number of 0.3 chosen for the present computations is high enough to be computationally tractable, yet still provides a reasonable representation of the incompressible conditions present in the experiment of references [6 through 9]. The computational grid used is a 197 × 97 O-mesh, shown in Figs. 1(*a*) and (*b*). Minimum spacing at the wall is 0.001 d, and the maximum grid extent is 20 d (the outer boundary is a distance 19.5 d from the cylinder surface). For all calculations up to $t^*=0.6$, a time step of $\Delta t=0.01$ was used. Past this time, larger time steps were used in order to advance the solution more quickly: $\Delta t=0.02$ between $t^*=6.0$ and 9.0, and $\Delta t=0.05$ above $t^*=9.0$.

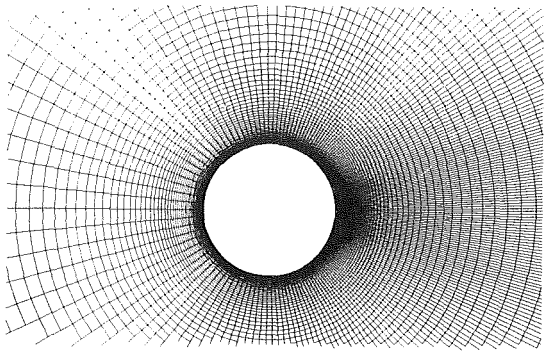

Fig. 1(*a*) Near grid

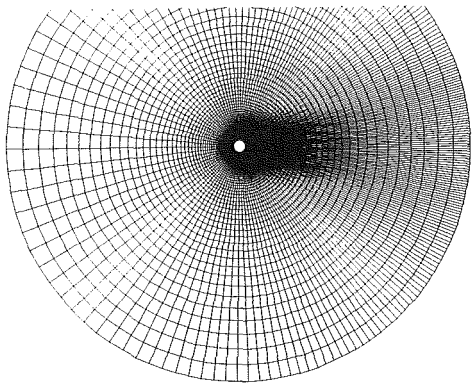

Fig. 1(*b*) Far-field grid

Fig. 1 197 × 97 O-mesh, $\Delta r_{min} \approx 0.001\ d, r_{max} = 20d$

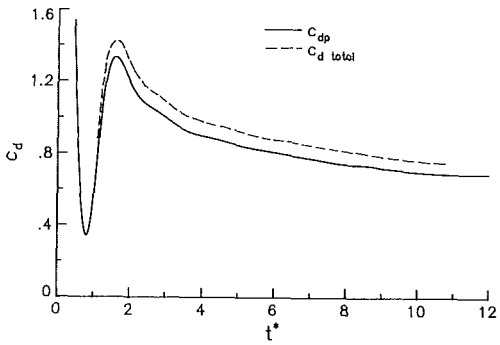

At the start of the computation, freestream conditions are imposed on the entire flowfield, modeling instantaneous acceleration to M = 0.3. Figure 2 shows the drag coefficient at times up to $t^*=12$. Upon the impulsive start of the circular cylinder flow, the drag coefficient jumps to a value of about 10, then decreases very rapidly as the flow sets up. A minimum drag occurs at approximately $t^*=0.8$, and a local drag maximum occurs at about $t^*=1.6$. Both pressure drag coefficient and total drag coefficient are plotted. The values of the local maximum drag coefficient are $c_{dp}=1.336$ and $c_{df}\approx 0.1$ for a total c_d of about 1.44. Sarpkaya [5] experimentally determined the local maximum drag coefficient value for start-up cylinder flows between Re = 15,000 and 120,000. He found that the maximum drag occurred near $t^*=4$ with a value between $c_d=1.4$ and 1.6. However, in a later report, Sarpkaya [18] reported a maximum drag between 1.5 and 1.6 to occur between $t^*=2$ and 2.5 for Reynolds numbers on the order of

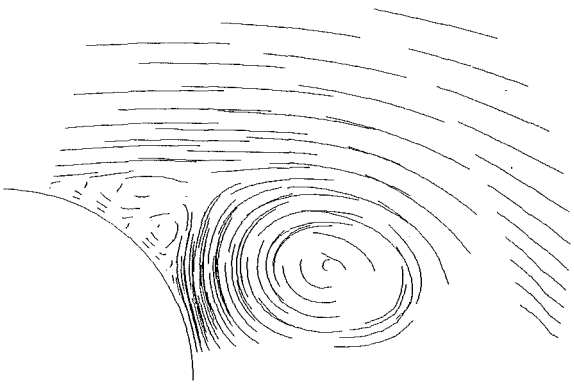

Fig. 3 Computed pathlines at $t^* = 2.4$

30,000. Hall [19] attributed these lower t^* values to a higher rate of acceleration during the tunnel start-up period. In other words, the experimental results from reference [18] more accurately represent an impulsively started cylinder than the results from reference [5]. The present computations, which model instantaneous acceleration to freestream, agree better with the data from the more rapidly accelerated experiment, as expected. Computationally, Ta Phuoc Loc [11] determined that a local maximum drag coefficient of about 1.2 occurs at $t^* = 2.0$ for a Reynolds number of 1000. This time to local maximum c_d agrees reasonably well with the present method.

If the computations are carried out long enough, machine-zero sized round-off errors result in asymmetries in the flowfield which grow in magnitude and eventually lead to periodic vortex shedding. Although not shown, present computations which are carried out to this extent yield a periodic flow with a Strouhal number of 0.222. This compares well with the experimental value of approximately 0.21. [2, 3]. The computed lift coefficient varies between -1.59 and 1.59, and pressure drag coefficient varies between 1.27 and 1.78.

In the experiments of Nagata et al. [9], the wake region shape was determined by taking time-lapse photographs of the flowfield containing aluminum dust tracers. The photographs thus represent flowfield pathlines. Pathlines are tedious to compute, however, since a significant amount of flowfield information prior to the time in question is required. Therefore, stream function contours are used in the present study to determine the wake region parameters. A comparative study at $t^* = 2.4$ between computed pathlines in Fig. 3 and computed stream function contours in Fig. 4(*d*) shows that both predict the exact same location of the vortex center: $Xc/d = 0.86$ and $Yc/d = 0.31$. Also, the wake regions appear to be about the same size. On the basis of this comparison it is believed that, at least for the purposes of this paper, the stream function contours depict wake region size and shape accurately enough.

Figures 4(*a*) through (*f*) depict the early development of the cylinder flowfield in comparison with the experimental pathlines. At all six times, the computed shape of the wake region agrees well with experiment. Details of the stream function contours near the surface of the cylinder are also given. These figures depict flowfield phenomena which were seen by Bouard and Coutanceau [4] in their experimental investigation. At $t^* = 1.1$ (Fig. 4(*a*)) the first evidence of a bulge phenomenon is seen, where a small distortion in the streamlines occurs at the body behind the separation point. Experimentally, this bulge first appears past $t^* = 1$. This bulge gives rise to an isolated secondary eddy at $t^* = 1.3$ (Fig. 4(*b*)), as was also seen in the experiments. By $t^* = 1.9$ (Fig. 4(*c*)), the isolated eddy has grown enough to reach the boundary of the main recirculating zone. This splits the main eddy into two parts, so that another secondary eddy is formed upstream of the first. Bouard and Coutanceau noticed this "α-phenomenon" past $t^* = 1.5$, in good agreement with the present results. Beginning at $t^* = 2.4$ (Fig. 4(*d*)) and continuing through $t^* = 2.9$ and 3.1 (Figs. 4(*e*) and (*f*)) the "α-phenomenon" disappears as the original secondary eddy decreases in size.

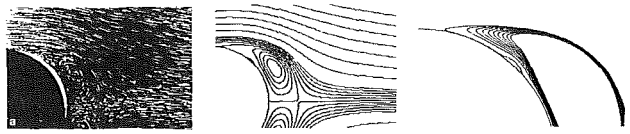

Fig. 4(*a*) $t^* = 1.1$, $c_d = 0.887$

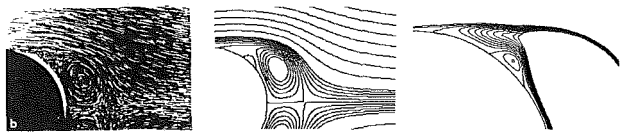

Fig. 4(*b*) $t^* = 1.3$, $c_d = 1.259$

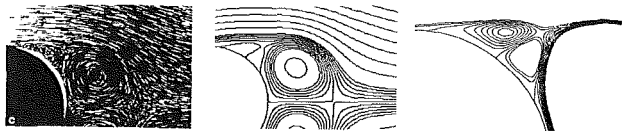

Fig. 4(c) $t^* = 1.9$, $c_d = 1.338$

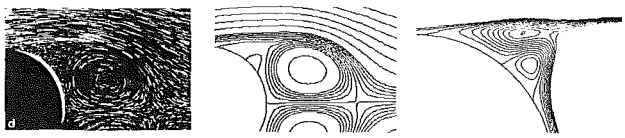

Fig. 4(*d*) $t^* = 2.4$, $c_d = 1.175$

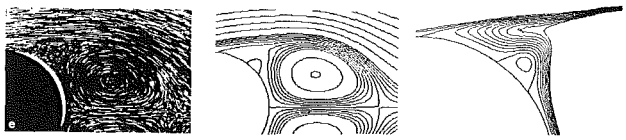

Fig. 4(*e*) $t^* = 2.9$, $c_d = 1.103$

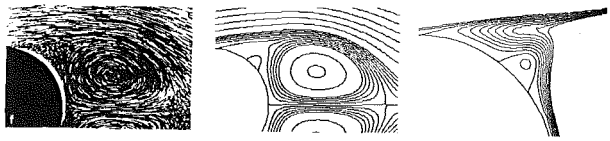

Fig. 4(*f*) $t^* = 3.1$, $c_d = 1.071$

Fig. 4 Development of the flow behind the cylinder: experimental pathlines, stream function contours in the wake, stream function contours near the cylinder

Figure 5 is a plot of various computed wake region parameters as a function of time, in comparison with the experimental results of Nagata et al.[9]. Although the length of the wake region is slightly overpredicted past $t^* = 2.0$, and Yc and b are computed a few percent high prior to $t^* = 2.5$, results overall agree very well. The effect of the grid size on these results will be discussed below.

As the flow develops in impulsively started flow, the separation point on the cylinder moves very rapidly from the rear stagnation point ($\Theta = 180$ deg) forward. A plot of the separation angle versus time, Fig. 6, shows that present theory generally underpredicts the experiment of Nagata et al. [7, 8] past about $t^* = 0.4$. This indicates that the separation point moves forward more quickly in the computations past $t^* = 0.4$ than in the experiment. This conclusion is borne out as well in a plot of skin friction versus time, Fig. 7. At $\Theta = 130$ deg, the time at which skin friction goes to zero (approximately $t^* = 0.4$) is nearly the same for theory and experiment. At

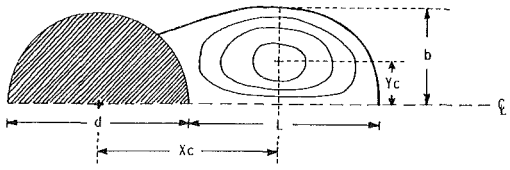

Fig. 5(a) Schematic representation

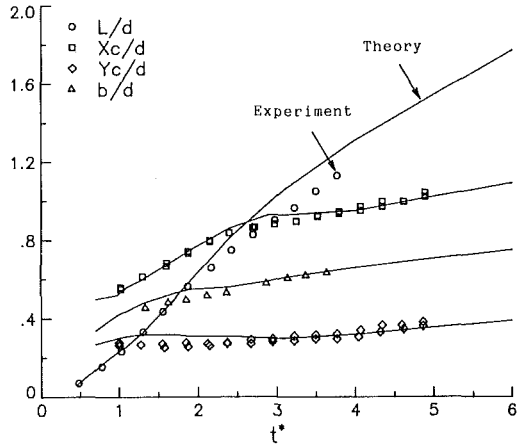

Fig. 5(b) Computed and experimental results

Fig. 5 Time history of the location of the vortex center and the size of the wake region

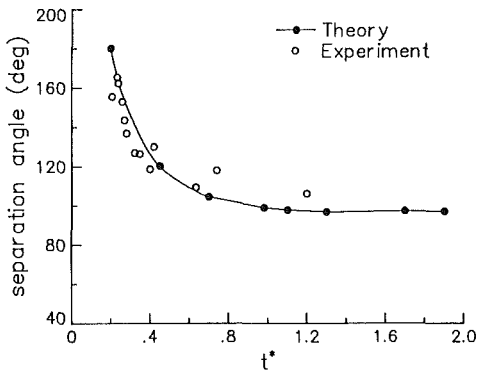

Fig. 6 Time history of separation angle

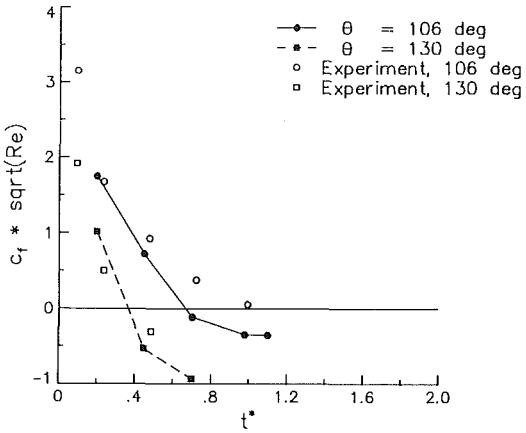

Fig. 7 Time history of skin friction coefficient at two locations

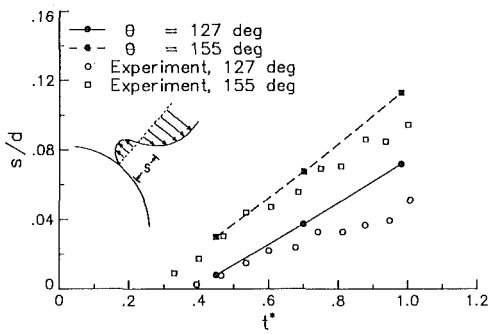

Fig. 8 Time history of reversed flow thickness at two locations

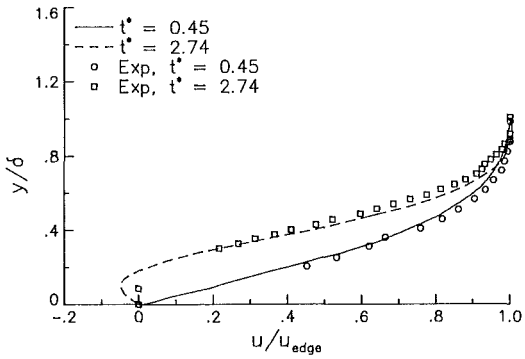

Fig. 9 Boundary layer profiles at θ = 106 deg

$\Theta = 106$ deg, however, computed flow reaches a skin friction of zero close to $t^* = 0.7$, while experiment shows zero skin friction past $t^* = 1$.

Figure 8 shows thickness of the region of reversed flow, s, versus time at two positions on the cylinder. At both $\Theta = 127$ and 155 deg, the present theory predicts a more rapid growth rate of the reversed flow region than the experiments of Nagata et al. [7]. Boundary layer profiles at $\Theta = 106$ deg are shown in Fig. 9 at two times of $t^* = 0.45$ and $t^* = 2.74$. Results agree very well with experiment, with the exception that the computed boundary layer at $t^* = 2.74$ shows a larger reversed flow region than the computations. All of these results are consistent with the fact that computations predict a more rapid movement of the separation point forward on the cylinder than experiment.

Figure 10(*a*) shows the horizontal velocity component on the symmetric axis of the wake at $t^* = 2.9$ in comparison to the experiment of Nagata et al. [9]. Negative values indicate reversed flow (i.e., toward the cylinder). Theory and experiment agree fairly well, although theory shows a larger bubble length (reversed flow up to $x/d = 1.49$, corresponding to $L/d = 0.99$), and the peak reversed flow velocity of $u/u_\infty = 1.28$ is lower than the experimental peak value of 1.4. A plot of maximum reversed flow velocity versus time in Fig. 10(*b*) shows that the present theory consistently underpredicts its value in comparison to experiment, but shows the same change in slope near $t^* = 3$.

Finally, the effect of grid size on the start-up circular cylinder solution is shown. Two grids in addition to the 197×97 O-mesh were used to compute the cylinder flow up to $t^* = 2.4$. These meshes are 99×49 and 50×25, respectively. Each successively coarser grid was created by removing every other grid point from the finer grid. In this way, an identical stretching distribution over the three grids is maintained. Figure 11 shows c_{dp} versus t^* for the three meshes. Both the finer grids produce nearly identical results, while the coarsest mesh overpredicts the local minimum drag value, and obtains the local maximum drag at a time $t^* = 1.8$, as opposed to $t^* = 1.6$ for the finer meshes.

The discriminating streamline shape is plotted for each of the three grids in comparison to experiment in Fig. 12. The

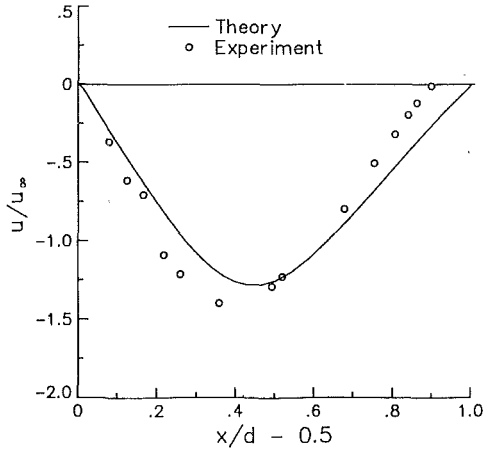

Fig. 10(*a*) Velocity distribution at $t^* = 2.9$

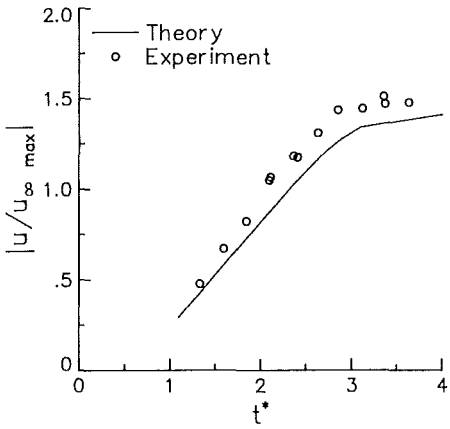

Fig. 10(*b*) Time history of the maximum reverse flow velocity

Fig. 10 Velocities on the symmetric axis of the wake

197×97 mesh comes closest to representing the shape of the bubble, although the length of the bubble is slightly overpredicted and the center of the vortex is predicted downstream and further from the center-line than that of the experiment. The finest mesh also shows a secondary recirculation eddy in close agreement with experiment. The 99×49 grid overpredicts the length of the vortical region even more, but yields the same vortex center location as the finest mesh. It predicts a secondary recirculation eddy that is significantly smaller than experiment. Finally, the coarsest mesh grossly underpredicts the width of the wake bubble, with the vortex center too close to the cylinder, and does not show any evidence of the secondary eddy at all. The present method has been demonstrated to be second order accurate in space [12, 16], i.e., doubling the mesh reduces truncation error by a factor of four. From the trends evident in Fig. 12, the 197×97 mesh appears to be fine enough to adequately model the discriminating streamline shape for the present application to start-up circular cylinder flow.

Summary

The present upwind Navier-Stokes method has been used to predict the unsteady laminar flow around a circular cylinder from impulsive start-up. The local maximum drag during the start-up flow is computed to be 1.44 at $t^* = 1.6$, and the Strouhal number of the computed periodic flow is 0.222. These values show generally good agreement with experiment. The development of the wake region through $t^* = 3.1$ is compared to experimental flow visualizations, and boundary layer parameters, skin friction, and profile shapes are compared to experimental results at early times below $t^* = 5$. Results are found to agree very well with experiment, although the present method predicts a more rapid onset of reversed flow over the cylinder than experiment. The effect of grid size on the start-up circular cylinder solution is also shown. The drag force variation with time is resolved by a grid as coarse as 99×49. However, the 99×49 grid results in a computed vortical region which is too long and an isolated secondary eddy which is too small in comparison with experiment. The finer 197×97 grid improves correlation with experiment.

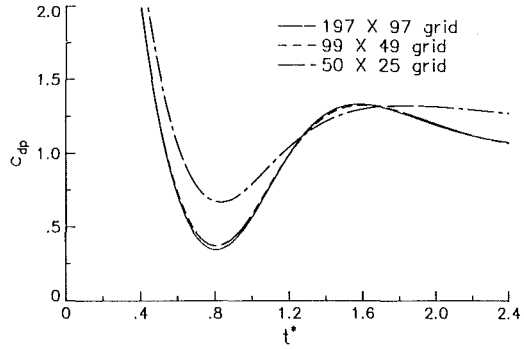

Fig. 11 Effect of grid size on drag coefficient time history

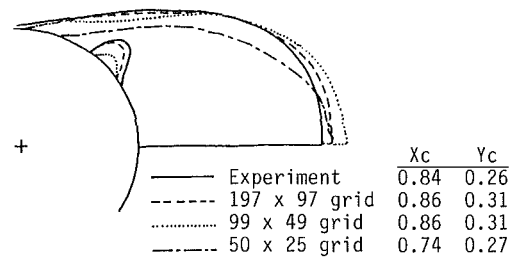

Fig. 12 Effect of grid size on the location of the vortex center and the size of the wake region, $t^* = 2.4$.

References

1 Thom, A., "The Flow Past Circular Cylinders at Low Speeds," *Proc. Roy. Soc.*, Series A141, 1933, pp. 651–669.

2 Morkovin, M., "Flow Around Circular Cylinder—A Kaleidoscope of Challenging Fluid Phenomena," ASME Symposium on Fully Separated Flows, 1964, pp. 102–118.

3 Roshko, A., "On the Development of Turbulent Wakes From Vortex Streets," NACA TN 2913, 1953.

4 Bouard, R., and Coutanceau, M., "The Early Stage of Development of the Wake Behind an Impulsively Started Cylinder for $40 < Re < 10^4$," *J. Fluid Mech.*, Vol. 101, Part 3, 583, 1980, pp. 583–607.

5 Sarpkaya, T., "Separated Flow About Lifting Bodies and Impulsive Flow About Cylinders," *AIAA Journal*, Vol. 3, No. 3, 1966, pp. 414–420.

6 Nagata, H., Kakehi, Y., Tsunekawa, M., and Hasegawa, T., "Unsteady Flow Past a Circular Cylinder Started Impulsively," *JSME*, Vol. 18, No. 123, 1975, pp. 992–1001.

7 Nagata, H., Minami, K., and Murata, Y., "Initial Flow Past an Impulsively Started Circular Cylinder," *JSME*, Vol. 22, No. 166, 1979, pp. 512–520.

8 Nagata, H., Matsui, T., and Ichikawa, M., "Velocity Field of the Flow Around a Circular Cylinder Started Impulsively, 2nd Report, Unsteady Boundary Layers," *JSME*, Vol. 23, No. 179, 1980, pp. 696–704.

9 Nagata, H., Funada, H., and Matsui, T., "Unsteady Flows in the Vortex Region Behind a Circular Cylinder Started Impulsively, 2nd Report, Velocity Fields and Circulations," *JSME*, Vol. 28, No. 245, 1985, pp. 2608–2616.

10 Lecointe, Y., and Piquet, J., "On the Use of Several Compact Methods for the Study of Unsteady Incompressible Viscous Flow Round a Circular Cylinder," *Computers & Fluids*, Vol. 12, No. 4, 1984, pp. 255–280.

11 Ta Phuoc Loc, "Numerical Analysis of Unsteady Secondary Vortices Generated by an Impulsively Started Cylinder," *J. Fluid Mech.*, Vol. 100, Part 1, 1980, pp. 111–128.

12 Rumsey, C., Thomas, J., Warren, G., and Liu, G., "Upwind Navier-Stokes Solutions for Separated Periodic Flows," AIAA Paper 86-0247, 1986.

13 Pulliam, T., "Euler and Thin Layer Navier-Stokes Codes: ARC2D, ARC3D," *Computational Fluid Dynamics*, UTSI Publication No. E02-4005-023-84, Tullahoma, Tenn., 1984, pp. 15.1-15.85.

14 Beam, R., and Warming, R., "An Implicit Factored Scheme for the Compressible Navier-Stokes Equations," *AIAA Journal*, Vol. 16, No. 4, 1978, pp. 393-402.

15 Van Leer, B., "Flux-Vector Splitting for the Euler Equations," ICASE Rept. No. 82-30, 1982; also: Lecture Notes in Physics, Vol. 170, 1982, pp. 501-512.

16 Belk, D., "Unsteady Three-Dimensional Euler Equations Solutions on Dynamic Blocked Grids," PhD Dissertation, Mississippi State, Mississippi, 1986.

17 Thomas, J., and Salas, M., "Far-Field Boundary Conditions for Transonic Lifting Solutions to the Euler Equations," AIAA Paper 85-0020, 1985.

18 Sarpkaya, T., "Impulsive Flow About a Circular Cylinder," Naval Postgraduate School, Publication No. NPS-6956-78-008, Monterey, Calif. 1978.

19 Hall, R., "Forebody and Missile Side Forces and the Time Analogy," AIAA Paper 87-0327, 1987.

Studies of Power Station Feed Pump Loss of Suction Pressure Incidents

R. R. Cranfield

Central Electricity Generating Board,
Technology Planning and Research Division,
Southampton, UK

Open cycle feed systems featuring a deaerator followed by the boiler feed pumps have been subject to unexpected loss in net positive suction head during transient operation. This has been traced to separation at the deaerator storage tank drain and the formation of a steam/water interface in the downcomer to the pumps. The outflow at separation when the storage tank water is subcooled is generally much greater than the maximum suction flow corresponding to the unit rating, but when the tank water boils, as during transients, it may be very much less. Thus with a high suction flow in the boiling mode, the new interface may descend in the downcomer to result in feed pump cavitation, pressure imbalance, vapor locking, severe vibration, damage to the pump and an inability to maintain forward flow. Model tests have been conducted to establish the criterion for the separation in terms of the critical outflow for specific operating conditions as a function of geometric ratios involving tank-water depth and tank/downcomer dimensions. The data obtained although scattered are in general agreement with the data from actual plant and may be used to assess safe operating parameters.

1 Introduction

This study focuses on open-cycle feed systems that feature a deaerator (D/A) which is a crucial component. In addition to providing condensate heating, deaeration and buffer storage over a wide range of normal and abnormal operating conditions, the elevation of the D/A storage tank (S/T) is utilized to provide a net positive suction head (NPSH) on the boiler feed pumps (BFP).

In recent years, increases in the rating of plant have meant that greater quantities of steam and water are handled in deaerators which have been scaled-up. Several forced and costly outages in the US have been attributed to deaerator failures (Liao, 1973). Realizing this, EPRI contracted with Sulzer Brothers Limited to collect and review existing knowledge on the problems (EPRI Report CS-4204, 1985).

Although the thermal performance has remained excellent, deaerators continue to be subject to noise and vibration (O'Connell and Rauscher, 1980). Other problems encountered are the loss of the deaerating function at high loads (Cranfield, 1982), S/T contents sloshing with the serious risk of a destructive "water-piston" phenomenon arising in the tank (Cranfield and Wilkinson, 1981) and loss of NPSH on the boiler feed pumps during transient operating conditions.

A loss of NPSH has been associated with, for example, rapid shutdown or load reduction of the main turbine giving rise to a steep decay in deaerator pressure. Also there are numerous circumstances where transient disturbances in the feed system may give rise to difficulties—for example where the water flow to the D/A is subjected to a rapid flow increase or temperature decrease caused by the condensate control valve opening or feed heater or deaerator bled steam valve (BSV) closing, Fig. 1.

These transients may result in the S/T water boiling while the D/A pressure decays to a thermal equilibrium at a lower pressure.

Models have been proposed to provide power plant engineers with methods for determining the limiting rate of D/A pressure decay to ensure that an adequate NPSH is maintained to prevent flashing at the BFP by Gage (1952), Karassik (1960), Thurston (1971) and Liao (1974). These models are based upon the assumption that the full deaerator hydrostatic head is applied to the BFP throughout the period of the pressure decay.

In plants where the rate of D/A pressure decay appears insufficient to cause difficulties with the BFP NPSH on the basis of the above models difficulties have nevertheless arisen; and Karassik (1981) has described how the use of so-called "anti-flashing" baffling in deaerators has proved of negligible value in overcoming this problem.

This paper examines the general question of deaerated water outflow from horizontal cylindrical tanks through square-edged drains and flooded vertical downcomers.

2 System Description and Experience

For cheapness and convenience of construction the tank drain orifice is usually flush and square-edged, formed simply by the abutment of the long vertical downcomer pipe to the suction pumps as shown in Fig. 1. The drain may be preceded

Contributed by the Fluids Engineering Division for publication in the JOURNAL OF FLUIDS ENGINEERING. Manuscript received by the Fluids Engineering Division April 30, 1987.

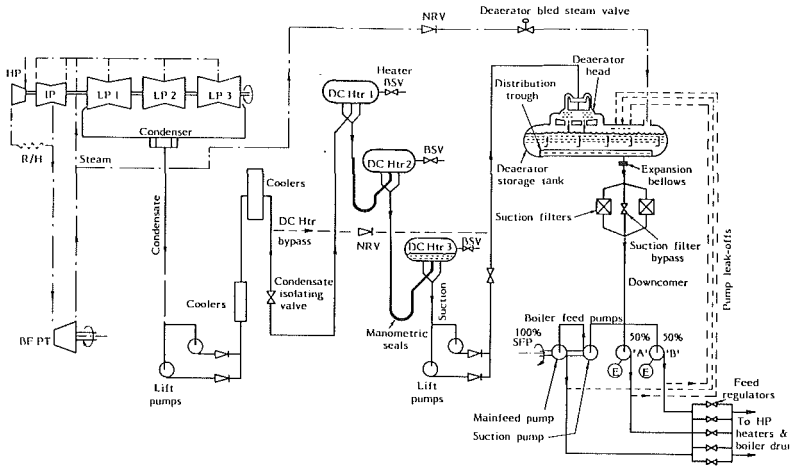

Fig. 1 Diagrammatic layout of an open cycle feed system

by flow through an open-ended and slotted inverted trough running almost the entire length of the tank, and intended to distribute the suction and inhibit the formation of stagnation zones.

The vertical downcomer may incorporate a corrugated expansion bellows and perhaps suction filters as shown in Fig. 1.

Satisfactory NPSH at the BFP has generally been maintained during steady operation. However, under transient operating conditions, difficulties have been experienced with loss of NPSH causing vapor locking of the BFP, pump overspeeding and an inability to maintain condensate flow. In some cases, loss of suction head or overspeeding has tripped the unit. Pump damage may also occur due to hydraulic shock on a sudden change of the fluid pumped and pressure imbalance across the pump, although BFP's now used may be capable of surviving disturbed suction conditions without failure (Otway (1969-70)).

A few specific examples are now given.

Case 1. Power station "A," having 500 MW units, a single downcomer 0.508 m in diameter, S/T 4.58 m in diameter, with the normal S/T water level of 4.11 m, MCRF 418 kg/s.

In Fig. 2 are shown how some of the relevant parameters change during a loss of feed incident. Operating close to full load of 500 MW a D/A high water level trip occurred (due to a faulty level detector). The trip signal initiated closure of the condensate isolating valve and BSV's on all the direct-contact (DC) heater and the D/A (Fig. 1). Deprived of bled steam enthalpy the pressure in the D/A immediately began to decay. Attempts were then made to re-establish the unit by opening the condensate isolating valve to restore condensate flow to the D/A. However, difficulty was experienced with repeated reclosure of the valve due to instability in the DC2 to DC3 manometric seal retripping the valve on heater high water levels. This resulted in oscillation in the BFP suction pump inlet pressure as condensate surged into the D/A. During this period the unit load was reduced to about 260 MW correspondingly reducing feed flow to the boiler drum and suction flow from the D/A and the drum level began to fall. At about 200 s from the initial trip condensate flow was fully reestablished and the drum level raised to normal. With the feed increased to about 54 percent MCRF at about 380 s a steep decay in BFP suction pressure was experienced, sufficient to cause the NPSH to fall below the manufacturers specification of 17 m WG (1.64 bar) and the suction pressure to converge

Nomenclature

C_D = coefficient of discharge (orifice flow)
g = gravitational acceleration, m/s^2
H = water depth in horizontal tank, m
H' = expanded (boiling) water depth in horizontal tank, m
p_H = hydrostatic pressure of tank water at drain orifice, N/m^2
p_f = pressure of steam in tank, N/m^2
p_v = vapour pressure of steam corresponding to tank water temperature, N/m^2
Q = total volumetric water flow rate in a single downcomer, m^3/s or l/s
Q_{sc}^c = total volumetric water flow rate in a single downcomer at separation in sub-cooled discharge, m^3/s
Q_B^c = total volumetric water flow rate in a single downcomer at separation in boiling discharge, m^3/s
r = internal radius of downcomer, m
R = internal radius of tank, m
t = time, s
U = water velocity, m/s
$\bar{U}^c$ = mean water velocity in a single downcomer at separation in boiling discharge, m/s
α = velocity coefficient
ρ = density, kg/m^3

Abbreviations

BFP = boiler feed pump
BFPT = boiler feed pump turbine
BSV = bled steam valve
D/A = deaerator
EFP = electric feed pump
DC = direct contact
HP = high pressure
IP = intermediate pressure
LP = low pressure
MCR = maximum continuous rating
MCRF = maximum continuous rating flow
NWL = normal water level
NPSH = net positive suction head
P.S. = power station
R/H = reheater
SFP = steam feed pump
S/T = storage tank
WG = water gauge

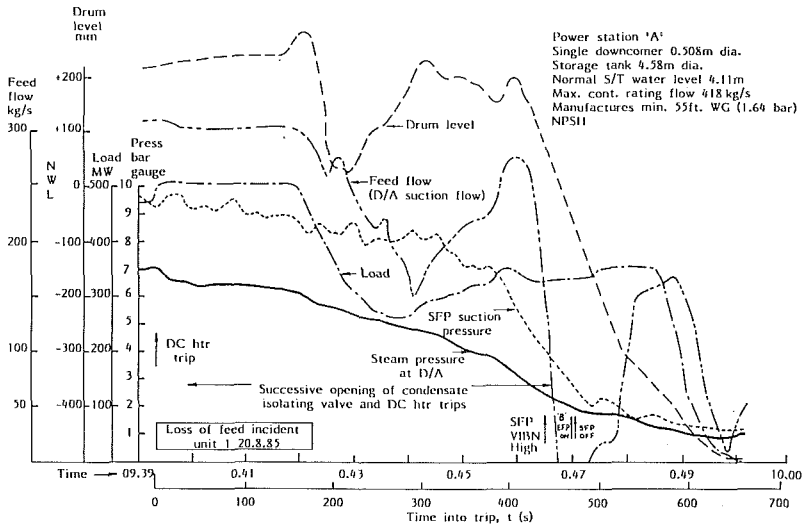

Fig. 2 Power Station "A." Recorded data during a loss of boiler feed pump net positive suction head incident.

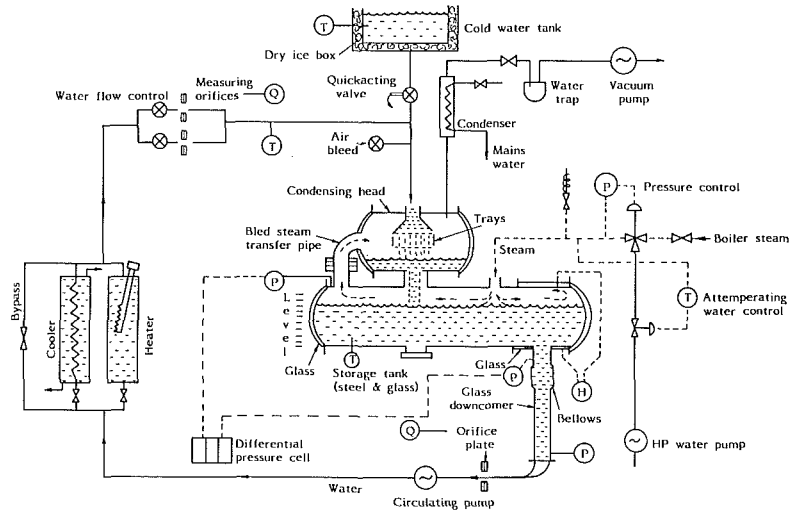

Fig. 3 Schematic of experimental apparatus

with the decaying D/A storage tank steam pressure. At about 410 s the feed flow had rapidly terminated, accompanied by the onset of severe vibration of the BFP and a rapid fall in drum level. At the same time, probably as a result of loss of pumping torque, the steam driven 100% MCRF main pump oversped which initiated its automatic trip-out and started a 50% MCRF electric standby pump (Fig. 1). This was followed by a surge in feed as the initially "cold" water in the electric pump inlet manifold was depleted. However, this pump also soon succumbed to the same difficulty and the flow again ceased. The boiler drum level could not be restored and so the unit was taken off-load. Other responses of the unit operators on seeing a termination of forward flow to the boiler drum has been to open the feed regulators wider. Again, this fails to rectify the situation. From experience it was found necessary to decrease the suction flow from the D/A by closing the feed regulators, described (correctly as will be shown) by the operators as "reflooding the system," in order to re-establish normal feed flow.

Case 2. Power station "B," 660 MW units, single downcomer 0.421 m diameter, S/T 4.27 m diameter, normal S/T water level 3.05 m, MCRF 423 kg/s.

During its early operation the units suffered repeated loss of BFP NPSH and some pump damage. Fortunately, in order to make accurate D/A outflow measurements for heat balance data, the S/T was provided with two parallel 0.374 m diameter downcomers which join the main downcomer just before the BFP at about 23 m below the S/T. Since operating on all three downcomers loss of NPSH during transient conditions has not occurred.

Case 3. Power station "C," 660 MW units, single downcomer of 0.457 m diameter, S/T 4.27 m diameter, normal S/T water level 3.35 m, MCRF 744 kg/s.

These units have a feed heater bypass facility as shown in Fig. 1. Following a trip which closed the condensate control valve, water from the condenser was pumped directly to the D/A causing a drop in the D/A inlet temperature from 120°C to 30°C in about 30 seconds. Normally the D/A BSV would remain open on bypass but a fault occurred whereby the BSV closed and a loss of BFP NPSH resulted. To guard against a recurrence the S/T outlet was increased to 0.788 m diameter and the downcomer provided with a conical inlet.

In Case 1 the immediate impression was that the downcomer suction filters (Fig. 1) had become sufficiently

blocked, possibly by the disturbance in the S/T water during transient operation stirring-up debris, to cause a high filter differential pressure with a fall of the local static pressure below vapor pressure. However, the filters were found to be clean and the differential pressure across the filter low. Indeed, opening the filter bypass does not prevent loss of suction incidents.

3 Apparatus

The apparatus, constructed in steel and glass and shown schematically in Fig. 3, did not scale any particular plant, as it was intended to examine discharge from feed heaters and deaerators in general. The fluids used were steam drawn from an adjacent package boiler and recirculating water.

The water flow was controlled on the discharge side of the circulating pump and measured by conventional orifice plates. However, instead of pressure tappings, low-flow rotameters were installed in bypass circuits. The advantage of this system is that there is a linear relationship between the rotameter and total flow. Calibration showed the indicated readings to have an accuracy of $\pm 2\frac{1}{2}$ percent.

The recirculating water, representing real plant feedwater flow, was allowed to cascade freely through a series of perforated steel trays in the head and it attracted steam from the package boiler by condensation. The steam flowed via a pressure reducing/regulating valve, pipework and storage tank to enter the condensing head through a bled steam transfer pipe.

The heated water then accumulated on the floor of the head and discharged freely via a short drain to the storage tank.

The tank was in the form of a horizontal drum constructed of steel and glass, 600 mm in diameter by about 2840 mm in total length including the glass end-closures.

From the glass section of the horizontal tank, suction for the circulating pump was taken via a square-edged drain orifice and a single glass drain pipe (downcomer) 1080 mm long. The glass sections of the model facilitated both visual observation and photography, the end closures being graduated to provide a direct measurement of S/T water level H, which could be read to within about ± 2 mm in the non-boiling condition, but only to about ± 10 mm in the disturbed boiling state H′.

The size of the drain orifice of the model tank was designed to be variable, with four possible diameters varying from 50.3 mm to 149.3 mm with matching glass downcomers and corrugated bellows, to give a drain/tank radius ratio r/R of 0.0838 to 0.249. The ratios were chosen to approximate the radius ratios of the power station feed heaters and deaerators under investigation.

Choice in the design of the drain orifice also allowed other outlet geometries to be studied, e.g, conical outlets, projecting downcomers, Borda mouthpieces, etc.

To provide accurate and consistent measurement of the flow in the downcomer for both subcooled and saturated water, or two-phase steam/water mixtures, various devices were tried and for which duty a square-edged orifice plate was found to be least affected by local cavitation and noise.

A precalibrated differential pressure cell for measuring the effective S/T water head acting on the drain was located beneath the tank. Tappings were taken from the S/T steam space and at locations in the downcomer close to the drain and the circulating pump inlet.

The outputs for effective S/T head, S/T static steam pressure, pump suction pressure and flow measured by the orifice plate were continuously recorded on an oscillograph, while the storage tank water temperature and level were recorded by hand.

4 Experimental Procedure

Normal operating procedure was to set a low water flow and evacuate the system with a vacuum pump until all air had been expelled. The selected temperature was then attained by opening the steam supply to provide condensing heat transfer, and balancing the loop cooling. It was necessary to heat the water to at least 85°C and circulate for about half an hour to reduce the dissolved oxygen content sufficiently to obtain separation and conduct the experiments.

In order to simulate real plant steady-state and transient operating conditions, two experimental states are required:

(1) the S/T contents subcooled.

(2) the S/T contents boiling.

For a subcooled run, starting from a high water level in the S/T, the recording oscillograph was started and the pump suction flow gradually increased until separation at the storage tank drain was observed, with the formation of a steam-water interface in the glass downcomer and the S/T water discharging into the downcomer as a jet. The circulating flow was then adjusted to maintain the interface in the upper section of the downcomer. All pressures together with the S/T water level and temperatures were recorded. The flow was then gradually reduced to reflood the downcomer and return to the condition of normal flooded discharge.

The experimental procedure for a boiling run was to set the pump suction flow to a low predetermined value at which separation was known not to occur. Then, with the recorder running, the quick acting valve (Fig. 3) was opened to allow cold water to mix with and chill the water entering the condensing head which caused the S/T contents to boil. The degree of boiling could be varied from light to vigorous by selection of the rate of cold water injection for a given volume of contents. With boiling established the pump suction flow was gradually increased to once again cause separation, the formation of an interface and jet-like discharge. While boiling in the S/T continued, it was possible to hold the interface in the downcomer by flow control valve adjustment for a sufficient period of time to obtain a set of readings.

On terminating the cold water injection by closing the quick-acting valve, the S/T boiling quickly decayed-away and the downcomer reflooded to give normal flooded discharge.

The procedure for subcooled and boiling runs was repeated for decreasing S/T water levels until it was noted that a vortex was beginning to form above the drain as the tank depth became about equal to the drain diameter, and at that stage the runs for the particular drain size were discontinued, the studies being for vortex-free discharge.

The apparatus was then rebuilt to give a different orifice, downcomer and bellows diameter and the experiments repeated.

5 Experimental Results—Visual Observations

5.1 Subcooled Discharge. For low flows the discharge was as shown in Fig. 4(*a*). With the drain fully flooded the depth of water in the storage tank is a dependent variable whose value is determined by the inventory of the system. With increasing pump suction flow it was noted that eventually streak-lines of water vapor (steam) formed on the longitudinal axis of the S/T in the region of the drain orifice. A further increase in flow brought about a milky appearance of small steam bubble formation at the upper part of the downcomer as the water separated at the orifice to issue from the S/T into the downcomer as a jet. If the flow were held steady with a steady water level H in the S/T, an interface could be held in the downcomer pipe. From this interface, entrained steam bubbles collapsed noisily in about 0.5 m of water depth. However, a very small decrease in the regulated flow caused the interface to ascend and reflood the downcomer while an increase in flow caused the interface to

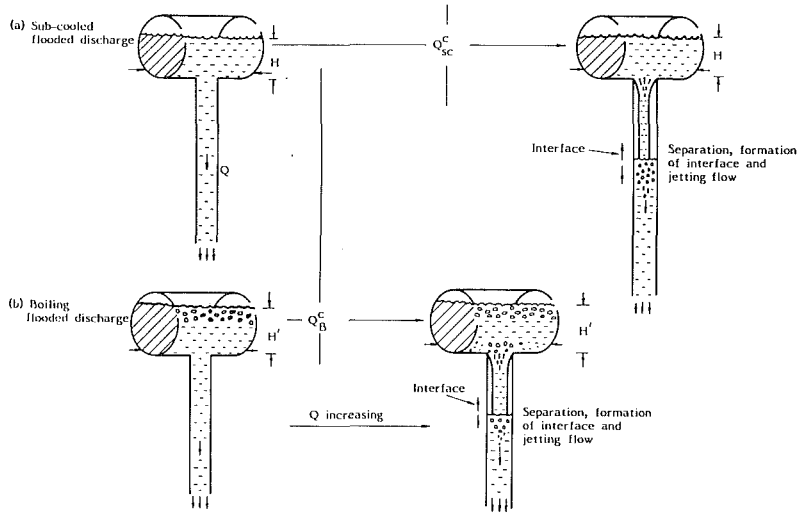

Fig. 4 Drum discharge via flooded drains, observed steam/water flow regimes, subcooled and boiling discharge

descend until steam was drawn into the suction pump accompanied by severe surging, noise and vibration of the pump.

5.2 Boiling Discharge. Having induced boiling of the S/T contents it was observed that for low suction flows, the drain remained fully flooded irrespective of the state of boiling, i.e., light to vigorous boiling of the tank water, Fig. 4(*b*). However, with an increase in suction flow very much less than that for the subcooled condition, separation at the drain orifice occurred in a similar way to result in the formation of an interface in the downcomer and jetting discharge.

Where steam bubble evolution was limited to the surface layers on the tank content, as in light to moderate boiling, no trapment of this steam at the drain was observed as separation occurred.

Maintaining the interface at a steady level in the downcomer the flow to the pump now fell to a somewhat variable value, much lower than that with subcooled discharge.

Again, a sufficient decrease in the suction rate caused the downcomer to reflood, with reflooding also occurring as soon as the S/T contents boiling decayed away as the water attained a new thermal equilibrium level at a lower temperature and pressure. Also, as before, increasing the suction rate caused the interface to descend and steam to enter the pump followed by the same severe pump disturbance. In one or two instances the imbalance of head became sufficient to cause the flow to reverse and a steam/water emulsion to surge back through the vapor filled pump, up the downcomer and empty into the expanded boiling contents of the S/T.

It was interesting to note that opening the air bleed (Fig. 3) in the separation regime either in the subcooled or boiling mode, caused the downcomer to immediately reflood. Separation was then inhibited until the water had once again been thoroughly deaerated.

6 Dimensional Analysis

Consider a smooth, horizontal tank of radius R containing water which discharges via a sharp-edged orifice of radius r, Fig. 5. Now at the point of onset of "incipient separation" from the edge of the orifice application of Bernoulli's equation along streamlines approaching the orifice gives

$$p_f + \rho g H - \frac{\rho U^2}{2} = p_v \tag{1}$$

where U is the peak velocity at entry to the downcomer.

As will be described in Section 8 we found that the difference between p_v, which is the vapor pressure corresponding to the temperature of the well-mixed tank contents, and steam pressure in the tank p_f was negligible during boiling discharge, i.e., $p_v \cong p_f$. The tank water depth is H and the water density ρ. As the apparatus is large the water viscosity and surface tension may be disregarded. The additional temperature dependent quantities, thermal conductivity, latent heat, specific heat and enthalpy are assumed to have little effect on the separation phenomenon. The initial and final deaerator temperatures of real plant during a decay incident are extremely variable. In the experiments the initial temperature for each run was set at about 88°C. For geometrically similar systems, the critical mean pipe velocity $\bar{U}^c$ ($= Q^c_B/\pi r^2$) might be written as

$$\bar{U}^c = \phi(\rho, p_v, g, H, R, r) \tag{2}$$

or using nondimensional groupings

$$\bar{U}^c/(gH)^{1/2} = f(H/R, r/R, p_v/\rho g R) \tag{3}$$

Deaerators may have a wide variation in the numerical value of the third term on the right-hand side of equation 3 depending on design and operating load. For the power station, Case 1 (para. 2) for example, $p_v/\rho g R$ may vary from 14.1 to 38.9. The corresponding value for the apparatus is about 20,

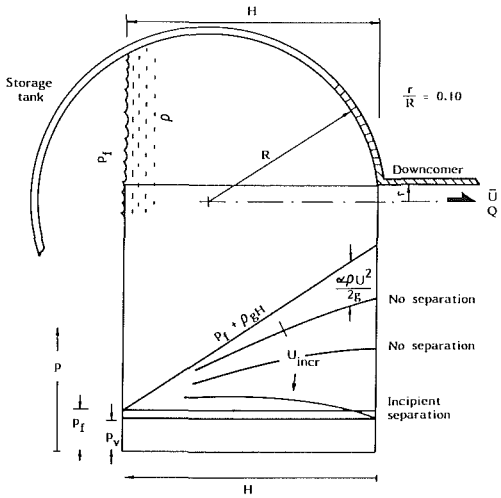

Fig. 5 Distribution and pressure at edge of drain orifice before and at onset of separation

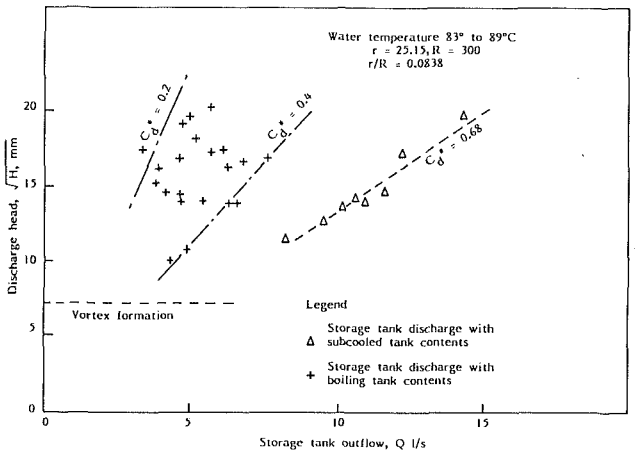

Fig. 6 Plot of results of head versus discharge for subcooled and boiling tank contents following separation. Precision: $H \pm 2$ mm (subcooled), $H \pm 10$ mm (boiling), $Q \pm 2.5$ percent.

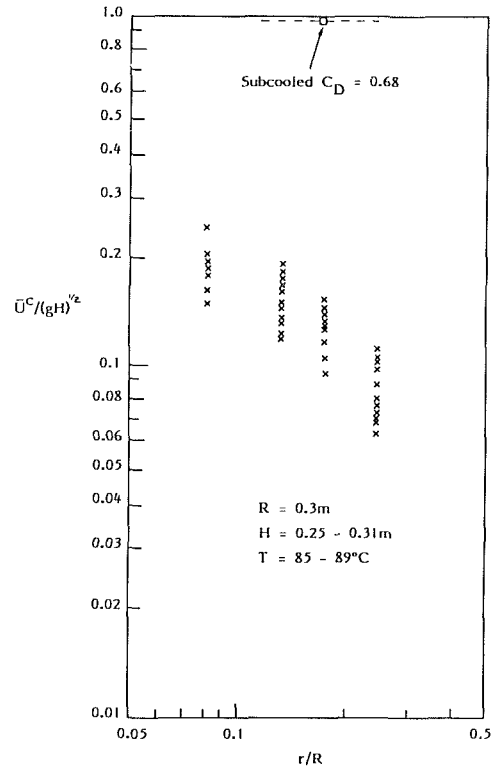

Fig. 7 Nondimensional plot of incipient separation in boiling discharge for the four-orifices studied. Uncertainty: $\bar{U}^c/(gH)^{1/2} \pm 4.6$ percent at 20:1 odds.

and is therefore considered to be representative of the real plant.

7 Experimental Measurements

A set of results for a discharge orifice radius $r = 25.15$ mm ($r/R = 0.0838$) is shown in Fig. 6 where discharge rate into the downcomer following separation is plotted as a function of S/T water depth.

In the case of the discharge of subcooled deaerated water consistent results were obtained in that separation occurred when the suction flow demanded exceeded the capability of the S/T outflow as governed by the usual notation for orifice type discharge, written simply as:

$$Q_{sc}^c = C_D \pi r^2 \left| \frac{2(p_f + p_H - p_v)}{\rho} \right|^{1/2} \tag{4}$$

where C_D is the coefficient of discharge, which was found to have the value of about 0.68 for this particular orifice/tank radius ratio. This is in fair agreement for horizontal tank discharge using air and water in jet type discharge of $C_D = 0.60$ as found by Kubie and Oates (1980).

8 Experimental Results for Boiling Discharge

The boiling discharge results, Fig. 6, for the 25.15 mm radius orifice, the S/T contents of varying depth and with light to vigorously boiling are scattered. There is no apparent correlation between the tank water depth and outflow, to give a generalized discharge coefficient, and so equation (4) is no basis to calculate the suction flow in the boiling mode. It will be noted however that using the rate of discharge as defined by equation (4) and putting $p_f = p_v$ and $p_H = \rho g H$, results in very low values of discharge coefficient of between 0.2 and 0.4. These low values of C_D are likely to be due to the variable amounts of steam drawn down through the drain.

By tapping the steam space in the S/T for p_f and the upper section of the downcomer for p_v, and then by using a suitable differential pressure measuring device, it was possible to compare the difference in the two steam pressures upon separation. For light to moderate S/T contents boiling the difference was found to be negligible while for very vigorous boiling 15 mm WG was the highest differential pressure seen ($p_f < p_v$). The largest difference is equivalent to a mean superheat in the water of only 0.06°C at 85°C. Thus the difference between p_f and p_v during boiling discharge is small compared to the hydrostatic pressure.

For the purpose of attempting to correlate the data for incipient separation in the boiling mode, a plot is made on log-log paper in Fig. 7 of the dimensionless groups $\bar{U}^c/(gH)^{1/2}$ and (r/R) for the four drain orifices investigated. For non-boiling discharge but where the tank pressure is held at the saturation pressure of the water, $p_v = p_f$, we might expect $\bar{U}^c/(gH)^{1/2}$ to be equal to the discharge coefficient $\sqrt{2}\, C_D$ and any shortfall represents the effect of the boiling of the tank contents.

In common with incipient cavitation, even in controlled laboratory experiments, wide variations in the critical velocity in the downcomer at incipient separation are found. For each particular orifice the measurements fail to remain consistent and result in scatter of the points. As in cavitation studies this appears to reflect a physical instability in the phenomenon rather than an inadequate test procedure.

The scatter of the experimental results and the small number of drain orifice sizes examined precludes any meaningful correlation, although from Fig. 7 over the range of drain sizes examined an interdependence of $\bar{U}^c/(gH)^{1/2}$ upon (r/R) does appear to emerge. For the smallest orifices, 25 and 41 mm radius ($r/R = 0.0838$ and 0.137), that this should remain so is perhaps surprising as discharge flow may more closely resemble that of an axisymmetric rather than an asymmetric system (Cranfield, 1981), when the critical suction flow at separation might be expected to remain about the same.

9 Discussion

The vortex-free, steady discharge of deep deaerated water from horizontal cylindrical tanks containing a steam atmosphere via flush square-edged orifices and flooded vertical drain pipes is shown to have two distinct flow regimes. For low suction flows the drain system runs fully flooded, whereas with increasing flow, separation takes place from the edge of the orifice to form a new steam/water interface in the downcomer pipe and jetting discharge from the tank.

For a given tank water depth, separation is governed by two

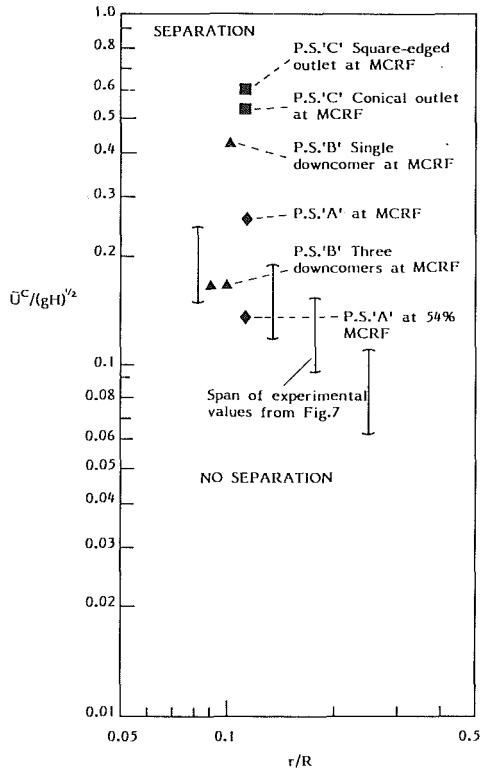

Fig. 8 Comparison of the separation from model experiments with real plant measurements for deaerators

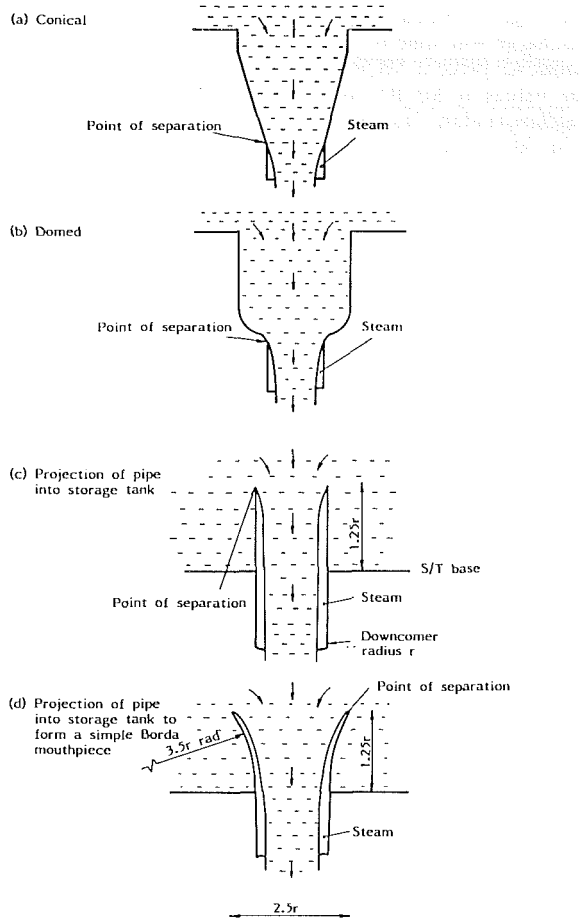

Fig. 9 Some designs examined as an alternative to square-edged drains for horizontal cylindrical tanks—none of which eliminated separation. Conditions following separation are shown.

separate critical suction flows dependent upon whether the tank contents are in a subcooled or boiling condition. The critical value for the boiling discharge is very much less than that when the contents are subcooled.

For subcooled tank contents, the critical flow for the transition between non-separating and separating discharge may be determined by use of the usual discharge coefficient C_D. For boiling tank contents discharge, which is considered of particular importance in deaerator design, it is suggested that for a given specific operating condition and geometries defined by tank water depth/tank radius ratio H/R, and by the drain/tank radius ratio r/R, the critical flow may be determined from modelling experiments. However, such is the degree of scatter of the experimental data that it indicates the need for further experiments and analysis to establish firm design criteria for a range of real plant operating conditions.

Boiler feed pumps taking their suction from deaerators have been subject to a loss of NPSH even though the plant appears to meet the requirements of the published and widely accepted models to ensure that this does not happen. We now have an explanation. In normal steady operation, the deaerator storage tank water is about 1° to 2°C subcooled relative to the tank pressure; with increased depth below the water surface the degree of subcooling increases, then the suction pipework may be designed with an adequate safety margin based on MCRF and an assumed value of $C_D \cong 0.68$ the downcomer will then operate in its normal fully flooded mode and will comply with the above models. However, during transient operation, where the deaerator may be subject to rapid pressure decay, the tank contents may boil when it is a lower critical flow which will apply with the coefficient of discharge falling as low as 0.2. Difficulties may then ensue from the loss of the pump suction pressure, steam formation and eventual transfer of steam into the suction pump as the new interface forms and descends in the downcomer leading to pump vapour locking, incorrect pressure balance across the pump, noise, vibration, overspeeding and an inability to maintain forward flow.

However, if the boiling period is brief, separation and reflooding of the downcomer may occur with no ill effect, remain undetected and may even be fairly common.

It is now interesting and informative to compare real plant experience with experimental results.

9.1 Deaerator S/T's with Single Downcomers. For Case 1, power station "A," assuming 1°C of subcooling and using equation (4) separation, might be expected to occur at a suction flow of 1370 kg/s. This would give a margin of safety based on MCRF of over 300 percent. However, if we calculate the value of $\bar{U}^c/(gH)^{1/2}$ for MCRF and NWL, and compare it with the experimental values of incipient separation as shown in Fig. 8, the plant value occurs well within the separation regime for boiling discharge. If we now refer to the recorded data for the loss of suction incident for this station, Fig. 2, on increasing the suction flow from 150 kg/s at $t = 290$ s a rapid collapse in suction pressure arises at $t = 380$ s as the flow reaches 225 kg/s, i.e., about 54 percent MCRF. This is in good agreement with the experimental results.

9.2 Deaerator S/T's With Multiple Downcomers. Also shown in Fig. 8 is data applicable to Case 2, power station "B." At MCR the nondimensional group $p_v/\rho gR$ (equation (3)) for this plant will be about 24.0, while H/R may vary from 0.78 to 1.78 from low to high water level, so the experimental results may also simulate specific conditions in this plant. Using a single downcomer, the plant value is well within

the region which implies that separation during boiling discharge will arise for MCRF or even for outflows exceeding about 45 percent MCRF. With the use of three downcomers the values at MCRF move towards the safe, nonseparating outflow region. Having a single suction pump the pipes must join at some point upstream of the pump inlet. The downcomer pipe junction in this case is some 26.3 m below the surface of the water in the S/T, at an adequate depth such that the increase in hydrostatic head less the (reduced) pipe friction losses is sufficient to keep the suction flow in the nonseparating region on its return to a single pipe downstream of the junction.

Multiple downcomers which are correctly sized will ensure that the downcomers remain fully flooded under transient conditions.

9.3 Deaerator S/T's With Shaped Downcomer Inlets. An obvious solution might be to shape the inlet of the downcomer, for example with a conical inlet, Fig. 9(a), adopted for Case 3, power station "C." Model tests show that separation no longer arises at the drain in the S/T floor which is increased in diameter, but merely transfers to the level where the cone rejoins the original downcomer. In the case of power station "C" this will result in an improvement in hydrostatic head from 3.35 to 4.24 m of water. The original value and the value with the cone of $\bar{U}^c/(gH)^{1/2}$ for this power station at MCRF are as plotted in Fig. 8. From this it will be seen that short conical outlets appear to offer no solution.

Discharge via the downcomer pipe projecting into the S/T was also examined. This was done for a simple parallel entrance and an entrance converging symmetrically to form a basic "Borda mouthpiece," Figs. 9 (*c*) and 9 (*d*). Neither were effective in inhibiting the subcooled or boiling separation.

Economics may dictate the consideration of alternative solutions to prevent separation in the suction pump downcomer. Some of these may be applicable to very large plant feed systems and are now discussed briefly.

9.4 Deaerator S/T's With Bypassing Arrangements. It has been proposed (Liao (1973a) that automatic opening of a valve initiated by S/T pressure decay might be used to bypass a predetermined quantity of the "cold" nondeaerated condensate flowing to the D/A. This bypass flow might be injected directly into the S/T contents above the drain to produce a local well-subcooled zone or into the downcomer to quench the feedwater flowing to the pump. Injection of cold water into the S/T was tried and appeared to work provided it was done before boiling and separation had occurred. However, injection into the downcomer would appear to generally offer no solution if limited to small bypass flows as the remainder will continue to pass via the S/T so that discharge may remain well within the separation region. Large bypassing flows would provide a solution unless the same trip or fault results in boiling in the final heater of the cascade (DC3, Fig. 1). Prevention of loss of pump suction pressure might be similarly achieved by ducting cooler water from the deaerator head directly to the S/T drain, with slots in the duct for inventory balance with the S/T contents. Although not tested on the model, these so called "anti-flashing baffles" have been evaluated on real plant, but were shown to have "negligible value" (Karassik (1981)). Bypassing the S/T contents may also result in stagnation of this water, which should be avoided.

9.5 Deaerators With Controlled Pressure Decay. An alternative, but perhaps costly solution is to control the D/A pressure decay rate with a detection/control system. By the admission of "live" steam from an alternative and separate supply the pressure might be "pegged" or let-down in a controlled manner to inhibit boiling. Control of D/A pressure by separate live steam sources seems fairly common practice on the Continent and similar systems have been described in the literature (Karassik, 1981a and Monks, 1984).

However, as transient pressure decay is a maximum in about 60 to 80 seconds after a turbine trip, the pegging steam must get to the D/A before that time. This calls for a special control and attention to steam-circuit design (O'Keefe, 1986).

A solution for P.S. "A" (Case 1, para. 2) is to be sought using the principle of controlled pressure decay. The condensate and D/A bled steam isolating valves, Fig. 1, will be replaced by control valves to allow small flows to be established following a trip to give a "balanced enthalpy" condition at the D/A. This will provide time to fully re-establish the feed system at low load without the S/T contents boiling and avoid a unit trip.

10 Conclusions

1. In tanks containing deep deaerated water in vortex free discharge through flooded downcomers a phenomenon may arise with separation at the drain orifice and formation of a new steam/water interface in the downcomer.
2. Separation may occur with the tank contents in either subcooled or boiling modes.
3. In open cycle feed systems with deaerators, outflow at separation in the subcooled mode may be many times the maximum continuous rating flow.
4. In open cycle feed systems with deaerators, outflow at separation in the boiling (transient) mode may be very much less than maximum continuous rating flow.
5. In the boiling mode the coefficient of discharge of the tank following separation may fall to very low values.
6. Following separation, an increase in the suction rate may cause the interface in the downcomer to descend such that the boiler feed pumps may be subject to cavitation, vapor locking, severe vibration, pressure imbalance and overspeeding with loss of forward flow and damage.
7. The experimental data for boiling discharge separation when plotted versus geometry expressed as the tank/downcomer radius ratio are scattered, but nevertheless show good agreement with available real plant data.

Acknowledgment

The work was carried out at the Marchwood Laboratories of the Technology Planning and Research Division and the paper is published with permission of the Central Electricity Generating Board, UK.

The author is grateful to his colleagues in the CEGB for their advice and help, in particular to Dr. D. E. Hobson and Mr. D. H. Wilkinson for their helpful comments, to Mr. E. Day for assistance in building and operating the experimental apparatus and Mr. B. Dash for Fig. 2 and data related to a loss of feed incident at an operational power station.

References

Cranfield, R. R., 1981, "Drain Discharge Characteristics of Horizontal Drums," *Journal of Mechanical Engineering Science*, Vol. 23, No. 2, pp. 77–83.

Cranfield, R. R., and Wilkinson, D. H., 1981, "Analysis of Power Plant Deaerator Storage Tank Instabilities," *Proceedings of Institution of Mechanical Engineers*, Vol. 195, pp. 251–259.

Cranfield, R. R., 1982, "Hydrodynamic Characteristics of Deaerator Drain Subject to an Adverse Differential Pressure," *Proceedings Institution of Mechanical Engineers*, Vol. 196, pp. 301–312.

Gage, A., 1952, "Criterion for the Suction Conditions of Feed Pumps," *4th International Congress on Industrial Heating*, Paris, Paper No. 36.

Karassik, I. J., 1980, "Steam Power Plant Clinic—Part XIV," *Combustion*, Jan., pp. 38–40.

Karassik, I. J., 1981, "Centrifugal Pump Clinic," *Pumps-Pompes-Pumpen*, pp. 569–571.

Karassik, I. J., 1981a, *Centrifugal Pump Clinic*, Marcell Dekker Publishing Corporation, Mechanical Engineering Series, Vol. 6, p. 396.

Kubie, J., and Oates, H. S., 1980, "Aspects of Outflow From Large Vessels," ASME, Vol. 102, pp. 324–329.

Liao, G. S., 1973, "Analysis of Power Plant Deaerator Under Transient Turbine Loads," ASME *Journal of Engineering for Power*, pp. 171–179.

Liao, G. S., 1973a, "Protection of Boiler Feed Pump Against Transient Suction Pressure Decay," ASME *Journal of Engineering for Power*, Paper No. 73-WA/Pwr-1, pp. 1–8.

Monks, C. J., 1984, "Feed-water Deaerators and Systems for Large Thermal Power Plant," *Institution of Mechanical Engineers, Seminar on Deaerators and Boiler Feed Pumps in Power Station Practice.*

O'Connell, L. P. F., and Rauscher, W. V., 1980, "Developments in Deaerator Design," *The 42nd Annual Meeting of the American Power Conference*, Chicago, Apr. 1980.

O'Keefe, W., 1986, "How to Avoid Transient Caused Problems in Boiler-Feed Pumps." *Power*, pp. 37–41.

Otway, F. O. J., 1969–70, "The Design Principles for Boiler Feed Pumps for CEGB 660 MW Units," *Proceedings of Institution of Mechanical Engineers*, pp. 11–17.

Sulzer Brothers Limited, 1985, "Suction Effects on Feedpump Performance: A Literature Survey," EPRI Report CS-4204.

Thurston, R. S., 1961, "Design of Suction Piping and Deaerator Storage Capacity to Protect Feed Pumps," ASME *Journal of Engineering for Power*, pp. 69–73.

Journal of Fluids Engineering

Technical Briefs

Very Low Reynolds Number Flow Through Screens

B. R. Munson[1]

Introduction

It is often necessary to know the pressure drop across a screen or grid structure when a fluid flows through it. Although a considerable amount is known about flow through screens in the moderate to large Reynolds number range [1, 2], such information is not available for the very low Reynolds number flows that result when the fluid is very viscous, the flow is very slow, and/or the number of strands per inch of the screen is very large.

The purpose of this note is to extend the screen pressure drop (or loss coefficient) data to very low Reynolds number flows. Such flows occur across the screens of cold oil pump inlets because of the large fluid viscosity. They are also important in the flight of tiny insects whose wings consist of minute, open-grid structures rather than the customary membrane-type structure of larger Reynolds number wings [3].

It has been shown that the pressure drop, Δp, across screens in moderate or large Reynolds number incompressible flows can be correlated by the pressure coefficient, $K = \Delta p/(\rho V^2/2)$, as

$$K = A_1 \, (1-\alpha^2)/\alpha^2 \qquad (1)$$

where $\alpha = (1 - d/l)^2$ is the porosity, d is the screen wire diameter, and l is the spacing between the wires [4]. The dependency of Δp on the screen porosity is adequately accounted for by the $(1-\alpha^2)/\alpha^2$ term, while the Reynolds number dependency is included in the fact that A_1 is a function of Reynolds number, $A_1 = A_1$ (Re). The Reynolds number is based on the wire diameter, $\mathrm{Re} = V d/v$. For Re > 1,000, the value of A_1 is essentially constant ($A_1 = 0.52$) [5], while for $20 < \mathrm{Re} < 1{,}000$, it is a slightly decreasing function of Re [4]. The purpose of this note is to provide A_1 (Re) for very small values of Re, in the range $5(10^{-5}) < \mathrm{Re} < 10^{-1}$.

Experimental Procedure

For this study we used square mesh, woven wire screens with wire diameter d and spacing l (see Fig. 1). The values of d, l and the porosity, α, for the five screens tested are shown in Table 1. The screen was placed in a pipe of 2.54-cm diameter connecting two reservoirs, and the flow was produced by applying a known pressure difference between the reservoirs. The pressure drop across the screen was assumed to equal this measured pressure difference minus the pressure drop required to produce the same flowrate without the screen. Since the Reynolds number was very small, fully developed flow in the pipe was established in a very short distance. Thus, the connecting pipe was relatively short (approximately 12 diameters) and most of the pressure drop was due to the screen. The flowrate was determined by direct measurement of the fluid volume displaced in a measured time interval. Uncertainties in the final data were determined to be ±7 percent in A_1 and ±5 percent in Re at 20:1 odds.

The fluid used was silicone oil with a kinematic viscosity of $v = \mu/\rho = 30{,}000$ centistokes (cs) and specific gravity 0.975. A few tests were conducted with oils of 1000 and 100 cs viscosity. Typical average velocities in the pipe were of the order 0.05 ft/s, with Re in the range of $5\ (10^{-5}) < \mathrm{Re} < 3$. Each of the five screens was tested at various flowrates with the 30,000 cs oil. Screen II was also tested with the 1000 and 100 cs oil.

Experimental Results

Generally, for most large Reynolds number flows, the pressure drop correlates with the dynamic pressure, $\rho V^2/2$, while for low Reynolds number flows it correlates with viscous effects, $\mu V/d$. This was found to be true for flow through screens also. For very low Reynolds number flow through screens the pressure drop was found to be directly proportional to the velocity, V, and viscosity. This dependence is indiciated in dimensionless form by the fact that the coefficient, A_1, is inversely proportional to the Reynolds number, Re. As shown in Fig. 2, the value of A_1 was found to be approximately $A_1 = 4.75/\mathrm{Re}$ for $\mathrm{Re} \lesssim 0.1$. For larger Re, the coefficient A_1 flares into its large Re value of 0.52 reported

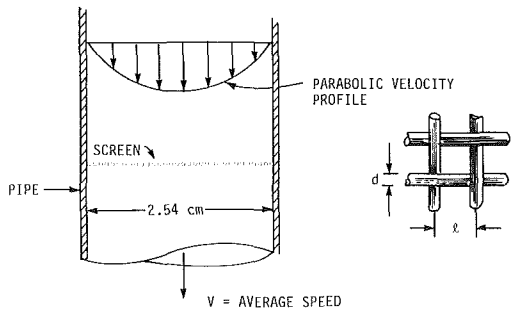

Fig. 1 Screen geometry

Table 1 Screen characteristics

Screen number	Mesh	d, mm	l, mm	α
I	40	0.250	0.635	0.368
II	20	0.381	1.270	0.490
III	20	0.356	1.270	0.518
IV	12	0.457	2.117	0.619
V	8	0.610	3.175	0.653

[1]Professor, Department of Engineering Science and Mechanics, Iowa State University, Ames, Iowa 50011.

Contributed by the Fluids Engineering Division of The American Society of Mechanical Engineers. Manuscript received by the Fluids Engineering Division January 16, 1986.

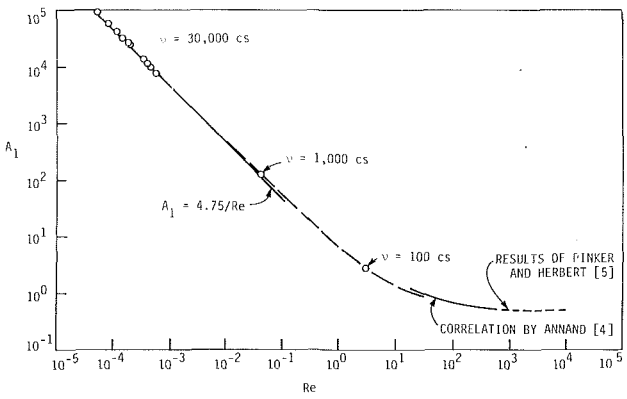

Fig. 2 The dependence of A_1 on Re. Low Reynolds number results of present study and previously reported moderate and large Re results.

in the literature. This Reynolds number dependence is very similar to that shown by the drag coefficient data for a sphere.

For moderate or large Re, the effect of porosity is incorporated into the loss coefficient data by the $(1-\alpha^2)/\alpha^2$ factor shown in equation (1) [4]. As shown in Fig. 3, for the screens tested ($0.368 \leq \alpha \leq 0.653$), this porosity factor also provides a reasonable correlation for very low Reynolds number screen flow. That is, all of the very low Reynolds number data for the five screens of different porosities fall (within experimental error) onto the curve $K = 4.75\ (1-\alpha^2)/(\alpha^2 \mathrm{Re})$.

The pressure drop across a screen at low Reynolds numbers can become quite large. Consider oil with $\nu = 30{,}000$ cs $= 0.323$ ft^2/s and specific gravity 0.975 flowing through screen II ($d = 0.00125$ ft, $\alpha = 0.490$) with an average speed of $V = 0.2$ ft/s. For this flow, $\mathrm{Re} = 7.74\ (10^{-4})$, $K = 1.94\ (10^4)$, and the pressure drop required is $\Delta p = K(\rho V^2/2) = 730$ lb/ft^2. This pressure drop is directly proportional to V and μ.

Conclusion

As indicated by the experimental results presented, the pressure drop across square-mesh wire screens is given by the correlation $\Delta p = 4.75\ (1-\alpha^2)\ (\rho V^2/2)/(\alpha^2 \mathrm{Re})$, provided $\mathrm{Re} \lesssim 0.1$. The dependence on the porosity, α, is the same as that given previously for large or moderate Reynolds number screen flow, and the inverse dependence on Re is as expected

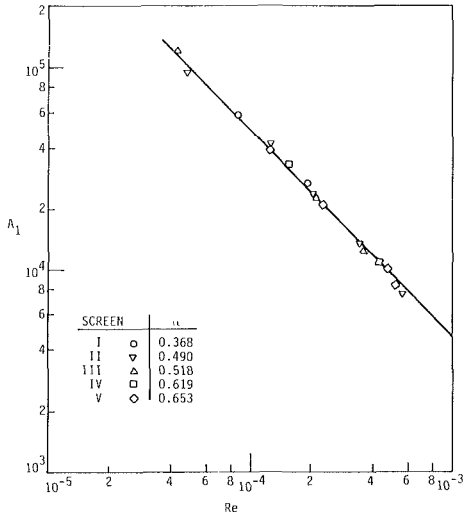

Fig. 3 The dependence of A_1 on Re for screens of various porosities

from other low Reynolds number flow situations. These results should provide a useful extension to the low Reynolds number regime of previous moderate Reynolds number results.

Acknowledgment

The support of the Iowa State University Research Institute and Deere and Company is appreciated.

References

1 Laws, E. M., and Livesey, J. L., "Flow Through Screens," *Annual Review of Fluid Mechanics*, Vol. 10, Annual Reviews, Inc., 1978, pp. 247–266.

2 Hoerner, S. A., *Fluid Dynamic Drag*, published by author, Midland Park, N.J., 1965.

3 Kueth, A. M., "On the Mechanics of Flight of Small Insects," *Swimming and Flying in Nature*, Vol. 2, Plenum Press, 1975, pp. 806–813.

4 Annand, W. J. D., "The Resistance to Air Flow of Wire Gauzes," *Journal of the Royal Aeronautical Society*, Vol. 57, 1953, pp. 141–146.

5 Pinker, R. A., and Herbert, M. V., "Pressure Loss Associated with Compressible Flow through Square-Mesh Wire Gauzes," *Journal of Mechanical Engineering Science*, Vol. 9, No. 1, 1967, pp. 11–23.